Technische Universität München
Institut für Energietechnik
Lehrstuhl für Thermodynamik

Prediction of Acoustic Modes in Combustors using Linearized Navier-Stokes Equations in Frequency Space

Jannis Gikadi

Vollständiger Abdruck der von der Fakultät für Maschinenwesen der Technischen Universität München zur Erlangung des akademischen Grades eines

Doktor – Ingenieurs

genehmigten Dissertation.

Vorsitzender:

Univ.-Prof. Dr.-Ing. habil. Nikolaus A. Adams

Prüfer der Dissertation:

1. Univ.-Prof. Dr.-Ing. Thomas Sattelmayer
2. Univ.-Prof. Dr.-Ing. Johannes Janicka
   Technische Universität Darmstadt

Die Dissertation wurde am 09.07.2013 bei der Technischen Universität München eingereicht und durch die Fakultät für Maschinenwesen am 08.11.2013 angenommen.

Für meinen Vater.

Vorwort

Die vorliegende Arbeit entstand in den Jahren 2009 bis 2013 während meiner Tätigkeit am Lehrstuhl für Thermodynamik der Technischen Universität München.

Zuallererst möchte ich meinem Doktorvater Herrn Professor Dr. Thomas Sattelmayer danken. Sein Vertrauen, die Freiheit neue Wege zu beschreiten und sein Rückhalt haben mir die Möglichkeit gegeben, dieses Promotionsprojekt erfolgreich abzuschließen. Von seinem breiten Erfahrungsschatz aus Industrie und Wissenschaft habe ich dabei sehr profitiert. Zudem möchte ich mich bei Herrn Professor Dr. Johannes Janicka für die Übernahme des Zweitgutachtens bedanken. Ich habe seine wissenschaftliche Arbeit immer bewundert und verfolgt. Nach der Durchführung meiner Diplomarbeit unter seiner Leitung schließt sich hier für mich ein Kreis. Ebenso gilt mein Dank Herrn Professor Dr. Adams für die Übernahme des Vorsitzes.

Meinen Kollegen am und außerhalb des Lehrstuhls möchte ich für die vielen wertvollen Diskussionen, gemeinsame Kaffeepausen und Erlebnisse in München danken. Insbesondere die Zusammenarbeit mit Christoph Jörg und Michael Wagner stellt für mich ein Benchmark in Sachen Teamarbeit dar. Ich bewundere Eure Professionalität und Hingabe zum Maschinenbau. Vielen Dank für Eure Freundschaft.

Im Rahmen des europäischen Projektes KIAI hatte ich das außerordentliche Glück Professor Thierry Schuller und Professor Jim McGuirk kennen und schätzen zu lernen. Ihnen danke ich für die intensiven Unterhaltungen und Diskussionen auf Konferenzen und während unserer halbjährigen Projekttreffen. Dieses europäische Projekt war Werbung für den europäischen Gedanken und Integration. Für die finanzielle Unterstützung der Europäischen Kommission im Rahmen des 7-ten Rahmenprogramms (Grant Agreement No.: 234009) bedanke ich mich deshalb sehr.

Meinen zahlreichen Studenten möchte ich ebenso danken. Ohne Euch wäre diese Arbeit in dieser Form nicht entstanden. Vor allem meinen Studenten und späteren Kollegen Wolfram Ullrich möchte ich an dieser Stelle heraus heben, bei dem ich das Glück hatte ihn zweimal zu betreuen.

Mein grösster Dank gilt jedoch meiner Freundin, meinem Bruder und meinen Eltern. Eure Liebe und euer unendliches Vertrauen in mich haben mir immer wieder die Kraft gegeben, meine Ziele weiter zu verfolgen. Erst durch meinen Vater entwickelte ich eine Faszination für den Maschinenbau. Ich kann Euren Anteil nicht genug würdigen!

München, im Januar 2014 Jannis Gikadi

Kurzfassung

Neue emissionsarme Brennkammern von Gasturbinen sind anfällig gegenüber dem Phänomen der thermoakustischen Instabilitäten. Diese entstehen durch die Koppelung der Wärmefreisetzung der Flamme und Druckfluktuationen und können zum Aufbau hoher Druckamplituden führen. Beschädigungen der Brennkammer sowie Einschränkungen des Betriebsbereiches der Turbine sind die Folgen. Aus diesen Gründen ist eine frühzeitige Vorhersage von Instabilitäten von hoher Bedeutung um hohe Zusatzkosten durch Entwicklung und Wartung zu vermeiden.

Zur Vorhersage von thermoakustischen Instabilitäten sind bereits eine Reihe von Methoden entwickelt worden. Aus der Sicht des Autors existiert eine Lücke zwischen Modellen niedriger Ordnung, die eine schnelle aber weniger genaue Vorhersage ermöglichen, und Modellen hoher Ordnung, die zwar sehr genau sind aber viel Rechenzeit in Anspruch nehmen. Diese Arbeit probiert diese Lücke mit der Einführung von linearisierten Navier-Stokes Gleichungen (LNSEs) zu schließen. Anders als Modelle mit niedriger Genauigkeitsordnung berücksichtigen diese Gleichungen die Interaktion von mittlerem Strömungsfeld und akustischen Wellen direkt. Zudem wird der Einfluss komplexer, dreidimensionaler Brennkammergeometrien sowie akustischer Impedanz-Randbedingungen und Flammen berücksichtigt. Dabei vereinfacht die Transformation der Gleichungen in den Frequenzbereich deren numerische Behandlung substanziell. Die Gleichungen werden in zwei Schritten gelöst: Zunächst wird eine inkompressible Strömungssimulation durchgeführt, um im Anschluss die LNSEs um das resultierende mittlere Strömungsfeld zu lösen. Dabei hat die Interaktion von mittlerer Strömung und akustischen Wellen meist einen stabilisierenden Effekt auf akustische Moden, kann aber auch umgekehrt destabilisierend wirken.

Diese Dissertation entwickelt Lösungen auf den unterschiedlichen Ebenen der wissenschaftlichen Wertschöpfungskette: Angefangen mit der Herleitung der theoretischen Grundlagen wird eine konsistente Behandlung der LNSEs im Rahmen von Finiten Elementen vorgeschlagen. Die diskretisierten Gleichungen können dann mittels einem eigens entwickelten iterativen Lösungsverfahrens für unterschiedliche Problemstellungen der Thermoakustik oder Aeroakustik gelöst werden.

Abstract

New low emission combustion technologies for gas turbines are prone to a phenomenon called thermoacoustic instability. Such instabilities arise from the coupling of the unsteady heat release rate of a flame and pressure fluctuations, imposing restrictions on the operability range and damaging hardware components. High costs may accumulate due to commissioning or operating the combustor under non-optimal conditions. Therefore, detection of instabilities in the early phases of a gas turbine development cycle is desired in order to avoid costly correction steps at later stages.

To predict thermoacoustic instabilities many tools are already available. However, a gap is present between lower order models which allow for a quick assessment of instabilities and higher order tools which are computationally expensive, like e.g. compressible large eddy simulations. This thesis fills this gap by introducing linearized Navier-Stokes equations (LNSEs) formulated in frequency space. Unlike lower order models, the LNSEs include the interaction of the mean flow with acoustic waves directly, and provide a good trade-off between computational costs and accuracy. The proposed model includes the effects of a multidimensional flow field and geometries, complex impedances and flames. It works as a two-step approach: First, performing an incompressible flow simulation using an appropriate turbulence closure and then, in a second step, solving the LNSEs around the resulting mean flow state. Interactions of acoustic waves with the flow field may lead to a stabilizing but also to a destabilizing effect on thermoacoustic instabilities.

The thesis provides a full scientific value chain: Starting from the basic theory it develops a consistent finite element procedure and provides especially designed iterative solvers which may efficiently solve the LNSEs for large-scale industrial configurations. This procedure is validated on a variety of different flow and combustion configurations including generic as well as more industrial cases.

Contents

Nomenclature

Abbreviations

AFR	air fuel ratio
Bi-CG	biconjugate gradients
BiCGstab	biconjugate gradients stabilized
CAA	computational aeroacoustics
CC	combustion chamber
CDR	convection diffusion reaction
CERFACS	Centre Europén de Recherche et de Formation Avancée en Calcul Scientifique
CFD	computational fluid dynamics
CFL	Courant–Friedrichs–Lewy
CG	conjugate-Gradient
CPU	Central processing unit
DS	downstream
EC	European Commission
FAR	Fuel air ratio
FDF	flame describing function
FEM	finite element method
FFT	fast Fourier transformation
FTF	flame transfer function
FGMRES	flexible generalized minimal residuals
GLS	galerkin/least-squares technique
GMG	geometric multi-grid
GMRES	generalized minimal residuals
GS	Gauß-Seidel

GTG	geometric two-grid
JAC	Jacobi
JAGS	just another Gibbs sampler
JD	Jacobi-Davidson
KIAI	knowledge for ignition and acoustic instabilities
LEEs	linearized Euler equations
LES	large eddy simulation
LHS	left hand side
LNSEs	Linearized Navier-Stokes equations
LP	lean premixed (combustion)
LPP	lean premixed pre-vaporized (combustion)
MGS	modified Gram-Schmidt
MUMPS	multifrontal massively parallel sparse direct solver
NGV	nozzle guide vane
NS	Navier-Stokes
ODV	ordinary differential equation
OGV	outlet guide vane
PARADISO	parallel direct sparse solver
PERM	partially evaporation rapid mixing
RANS	Reynolds averaged Navier-Stokes simulation
RHS	right hand side
RQL	rich (quick) quench/mix lean (combustion)
SFEM	stabilized finite element method
SGS	subgrid scale
SOR	successive over relaxation
SU	streamline-upwind
SUPG	streamline-upwind/Petrov-Galerkin
SUR	successive under relaxation
TUM	Technische Universität München
US	upstream
WALE	wall attached layer eddy

Notations

Bilinear forms

$B(*;*)$	bilinear form
$B_C(*;*)$	bilinear form of stabilization term - LNSEs continuity
$B_M(*;*)$	bilinear form of stabilization term - LNSEs momentum
$B_E(*;*)$	bilinear form of stabilization term - LNSEs energy

Domains and boundaries

$\partial\Omega$	domain boundary
$\partial\Omega_D$	Dirichlet boundary
$\partial\Omega_N$	Neumann boundary
$\partial\Omega_Z$	impedance boundary
$\partial\Omega_e$	element boundary
$\partial\Omega'$	union of all interior element boundaries
Ω	computational domain
Ω^e	single element domain
Ω'	union of element interiors

Finite Element matrices and vectors

$\mathbf{A}$	global system matrix
$\mathbf{A}^e$	element system matrix
$\mathbf{C}$	convective matrix CDR
$\mathbf{D}$	diffusive matrix CDR
$\mathbf{E}$	Dirichlet boundary vector CDR
$\mathbf{M}$	frequency dependent mass matrix CDR
$\mathbf{N}$	Neumann boundary vector CDR
$\mathbf{M}$	frequency dependent mass matrix CDR

Linear solution algorithms matrices and vectors

$\mathcal{K}_m$	Krylov subspace of size m
$\mathbf{H}$	upper Hessenberg matrix
$\mathbf{L}$	lower triangular matrix
$\mathbf{P}_R$	right preconditioning matrix

$\mathbf{P}_L$	left preconditioning matrix
$\mathbf{Q}$	orthonormal unitary matrix
$\mathbf{Q}$	matrix containing orthogonal Krylov subspace vectors
$\mathbf{R}$	upper right matrix
$\mathbf{U}$	upper triangular matrix
$\mathbf{b}$	right hand side vector
$\mathbf{d}$	defect GMG
$\mathbf{e}$	error GMG
$\mathbf{r}$	residuum
$\mathbf{x}$	vector of unknown quantities
$\mathbf{y}$	eigenvector of Hessenberg matrix

Function spaces

$\mathcal{H}^1(\Omega)$	Sobolev space of square-integrable functions with square-integrable derivatives
$\mathcal{S}_{\{\rho,\mathbf{u},p\}}$	combined solution function space of LNSEs
$\mathcal{V}_{\{\rho,\mathbf{u},p\}}$	combined weighting function space of LNSEs

Mathematical symbols

$\langle * \rangle$	time average
$\vert * \vert$	absolute value, amplitude
$(*,*)_\Omega$	L_2-inner product
$\vert\vert \dots \vert\vert_0$	L_2-norm on Ω
$\widehat{(\dots)}$	linearization
$\forall$	for all
$\in$	in
$\mathbb{C}$	complex space
$\Phi(*)$	phase value
$\mathcal{O}$	order symbol
$\Im$	imaginary part
$\Re$	real part
$\mathbb{R}$	real space

Operator symbols

∇	gradient operator
$\nabla\cdot$	divergence operator
$\nabla\times$	rotation operator
Δ	Laplace operator
$\mathcal{L}$	differential operator NS
$\mathcal{L}^*$	adjoint differential operator NS
$\mathcal{P}$	differential operator SFEM
$\mathcal{P}^*$	adjoint differential operator SFEM
$\mathcal{R}_C$	residual of LNSEs continuity equation
$\mathcal{R}_M$	residual of LNSEs continuity equation
$\mathcal{R}_E$	residual of LNSEs energy equation

Scalars - Greek symbols

α	damping rate, $= \Im(f)$
γ	type of GMG cycle
δ_a	acoustic boundary layer thickness
δ_f	flame sheet thickness
δ_h	hydrodynamic boundary layer thickness
ϵ	error, small value
κ	ratio of specific heats
$\kappa(*)$	condition number
λ	thermal diffusivity
λ	air-fuel equivalence ratio
λ_a	wavelength of acoustic mode
λ_v	wavelength of vortical mode
λ_s	wavelength of entropy mode
λ_i	Ritz eigenvalues
μ	dynamic physical viscosity
μ	eigenvalue of shifted problem
ν	kinematic physical viscosity

ν_{art}	kinematic artificial viscosity
ν_1	number of pre-smoothing iterations GMG
ν_2	number of post-smoothing iterations GMG
ξ_{min}, ξ_{max}	minimal and maximal eigenvalues of acoustic exergy matrix
ρ	density
$\rho(*)$	spectral radius
σ	reaction coefficient
σ	target value for shift and invert method
τ	time delay of n-τ model
τ_l	local time delay of n-τ model
τ_{stab}	stabilization parameter
τ_C	stabilization parameter - LNSEs continuity
τ_M	stabilization parameter - momentum
τ_E	stabilization parameter - LNSEs energy
ϕ	arbitrary variable
ω	pulsation
ω	scalar vorticity
ω_{SOR}	relaxation parameter SOR

Scalars - Latin symbols

A	area
B_1, B_2	Bessel functions of first and second order
E	energy
$\mathcal{F}$	flame transfer function
K_R	Rayleigh conductivity
L	length
L_f	reaction zone thickness
L_a	characteristic acoustic length scale, i.e. wavelength
N_e	number of finite elements
N_v	number of vertices
P	acoustic power
$\dot{Q}$	global heat release rate
R	reflection coefficient
R	specific gas constant

T	temperature
T	acoustic oscillation period
V	volume
V_f	flame volume
W	acoustic power
Z	complex impedance
c	speed of sound
c_p	specific heat at constant pressure
c_v	specific heat at constant volume
d	diameter
e	specific energy per unit volume
f	frequency
h	specific enthalpy
h	typical FEM element size
h_ϕ	Neumann boundary term for CDR equation
i	imaginary number
k	wave number
m	dimensions of upper Hessenberg matrix
m_{air}	air mass flow
n	strength of flame response of n-τ model
n_l	strength of flame response of n-τ model
p	pressure
p	order of interpolation functions
$\dot{q}_V$	heat release rate per unit volume
s	entropy
s_ρ	source of NS continuity equation
s_p	source of NS energy equation
s_ϕ	source of CDR equation
t	thickness
t	time
w_ρ	weighting function LNSEs continuity
w_p	weighting function LNSEs energy
w_ϕ	weighting function CDR

x_f	flame location

Tensors and tensor related notations

$\mathbf{S}$	scattering matrix
$\mathbf{S}_e$	scattering matrix in terms of exergy
δ_{ij}	Kronecker delta
h_{ij}	coefficients of upper Hessenberg matrix
τ, τ_{ij}	viscous stress tensor
σ, σ_{ij}	stress tensor
$(.)^T$	transpose of tensor
$(.)^*$	hermitian transpose

Value specifications

$(.')$	fluctuating quantity in time space
$(\bar{.})$	mean quantity
$(\hat{.})$	amplitude in frequency space
$(.)^h$	discrete quantity
$(.)_i$	value at iteration step i

Vectors

I_i	acoustic energy flux vector
$\mathbf{P}$	vector of unknown pressure (and entropy) fluctuations
$\mathbf{f}$	acoustic forcing vector
$\mathbf{g}, g_i$	gravity force vector
$\mathbf{g}$	Dirichlet boundary vector
$\mathbf{h_u}$	Neumann boundary vector
$\mathbf{n}, n_i$	normal unitary vector
$\mathbf{q}$	orthogonal vectors of the Krylov subspace
$\mathbf{s_u}$	source vector for NS momentum equation
$\mathbf{u}, u_i$	velocity vector
ω	vorticity vector
$\mathcal{V}$	eigenvector
$\mathbf{w_u}$	weighting function vector LNSEs momentum

$\mathbf{x}, x_i$	spatial coordinate vector
$\boldsymbol{\omega}$	vorticity vector

Non-Dimensional Numbers

He	Helmholtz number
Ma	Mach number
Nu	Nußelt number
Pe	Péclet number
Pr	Prandtl number
Re	Reynolds number
St	Strouhal number

1 Introduction

The increase of worldwide energy demand poses significant challenges for the future. Although energy generated by renewable sources is predicted to increase significantly, the major part of the global energy of about 80% will still be contributed by liquid fuels, coal or natural gas in 2035 according to the U. S. Energy Information Administration (2010). Especially the consumption of natural gas to generate electric power is projected to increase by 44%.

Gas turbines are used to transform the energy bound in chemical molecules into electric power or propulsion. They provide a large part of the world's electricity (21% in 2010, see International Energy Agency) and represent the only source for aviation propulsion systems. Considering the finite availability of fossil fuels, the efficiency of gas turbines has to be significantly increased in order to reduce fuel consumption. However, the increase in efficiency is constrained by the demand to produce lower emissions. Both goals are generally not fully congruent: While carbon dioxide, a gas known to enhance the greenhouse effect, can only be reduced by increasing the efficiency, the emission of nitrogen oxides (NO_x) strongly depends on the combustion process considered.

NO_x emissions in gas turbines are strongly temperature dependent. By decreasing the stoichiometry of the combustion process, combustion temperatures can be decreased, which as a result decreases the NO_x production (Correa, 1993). In the stationary gas turbine industry, this was achieved through the introduction of lean premixed combustion. A similar technology, termed lean premixed pre-vaporized (LPP) technology, was also established for liquid fueled gas turbines of the stationary gas turbine industry (Jansohn et al., 1997). Very recently, this concept is also being adopted by the aeroengine industry. The extension 'pre-vaporized' results from the fact that the liquid fuel employed needs to be vaporized first in order to be burnt. These lean premixed technologies were found, however, to be par-

ticularly susceptible to a phenomenon called combustion or thermoacoustic instability (Lieuwen and McManus, 2003).

1.1 Combustion Instabilities

Combustion instabilities arise due to the interaction of unsteady flame and acoustic field of the combustion chamber. The unsteady heat release acts as a source of sound and, under unfavorable conditions, may excite an acoustic resonance of the combustion chamber. The acoustic mode, in turn, may perturb the flame even stronger, establishing a feedback loop which leads to significantly high pulsation amplitudes. For gas turbine applications, these oscillations may reach amplitude levels of the order of a few percent compared to the static pressure ($\backsim \mathcal{O}(100\,\mathrm{Pa})$).

The conditions, under which a thermoacoustic feedback loop is likely to occur, can be expressed in terms of the well-known Rayleigh criterion (see Rayleigh, 1878, 1926): If the phase relationship between pressure and heat release fluctuations is just right, i.e. both are in-phase, instabilities are amplified and grow in time, viz.

$$\mathcal{R} = \int_t \int_\Omega p'(\mathbf{x},t) q'(\mathbf{x},t)\; d\Omega\; dt \tag{1.1}$$

When $\mathcal{R} > 0$, flame-acoustics coupling promotes the appearance of instabilities.

Structural damage and enhancement of high-cycle fatigue caused by large amplitude pressure fluctuations are the consequences of operating combustion chambers under such unstable conditions. In fact, a majority of the non-fuel costs of stationary gas turbines are attributed to maintenance, i.e. repair and replacement of hot-section components. Damages occurring in these sections are often related to combustion-driven instabilities (Lieuwen and Yang, 2005). Hardware failure can be prevented by incorporating appropriate monitoring systems. However, in this case, combustion instabilities still restrict the region of operability of combustion chambers, preventing gas turbine operation at optimal efficiency and emission levels. Other undesirable phenomena are the high noise levels produced, which may be radiated into the far-field at the gas turbine exhaust of aeroengines or

may cause wear of system components. Combustion instabilities also cause higher NO_x emissions and may favor circumstances under which flame flash-back or blow-off occurs.

Combustion instabilities are observed in various combustion applications, such as rocket engines, furnaces, or even heating devices. For civil aero-engines, combustion instabilities are less frequently encountered and are less severe as for their power generation counterpart (Lieuwen and Yang, 2005). It can be expected, however, that this topic will become more and more problematic, because increasing regulatory standards on future emissions force the aero-industry to adapt the lean-premixed combustion technology (Mongia et al., 2003). Based on this background, the European Union founded a project called 'KIAI - knowledge for ignition and acoustic instabilities'[1] which was launched in 2009. Its main aim is to provide accurate simulation tools to predict combustion instabilities in early design phases, minimizing the risks and costs of undergoing the development cycle multiple times. Thus, using such predictive tools may help to increase the future standards of engine's reliability, safety and economical viability and may foster the understanding of the mechanisms behind combustion instabilities. This thesis evolved as a part of the KIAI project.

Methods predicting combustion instabilities aim at providing the frequencies at which coupling occurs and whether the corresponding acoustic mode grows in time or is attenuated by acoustic loss processes. In addition to the frequencies of oscillation, the corresponding eigenmode or eigenfunction is obtained, which gives insights into the spatial distribution of the fluctuating quantities like pressure, velocity and temperature and may yield the necessary information for the installation of active or passive damping devices. Moreover, information about the finite amplitude of oscillation (limit cycle amplitude) is generally thought for. Other than computational expensive large eddy simulations, no method available at present takes the complex geometry and multidimensional flow conditions into account. The flow field, however, has a significant influence on the frequency and mode shape of oscillation. Without its proper incorporation, also limit cycle amplitudes may not be predicted accurately. This thesis developes a consistent method to account for flow fields and their effect on combustion instabilities.

[1] http://www.kiai-project.eu

As the topic of combustion instabilities attracts growing attention to research groups worldwide and many gas turbine manufacturers become increasingly sensitive, a huge amount of knowledge has been gathered so far. Covering all fundamental aspects of thermoacoustic instabilities and details on predictive methodologies is thus not possible in this thesis. For a decisive and comprehensive review the work of Candel (2002) is therefore recommended. More recently, Huang and Yang (2009) dedicate their review article to swirl-stabilized combustion dynamics. Books have also been published: An introduction to thermoacoustic instabilities is provided in Poinsot and Veynante (2005), while Lieuwen and Yang (2005) provide a particular focus on gas turbines.

1.2 Prediction of Combustion Instabilities

In order to account for the effect of the mean flow onto combustion instabilities this thesis proposes to linearize the set of Navier-Stokes equations (LNSEs). Other publications found in the literature, e.g. the ones of Bogey et al. (2002); Ewert and Schröder (2003); Seo and Moon (2005), introduce further assumptions in order to partially decouple the system of linearized transport equations and to reduce numerical difficulties involved in their solution process. By doing so, however, the main interaction processes are either not accounted for or only to some partial extent. Thus, unlike in these publications, this thesis solves the full set of linearized governing equations. The resulting numerical difficulties are resolved by solving the equations in frequency space and introducing stabilized finite element techniques. Latter methods introduce low amounts of numerical diffusion to avoid spurious oscillations of the solution. When solved using Krylov subspace methods conjointly with a multigrid preconditioner, also proposed in this thesis, this results in a highly robust and efficient technique. In this section an overview of different prediction methods to study combustion instabilities is provided and the LNSEs approach is integrated into this global framework.

Depending on the available resources, predictive methods with different capabilities and prediction accuracies can be applied. Common to all of them is that they are based on the Navier-Stokes equations with different levels of approximation. A most common approach found in the literature is based

on the approximation of a combustor through a network of one or quasi two dimensional homogeneous elements (constant density and speed of sound). Each individual element is connected to the other via jump relations, which enforce continuity in pressure and conservation of mass flow rate. Amplitudes of the forward and backward propagating waves must satisfy these relations. The flame is considered to be infinitely thin and connects the reactive mixture to the burnt gases segment. A dispersion problem can be formulated analytically, whose discrete roots ω describe the eigenmodes of the combustor and satisfy all jump relations across the individual elements. The main advantage of this approach is related to its simplicity: Complex geometries are described through a few lumped elements. Fast assessment of the combustion chamber eigenmodes can be achieved. The methodology is therefore extensively be used as a predesign tool (Nicoud et al., 2007). Extensions to azimuthal spinning modes (Evesque and Polfike, 2002; Evesque et al., 2003) and quasi two dimensional space (Benoit, 2005) can also be found in literature. However, the main drawback of the method is that it is not able to account for the geometrical complexity of combustion chambers. Mean flow effects of complex elements can only be accounted for, if external information obtained from higher order numerical analysis or experimental measurements is included.

An alternative is the use of a wave equation which can be discretized, e.g. using a finite element technique, for an arbitrary combustion chamber geometry including geometrical details (Pankiewitz and Sattelmayer, 2003). Fields of density and speed of sound are inputs to such a solver. The acoustic field is initialized with a random distribution of pressure fluctuations and the wave equation is solved in time domain. Depending on the acoustic-flame coupling certain modes of instabilities are amplified and grow exponentially. This method represents a very intuitive way to predict combustion instabilities. However, as it is discussed in the following chapters, solving the problem in physical space introduces certain difficulties. One is related to the fact that accounting for frequency dependent impedance boundaries is not trivial when solving in time domain. Moreover, starting from the initial fields multiple unstable modes may be amplified. Depending on their respective strength, only the most amplified mode can be observed in detail. The least amplified mode, however, can also be threatening when thermoacoustic instabilities are observed.

A more convenient alternative is the the use of the Helmholtz equation, the frequency domain counterpart of the wave equation (Benoit and Nicoud, 2005; Nicoud et al., 2007). This resolves the impedance boundary problem and transforms the initial value problem of the wave equation into an eigenvalue problem. Pairs of eigenfunctions and eigenfrequencies of every single mode are solutions to this method, which admits a detailed analysis of every individual combustion chamber mode and its respective growth rate. The main disadvantage to these type of methods (wave- or Helmholtz eq.) is that the equations are derived for a quiescent medium ($\bar{u} \backsimeq 0$) and thus acoustic-flow coupling and its related acoustic losses are not taken into account. This leads to the point that if an unsteady flame is incorporated into the formulation, certainly some eigenmodes will exhibit an unstable behavior. A method which incorporates stability reserves through acoustic-flow coupling though, will predict a more stable combustion operation by trend. Until now, no clear justification has been provided to neglect mean flow field effects, see e.g. Keller et al. (1985); Polifke et al. (2001); Sattelmayer (2003). Even on the contrary, there is strong evidence that the mean flow may significantly alter the eigenmode appearance and introduce stronger damping to the system (Dowling, 1995; Nicoud and Wieczorek, 2009).

An approach taking into account acoustic coupling with the flow field and even with chemistry and turbulence is the large eddy simulation or LES (Martin et al., 2006; Selle et al., 2004). However, main drawback of an LES is its computational costs: As turbulence is resolved up to smaller scales, a high numerical resolution is required. Moreover, for low Mach number flows a large disparity in time scales between mean flow and acoustic fluctuations exists, which severely restricts the time step. It is also needless to say that, as LES is a time domain approach, it also involves the same problems as discussed above for the wave equation, i.e. impedance boundary formulation and proper analysis of all combustor eigenmodes. Despite the method's high potential in the future, LES still represents a costly and complex approach and its application is not practicable for many cases of technical interest.

A proper alternative is to linearize the set of Navier-Stokes equations (LNSEs) around an arbitrary flow state (see Chu, 1965). The unsteady heat release rate then appears as a source term in the linearized energy equation. The resulting set of equations describes the propagation of three different kind of waves: Acoustic, vorticity and entropy waves (Chu and

Kovasznay, 1958; Kovasznay, 1953). While acoustic waves travel with the speed of sound augmented by the local flow velocity, entropy and vorticity waves are convected by the mean flow. Gradients in the mean flow lead to their coupling and result in energy transfer from one mode of fluctuation into the other. The LNSEs may be transformed into frequency space, making use of the above mentioned advantages. The transformation further provides a remedy to the problem observed with the corresponding time domain approaches: Unbounded growth of Kelvin-Helmholtz instabilities in time. These disturbances in vorticity may obscure the acoustic solution and may -in some cases- hinder from retrieving meaningful results (Rao and Morris, 2006).

Similarly to the Helmholtz equation, an eigenvalue problem may be formulated. Inclusion of a time delayed flame response makes the eigenvalue problem non-linear and an iterative routine originally proposed for the Helmholtz equation (by Nicoud et al., 2007) needs to be introduced. The resulting eigenvalues take acoustic-flow interaction processes, i.e. acoustic-vorticity coupling and acoustic-entropy coupling fully into account, providing information about attenuation and amplification effects of acoustic waves when submitted to the mean flow of combustion chambers. The method can be considered as trade-off between a highly resolved LES and a low-cost Helmholtz equation simulation.

A different possibility proposed in this thesis is to use LNSEs to determine network elements of combustion chambers, e.g. like swirl atomizer nozzles or perforated screens. For this concept, the presence of a flame is excluded and the respective elements are treated separately. By incorporating such elements in a network analysis it is possible to take the fundamental attenuation and amplification effects of complex flow configurations into account.

1.3 Proposed Methods

Two methods are proposed in this thesis for the prediction of combustion instabilities: The first method uses frequency space linearized Navier-Stokes equations to determine the passive scattering properties of complex acoustic elements of combustion chambers, e.g. swirl atomizer nozzles or perfo-

rated screens. Scattering matrices obtained in this way, contain information about the physical attenuation or amplification of sound generated through acoustic-flow interaction processes. The information about the scattering matrices may then be integrated into a low-order network model approach describing the acoustic behavior of complete combustion chambers. A dispersion relation can be obtained in this way, whose solutions are the frequencies of the acoustic modes in a combustion chamber. In this way, eigenfrequencies of annular combustion chambers can be retrieved very efficiently. The combination of a high fidelity and robust LNSEs procedure with a low effort lumped network analysis may bear a high potential in order to improve the robustness and accuracy of state-of-the-art stability analysis using a network model approach.

The second method directly determines the eigenfrequencies of combustion chambers using LNSEs. A finite element approach is used to discretize the frequency space LNSEs in an arbitrary three dimensional and complex combustor domain, taking into account the acoustic coupling with a multidimensional flow field and flame. By formulating it as an eigenvalue problem, the shift-invert Arnoldi algorithm can be used in order to efficiently determine the eigenfrequencies of the resulting system matrices. For both considered methods, high amounts of degrees of freedom are generally involved and the resulting system matrices need to be inverted. For this task, a specially designed Generalized-Minimum Residual method in combination with a highly efficient multigrid preconditioning algorithm is used.

Both methods are sequential approaches and the following steps need to be performed in order to retrieve solutions of the acoustic fields or eigenvalues respectively: Main input to both methods is a mean flow field computed from a computational fluid dynamic simulation incorporating an appropriate turbulence closure. The Navier-Stokes equations are then linearized around this mean flow state. While the first approach does not need any further inputs, the eigenvalue analysis needs information about the unsteady source of the flame. This can be achieved analytically, experimentally or numerically. The present analysis uses an experimental approach to retrieve this piece of information. Overall, both methods require higher computational resources than, e.g., stability analysis using network models or the Helmholtz equation, but they contain a much lower amount of assumptions.

1.4 Thesis Structure

Chapter 2 introduces the underlying governing equations which are used in the present analysis. These comprise the linearized Navier-Stokes equations, linearized Euler equations and the scalar Helmholtz equation. Physical mechanism involved in thermoacoustic instabilities and acoustic-flow interaction processes is provided and important input parameters as acoustic boundary conditions and acoustic-flame coupling are discussed in more detail.

This thesis employs a finite element strategy to solve the acoustic governing equations. However, convective and reactive terms in the LNSEs or LEEs introduce spurious oscillations to the solution when applying a standard Bubnov-Galerkin technique. Therefore, stabilized finite element schemes, also known as Petrov-Galerkin schemes, are introduced to address aeroacoustic and thermoacostic problem sets in a consistent manner. This is done in Chapter 3. The schemes provide equation stabilization without introducing high amounts of artificial viscosity. Different stabilization techniques, like streamline-upwind/Petrov-Galerkin, Galerkin/least-squares or Galerkin/least-squares-minus are introduced and their application to LNSEs is discussed. Depending on the approach chosen, the matrices are assembled in two different ways and the resulting problem formulations are introduced.

For three dimensional problems, direct solution methods become computationally inefficient and the assembled matrices of Chapter 3 must be solved using iterative solution routines. These are introduced in Chapter 4. It is shown that system matrix characteristics depend strongly on frequency and flow state, and especially on mean flow gradients. The system matrices are non-hermitian (non-symmetric) and indefinite. A broad overview of the different solvers and preconditioners is provided for the purpose of inverting the resulting system matrices. The methods mainly belong to the class of Krylov subspace solvers. Finally, three different solver-preconditioner combinations are designed and calibrated in order to solve the LNSEs efficiently. Their performance is compared against each other for a generic combustor configuration. The fourth chapter also discusses the solution of the eigenvalue problem using an Arnoldi algorithm to which the same solvers are applied.

With the definition of a suitable finite element discretization of Chapter 3 and an efficient solution algorithm of Chapter 4, the resulting method is validated for acoustic-vorticity interaction on a variety of different flow configurations in Chapter 5. These include an area expansion, an orifice, a T-joint and a realistic combustion chamber flow employing an industrial swirl injector. The suitability of the LNSEs is shown to describe all acoustic-flow interactions with high accuracy. Some limitations of the linearized theory are highlighted in the case of a T-joint.

Finally, acoustic-entropy coupling is also considered for more combustor like configurations. The isentropic assumption made to study acoustic-vortex interactions in Chapter 5 is then dropped for Chapter 6. First, the predictive capabilities of the eigenvalue problem formulated with LNSEs is assessed for a generic combustor configuration. Then, in a next step the method is validated against the damping generated in a realistic combustor flow of an atmospheric combustor test rig at the Technical University of Munich. State-of-the-art damping measurements are performed for this task. Finally, the assessment of combustion instabilities of a self-excited configuration including acoustic-flame coupling is dealt with. The complexity of the problems considered increases with every validation test case.

A conclusion and outlook is given in Chapter 7.

2 Acoustic Governing Equations

To derive the acoustic governing equations we will consider a gas mixture where all species share the same molar weight and heat capacities. The medium considered is further assumed to act like a calorically perfect gas. Molecular diffusion of heat and gravity forces are neglected in the present analysis ($\lambda = 0$ and $g_i = 0$), while molecular diffusion of momentum is conserved for the derivation. Under the preceding assumptions, the mass, momentum and energy equations read, respectively,

$$\frac{\partial \rho}{\partial t} + \frac{\partial}{\partial x_i}\left(\rho u_i\right) = 0, \tag{2.1}$$

$$\frac{\partial}{\partial t}(\rho u_i) + \frac{\partial}{\partial x_j}(\rho u_i u_j) + \frac{\partial p}{\partial x_i} = \frac{\partial \tau_{ij}(u_k)}{\partial x_j}, \tag{2.2}$$

$$\frac{\partial p}{\partial t} + u_i \frac{\partial p}{\partial x_i} + c^2 \rho \frac{\partial u_i}{\partial x_i} = \left(\kappa - 1\right) \dot{q}_V + \left(\kappa - 1\right) \tau_{ij}(u_k) \frac{\partial u_i}{\partial x_j}. \tag{2.3}$$

where ρ, u_i and p denote the instantaneous density, velocity vector and pressure variables, κ is the ratio of specific heats of the mixture and $\dot{q}_V$ denotes the heat release rate per unit volume. The viscous stress tensor is defined as

$$\tau_{ij}(u_k) = \mu \left(\frac{\partial u_i}{\partial x_j} + \frac{\partial u_j}{\partial x_i} - \frac{2}{3} \frac{\partial u_k}{\partial x_k} \delta_{ij} \right), \tag{2.4}$$

and together with the equation of state

$$p = \rho R T, \tag{2.5}$$

and entropy expression

$$s - s_{ref} = c_v \ln\left(\frac{p}{p_{ref}}\right) - c_p \ln\left(\frac{\rho}{\rho_{ref}}\right), \tag{2.6}$$

this set of transport equations describes the spatiotemporal evolution of all physical quantities. The heat capacities of the gas mixture are defined by c_v and c_p, whereas $R = c_p - c_v$ is the specific gas constant. These parameters may vary with temperature, but are assumed constant to simplify the derivation. The index 'ref' denotes a certain reference state.

2.1 Linearized Navier-Stokes Equations

Acoustic governing equations may be obtained by linearizing the full set of compressible Navier-Stokes equations, Eqs. (2.1)-(2.3), around an arbitrary mean flow state, which by itself satisfies continuity of mass, momentum and energy. We consider large scale small amplitude fluctuations $(.')$ superimposed to a mean flow field $(\bar{.})$ which is solely a function of space. Then, instantaneous fields of density, velocity, pressure and heat release rate can be written as

$$\rho = \bar{\rho} + \rho', \quad u_i = \bar{u}_i + u_i', \quad p = \bar{p} + p', \quad \dot{q}_V = \bar{\dot{q}}_V + \dot{q}_V', \tag{2.7}$$

where the quantities $\rho'/\bar{\rho}$, $|u_i'|/\bar{c}$, $p'/\bar{p}$ and $T'/\bar{T}$ are of small order ϵ, where $\epsilon \ll 1$ and $\bar{c}^2 = \kappa R\bar{T}$ is the mean speed of sound. Temporal fluctuations of material properties can generally be neglected, see Olson and Swift (1994). Introducing the preceding expansion into Eqs. (2.1)-(2.3) and keeping only terms of the order of ϵ, the following set of linear equations is obtained

$$\frac{\partial \rho'}{\partial t} + \frac{\partial}{\partial x_i}\left(\bar{u}_i\rho' + \bar{\rho}u_i'\right) = 0, \tag{2.8}$$

$$\frac{\partial \bar{\rho}u_i'}{\partial t} + \frac{\partial}{\partial x_j}\left(\bar{\rho}\bar{u}_j u_i'\right) + \left(\bar{\rho}u_j' + \bar{u}_j\rho'\right)\frac{\partial \bar{u}_i}{\partial x_j} + \frac{\partial p'}{\partial x_i} = \frac{\partial \tau_{ij}(u_k')}{\partial x_j}, \tag{2.9}$$

$$\begin{aligned} \frac{\partial p'}{\partial t} + \frac{\partial}{\partial x_i}\left(\bar{u}_i p' + \kappa\bar{p}u_i'\right) + (\kappa-1)\left(p'\frac{\partial \bar{u}_i}{\partial x_i} + u_i'\frac{\partial \bar{p}}{\partial x_i}\right) = \\ (\kappa-1)\left[\dot{q}_V' + \left(\tau_{ij}(u_k)\frac{\partial u_i}{\partial x_j}\right)'\right], \end{aligned} \tag{2.10}$$

which describe the spatiotemporal evolution of fluctuating quantities ρ', u_i' and p'. To simplify the derivation, the last term of the energy equation Eq. (2.10) attributed to the molecular stresses, is not yet linearized. The superscript $(\ldots)'$ over the brackets denotes that this operation still needs to be performed. Note that the linearized continuity Eq. (2.8) was used to simplify the linearized momentum Eq. (2.9). By linearization any second order effects are excluded from the considerations. This includes the term $u_i'u_j'$ as well, which is mainly associated with turbulence.

In Eq. (2.10) pressure fluctuations are chosen as primitive variable for the linearized energy equation. Similarly, the equation may be formulated in

terms of fluctuating entropy s' variable, see e.g. Nicoud and Wieczorek (2009) and Appendix B,

$$\frac{\partial s'}{\partial t} + u_i' \frac{\partial \bar{s}}{\partial x_i} + \bar{u}_i \frac{\partial s'}{\partial x_i} = \frac{R\dot{q}_V'}{\bar{p}} - \frac{R\bar{\dot{q}}_V p'}{\bar{p}^2} + \frac{R}{\bar{p}^2}\left(\bar{p} - p'\right)\left(\tau_{ij}(u_k)\frac{\partial u_i}{\partial x_j}\right)'. \quad (2.11)$$

The equation illustrates that the fluctuating flow is isentropic if one of the following conditions is satisfied: (1) if the velocity fluctuations are orthogonal to the mean entropy gradient $\nabla\bar{s}$; (2) the mean flow velocity is orthogonal to the fluctuating entropy gradient $\nabla s'$; (3) for vanishing viscous stress tensor ($\mu = 0$) and (4) in absence of a flame ($\dot{q}_V = 0$). Viscous stresses are generally of low order for low frequency sound propagation, see Appendix A. So condition (3) is approximately met. In absence of a flame only the two divergence terms on the equation's LHS remain. For practical applications, the baseline flow is generally non zero ($\bar{u}_i \neq 0$) and multidimensional. Thus, conditions (1) and (2) are generally not fulfilled. They may only be satisfied for a vanishing flow without any heat addition since then $\nabla\bar{s} \backsimeq -c_p\nabla\bar{\rho}/\bar{\rho} = 0$. Hence, assuming isentropic behavior of the fluctuation components is highly restrictive and generally not satisfied for multidimensional complex flow fields.

The system of equations (2.8)-(2.10) are the so-called linearized Navier-Stokes equations (LNSEs) which describe the propagation of three modes of fluctuations: Acoustic, vorticity and entropy (Kovasznay, 1953). Vorticity and entropy waves are convected by the mean flow, whereas acoustic waves travel with the speed of sound, altered by the local flow velocity. Although being in a linear regime, these types of modes are strongly coupled, making differentiation between the modes difficult (Myers, 1991). Incorporating these three different mode types in a stability analysis enables a detailed description of phenomena most relevant to gas turbine applications: Acoustic flame coupling leads to the formation of so-called hot-spots (entropy waves) which are convected away from the flame by the baseline flow. On the one hand, the generated entropy waves lead to a modification of the fields of fluctuating variables in the flame region. On the other hand, they are convected to the downstream turbine vane passage, where they are partially transformed into acoustic waves and reflected back into the combustion chamber (Marble and Candel, 1977). Thus, the accelerated entropy spots may also participate in the thermoacoustic feedback loop. Another important effect is the coupling of acoustic with vorticity waves

(Boij and Nilsson, 2006). At flow separation edges vortical structures are triggered by acoustic fluctuations. While convected downstream, these may continuously interact with the acoustic field, leading to sound attenuation or sound amplification. Hence, acoustic-entropy (Dowling, 1995) as well as acoustic-vorticity coupling (Bechert, 1980; Fukumoto and Takayama, 1991; Wendoloski, 1998) may lead to net dissipation or production of acoustic energy due to acoustical energy transfer to the entropy and vorticity mode or vice versa. The specific amount of energy transferred is highly important as it determines the stability reserves of a combustion chamber. When an unsteady heat release source term $\dot{q}'_V$ is introduced, the additional acoustic energy produced may either compensate or overcome the acoustic losses leading to stable or unstable combustor operation, respectively.

Up to now, fluctuating quantities in the LNSEs depend on time. This considerably complicates their treatment because of five main reasons: The first being that boundary conditions depend significantly on frequency. In time space broadband waves impinge simultaneously on a computational boundary and the boundary condition imposed must relate each fraction of the fluctuations to a certain frequency of impinging waves. This is a non trivial task and requires the use of complicated filter algorithms and monitor planes. A large variety of studies is devoted to this task, see e.g. Kaess et al. (2008); Poinsot and Lele (1992). Secondly, the flame is frequently modeled as a function of a time delayed velocity fluctuation at a reference location requiring the storage of the point's time history. This may complicate the solution algorithm. Thirdly, in time space many unstable modes at different frequencies may coexist at the same time. Discrimination between the different modes becomes difficult as the most amplified one dominates the fluctuating field. Fourthly, the LNSEs describe multiscale phenomena with a large disparity in different time scales (Lele, 1997). These include convective as well as acoustic scales. Thus, the time step is considerably restricted. Finally, as a result from the linearization procedure, the LNSEs promote the unbounded growth of Kelvin-Helmholtz instabilities with space and time. In reality, however, these instability waves are saturated by nonlinear effects, like e.g. turbulence. Especially due to the temporal growth of the Kelvin-Helmholtz instability wave, the acoustic solution may be obscured (Agarwal et al., 2004) or the linear solution algorithm may even diverge after a certain time span. Maintaining finiteness of the time space

solution is a main aim of many publications, see e.g. the review article of Richter et al. (2011) or Prax et al. (2008). Due to these reasons it is advantageous to introduce harmonic variations at a frequency $f = \omega/(2\pi)$ for density, velocity, pressure and local heat release perturbations, as proposed by Rao and Morris (2006):

$$\rho' = \hat{\rho}(x_i)e^{i\omega t}, \quad u_i' = \hat{u}_i(x_k)e^{i\omega t}, \quad p = \hat{p}(x_i)e^{i\omega t}, \quad \dot{q}_V' = \hat{\dot{q}}_V(x_i)e^{i\omega t}. \tag{2.12}$$

This completely resolves the unbounded growth of Kelvin-Helmholtz instabilities with time and allows to analyze each combustor eigenmode at a discrete ω separately. Introducing Eq. (2.12) into the LNSEs leads to their frequency domain counterpart:

$$i\omega\hat{\rho} + \frac{\partial}{\partial x_i}\left(\bar{u}_i\hat{\rho} + \bar{\rho}\hat{u}_i\right) = 0, \tag{2.13}$$

$$i\omega\bar{\rho}\hat{u}_i + \frac{\partial}{\partial x_j}\left(\bar{\rho}\bar{u}_j\hat{u}_i\right) + \left(\bar{\rho}\hat{u}_j + \bar{u}_j\hat{\rho}\right)\frac{\partial\bar{u}_i}{\partial x_j} + \frac{\partial\hat{p}}{\partial x_i} = \frac{\partial\tau_{ij}(\hat{u}_k)}{\partial x_j}, \tag{2.14}$$

$$\begin{aligned} i\omega\hat{p} + \frac{\partial}{\partial x_i}\left(\bar{u}_i\hat{p} + \kappa\bar{p}\hat{u}_i\right) + (\kappa-1)\left(\hat{p}\frac{\partial\bar{u}_i}{\partial x_i} + \hat{u}_i\frac{\partial\bar{p}}{\partial x_i}\right) = \\ (\kappa-1)\left[\hat{\dot{q}}_V + \widehat{\left(\tau_{ij}(u_k)\frac{\partial u_i}{\partial x_j}\right)}\right]. \end{aligned} \tag{2.15}$$

Herein, the mean flow quantities $(\bar{\rho}, \bar{u}_i, \bar{p})$ as well as the unknown complex quantities of density, velocity and pressure amplitudes depend solely on space x_i.

A different set of equations can be obtained by neglecting any viscous effects in the equations ($\mu = 0$). This results in the so-called linearized Euler equations (LEEs), the non-viscous counterpart of the LNSEs, which are frequently used for time-space computational aeroacoustics (Bailly and Juvé, 2000; Billson et al., 2005; Mankbadi et al., 1998) or, more recently, also for generic thermoacoustic problems (Nicoud and Wieczorek, 2009).

2.2 Linearized Equation of State and Entropy

Apart from the heat release term, Eqs. (2.8)-(2.10) are closed. However, especially for the analysis of thermoacoustic instabilities, information about

the temperature and entropy fluctuations, T' and s' respectively, is desirable. This information can be derived from the equations of state, Eq. (2.5), and entropy, Eq. (2.6), by performing a Taylor series expansion around an arbitrary mean flow state and keeping only first order terms of the fluctuating quantities. In this sense, the linearized versions of the equation of state and entropy read

$$\frac{p'}{\bar{p}} - \frac{\rho'}{\bar{\rho}} - \frac{T'}{\bar{T}} = 0, \tag{2.16}$$

$$s' = c_v \frac{p'}{\bar{p}} - c_p \frac{\rho'}{\bar{\rho}}, \quad \text{or} \quad s' = c_p \frac{T'}{\bar{T}} - R \frac{p'}{\bar{p}}. \tag{2.17}$$

As discussed above, assuming isentropic behavior of fluctuating quantities is very restrictive. However, many studies, e.g. those by Boij and Nilsson (2003); Gabard (2007), indicate the suitability of assuming $s' = 0$ for low Mach number flows without heat addition. This assumption considerably eases the calculation since density and pressure fluctuations become directly coupled by the isentropic relation

$$p' = \bar{c}^2 \rho'. \tag{2.18}$$

Hence, the LNSEs system reduces by one equation, equivalently reducing the degrees of freedom of the problem by a factor of approximately 4/5. It is then straightforward to transform the isentropic relation Eq. (2.18) as well as the linearized equation of state and entropy, Eqs. (2.16)-(2.17), into frequency space using Eq. (2.12).

2.3 Material Properties

The dynamic viscosity of the fluid is assumed to vary with temperature $\bar{T}$ according to Sutherland's law:

$$\mu = \left(\frac{\bar{T}}{T_{ref}} \right)^{\frac{3}{2}} \left(\frac{T_{ref} + S}{\bar{T} + S} \right) \mu_{ref}, \tag{2.19}$$

where T_{ref} and μ_{ref} denote reference temperature and viscosity respectively and S is the Sutherland temperature. In cases of higher Mach number flows

molecular diffusion of heat may become important in regions of shocks. Then, the property λ can be assumed to vary with

$$\lambda = \frac{c_p}{Pr}\mu, \tag{2.20}$$

using the Prandtl number $Pr = c_p\mu/\lambda$. As the mean flows considered in this thesis are fully sub-sonic, molecular diffusion of heat is not accounted for in the present formulation of the linearized energy equation. This is a very common assumption for the analysis of low frequency acoustic perturbations.

2.4 Wave- or Helmholtz Equation

Assuming a medium at rest $\bar{u}_i = 0$ and neglecting molecular diffusion of momentum and heat ($\mu = 0$ and $\lambda = 0$) reduces the linearized equation of mass, momentum and energy, Eqs. (2.13)-(2.15) to

$$\frac{\partial \rho'}{\partial t} + \bar{\rho}\frac{\partial u_i'}{\partial x_i} + u_i'\frac{\partial \bar{\rho}}{\partial x_i} = 0, \tag{2.21}$$

$$\frac{\partial u_i'}{\partial t} + \frac{1}{\bar{\rho}}\frac{\partial p'}{\partial x_i} = 0, \tag{2.22}$$

$$\frac{\partial p'}{\partial t} = (\kappa - 1)\,\dot{q}_V'. \tag{2.23}$$

The assumption of a quiescent medium is valid as long as the characteristic Mach number of the flow $Ma = |\bar{u}_i|/\bar{c}$ is small compared to L_f/L_a, where L_f is the the reaction zone thickness and L_a is the characteristic acoustic length scale, see paper of Nicoud et al. (2007) and considerations therein. This justifies the quiescent assumption $\bar{u}_i = 0$ for many applications. The assumption further implies that $\nabla\bar{p} = 0$ from Eq. (2.2) as well as $\bar{\dot{q}}_V = 0$ from Eq. (2.3). Moreover, the time derivative of fluctuating quantities reduces equivalently to $D/Dt = \partial/\partial t$, since convective terms vanish with $\bar{u}_i = 0$.

Taking the time derivative of Eq. (2.21), adding the divergence of Eq. (2.22) over $\bar{\rho}$ and using Eq. (2.17) to eliminate ρ', yields the following scalar wave equation for the pressure fluctuations p':

$$\frac{1}{\bar{c}^2}\frac{\partial^2 p'}{\partial t^2} - \bar{\rho}\frac{\partial}{\partial x_i}\left(\frac{1}{\bar{\rho}}\frac{\partial p'}{\partial x_i}\right) = \frac{(\kappa-1)}{\bar{c}^2}\frac{\partial \dot{q}'_V}{\partial t}. \tag{2.24}$$

In case of $\dot{q}'_V = 0$, solely the mean density and speed of sound distributions may account for the effect of the flame.

A natural way of gaining information about the whole set of thermoacoustic modes, is then to consider the Helmholtz equation, the frequency domain version of the wave equation (Benoit and Nicoud, 2005; Nicoud et al., 2007). Applying the harmonic ansatz of Eq. (2.12) yields

$$-\frac{\omega^2}{\bar{c}^2}\hat{p} - \bar{\rho}\frac{\partial}{\partial x_i}\left(\frac{1}{\bar{\rho}}\frac{\partial \hat{p}}{\partial x_i}\right) = i\omega\frac{\kappa-1}{\bar{c}^2}\hat{\dot{q}}_V. \tag{2.25}$$

Transformation into frequency space results in pressure amplitudes that are solely a function of space not time. When discretizing the equations over a certain combustor domain, a quadratic eigenvalue problem may be formulated. If a model for the heat release rate $\hat{\dot{q}}_V$ is included, the quadratic eigenvalue problem becomes non-linear and an iterative routine has to be applied in order to determine the eigenfrequencies. Discretization of the Helmholtz equation using finite elements and illustrations on how to solve the respective eigenvalue problem are shown in the Appendix E.

The main weakness of performing linear stability analysis using the wave or Helmholtz equation is the quiescent assumption made. Any acoustic mean flow interaction processes leading to acoustic attenuation or amplification processes, respectively, are neglected. This poses severe limitations to the reliability of the predicted eigenfrequencies.

2.5 Low-Order Network Modeling

As described in the previous sections, predicting the frequencies of oscillations is a complex task and, depending on the degree of modeling, can involve high computational costs. A widespread method to analyze thermoacoustic instability is the so-called low-order network modeling approach.

Essentially, the modeling subdivides a combustion chamber into its individual elements. Each element can than be represented in terms of an acoustic scattering matrix

$$\begin{pmatrix} \hat{p}_d^+ \\ \hat{p}_u^- \end{pmatrix} = \begin{pmatrix} T^+(\omega) & R^-(\omega) \\ R^+(\omega) & T^-(\omega) \end{pmatrix} \begin{pmatrix} \hat{p}_u^+ \\ \hat{p}_d^- \end{pmatrix}, \tag{2.26}$$

where the pressure wave amplitudes $\hat{p}_u^+$, $\hat{p}_u^-$, $\hat{p}_d^+$ and $\hat{p}_d^-$ represent the plane acoustic waves traveling along an element in upstream $(+)$ or downstream $(-)$ direction, respectively. Their locations are indicated by the subscripts u for upstream and the subscript d for downstream of the acoustic element. Complex pressure wave amplitudes are related to the acoustic velocity $\hat{u}$ and the pressure $\hat{p}$ by

$$\hat{p}_{u/d}^+ = \frac{1}{2}\left(\hat{p}_{u/d} + \bar{\rho}\bar{c}\hat{u}_{u/d}\right), \tag{2.27}$$

$$\hat{p}_{u/d}^- = \frac{1}{2}\left(\hat{p}_{u/d} - \bar{\rho}\bar{c}\hat{u}_{u/d}\right). \tag{2.28}$$

The coefficients of a scattering matrix Eq. (2.26) can be interpreted as reflection and transmission coefficients R and T for the pressure waves amplitudes traveling in downstream or upstream direction, $+$ and $-$ respectively. An equivalent description to the scattering behavior of acoustic elements is the so-called transfer matrix. It can be obtained when inserting Eqs. (2.27) and (2.28) in the scattering matrix of Eq. (2.26), yielding

$$\begin{pmatrix} \frac{\hat{p}}{\bar{\rho}\bar{c}} \\ \hat{u} \end{pmatrix}_d = \begin{pmatrix} T_{11}(\omega) & T_{12}(\omega) \\ T_{21}(\omega) & T_{22}(\omega) \end{pmatrix} \begin{pmatrix} \frac{\hat{p}}{\bar{\rho}\bar{c}} \\ \hat{u} \end{pmatrix}_u. \tag{2.29}$$

The coefficients of the transfer matrix relate the acoustic velocity $\hat{u}$ and pressure $\hat{p}$ upstream and downstream of the duct to each other. They depend on the geometry, the frequency as well as on the flow state considered. Finally, these individual elements can be connected to each other enforcing pressure continuity and flow rate conservation. When coupling the transfer matrices of a given system and using appropriate boundary conditions, the complete network of elements can be analytically merged into a matrix relation of the form

$$\mathbf{S}(\omega)\mathbf{P} = 0, \tag{2.30}$$

where $\mathbf{P} = (\hat{p}_1, \hat{u}_1, \hat{p}_2, \hat{u}_2, \ldots, \hat{p}_n, \hat{u}_n)$ is the unknown solution vector containing complex pressure and velocity amplitudes while $\mathbf{S}$ is the coefficient matrix containing the $n-1$ transfer matrices of all network elements and boundary conditions. Only a discrete number of pulsations ω will satisfy the jump relations across the individual elements and boundary conditions. These are the roots of the dispersion relation $\det \mathbf{S}(\omega) = 0$ which are the eigenfrequencies of the system. Since the transfer matrices of typical network models have a complex frequency dependance, the dispersion relation resulting from Eq. (2.30) needs to be solved numerically (Polifke, 2003).

With the chosen formalism of Eq. (2.12), the real part of the eigenfrequencies indicates the frequency of oscillations, while the imaginary part provides information about the growth or damping of the specific mode. One may differentiate between the two different cases:

$$\begin{aligned} \Im(\omega) > 0 \quad & \text{stable operation,} \\ \Im(\omega) < 0 \quad & \text{unstable operation.} \end{aligned} \tag{2.31}$$

and oscillations decay or are amplified exponentially at a rate of $\Im(\omega)$. The main advantage of the method is that complex systems including acoustic losses can be described by a few lumped elements, leading to a low-order model that can be extensively used for predesign purposes, see e.g. Bade et al. (2013a,b).

A main requirement of the approach, however, is that all its individual elements have to be known a priori. In case of simple configurations, e.g. ducts or discrete area changes, analytical modeling is possible. For example, Boij and Nilsson (2003, 2006) derive a dispersion relation which incorporates the flow-acoustic coupling of sound waves with the unstable shear layer of an area expansion. In case for more complex geometries and flow conditions, however, only experimental or numerical approaches are feasible.

Experimental approaches rely on the two-source method (Munjal and Doige, 1990a; Åbom and Bodén, 1995), where the element at interest is excited acoustically once from upstream and once from downstream direction. By measuring the pressure fluctuations at both respective locations the individual coefficients of the scattering and transfer matrix are determined. Typically, experimental setups are unavailable or too costly in early design phases and the use of numerical methods becomes more favorable. Existing numerical approaches perform a compressible LES or an unsteady

Reynolds averaged Navier-Stokes simulation (URANS) using harmonic or broadband excitation signals. Approaches applying harmonic excitation are highly inefficient in retrieving broadband frequency responses since for every pulsation ω a single simulation has to be performed. Combining broadband signal excitation with system identification techniques like Föller and Polifke (2012), however, one is able to provide response within one simulation. A different method is presented in this thesis. It employs the LNSEs or LEEs in frequency space to determine the scattering or transfer matrix coefficients. This approach is less costly compared to a compressible LES and may compute the broadband response of acoustic elements by only a few matrix inversions.

Another main disadvantage of network models is that they require each element to act individually, which is generally not satisfied for relatively compact combustion chambers. Moreover, it is solely a one dimensional representation of complex three dimensional configurations and is purely restricted to plane wave propagation.

2.6 Heat Release Rate

To close the system of partial differential equations Eqs. (2.8)-(2.10), the fluctuating heat release rate $\hat{\dot{q}}_V$ has to be modeled in terms of fluctuating density $\hat{\rho}$, velocity $\hat{u}_i$ and pressure $\hat{p}$. This is done by the so-called flame transfer function $\mathcal{F}$ (FTF) which is expressed in its most general form as

$$\hat{\dot{q}}_V = \mathcal{F}(\omega, \hat{\rho}, \hat{u}_i, \hat{p}). \tag{2.32}$$

A steady flame may be perturbed, causing fluctuations in heat release rate $\hat{\dot{q}}_V$, for various reasons:

- Merk (1956) shows that acoustic velocity fluctuations at the flame front may perturb its position significantly and lead to perturbations of flame area and hence perturbations in heat release rate as $\dot{q}_V \sim s_t A$.
- Velocity and pressure fluctuations in shear layers may lead to modulations of the laminar or turbulent flame speed. These fluctuations perturb the turbulence intensity and length-scale, contributing to per-

turbations of the turbulent flame speed s_t. This, in turn, gives rise to perturbations of the overall heat release rate.

- Large-scale coherent vortical structures may be convected in the shear layer to the flame front. These vortex structures are generated through velocity fluctuations in the burner month (Külsheimer and Büchner, 2002) which trigger hydrodynamic instabilities of shear layers (Poinsot et al., 1987). On the one hand, the vortical structures cause wrinkling of the flame front and therefore perturbations in flame area and heat release rate. On the other hand, they perturb the turbulent flame speed s_t (Yang and Culick, 1986).

- For practical configurations, the reactive mixture is never ideally premixed. At the point of fuel injection, acoustic fluctuations may modulate the fuel or air mass flow rate rate resulting in equivalence ration ϕ' fluctuations (Keller, 1995; Lieuwen and Zinn, 1998). After a convective time lag, these equivalence ratio fluctuations reach the flame front where they perturb the turbulent flame speed and enthalpy of reaction per unit volume. Consequently, the flame area and heat release rate per unit area are altered.

- In combustion chambers employing liquid fuels, e.g. kerosene, acoustic waves may couple with fluctuations in atomization and droplet vaporization (Priem, 1965; Priem and Guentert, 1962). As found by Tong and Sirignano (1986, 1987) unsteady droplet vaporization is a potential mechanism driving combustion instabilities. Other studies of Heidmann and Wieber (1966), however, assess a rather weak energy contribution, while some publications claim that the condensing and vaporization process rather attenuates acoustic waves (Marble, 1969; Marble and Candel, 1975; Marble and Wooten, 1970).

Other mechanisms for acoustic flame coupling and influencing factors are discussed in the literature, e.g. swirl number fluctuations (Gentemann et al., 2004; Hauser et al., 2011b; Komarek and Polifke, 2010; Palies et al., 2010) or the influence of a precessing vortex core (Moeck et al., 2012; Syred, 2006). The effect of confinement is investigated in Hauser et al. (2011a) and Cuquel et al. (2011).

The flame transfer function $\mathcal{F}$ mostly depends on a selection of the aforementioned contributions. Which of the effects is more predominant depends on the character of the combustion system, i.e. if it is operated under perfectly premixed, partially premixed or non-premixed conditions, if a laminar or turbulent flame is considered or if the fuel is of gaseous or liquid character. Its determination represents a crucial part to the success of any stability analysis (Lieuwen, 2003) and may be achieved either through analytical modeling, experimental measurements or numerical simulations.

2.6.1 Analytical Modeling

In general, the relationship between unsteady heat release rate and velocity or equivalence ratio perturbations has a complex dynamic (see above). However, in cases where the typical length scale of the flame is small compared to the characteristic acoustic wavelength that is an acoustically compact flame, analytical models may be derived describing the global heat release rate fluctuations (integrated over space). In this sense, models have been proposed, describing the response of conical or V-shaped laminar flames (Baillot et al., 1992; Schuller et al., 2003), the effect of equivalence ratio fluctuations (Lieuwen and Zinn, 1998; Sattelmayer, 2003) and swirling premixed flames (Palies et al., 2011). Especially for laminar flames and premixed Bunsen-type flames the heat release fluctuations are mainly caused by kinematic effects and can be modeled with a g-equation ansatz, describing the displacement of the flame surface. The charm of such models is that analytical solutions for the linearized perturbations can be retrieved (Fleifil et al., 1996; Schuller et al., 2003). For more realistic technical configurations including technically premixed, turbulent flames which may be operated with liquid fuels in extreme cases, pure analytical modeling becomes ambiguous.

A fairly simple model accounting for acoustic flame interaction is the famous $n-\tau$ model which is based on the ideas of Crocco (1951, 1952). Essentially this is a one dimensional model which links the global heat release at time t to a time lagged acoustic velocity at an upstream reference position, usually chosen in the burner mouth:

$$\dot{Q}'(t) = n\frac{\bar{\dot{Q}}}{\bar{u}_b}u_i'(x_{ref}, t-\tau)n_{ref}, \tag{2.33}$$

where $\dot{Q}'(t)$ is the global fluctuating heat release rate, $\bar{\dot{Q}}$ is its mean counterpart and $\bar{u}_b$ is the bulk velocity at the reference location. Generally, the factor n governs the strength of the flame response and is called the interaction index. τ describes the time lag and controls the phase between acoustic pressure and unsteady heat release of the flame and thus, the sign of the Rayleigh integral, Eq. (1.1). For premixed flames the main idea behind this modeling approach is that the heat release rate depends on the flame surface area which, considering a given flame speed, is mainly controlled by the flow rate of the reactive mixture. The time lag than represents a convective time scale for inhomogeneities traveling from the injector to the flame front. However, it can also be applied to technically premixed configurations where τ is interpreted as a convective time lag which also incorporates the traveling time of mixture inhomogeneities. This compact n-τ model is used frequently in network models.

The compactness assumption is, however, not always justified for modern gas turbines where the heat release is spatially distributed. In such cases the compact n-τ model of Eq. (2.33) can be reformulated to relate the local heat release fluctuations to a velocity fluctuation at the reference location

$$\dot{q}'_V(x_i,t) = n_l(x_i)\frac{\bar{\dot{q}}_V(x_i)}{\bar{u}_b}u'_i(x_{ref},t-\tau_l(x_i))n_{ref}, \tag{2.34}$$

where $\dot{q}'_V$ is the local unsteady heat release rate per unit volume. Now, local interaction index $n_l(x_i)$ and the local time delay $\tau_l(x_i)$ are spatially distributed in the flame zone which permits differences in the local response of the flame.

Both models, global as well as local, require the knowledge of n or $n_l(x_i)$ and τ or $\tau_l(x_i)$ to close the system. These can either be retrieved through experimental measurements (Ducruix et al., 2000; Hirsch et al., 2005; Schuller et al., 2003) or through numerical simulations (Martin et al., 2006; Tay Wo Chong et al., 2012; Varoquié et al., 2002). In the present study this is achieved using an atmospheric pressure test rig to measure the FTF experimentally. Global n and τ parameters are derived from the experiments which are, however, only valid for a compact flame. When predicting combustion instabilities using a spatial approach, e.g. LNSEs or Helmholtz equation, the flame needs a finite dimension and cannot be considered as compact. Consequently, in numerical simulations the flame is given a small,

finite space and a local n-τ model is chosen, Eq. (2.34), having a constant $\tau_l(x_i) = \tau$ and relating the local interaction index to the global one using

$$n_l(x_i) = \frac{n\bar{\dot{Q}}}{\bar{\dot{q}}_V V_f}, \tag{2.35}$$

where V_f represents the finite volume of the flame region. For simplicity reasons, dependance of the n-τ model parameters on frequency was not explicitly mentioned, but its is obvious that these parameters depend significantly on frequency. A model using only a single interaction index and time delay can hardly represent the flame response over a broad frequency spectrum.

2.6.2 Experimental Measurements

Experimental measurements are based on the concept of FTFs which correlate the unsteady global heat release rate to a velocity perturbation at a reference position mostly located in the burner mouth

$$\mathcal{F}(\omega) = \frac{\dot{Q}'(\omega)/\bar{\dot{Q}}}{u'(x_{ref},\omega)/\bar{u}(x_{ref})}. \tag{2.36}$$

For perfectly premixed flames, the heat release fluctuations $\dot{Q}'$ can be correlated with the OH*or CH*chemiluminescence signals, which are measured using intensified cameras (Keller and Saito, 1987; Price et al., 1969). Assuming spatial proportionality is justified as long as laminar flames are considered, see e.g. Hardalupas and Orain (2004), and under some constraints locally distributed $n_l(\mathbf{x})$ and $\tau_l(\mathbf{x})$ may be measured. However, for turbulent premixed flames the chemiluminescence signal becomes a function of turbulence intensity and only the integral chemiluminescence intensity can be correlated with the integral heat release rate as shown by Lauer and Sattelmayer (2010). Thus, in this case, only global n and τ parameters can be obtained. For technically premixed systems the situation becomes even more complex as the chemiluminescence intensities also depend on local equivalence ratios. In this case, even the global integrated chemiluminescence signal is not proportional to the global heat release rate.

For flame configurations, such as kerosene flames, where the heat release rate is not accessible from chemiluminescence intensities, a different approach

based on acoustic analogies must be employed, see e.g. Alemela (2009). Therein, global balances of fluctuating mass, momentum and energy across the flame can be recasted into a transfer matrix notation of Eq. (2.29). The relations used are the so-called Rankine-Hugonoit relations which are valid for compact flames (Dowling, 1995; Keller et al., 1985). Inserting the relation of Eq. (2.36), the procedure yields the following purely theoretical transfer matrix

$$\begin{pmatrix} \frac{\hat{p}}{\bar{\rho}\bar{c}} \\ \hat{u} \end{pmatrix}_d = \begin{pmatrix} \frac{\bar{\rho}_c \bar{c}_c}{\bar{\rho}_h \bar{c}_h} & -\frac{\bar{\rho}_c \bar{c}_c}{\bar{\rho}_h \bar{c}_h}\left(\frac{\bar{T}_h}{T_c}-1\right)\left(1+\mathcal{F}(\omega)\right) Ma_c \\ -\left(\frac{\bar{T}_h}{T_c}-1\right)\kappa Ma_c & 1+\left(\frac{\bar{T}_h}{T_c}-1\right)\mathcal{F}(\omega) \end{pmatrix} \begin{pmatrix} \frac{\hat{p}}{\bar{\rho}\bar{c}} \\ \hat{u} \end{pmatrix}_c . \tag{2.37}$$

As transfer matrices can simply be determined using a two-source location method (Munjal and Doige, 1990b), the flame transfer matrix can be accessed by measuring the acoustic states up- and downstream of the flame. This transfer matrix, however, contains also information about the acoustic transfer behavior of the swirl atomizer nozzle, which is not desired. Therefore, this piece of information is extracted from the transfer matrix by measuring the transfer matrix of the swirl atomizer nozzle under non-reactive conditions independently.

In order to treat the non-linear saturation effects of the heat release rate, Noiray et al. (2008) have extended the experimental FTF analysis to take the specific amplitude of velocity perturbations at the burner mouth into account, i.e. $\mathcal{F}(\omega, \hat{u})$. The authors call this modified flame transfer function a flame describing function (FDF). In this way, non-linear saturation amplitudes can be determined using linear stability analysis and assuming that the main driver of non-linearities is the flame.

2.6.3 Numerical Simulations

As experimental measurements are expensive from an infrastructural and operational point of view, a relatively cheap alternative is the numerical determination of flame transfer functions. Due to the exact knowledge of all physical quantities and a certain subspace of chemical species, even spatially distributed FTFs can be determined.

These methods are based on acoustically exciting the flame either through harmonic (Giauque et al., 2005; Selle et al., 2006) or through broadband excitation signals (Kim et al., 2010; Tay Wo Chong et al., 2010, 2012). Obviously, later method represents the most efficient way of identifying FTFs over the complete frequency spectrum, since only a single simulation is needed compared to multiple harmonic excitations using the first mentioned method. It requires, however, the use of more advanced system identification techniques (Föller and Polifke, 2010; Föller et al., 2010a) in order to extract the frequency dependent flame responses. A main remedy of a numerical approach is the high degree of modeling, especially concerning the effect of the turbulent subgrid scales, as well as the limited chemistry subspace. Independently of these constraints, the methods (especially LES), feature a high potential for the near future.

2.7 Acoustic Boundary Conditions

Boundary conditions represent important input parameters to any stability analysis. They govern the acoustic energy flux out of the system and therefore contribute to the systems overall energy content. Only physically motivated absorption or introduction of acoustic energy is desired. Moreover, since boundaries reflect acoustic waves with a certain phase-shift, they constitute to the thermoacoustic feedback loop. This is shown e.g. in Tran et al. (2009), who varied the inlet and outlet boundary conditions of a combustion chamber and therewith directly controlled the system stability. Their measurements highlight the importance of the acoustic boundary conditions and their effect the on the thermoacoustic feedback loop.

In order to define a well-posed physical problem this thesis follows the general ideas of Hadamard (1902): A problem is well-posed if the solution depends on initial and boundary conditions in a continuous way. The number of conditions to be defined at each boundary depends on the number of characteristics entering or leaving the domain (Hirsch, 1990). These characteristics are the upstream and downstream traveling acoustic waves, as well as convectively transported vorticity and entropy waves.

In this section, first, an introduction to the acoustic reflection behavior of characteristic boundaries found in practice is given. Such boundaries

are typically represented by their complex impedance. Then, the general cases of computational boundaries for confined geometries: mass flow inlets, outlets and walls are considered. It is shown how vorticity and entropy waves at boundaries are generally treated in this thesis.

2.7.1 Impedance Boundary Conditions

The reflection of acoustic waves at a computational boundary is fully described through its complex impedance $Z(\omega)$ which relates perturbations in pressure $\hat{p}$ to velocity $\hat{u}_i$ by

$$Z(\omega) = \frac{1}{\bar{\rho}\bar{c}} \frac{\hat{p}}{\hat{u}_i n_i}, \qquad \text{on } \partial\Omega_Z, \tag{2.38}$$

where Ω denotes the computational domain and $\partial\Omega_Z$ is its impedance boundary. The impedance is the most general form of an acoustic boundary, since it is used to describe the reflection behavior of very different combustion chamber boundaries such as perforated screens, inlet diffusors or outlet high pressure vanes. Analogously, an acoustic boundary may be represented by its complex reflection coefficient $R(\omega)$ which describes the ratio of reflected to incident acoustic waves,

$$R(\omega) = \frac{\hat{p}^{+/-} e^{i\omega t}}{\hat{p}^{-/+} e^{i\omega t}}, \tag{2.39}$$

and is a more intuitive variable. It can easily be derived from the complex impedance $R = Z - 1/Z + 1$. While impedances or reflection coefficients describe the acoustic reflection behavior, they provide no answer to the question of how these boundaries acoustically reflect impinging entropy or vorticity fluctuations generated in flame or flow separation regions, respectively.

Subscribing impedances of Eq. (2.38) to computational boundaries using LNSEs for configurations with multidimensional flow fields is difficult. In such situations a modified formulation of the impedance must be introduced which takes gradients in the mean flow field into account (Ingard, 1959; Myers, 1980). Otherwise, unphysical instability waves may be created in the numerical solution (Brambley et al., 2012; Rienstra et al., 2013). The coupling of acoustic waves with impedance boundaries in presence of boundary layers is not trivial, even in frequency space.

2.7.1.1 Subsonic Nozzle or Diffusor

Generally, at the air inlet of a combustion chamber the flow is decelerated in a diffusor to reach lower Mach numbers. Part of the inlet air takes part in the combustion process while another part is used to cool the combustion chamber walls. When the burnt gases reach the combustion chamber outlet the mixture is accelerated in the first vane passage, which is also referred to as nozzle guide vane (NGV). These in- and outflow boundaries define the acoustic boundary conditions to any thermoacoustic stability analysis of gas turbines combustion chambers.

Depending on whether the flow state is sub-critical or choked, a nozzle or diffusor reflects acoustic waves differently. In case the flow is choked at its critical section ($Ma^* = 1$), acoustic waves are generally fully reflected. However, with increasing frequency reflection amplitudes generally decrease. In the other case, where the flow is sub-critical, acoustic waves may pass through the nozzle. Then, the reflection behavior does not only depend on the nozzle flow but also on the acoustic boundary condition up- or downstream of the diffuser or nozzle, respectively. With this knowledge available, the reflection behavior may be exactly specified using numerical or analytical tools.

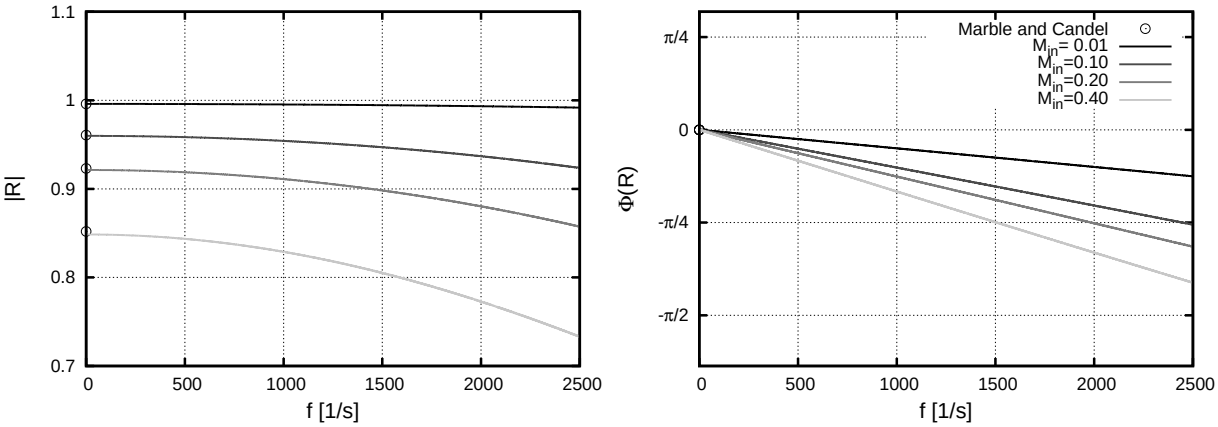

Figure 2.1: Mach number dependance of the reflection coefficient of a subsonic flow through a given nozzle configuration. The inlet flow Mach numbers are varied $Ma = 0.01, 0.1, 0.2$ and 0.4. Compact theory of Marble and Candel (1977) is compared to a non-compact one dimensional LEEs tool of Lamarque and Poinsot (2008).

Measurement of the acoustic reflection behavior of accelerated flows is generally difficult for various reasons. Therefore, analytical and numerical routines are generally preferred. Analytical models are restricted to one dimensional or at most two dimensional configurations. They are based on one dimensional solutions of the linearized Euler equations. Such models comprise the work on compact nozzles or nozzles having finite length of Marble and Candel (1977) or Cumpsty and Marble (1977). Mani (1981) also derives a theory for a nozzle's isentropic reflection behavior. All aforementioned authors, however, make assumptions on the axial flow distribution inside the nozzle. To avoid any assumption made, the one dimensional LEEs may be discretized using a finite difference method as shown by Lamarque and Poinsot (2008). Their routine is implemented in a Matlab code and is explained in detail in Appendix F, which also contains a variety of different validation test cases. Fig. 2.1 illustrates the difference between the theory of Marble and Candel (1977) assuming a compact nozzle configuration and the results of the one dimensional LEEs solver. As the compact theory is derived for the low frequency limit, results agree well in this region but will increasingly deviate towards higher frequencies. This code will be used to retrieve the acoustic impedance of a subsonic nozzle, placed at the end of an atmospheric combustion test rig in Section 6.2. Also compressible CFD, e.g. LES, can be used to study the acoustic reflection behavior of nozzle flows as shown e.g. by Lamarque and Poinsot (2008).

The acoustic reflection coefficient computed with the above mentioned methods is -strictly speaking- only valid for longitudinal waves impinging onto the inlet diffusor or outlet NGV. In annular combustion chambers, however, the acoustic modes tend to be circumferential in shape. Nevertheless, Stow et al. (2002) show that reflection coefficients obtained through one of the methods are still applicable to annular combustion chambers in first order principle.

Besides the reflection of acoustic waves, the accelerated flow inside a turbine stage may itself act as a source of sound. Non-uniformities of the equivalence ratio or of the pressure distributions inside the combustion zone create fluctuations in temperature or so-called hot-spots (Chu, 1953). After their convective transport to the exit of a combustion chamber, these are accelerated in the first turbine stage causing pressure and density fluctuations which are reflected back into the combustion chamber as

sound (Crocco, 1953; Tsien, 1952). This effect has already been covered by many publications including experimental investigations by Bake et al. (2009) and one dimensional modeling by (Leyko et al., 2009; Mani, 1981; Marble and Candel, 1977; Moase et al., 2007). The role of entropy waves for combustion driven instabilities is also analyzed by Eckstein et al. (2006).

2.7.1.2 Open Outlet

Open outlets are encountered at boundaries where a fluid discharges into atmosphere. This is for example the case at an aeroengine exhaust, where relatively high outlet Mach-numbers are reached. In terms of acoustics, the problem can be reduced to a straight circular duct which radiates noise into the surrounding atmosphere.

This kind of problem was first addressed by Levine and Schwinger (1948) who derive an analytical solution of the plane wave reflection coefficient with a fluid at rest and ambient conditions. For the compact case, i.e. duct radius considerably smaller than the plane wave length $r \ll \lambda$, the reflection coefficient amplitude is close to unity, see Fig. 2.2 for $He \to 0$. Later, their results were experimentally confirmed by Peters et al. (1993). A simple

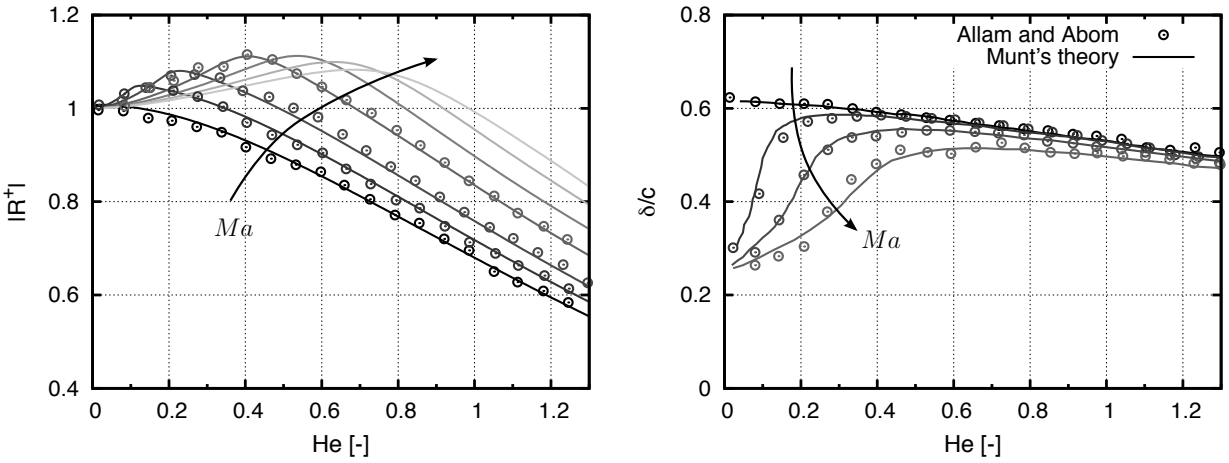

Figure 2.2: Mach number dependance of the reflection coefficient and extended length of a flow discharging into atmosphere. Flow Mach numbers are varied using $Ma = 0.05, 0.1, 0.2, 0.3, 0.4$. Experiments of Allam and Åbom (2006) are compared to the analytical theory of Munt (1990). Arrows indicate direction of increasing Mach numbers.

numerical representation of their findings is to prescribe vanishing pressure fluctuations

$$\hat{p} = 0, \quad \text{on} \quad \partial\Omega_D, \tag{2.40}$$

on Dirichlet outlet boundaries which is similar to prescribing $Z = 0$ in Eq. (2.38). This condition introduces a π-phase shift of the reflected wave. However, the assumptions of zero mean flow and compactness are highly restrictive and lose validity at higher frequencies. There, aero-acoustic interaction effects, especially interaction of acoustic waves with hydrodynamically unstable shear layers, lead to reflection coefficients exceeding one, which is theoretically explained by Howe (1979b).

The frequency dependant mean flow effect of acoustic reflections of open outlets was first addressed in a theoretical model by Munt (1977, 1990). The model takes aero-acoustic interaction effects into account and results in reflection coefficients above unity. His findings were confirmed by experiments performed e.g. by Allam and Åbom (2006) over a wide range of Mach-numbers at ambient temperature conditions. Munt's theoretical predictions and the experimental results of Allam and Åbom (2006) are compared against each other in Fig. 2.2 for various jet Mach-numbers. Therein, the phase of the reflection coefficient also shows a non trivial behavior. It is plotted as extended length, which can be interpreted as the virtual length, planar waves would travel into the opening before being reflected.

Very recently, Jörg et al. (2013) extended the analysis to higher exhaust gas temperatures which are more realistic for engine like conditions. Using a LNSEs based approach, they are able to show the significant influence of exhaust gas temperature. At higher Helmholtz numbers the reflection coefficient decreases significantly with respect to the temperature ratio T_{jet}/T_∞. The results also indicate possible limitations of Munt's theory as the model increasingly deviates from the numerically predicted results with rising temperature ratio. Fig. 2.3 compares the results obtained by LNSEs predictions and Munt's model for different elevated exhaust gas temperatures up to $T_{jet} = 1200K$. Note that the velocity correction proposed by Allam and Åbom (2006) is consistently used to correct Munt's model.

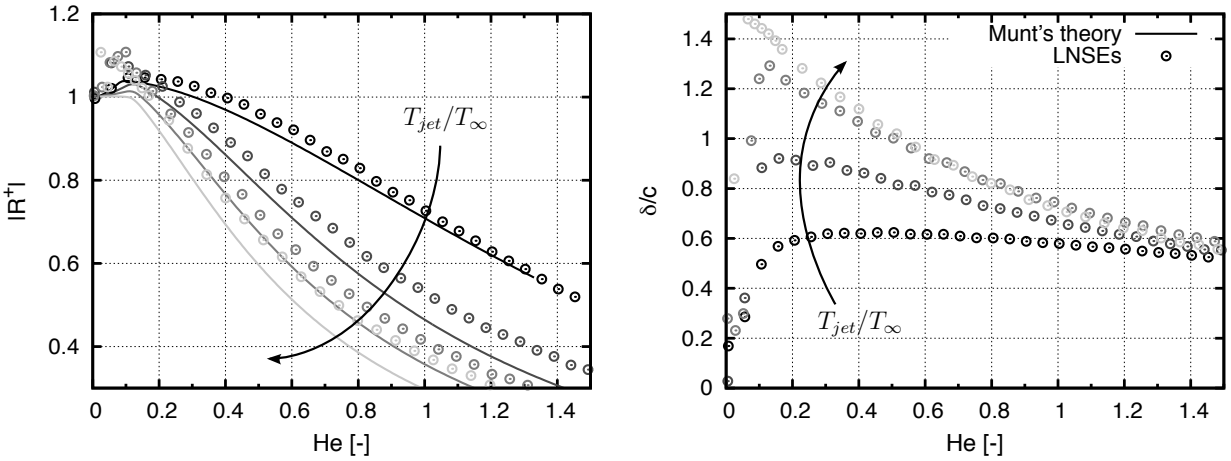

Figure 2.3: Jet temperature dependance of the reflection coefficient and extended length of a flow discharging into atmosphere. Flow temperatures are varied between $T_{jet} = 293, 600, 900$ and $1200\,\mathrm{K}$ at a constant outlet Mach number $Ma = 0.05$. Analytical model of Munt (1990) using a velocity correction proposed by Allam and Åbom (2006) is compared to the numerical simulations using a LNSEs approach by Jörg et al. (2013). Arrows indicate direction of increasing jet temperatures.

2.7.1.3 Perforated Screen

Another important type of boundaries frequently encountered in combustion chambers are perforated screens. In order to ensure thermal protection of the combustor walls, these are perforated by small diameter holes ($\sim \mathcal{O}(10^{-4})$ meters). Jets of cooling air issue from these holes. Through their coalescence, a cooling film is established which isolates the walls from the hot combustion gases. Although perforated plates are not considered in the present analysis, they are illustrated briefly for reasons of completeness of a thermoacoustic stability analysis.

From an acoustical point of view, perforated plates behave very differently to convectively cooled walls. On the one hand, the liner perforations lead to transmission of acoustic waves and therewith to a communication between the combustor and its periphery. On the other hand, perforations introduce damping of incident acoustic waves and thus may attenuate combustion instabilities (Howe, 1979a), a characteristic highly important for combustion chamber stability analysis. The mechanism behind the attenuation process can be explained by the conversion process of acoustic into vortical energy (Bechert, 1979; Howe, 1979a). Perforated screens have been

analyzed extensively analytically (Bellucci et al., 2004; Howe, 1979a, 1998), experimentally (Allam and Åbom, 2011; Bellucci et al., 2004; Eldredge and Dowling, 2003; Hughes and Dowling, 1990; Jing and Sun, 1999; Tran et al., 2009) and numerically (Dassé et al., 2008; Eldredge et al., 2007).

Accounting for perforated liners in the thermoacoustic stability analysis directly using LNSEs, would require the full resolution of all jets issuing from the perforated screens. Since these are small in diameter and high in number, this would require high amounts of grid cells clustered in near wall regions and would mostly be out of scale of any stability analysis. Therefore, impedance models are generally used to account for the damping effect of perforated liners (Bauer, 1977; Bellucci et al., 2004; Howe, 1979a; Jing and Sun, 1999). Mendez and Eldredge (2009) show that the modified model developed by Howe (1979a) and Jing and Sun (1999) represents the experimental measured reflection coefficients of Bellucci et al. (2004) with high accuracy. It is based on the assumption that the impedance of the perforated screen is composed of two parts, a wall impedance Z_p and a cavity impedance Z_c,

$$Z_{liner} = Z_p + Z_c. \tag{2.41}$$

In the cavity, planar wave propagation can be assumed

$$Z_c = -\frac{i\rho c}{tan\,(kl)}, \tag{2.42}$$

where l denotes the distance to the back wall of the cavity. The impedance of the perforated screen can be expressed in terms of a Rayleigh conductivity K_R

$$Z_p = \frac{i\omega\rho d^2}{K_R}, \tag{2.43}$$

where d denotes the hole spacing. The Rayleigh conductivity K_R is expressed in terms of first and second order Bessel functions B_1 and B_2 respectively

$$\begin{aligned} K_R &= 2r\left(\frac{1}{k_r} + \frac{2}{\pi}\frac{h}{r}\right)^{-1}, \quad \text{and} \\ k_r &= 2r\left(1 + \frac{\frac{\pi}{2}B_1(St)e^{-St} - iB_2(St)\sinh(St)}{St\left[\frac{\pi}{2}B_1(St)e^{-St} + iB_2(St)\cosh(St)\right]}\right). \end{aligned} \tag{2.44}$$

St denotes the Strouhal number of a single jet and r is the hole radius. The influence of perforated liners on the eigenmodes of an annular combustion chamber is shown by Gullaud and Nicoud (2012). Their findings illustrate that the overall damping reached by incorporating the effect of perforated combustor walls is of lower magnitude. The present study will show that damping contribution of the acoustic interactions with the swirled mean flow are generally an order of magnitude higher.

Taking into account perforated liners using complex impedances on duct wall boundaries in a LNSEs solver can result in the artificial excitation of Kelvin-Helmholtz instabilities (see Brambley et al., 2012; Rienstra et al., 2013). Such flow instabilities arise in the fluid dynamic boundary layer of the computation and are not observed in real applications. A Kelvin-Helmholtz instability is generally caused by an inflection point in the mean flow profile. However, in duct boundary layer profiles inflection points are normally absent. This is changed when imposing a complex impedance. The problem can be resolved by subscribing a modified impedance condition proposed by Ingard (1959) and Myers (1980).

2.7.2 Additional boundary conditions for LNSEs

After having addressed the acoustic reflection behavior of characteristic combustion chamber elements, the following sections provide a more general view on the computational boundary conditions for the use in a LNSEs solver. In order to define a well-posed problem, additional boundary conditions need to be imposed, which especially address the characteristic waves of vorticity and entropy not considered so far. This section provides different possibilities of boundaries and therewith completes the computational boundary treatment.

2.7.2.1 Mass Flow Inlet

At a mass flow inlet, five or four conditions need to be imposed in three dimensional space depending on whether the flow is super- or subsonic, respectively. For a subsonic flow, the involved characteristics entering the domain are the downstream traveling acoustic wave $(\bar{c} + \bar{u})$, the vorticity

wave vector and an entropy wave (both traveling with $\bar{u}$). At a supersonic inlet, the velocity speed of the upstream traveling wave changes sign ($\bar{c}-\bar{u}$) and, thus, an additional condition needs to be imposed.

Generally, no information is available concerning entropy and vorticity fluctuations at the inlet. Therefore, it is justified to assume that neither entropy nor vorticity waves enter the computational domain at its inlet. Setting zero entropy waves at the inlet leads to the following Dirichlet condition for the linearized energy equation

$$\hat{s} = 0, \quad \text{yielding} \qquad \hat{p} = \bar{c}^2 \hat{\rho} \qquad \text{on } \partial\Omega_D. \tag{2.45}$$

This is the same isentropic relation of Eq. (2.18). The assumption, however, may be too restrictive when the upstream boundary is choked. In this case acoustic waves that propagate upstream may interact with the shock that defines the boundary (Leyko et al., 2008). Interaction may lead to the generation of entropy waves that are convected downstream by the flow. In such situations, Eq. (2.45) can be replaced by assuming zero enthalpy fluctuations $\hat{h} = c_p \hat{T} + \bar{u}_i n_i \hat{u}_i n_i$, which directly translates to the following condition for the entropy perturbations

$$\hat{s} = \frac{1}{\bar{T}} \left(\frac{\hat{p}}{\bar{\rho}} + \bar{u}_i n_i \hat{u}_i n_i \right). \tag{2.46}$$

Alternatively, if the inlet is choked mass flow fluctuations vanish $\dot{m}' = (\rho u)' = 0$ or in other words

$$\hat{\rho}\bar{u} + \bar{\rho}\hat{u} = 0, \qquad \text{on } \partial\Omega_D. \tag{2.47}$$

As described above, generally no information about vorticity fluctuations is available at the domain inlet. In these situations it is natural to assume zero vorticity fluctuations for the linearized momentum equations by setting

$$\hat{u}_{||} = 0, \qquad \text{on } \partial\Omega_D. \tag{2.48}$$

The index $||$ refers to the components parallel to the respective boundary.

2.7.2.2 Mass Flow Outlet

At the mass flow outlet the situation is different: Vorticity and entropy waves are convected out of the domain and no boundary condition needs

to be imposed for these types of fluctuations. Solely acoustic waves are reflected back into the system when the flow is subsonic and have to be accounted for. Hence, in order to define a well-posed physical problem, only one boundary condition is necessary in case of a subsonic outlet, whereas no condition needs to be prescribed when the flow is supersonic. If no other information is available it is sufficient to impose an impedance boundary condition. Of course the outlet may also be assumed as choked, leading to the simple condition of Eq. (2.47) for the linearized momentum equations.

2.7.2.3 Wall Boundaries

In the vicinity of walls, fluid dynamic and acoustic boundary layers are formed due to adhesion forces of molecular particles. Thus, fluctuations of velocity must vanish in near wall regions, leading to

$$\hat{u}_i = 0, \qquad \text{on } \partial\Omega_D. \tag{2.49}$$

Prescribing this so-called no-slip condition to wall boundaries leads to the formation of an acoustic boundary layer, which needs to be resolved numerically. However, its thickness, which may be estimated for a quiescent medium as

$$\delta_a = \sqrt{\frac{2\nu}{\pi f}}, \tag{2.50}$$

decreases significantly with increasing frequency. Already at moderate frequencies the acoustic boundary layer δ_a is an order of magnitude smaller than the hydrodynamic layer δ_h. Thus, subscribing no-slip boundary conditions would result in a high clustering of finite elements in near wall regions. Gikadi et al. (2012) have shown that the effect of the acoustic boundary layer on the scattering behavior of an area expansion and a single hole orifice is insignificantly low. They state that, if the fluid dynamic boundary layer is resolved sufficiently the aeroacoustic interactions are captured correctly. In this case the acoustic boundary layer may be neglected by prescribing slip boundary conditions for the linearized momentum equation to all wall elements, i.e.

$$\hat{u}_i n_i = 0, \qquad \text{on } \partial\Omega_D, \tag{2.51}$$

which weakens the constraint of no velocity fluctuations to zero velocity fluctuations in normal to wall directions n_i.

For the energy equation Eq. (2.10) we may further assume that the combustion chamber walls have a constant temperature $T_w = \text{const.}$ and temperature fluctuations $\hat{T} = 0$ vanish. This leads to the following relationship from Eq. (2.16)

$$\hat{p} - \frac{\bar{p}}{\bar{\rho}}\hat{\rho} = 0, \qquad \text{on } \partial\Omega_D. \tag{2.52}$$

A suitable alternative is to prescribe a Neumann type of boundary condition, imposing zero gradient of fluctuating pressure and/or density,

$$\frac{\partial\hat{p}}{\partial x_i}n_i = 0, \qquad \frac{\partial\hat{\rho}}{\partial x_i}n_i = 0, \qquad \text{on } \partial\Omega_N. \tag{2.53}$$

With the definitions of the homogeneous boundary conditions, Eqs. (2.38)-(2.53) on $\partial\Omega = \partial\Omega_D \cup \partial\Omega_N \cup \partial\Omega_Z$ and $\hat{\dot{q}}_V = 0$, Eqs. (2.8)-(2.10) define either a linear eigenvalue problem with unknown complex ω, or a linear matrix inversion problem where ω is real and explicitly prescribed.

2.8 Acoustic Energy

Stability analysis of combustion chambers is based on the evaluation of the total acoustic energy in a given system. From the linearized mass, momentum and energy equations, Eqs. (2.8)-(2.10), an equation describing the temporal evolution of the system energy is obtained

$$\frac{\partial e}{\partial t} + \frac{\partial I_i}{\partial x_i} = Q, \tag{2.54}$$

where the value e is the (local) energy of perturbations per unit volume and I_i is an acoustic energy flux. Q defines a source term which includes the effect of the heat release but also other field sources due to acoustic-flow interaction or coupling with entropy waves. Integration over a stationary volume, interchanging integration with the partial derivative for e and applying the Gaussian divergence theorem leads to the integral form of the energy equation

$$\frac{\partial E}{\partial t} + \int_{\partial\Omega} I_i n_i dS = \int_{\Omega} Q dV, \tag{2.55}$$

where E is the (global) energy of perturbations integrated over the domain and the acoustic intensity I_i is only defined on the domain boundaries. The global acoustic energy budget includes internal and external energy. Whether a given system is unstable (the total energy of the system increases over time) or is stable (the total energy of the system decreases) depends on the temporal evolution of the system's global energy E and thus on the first term of Eq. (2.55). Assuming that the acoustic energy grows or decays similarly to $p'p'$ and thus proportional to $\exp(2\alpha t)$ yields for the rate of attenuation or amplification α:

$$\alpha = \frac{1}{2}\frac{\frac{\partial E}{\partial t}}{E}. \tag{2.56}$$

Substitution into Eq. (2.55) equivalently yields

$$\alpha = \frac{1}{2}\frac{\int_\Omega Q \; dV - \int_{\partial\Omega} I_i n_i \; dS}{E}, \tag{2.57}$$

a criterion for the stability of a combustion system. If $\alpha < 0$, the system damps energy. If $\alpha > 0$, the system amplifies energy and instability is observed. From the criterion of Eq. (2.57) damping and attenuation effects can be explained by comparing energy input to the energy output. Thus, system stability depends on the sign of the numerator.

Derivations of the terms for the energy E and acoustic flux I_i is non trivial, since energy is normally composed of second order terms of the perturbations. As the LNSEs, however, only contain terms of first order while all second order terms were omitted for the derivation of the equations, their explicit formulation is not trivial. For the simplest case of a quiescent medium or an isentropic medium, the acoustic energy can easily be derived. This is exemplarily performed in Appendix C. However, when considering a non-isentropic and non-quiescent medium the derivation gets far more complex. The classical definition of acoustic energy is then not sufficient anymore and a generalized disturbance energy corollary including entropy fluctuations needs to be derived (Nicoud and Poinsot, 2005). This is done by Myers (1991) who describes the energy of perturbations of an arbitrary steady flow. Karimi et al. (2008) further extend his theory by incorporate combustion terms. With availability of the complete perturbed fields using the methods presented in this thesis, an energy consideration becomes highly interesting for further investigations of the results from a phenomenological perspective.

2.9 Vortex-Acoustic Interaction

Configurations where shear layers in the mean flow are present are subjected to acoustic-flow coupling. Depending on the Strouhal number, perturbation energy may be transferred either to or from the acoustic field, leading to amplification or attenuation of the incident acoustic waves, respectively. In severe cases, amplification can lead to self-sustained oscillations in pipe systems, a phenomenon which is also called whistling (see Nelson et al., 1981, 1983).

The underlying mechanism of acoustic-flow interaction results from triggering of hydrodynamic instabilities or vortical disturbances in regions of flow separation. While they are convectively transported within the shear layer, they may continuously interact with the acoustic field. As described by Hofmans (1998) the interaction depends significantly on the incidence of the acoustic waves, i.e. on the spatial distribution of the acoustic velocity across a vortical structure. If, additionally, the shear layer features a hydrodynamic instability (Michalke, 1965), energy is transferred from the mean flow field into the vortical modes contributing to their growth. Thus, the interaction between acoustic waves and vortical structures may become stronger when hydrodynamic instabilities of the shear layer are present. This effect applies equivalently to attenuation and amplification processes.

The magnitude of the interaction can be estimated using the low-Mach number approximation for the time averaged acoustic power derived by Howe (1975, 1980, 1998):

$$\langle P \rangle = -\bar{\rho} \int_V \langle \boldsymbol{\omega} \times \mathbf{u} \rangle \cdot \mathbf{u}' \mathrm{d}V, \tag{2.58}$$

where $\boldsymbol{\omega} = \nabla \times \mathbf{u}$ is the vorticity vector, $\mathbf{u}$ is the local flow velocity and $\mathbf{u}'$ denotes the local acoustic perturbation velocity. Integration is performed over the volume enclosing the vorticity V. If the time-averaged power is negative, acoustic energy is lost to the hydrodynamic field. Conversely, sound is generated when the time-averaged power is positive (Karlsson and Åbom, 2010).

2.10 Non-Linearity and Non-Orthogonality

The current analysis focuses on linear stability of combustion systems. This assumption seems to be well justified at the time of the onset and initial growth of instabilities where the amplitudes of oscillations are small (Zinn and Lieuwen, 2005). Thus, linear models are well suited to discriminate between unstable and stable combustor operation. However, after the onset of instability the oscillation amplitudes increase and non-linear phenomena start to govern the driving and damping behavior of combustors.

The main driver for non-linearities is the convective term $\nabla(\rho u_i u_j)$ in the Navier-Stokes equations Eqs. (2.1)-(2.3). Non-linearities determine limit cycle amplitudes (the finite amplitude of oscillations), instability triggering (the mechanism by which an unstable oscillation appears when the system experiences a finite amplitude perturbation), mode switching (the change in frequency observed during operation of practical devices) and hysteresis (Dowling, 1997, 1999; Lieuwen and Neumeier, 2002; Wicker et al., 1996). In terms of energy, the non-linear terms neglected in the present analysis, may also lead to a redistribution of energy among different length scales, i.e. eigenmodes, see Schmid and Henningson (2001).

When considering the flame to be the only or main driver of instabilities (Dowling, 1997), the effect of saturation may also be captured in a purely linear framework by incorporating the so-called flame describing function (FDF) (Noiray et al., 2008). In their work the authors extend FTFs, Eq. (2.32), by taking the amplitude of velocity perturbations at the burner mouth into account, viz. $\mathcal{F}(\omega, \hat{u}_{ref})$. Generally, this leads to decreasing flame responses with increasing velocity amplitude as non-linear damping processes increase.

Another characteristic of a linear system is the non-orthogonality of its eigenvectors. If the eigenvectors are not orthogonal to each other, they may interact in a way that short term transient growth may occur even though a linearly stable behavior is predicted. In the long term, however, the system will reach its initial stable state. The theory of non-normal interactions is introduced to thermoacoustics analysis by Balasubramanian and Sujith (2008). Parameters influencing the orthogonality of the eigenfunctions are

boundary conditions, heat release rate and a non-zero and multidimensional baseline flow (Crighton, 1975; Wieczorek et al., 2010).

3 The Finite Element Method

To solve the acoustic problem, the frequency space LNSEs Eqs. (2.13)-(2.15) need to be discretized using a finite volume, finite difference or finite element technique. Despite the popularity of finite elements for the use in structural dynamics, it is far from being popular in the field of fluid mechanics. This development may be explained through the fact (among others) that the best approximation character of finite elements is lost when considering non-elliptic partial differential equations (Hughes, 2000). In such cases the differential operators are not self-adjoint, a characteristic which is mostly found in fluid mechanics. Structural dynamics problems, on the other hand, are of elliptic type and therefore keep the best approximation feature of finite elements.

Finding a suitable discretization technique for computational acoustic problems is somewhat complex: The scalar Helmholtz equation Eq. (2.25), frequently used for thermoacoustic analysis, is indeed of elliptic character and finite elements are well-suited. However, when considering frequency space LNSEs the elliptic character of the equations is partially lost and the finite element technique loses its main advantage over, e.g., a finite volume technique. As it is a main aim of this thesis to develop a unified framework to study thermoacoustic instabilities, these conflicting requirements for the choice of discretization technique cannot be resolved. However, with the development of stabilized finite element techniques (Hughes and Brooks, 1979; Hughes et al., 1989, 2004, 2010), the finite element method has become competitive for the use in fluid mechanic problems. Therefore, the finite element procedure is selected as the method of choice in this thesis to discretize both, the LNSEs as well as the Helmholtz equation. The following sections focus on the finite element treatment of the LNSEs, while details on the treatment of the Helmholtz equation can be found in Appendix E.

To simplify the derivation, we will rewrite the LNSEs for a three dimensional cartesian coordinate system in a more compact notation, using nabla operators:

$$i\omega\hat{\rho} + \nabla \cdot (\bar{\mathbf{u}}\hat{\rho} + \bar{\rho}\hat{\mathbf{u}}) = s_\rho, \tag{3.1}$$

$$i\omega\bar{\rho}\hat{\mathbf{u}} + \nabla \cdot (\bar{\rho}\bar{\mathbf{u}}\hat{\mathbf{u}}) + \nabla\hat{p} + (\bar{\rho}\hat{\mathbf{u}} + \bar{\mathbf{u}}\hat{\rho}) \cdot \nabla\bar{\mathbf{u}} = \nabla \cdot \boldsymbol{\tau}(\hat{\mathbf{u}}) + \mathbf{s}_\mathbf{u}, \tag{3.2}$$

$$i\omega\hat{p} + \nabla \cdot (\bar{\mathbf{u}}\hat{p} + \kappa\bar{p}\hat{\mathbf{u}}) + (\kappa - 1)\left[\hat{p}\nabla \cdot \bar{\mathbf{u}} - \hat{\mathbf{u}} \cdot \nabla\bar{p}\right] = s_p. \tag{3.3}$$

The LNSEs are composed into four different parts starting from the very left: A frequency dependent term, a convective term, a reactive term (absent in Eq. (3.1)), a diffusive term and source terms s_ρ, $\mathbf{s}_\mathbf{u}$ and s_p , e.g. including the heat release term. Compared to the LNSE representation of Section 2.1, $\boldsymbol{\tau}(\hat{\mathbf{u}})$ represents the linearized stress tensor. The term including the stress tensor in the linearized energy equation Eq. (2.15) is included into the source term s_p to simplify the derivation. Other forms used in the literature to represent LNSEs are shown in Appendix B. For illustration purposes the Navier-Stokes equations are often recasted into a scalar convection-diffusion-reaction (CDR) equation of an arbitrary variable ϕ. Doing so for a fluctuating variable ϕ in frequency space, yields

$$i\omega\hat{\phi} + \nabla \cdot \left(\bar{\mathbf{u}}\hat{\phi}\right) + \sigma\hat{\phi} = \nu\Delta\hat{\phi} + s_\phi, \tag{3.4}$$

where σ is the constant coefficient of the reactive term and s_ϕ is a source term. Note that this scalar equation is equally structured to the LNSEs of Eqs. (3.1)-(3.3).

It is again noted that the full set of LNSEs are solved in this thesis. This is not commonly the case for aeroacoustic applications found in literature, which mainly introduce simplifications to the reactive terms of Eqs. (3.2) and (3.3) in order to avoid or suppress Kelvin-Helmholtz instabilities. Ewert and Schröder (2003) e.g., assume a vortex free velocity field, viz. $\boldsymbol{\omega} \times \mathbf{u} = 0$ where $\boldsymbol{\omega} = \nabla \times \mathbf{u}$. Other publications simply neglect all mean gradient terms (cp. Tester et al., 2008) or, like Bogey et al. (2002); Zhang et al. (2004), only remove a distinct set of mean gradient terms. Latter procedure mainly affects the reactive terms of Eqs. (3.2) and (3.3) which are responsible for the acoustic flow coupling processes. A small review on the different methods to suppress shear layer instability is provided by Richter et al. (2011). Equations simplified in this way are well suited for the description of far fields in aeroacoustic problems, where a uniform or no flow is present.

However, by doing so, it is believed that the coupling process of acoustic waves with vortical or entropy disturbances is not captured correctly. This will consequently affect the prediction accuracy of sound attenuation and amplification processes, which this thesis aims to predict. Therefore, no simplifications are introduced and Kelvin-Helmholtz instabilities become part of the solution.

Keeping Kelvin-Helmholtz instabilities in the solution, however, may lead to numerical difficulties. On one hand, their unbounded growth in time leads to strong local gradients for the solution variables. On the other hand, an insufficient numerical resolution of the vortical disturbances may lead to spurious oscillations or grid dependence of the acoustic solution (Seo and Moon, 2005). The first problem of unbounded transient growth was resolved in Section 2.1 by transforming the LNSEs into frequency space, Eqs. (3.1)-(3.3), and therewith allowing only spatial growth of instabilities. The second problem is resolved by introducing stabilized finite element techniques, which can be thought of as approximations of a variational multiscale approach (Hughes et al., 1998). This approach models the effect of the unresolved scales and therefore numerically stabilizes the solution.

In this chapter the standard Galerkin finite element method will be introduced first, as this is the standard procedure. Following Hughes (2000) we will adopt the four step procedure of spatial discretization: (i) Starting from the strong form of partial differential equations developed in Chapter 2, (ii) we will introduce a weak form based on the method of weighted residuals. While the weak form is still an exact representation of the governing equations, (iii) introducing Galerkin finite element functions leads to their approximative form. The preceding efforts may then be summarized in a matrix form (iv) which is delivered to the numerical solver discussed in the next Chapter 4. Due to the character of the LNSEs numerical difficulties will arise using the standard Galerkin technique. Therefore, stabilized finite element procedures are introduced.

Books for further in-depth studies and reviews found on the finite element techniques in literature are for example the one of Hughes (2000) or Johnson (1987); Zienkiewicz and Taylor (2000). From a fluid mechanics point of view, the books of Donea and Huerta (2003) and Gresho and Sani (1998) show illuminating insights.

3.1 Standard Galerkin Approach

First, the residuals of the linearized equation of mass, momentum and energy, respectively, are introduced

$$\mathcal{R}_C(\hat{\rho}) = i\omega\hat{\rho} + \nabla\cdot(\bar{\mathbf{u}}\hat{\rho} + \bar{\rho}\hat{\mathbf{u}}) - s_\rho, \tag{3.5}$$

$$\mathcal{R}_M(\hat{\mathbf{u}}) = i\omega\bar{\rho}\hat{\mathbf{u}} + \nabla\cdot(\bar{\rho}\bar{\mathbf{u}}\hat{\mathbf{u}}) + \nabla\hat{p} + (\bar{\rho}\hat{\mathbf{u}} + \bar{\mathbf{u}}\hat{\rho})\cdot\nabla\bar{\mathbf{u}} - \nabla\cdot\boldsymbol{\tau}(\hat{\mathbf{u}}) - \mathbf{s}_\mathbf{u}, \tag{3.6}$$

$$\mathcal{R}_E(\hat{p}) = i\omega\hat{p} + \nabla\cdot(\bar{\mathbf{u}}\hat{p} + \kappa\bar{p}\hat{\mathbf{u}}) + (\kappa-1)\left[\hat{p}\nabla\cdot\bar{\mathbf{u}} - \hat{\mathbf{u}}\cdot\nabla\bar{p}\right] - s_p. \tag{3.7}$$

The weak or variational form of the problem may then be derived by multiplying the residuals of Eqs. (3.5)-(3.7) with weighting functions w_ρ, $\mathbf{w}_u$, w_p and performing an integration over the domain Ω

$$\int_\Omega \mathcal{R}_C w_\rho \; d\Omega = 0, \qquad \int_\Omega \mathcal{R}_M \mathbf{w}_\mathbf{u} \; d\Omega = 0, \qquad \int_\Omega \mathcal{R}_E w_p \; d\Omega = 0. \tag{3.8}$$

The method is generally termed as weighted residual method. In this form, the condition for the fulfillment of the set of governing equations at every point of the domain is weakened to the integral fulfillment over the complete domain Ω. Thus, the finite element method can be considered as conservative in a global fashion. Eqs. (3.8) may be written in compact form by introducing the L_2-inner product in the domain Ω:

$$(a,b)_\Omega = \int_\Omega ab \; d\Omega. \tag{3.9}$$

After performing integration by parts of the Cauchy stress tensor, including the pressure and diffusive term of the linearized momentum equation, the weak form of the LNSEs is obtained

$$(w_\rho, i\omega\hat{\rho})_\Omega + (w_\rho, \nabla\cdot(\bar{\mathbf{u}}\hat{\rho} + \bar{\rho}\hat{\mathbf{u}}))_\Omega = (w_\rho, s_\rho)_\Omega\,, \quad \forall w_\rho \in \mathcal{V}_\rho, \tag{3.10}$$

$$\begin{aligned}(\mathbf{w}_\mathbf{u}, i\omega\bar{\rho}\hat{\mathbf{u}})_\Omega + (\mathbf{w}_\mathbf{u}, \nabla\cdot(\bar{\rho}\bar{\mathbf{u}}\hat{\mathbf{u}}))_\Omega + (\nabla\cdot\mathbf{w}_\mathbf{u}, \hat{p})_\Omega + (\mathbf{w}_\mathbf{u}, (\bar{\rho}\hat{\mathbf{u}} + \bar{\mathbf{u}}\hat{\rho})\cdot\nabla\bar{\mathbf{u}})_\Omega = \\ -(\boldsymbol{\tau}(\mathbf{w}_\mathbf{u}), \boldsymbol{\tau}(\hat{\mathbf{u}}))_\Omega + (\mathbf{w}_\mathbf{u}, \mathbf{s}_\mathbf{u})_\Omega + (\mathbf{w}_\mathbf{u}, \mathbf{h}_\mathbf{u})_{\partial\Omega_N}\,, \qquad \forall \mathbf{w}_\mathbf{u} \in \mathcal{V}_\mathbf{u},\end{aligned} \tag{3.11}$$

$$\begin{aligned}(w_p, i\omega\hat{p})_\Omega + (w_p, \nabla\cdot(\bar{\mathbf{u}}\hat{p} + \kappa\bar{p}\hat{\mathbf{u}}))_\Omega + (w_p, (\kappa-1)\left[\hat{p}\nabla\cdot\bar{\mathbf{u}} - \hat{\mathbf{u}}\cdot\nabla\bar{p}\right])_\Omega = \\ (w_p, s_p)_\Omega\,, \qquad \forall w_p \in \mathcal{V}_p,\end{aligned} \tag{3.12}$$

where $\mathcal{V}_{\{\rho,\mathbf{u},p\}}$ are the weighting function spaces for the respective weighting functions w_ρ, $\mathbf{w_u}$ and w_p. Similarly, the solution function spaces $\mathcal{S}_{\{\rho,\mathbf{u},p\}}$ are assumed for the solution variables $\hat{\rho}$, $\hat{\mathbf{u}}$ and $\hat{p}$, see Donea and Huerta (2003) for elaboration. For the momentum equation a 'natural' Neumann boundary term arises in the formulation

$$\mathbf{n} \cdot (-\hat{p}\mathbf{I} + \boldsymbol{\tau}(\hat{\mathbf{u}})) = \mathbf{h_u}, \text{ on } \quad \partial\Omega_N \tag{3.13}$$

which is equal to some $\mathbf{h_u}$. The weak form poses lower demands on the differentiability, as the formulation includes only first order derivatives instead of formerly derivatives of second order. Finally, to complete the weak formulation it is required to chose the solution and weighting function spaces according to

$$\mathcal{S}_{\{\rho,\mathbf{u},p\}} = \left\{ \{\hat{\rho}, \hat{\mathbf{u}}, \hat{p}\} \in H^1(\Omega)^d | \, \{\hat{\rho}, \hat{\mathbf{u}}, \hat{p}\} = \mathbf{g}, \quad \text{on } \partial\Omega_D \right\}, \tag{3.14}$$

$$\mathcal{V}_{\{\rho,\mathbf{u},p\}} = \left\{ \{w_\rho, \mathbf{w}_u, w_p\} \in H^1(\Omega)^d | \, \{w_\rho, \mathbf{w}_u, w_p\} = \mathbf{0}, \quad \text{on } \partial\Omega_D \right\}, \tag{3.15}$$

where $H^1(\Omega)$ describes the Sobolev space of square-integral functions and square-integral first derivatives and $\mathbf{g}$ is the respective vector at the Dirichlet boundary. Further remarks on this Sobolev space can be found in the existing literature.

In a next step, the problems geometry is discretized into a number N_e finite elements with subdomains Ω_e $(e = 1, ..., N_e)$ and a number N_v vertices v_k $(k = 1, ..., N_v)$ of which N_D are located on $\partial\Omega_D$ where

$$\Omega' = \bigcup_{e=1}^{N_e} \Omega_e, \quad \text{and} \quad \partial\Omega' = \bigcup_{e=1}^{N_e} \partial\Omega_e | \partial\Omega, \tag{3.16}$$

denote the union of all element interiors and element boundaries excluding the domain boundary $\partial\Omega$, respectively. The Galerkin finite element approximation can then be obtained by replacing the (quasi) infinite dimensional subspaces $\mathcal{S}_{\{\rho,\mathbf{u},p\}}$ and $\mathcal{V}_{\{\rho,\mathbf{u},p\}}$ by their finite dimensional counterparts $\mathcal{S}^h_{\{\rho,\mathbf{u},p\}}$ and $\mathcal{V}^h_{\{\rho,\mathbf{u},p\}}$. Accordingly, the solution variables become also discrete or finite which is denoted by the superscript h. They may be expressed in terms of unknown parameters $\hat{\rho}_A$, $\hat{\mathbf{u}}_A$ and $\hat{p}_A$ and shape functions N_A, which are mostly represented by polynomial functions. Introducing these approximations yields

$$\hat{\rho}^h = \sum_{A=1}^{N_{dofs}} N_A \hat{\rho}_A, \quad \hat{\mathbf{u}}^h = \sum_{A=1}^{N_{dofs}} N_A \hat{\mathbf{u}}_A, \quad \hat{p}^h = \sum_{A=1}^{N_{dofs}} N_A \hat{p}_A, \tag{3.17}$$

where N_{dofs} is the number of degrees of freedom. Similarly, introducing the same approximations for the weighting functions leads to

$$w_\rho^h = \sum_{B=1}^{N_{dofs}} N_B w_{\rho,B}, \quad \mathbf{w}_\mathbf{u}^h = \sum_{B=1}^{N_{dofs}} N_B \mathbf{w}_{\mathbf{u},B}, \quad w_p^h = \sum_{B=1}^{N_{dofs}} N_B w_{p,B}, \tag{3.18}$$

the standard Galerkin approach, which is also known as Bubnov-Galerkin approach. When the weighting functions are chosen differently from the solution functions the approach is generally referred to as Petrov-Galerkin approach. In the present analysis Lagrangian shape functions of a certain polynomial order p are chosen for Eq. (3.17) and Eq. (3.18). Finally, the standard Galerkin finite element formulation in its discrete form reads as: find $\hat{\rho}^h \in \mathcal{S}_\rho^h$ to satisfy

$$\begin{aligned} B\left(w_\rho^h, \hat{\rho}^h\right)_\Omega &= \left(w_\rho^h, s_\rho\right)_\Omega, \quad \text{where} \\ B\left(w_\rho^h, \hat{\rho}^h\right)_\Omega &= \left(w_\rho^h, i\omega\hat{\rho}^h\right)_\Omega + \left(w_\rho^h, \nabla\cdot\left(\bar{\mathbf{u}}\hat{\rho}^h + \bar{\rho}\hat{\mathbf{u}}^h\right)\right)_\Omega, \end{aligned} \tag{3.19}$$

$\hat{\mathbf{u}}^h \in \mathcal{S}_\mathbf{u}^h$ for

$$\begin{aligned} B\left(\mathbf{w}_\mathbf{u}^h, \hat{\mathbf{u}}^h\right)_\Omega &= \left(\mathbf{w}_\mathbf{u}^h, \mathbf{s}_\mathbf{u}\right)_\Omega + \left(\mathbf{w}_\mathbf{u}^h, \mathbf{h}_\mathbf{u}\right)_{\partial\Omega_N}, \quad \text{where} \\ B\left(\mathbf{w}_\mathbf{u}^h, \hat{\mathbf{u}}^h\right) &= \left(\mathbf{w}_\mathbf{u}^h, i\omega\bar{\rho}\hat{\mathbf{u}}^h\right)_\Omega + \left(\mathbf{w}_\mathbf{u}^h, \nabla\cdot\left(\bar{\rho}\bar{\mathbf{u}}\hat{\mathbf{u}}^h\right)\right)_\Omega + \left(\nabla\mathbf{w}_\mathbf{u}^h, \hat{p}^h\right)_\Omega \\ &\quad + \left(\mathbf{w}_\mathbf{u}^h, \left(\bar{\rho}\hat{\mathbf{u}}^h + \bar{\mathbf{u}}\hat{\rho}^h\right)\cdot\nabla\bar{\mathbf{u}}\right)_\Omega + \left(\boldsymbol{\tau}(\mathbf{w}_\mathbf{u}^h), \boldsymbol{\tau}(\hat{\mathbf{u}}^h)\right)_\Omega, \end{aligned} \tag{3.20}$$

and $\hat{p}^h \in \mathcal{S}_p^h$ for

$$\begin{aligned} B\left(w_p^h, \hat{p}^h\right) &= \left(w_p^h, s_p\right)_\Omega, \quad \text{where} \\ B\left(w_p^h, \hat{p}^h\right) &= \left(w_p^h, i\omega\hat{p}^h\right)_\Omega + \left(w_p^h, \nabla\cdot\left(\bar{\mathbf{u}}\hat{p}^h + \kappa\bar{p}\hat{\mathbf{u}}^h\right)\right)_\Omega \\ &\quad + \left(w_p^h, (\kappa-1)\left[\hat{p}^h\nabla\cdot\bar{\mathbf{u}} - \hat{\mathbf{u}}^h\cdot\nabla\bar{p}\right]\right)_\Omega. \end{aligned} \tag{3.21}$$

In a similar manner, the standard Galerkin problem of the general convection-diffusion-reaction equation Eq. (3.4) can be formulated for the appropriate solution $\mathcal{S}_\phi^h$ and weighting function space $\mathcal{V}_\phi^h$ as find $\hat{\phi}^h \in \mathcal{S}_\phi^h$ to satisfy

$$\begin{aligned} B\left(w_\phi^h, \hat{\phi}^h\right)_\Omega &= \left(w_\phi^h, s_\phi\right)_\Omega + \left(w_\phi^h, h_\phi\right)_{\partial\Omega_N}, \quad \text{where} \\ B\left(w_\phi^h, \hat{\phi}^h\right)_\Omega &= \left(w_\phi^h, i\omega\hat{\phi}^h\right)_\Omega + \left(w_\phi^h, \nabla\cdot\left(\bar{\mathbf{u}}\hat{\phi}^h\right)\right) \\ &\quad + \left(w_\phi^h, \sigma\hat{\phi}^h\right) + \left(\nabla w_\phi^h, \nu\nabla\hat{\phi}^h\right) \end{aligned} \tag{3.22}$$

and h_ϕ denotes the Neumann boundary arising naturally from integration-by-parts of the diffusive term.

As already mentioned above, the standard finite element method looses its best approximation characteristic (minimum error) when considering LNSEs. The main reasons is that the convective operator in the LNSEs is not self-adjoint, which will lead to numerical problems in the solution process. For high Reynolds and Péclet number flows, this effect has been illustrated multiple times for a one dimensional stationary convective-diffusion equation., e.g. in Donea and Huerta (2003). There, it is shown that for element Péclet numbers $Pe^e > 1$, describing the ratio of convection and diffusion,

$$Pe^e = \frac{uh}{2\nu}, \tag{3.23}$$

where h is the characteristic element length and u the velocity of the fluid, the numerical solution oscillates. To avoid such spurious oscillations using the standard Galerkin technique, the domain has to be discretized in such a way to fulfill $Pe^e < 1$ in the complete domain. Since the physical conditions of the problem considered cannot be changed, the only way to achieve the requirement is to increase the number of elements and thereby to decrease h. Then, the convective effect related to the individual element becomes not dominant any more. However, doing so results in excessive numerical refinements, especially in boundary layer regions or regions in which strong shear layers exist. By modeling the effect of the unresolved scales using Petrov-Galerkin schemes, excessive refinements can be avoided.

3.2 Artificial Diffusion Schemes

When comparing a discrete Galerkin scheme to an exact difference scheme for convection-diffusion problems, it can be shown that the Galerkin term introduces a truncation error of the form of a diffusion operator (Donea and Huerta, 2003). For element Péclet numbers exceeding one, its sign is negative and thus a negative diffusion is introduced to the problem. This implies that actually, a modified convection-diffusion equation is solved characterized by a reduced diffusion effect. For this case, no generally stable solution

can be guaranteed. It is then intuitive and obviously simple to add an artificial viscosity term to compensate the numerically introduced negative diffusion, e.g. to the momentum equation Eq. (3.20)

$$B\left(\mathbf{w}_{\mathbf{u}}^h, \mathbf{u}\right)_\Omega + \sum_{e=1}^{N_e} \left(\boldsymbol{\tau}(\mathbf{w}_{\mathbf{u}}^h), \frac{\bar{\rho}\nu_{art}^e}{\mu}\boldsymbol{\tau}(\hat{\mathbf{u}}^h)\right)_{\Omega_e} = \left(\mathbf{w}_{\mathbf{u}}^h, \mathbf{s}_{\mathbf{u}}\right)_\Omega + \left(\mathbf{w}_{\mathbf{u}}^h, \mathbf{h}_{\mathbf{u}}\right)_{\partial\Omega_D}, \tag{3.24}$$

which reduces the element Péclet number. The artificial viscosity ν_{art}^e acts on all element interiors and can be specified for example as

$$\nu_{art}^e = \begin{cases} \frac{|\bar{u}|h}{2}\frac{Pe^e}{3} & \text{for} \quad Pe^e < 3 \\ \frac{|\bar{u}|h}{2} & \text{for} \quad Pe^e \geq 3 \end{cases}. \tag{3.25}$$

Such a procedure, however, is not adopted in the present study for the following reasons: In one dimensional space an appropriate choice of the artificial diffusion ν_{art}^e would lead to nodal exact solutions for a convection-diffusion equation. However, when the equations are solved in three dimensional space, such artificial diffusion terms introduce significant amounts of additional diffusion, which may significantly exceed the physical observed magnitude. It is isotropically introduced in all directions, acting in streamline but also in crosswind direction. Following Johnson (1987) and John and Knobloch (2007) such procedures lead to an accuracy of at most first order $\mathcal{O}(h)$. Thus, increasing the polynomial order p of the shape functions, does not equivalently increase the computational accuracy.

Moreover, there is no stabilization of reactive terms, which is a crucial point when considering LNSEs. Many publications in aeroacoustic problems introduce simplifications to the reactive terms in order to avoid numerical difficulties, see e.g. (Bogey et al., 2002). Thus, numerical instabilities stemming form the reactive terms may still be observed, even though artificial viscosity is introduced. Similarly, the source terms are not specially treated using artificial viscosity methods, which for some cases may also lead to instabilities and inaccuracies in the solution. Therefore, despite the simplicity of artificial diffusion methods, care has to be taken with their application. They have been added to the present thesis to highlight analogies to Petrov-Galerkin schemes discussed in the next chapter, but also to show their inferiority.

3.3 Petrov-Galerkin Approach

Stabilized finite elements methods (SFEMs) have been introduced to various problems in fluid dynamics. It can be referred to the review articles of Codina (1998) for convection-diffusion(-reaction) equations, of Hughes et al. (2004) for convection-diffusion and incompressible Navier-Stokes equations and of Hughes et al. (2010) for compressible Navier-Stokes equations. Independently of their explicit derivation, all stabilization techniques have a similar form. When introducing SFEMs to the standard Galerkin approach an additional term arises on the LHS. This is exemplarily shown in the case of the scalar convection-diffusion-reaction equation, Eq. (3.22), yielding

$$B(w_\phi^h, \phi^h)_\Omega + \left(\mathcal{R}_\phi, \tau_{\text{stab}}\mathcal{P}(w_\phi^h)\right)_{\Omega|\partial\Omega} = \left(w_\phi^h, s_\phi\right)_\Omega , \tag{3.26}$$

where $\mathcal{P}(w_\phi)$ is a certain operator applied to the weighting function, τ_{stab} is the stabilization parameter and $\mathcal{R}_\phi$ represents the equations residual. All stabilization techniques differ in the explicit choice of the operator $\mathcal{P}(w_\phi)$. In this section we will mainly provide an overview of the methods which were directly applied in the current work. These incorporate the streamline-upwind/Petrov-Galerkin technique and two variants of the Galerkin/least-squares stabilization technique. Overviews describing the evolution of stabilized finite element schemes are found in Donea and Huerta (2003); Hughes et al. (1994) and Wall (1999).

3.3.1 Streamline-Upwind/Petrov-Galerkin Technique

The development of the streamline-upwind/Petrov-Galerkin technique (SUPG) originates from the idea to overcome the disadvantages introduced through isotropic artificial diffusion schemes: While imposing additional viscosity in streamline direction, the same amount is also imposed in crosswind direction, where convective effects are low. To overcome the inherent crosswind diffusion, Hughes and Brooks (1979) replaced the scalar artificial diffusion term with an artificial diffusion tensor taking into account the respective flow direction. Their so-called streamline-upwind (SU) method adds diffusion in streamline direction without being overly diffusive in crosswind direction. However, the technique was designed in such a way that

the operator $\mathcal{P}(w_\phi)$ would act only on the convective term and not on the hole residuum $\mathcal{R}_\phi$, like depicted in Eq. (3.26). Therefore, the method still lacks in consistency. Brooks and Hughes (1982) then applied the same operator on the complete residuum, ensuring consistency of the newly developed SUPG approach. The SUPG operator then writes for the general convection-diffusion-reaction equation Eq. (3.22)

$$\mathcal{P}_{\mathrm{SUPG}}(w_\phi^h) = \nabla \cdot \left(\bar{\mathbf{u}} w_\phi^h\right). \tag{3.27}$$

When introducing Eq. (3.27) to the standard Galerkin approximation of Eq. (3.26) the equations may be rearranged in such a way that a standard Bubnov-Galerkin form is reached, but this time including a modified test function

$$\tilde{w}_\phi = w_\phi^h + \tau_{\mathrm{stab}} \nabla \cdot \left(\bar{\mathbf{u}} w_\phi^h\right). \tag{3.28}$$

In fact, this illustrates the reason why SUPG belongs to the family of Petrov-Galerkin approaches, since the space of the test function does not coincide with the space of the interpolation functions. The SUPG technique can then be directly applied to the LNSEs, which yields extra terms for the linearized equation of mass, momentum and energy of the form

$$B_{\mathrm{SUPG}}^C \left(w_\rho^h, \hat{\rho}^h\right)_{\Omega|\partial\Omega} = \left(\mathcal{R}_C(\hat{\rho}^h), \tau_C \nabla \cdot \left(\bar{\mathbf{u}} w_\rho^h + \bar{\rho} \mathbf{w}_{\mathbf{u}}^h\right)\right)_{\Omega|\partial\Omega}, \tag{3.29}$$

$$B_{\mathrm{SUPG}}^M \left(\mathbf{w}_{\mathbf{u}}^h, \hat{\mathbf{u}}^h\right)_{\Omega|\partial\Omega} = \left(\mathcal{R}_M(\hat{\mathbf{u}}^h), \boldsymbol{\tau}_M \nabla \cdot \left(\bar{\rho} \bar{\mathbf{u}} \mathbf{w}_{\mathbf{u}}^h\right)\right)_{\Omega|\partial\Omega}, \tag{3.30}$$

$$B_{\mathrm{SUPG}}^E \left(w_p^h, \hat{p}^h\right)_{\Omega|\partial\Omega} = \left(\mathcal{R}_E(\hat{p}^h), \tau_E \nabla \cdot \left(\bar{\mathbf{u}} w_p^h + \kappa \bar{p} \mathbf{w}_{\mathbf{u}}^h\right)\right)_{\Omega|\partial\Omega}, \tag{3.31}$$

where τ_C, $\boldsymbol{\tau}_M$ and τ_E define the stabilization parameters of the linearized continuity, momentum and energy equation. A mathematical analysis proves that SUPG may feature an order of accuracy $\mathcal{O}(h^{p+1/2})$ for convection dominated problems and an order $\mathcal{O}(h^{p+1})$ for diffusion dominated problems (Johnson, 1987). Latter order of accuracy is identical to the one reached within a classical Galerkin approach. The mathematical analysis shows that the SUPG method provides convergence characteristics superior to the above mentioned methods (SU or artificial diffusion) which are at most first order accurate. This becomes especially important when choosing higher order interpolation functions, i.e. changing the order p. It has to be noted though that in order to ensure the order of accuracy of the mentioned methods, τ_{stab} has to be chosen accordingly. The formulation of the stabilization parameter will be treated in a separate section.

As Hughes (1987) argues, including the term 'upwinding' in the name is misleading, since it is generally related to the classical form of finite difference upwinding which is well-known to the field of fluid mechanics. There, these methods feature increased stability at the cost of accuracy. This is not the case with SUPG, which rather combines high accuracy with solid stabilization characteristics, especially if higher order polynomials are considered.

In regions of steep gradients SUPG may still produce overshoots of the solution. To avoid overshoots and to assure smooth approximations of the solution, Hughes et al. (1986) have developed an additional discontinuity capturing term. The term is non-linear in nature and is thus impracticable to incorporate into a framework of fully linear equations like the LNSEs. The main reason for this is related to an increase in computational resources necessary to solve the non-linear terms using non-linear solution algorithms. Circumventing the problem by linearization of the non-linear discontinuity capturing term proved to yield overly diffusive results.

The added SUPG stabilization term is not symmetric which introduces some difficulties in establishing stability. This non-symmetric stability term can be avoided by applying the Galerkin/least-squares ansatz, introduced in the next section.

3.3.2 Galerkin/Least-Squares Technique

The Galerkin/least-square approach (GLS) originates from the purely mathematical idea to minimize the least-square error of the residuum of any given governing equation. This is directly illustrated by minimizing

$$\int_{\Omega} \mathcal{R}_{\hat{\phi}}^2 \, d\Omega = \int_{\Omega} (\mathcal{L}(\hat{\phi}) - s_{\phi})^2 \, d\Omega \rightarrow 2 \int_{\Omega} (\mathcal{L}(\hat{\phi}) - s_{\phi}) \mathcal{L}(\delta\hat{\phi}) \, d\Omega = 0, \qquad (3.32)$$

where $\mathcal{L}$ is the differential operator of the governing equation. Interpreting variations of $\delta\hat{\phi}$ as test function and restricting the influence of the whole term using a stabilization parameter τ_{stab}, yields the final form of the GLS stabilization term. Thus, the complete differential operator is used for the Petrov-Galerkin formulation of Eq. (3.26), yielding a symmetric stabilization term (Hughes et al., 1989) of the form

$$\mathcal{P}_{\text{GLS}}(w_{\phi}^h) = \nabla \cdot \left(\bar{\mathbf{u}} w_{\phi}^h\right) + \sigma w_{\phi}^h - \nu \Delta w_{\phi}^h, \qquad (3.33)$$

wherein the first term can be identified as the convective operator already used in SUPG. In fact, the major difference to SUPG is the inclusion of a diffusive and a reactive term in the stabilization operator. Both methods become identical for convection-diffusion (no reaction) problems using linear elements. For the linearized continuity equation Eq. (3.1) both methods are indeed equal, independently of the polynomial order p chosen.

In case a positive reactive term is introduced to the governing equations, GLS weights the term $1+\tau_{\text{stab}}\sigma$ more than the SUPG technique, which may amplify arising instabilities. To resolve this problem Douglas and Wang (1989) and Franca et al. (1992) propose the use of the adjoint operator

$$\mathcal{P}_{\text{GLS-}}(w_\phi^h) = -\mathcal{P}^*_{\text{GLS}}(w_\phi^h) = \nabla\cdot\left(\bar{\mathbf{u}}w_\phi^h\right) - \sigma w_\phi^h + \nu\Delta w_\phi^h, \tag{3.34}$$

in this way the reactive term is now weighted $1-\tau_{\text{stab}}\sigma$ and thus less than for the SUPG approach. This approach is generally referred to as GLS- technique and represents an approximative version of the multiscale or sub-grid scale approach developed later by Hughes (1995). Latter approach is based on a mathematical analysis of the physical problem for which an analytical solution for the stabilization parameter τ_{stab} is obtained. Then, the stability coefficient models the effect of the unresolved scales (subgrid scales) onto the finite element solution (resolved scales). For this reason, SUPG and GLS technique can be considered as approximations of the multiscale approach. The order of accuracy of GLS is $\mathcal{O}(h^{2p+1})$ for the primitive variables and is derived mathematically in Hughes et al. (1989).

The mathematical application of GLS or GLS- to the LNSEs is straightforward, and leads to stabilization terms of

$$B^C_{\text{GLS}\pm}\left(w_\rho^h,\hat{\rho}^h\right)_{\Omega|\partial\Omega} = \left(\mathcal{R}_C(\hat{\rho}^h),\tau_C\left[\nabla\cdot\left(\bar{\mathbf{u}}w_\rho^h+\bar{\rho}\mathbf{w}_\mathbf{u}^h\right)\right]\right)_{\Omega|\partial\Omega}, \tag{3.35}$$

$$\begin{aligned} B^M_{\text{GLS}\pm}\left(\mathbf{w}_\mathbf{u}^h,\hat{\mathbf{u}}^h\right)_{\Omega|\partial\Omega} = \big(\mathcal{R}_M(\hat{\mathbf{u}}^h),\boldsymbol{\tau}_M\big[&\nabla\cdot\left(\bar{\rho}\bar{\mathbf{u}}\mathbf{w}_\mathbf{u}^h\right)+\nabla w_p^h \\ &\pm\left(\bar{\rho}\mathbf{w}_\mathbf{u}^h+\bar{\mathbf{u}}w_\rho^h\right)\cdot\nabla\bar{\mathbf{u}}\mp\nabla\cdot\boldsymbol{\tau}(\mathbf{w}_\mathbf{u}^h)\big]\big)_{\Omega|\partial\Omega}, \end{aligned} \tag{3.36}$$

$$\begin{aligned} B^E_{\text{GLS}\pm}\left(w_p^h,\hat{p}^h\right)_{\Omega|\partial\Omega} = \big(\mathcal{R}_E(\hat{p}^h),\tau_E\big[&\nabla\cdot\left(\bar{\mathbf{u}}w_p^h+\kappa\bar{p}\mathbf{w}_\mathbf{u}^h\right) \\ &\pm(\kappa-1)\left[w_p^h\nabla\cdot\bar{\mathbf{u}}-\mathbf{w}_\mathbf{u}^h\cdot\nabla\bar{p}\right]\big]\big)_{\Omega|\partial\Omega}, \end{aligned} \tag{3.37}$$

where the sign $\pm$ or $\mp$ depends on which stabilization scheme is employed, i.e. the standard GLS or GLS- respectively. Note that generally the term

related to the molecular stresses in the linearized energy equation should also appear in the formulation. Since, it was omitted for simplification reasons it is not included here for consistency.

3.3.3 Stabilization Parameter

To close the above stabilization schemes, the stabilization parameter τ_{stab} needs to be specified. Its choice is highly important to the success of any stabilized finite element method and mainly determines the order of accuracy reached by the computation. Original stability parameters for the SUPG technique proposed by Brooks and Hughes (1982) were derived by comparing finite difference stencils and were limited to linear interpolation functions. Later, stability parameters used also accommodated higher order interpolation functions. They can be generally understood a posteriori based on a priori error analysis, see e.g. Franca et al. (1992).

Various formulations exist in literature and have been tested on scalar convection-diffusion-reaction equations. Three of these will be introduced in their chronological order of their appearance. Rao and Morris (2006) applied a definition of the τ_{stab} parameter introduced by Le Beau et al. (1993) to stabilize their acoustic LEEs equations

$$\boldsymbol{\tau}_{\text{stab}} = \max\left(\frac{\alpha h_i}{\lambda_i}\right)\mathbf{I}, \tag{3.38}$$

where α is a certain stabilization constant and λ_i the spectral radius of a constant coefficient convective matrix in a direction i (compare with Appendix B.3 for more details). The characteristic size of the element in i-th direction is denoted by h_i. According to Hughes et al. (1986), lower bounds for the parameter α can be determined empirically (e.g. $\alpha > 0.1$ or $\alpha > 0.01$ for quadrilateral elements with different numbers and location of nodes) depending on the element type (e.g. triangular or quadrilateral in 2d space) and polynomial order chosen. These lower bounds were derived on a very similar formulation to Eq. (3.38) of the stabilization parameter. Later, Codina (2000) proposed a second order accurate formula for τ_{stab} for a general convection-diffusion-reaction equation according to

$$\tau_{\text{stab}} = \left(\frac{2u}{h} + \frac{4\nu}{h^2} + \sigma\right)^{-1}. \tag{3.39}$$

More recently, a fourth order accurate formula was proposed by the group of Shakib,

$$\tau_{\text{stab}} = \left(\left(\frac{2u}{h} \right)^2 + 9 \left(\frac{4\nu}{h^2} \right)^2 + \sigma^2 \right)^{-1/2}, \tag{3.40}$$

which yielded better convergence than Eq. (3.39). However, all aforementioned parameters were formulated for general convection-diffusion(-reaction) equations. Especially for acoustic problems, a rigorous definition of a stabilization term is still missing. For the present implementation, all stability constants are chosen equally $\tau_C = \boldsymbol{\tau}_M = \tau_E$ for linearized continuity, momentum and energy equation.

3.3.4 Problem Formulations

The discrete LNSEs of Eqs. (3.19)-(3.21) with an additional stabilization technique like SUPG, Eqs. (3.29)-(3.31), or GLS, Eqs. (3.35)-(3.37), finally have to be formulated into a matrix notation which is provided to a numerical solver in the next section. This can be done in two different ways defining two very different problem sets. The first problem is a matrix inversion problem and is discussed next. The second is an eigenvalue problem and is discussed in Section 3.3.6.

3.3.5 Matrix Inversion Problem

For the matrix inversion problem $\omega \in \mathbb{R}$ is explicitly prescribed and thus the coefficients of the frequency dependent term of Eqs. (3.10)-(3.12) are known. This is exemplarily shown for the general convection-diffusion-reaction equation in Eq. (3.22),

$$\mathbf{M}(\omega)\boldsymbol{\phi} + [\mathbf{C} + \mathbf{D} + \boldsymbol{\sigma}]\,\boldsymbol{\phi} = \mathbf{N} - \mathbf{E} \tag{3.41}$$

Therein, $\boldsymbol{\phi}$ is the vector incorporating the unknown coefficients ϕ_A. In Eq. (3.41), $\mathbf{M}$, $\mathbf{C}$, $\mathbf{D}$ and $\boldsymbol{\sigma}$ denote the frequency dependent matrix, the convective, diffusive and reactive matrix, respectively. $\mathbf{N}$ and $\mathbf{E}$ indicate the right hand side vectors due to the Neumann boundary condition and due to the essential Dirichlet boundary conditions, respectively. Such conditions

were already described for the LNSEs in Section 2.7. The matrix system of the LNSEs is slightly more complex due to the inherent coupling of the equations. Nevertheless, it can be derived in a similar manner. The pulsation ω is chosen to be real in the present study, however, similarly imaginary components can be ascribed as well.

The different matrices of Eq. (3.41) of the complete system may then be summoned into one global matrix $\mathbf{A}(\omega)$

$$\mathbf{A}(\omega)\mathbf{x} = \mathbf{b}. \tag{3.42}$$

where $\mathbf{x}$ is now chosen to represent the vector of unknowns. For the LNSEs, the $\mathbf{x}$ incorporates the unknown coefficients $\hat{\rho}_A$, $\hat{\mathbf{u}}_A$ and $\hat{p}_A$ of the discretization introduced in Eq. (3.17).

Assembling the LNSEs in the way of Eq. (3.42) enables one to determine the scattering or transfer matrix coefficients of Eq. (2.26) and (2.29), respectively. This can be performed for confined configurations, such as area expansions, orifices or tubular combustion chambers with two or more inflow and outflow boundaries.

Any given configuration needs to be acoustically excited once from upstream and once from downstream direction following a two-source strategy (Munjal and Doige, 1990a; Åbom, 1991). Eq. (3.42) then needs to be solved twice for every discrete pulsation ω. The two different excitation states are labeled in the following by the subscripts I and II. Both acoustic states are designed by incorporating appropriate volumetric source terms in the LNSEs formulation, Eqs.(3.1)-(3.3), to retrieve the non-trivial solutions of the problem. Such a procedure is valid for frequencies below the first cut-on frequency of higher order modes, where solely longitudinal waves propagate along the system's feeding ducts. Then, an analytical solution exists for the longitudinal waves, which is of the form

$$\hat{p}_{u/d} = \hat{p}^{+}_{u/d} e^{-ik^{+}x} + \hat{p}^{-}_{u/d} e^{ik^{-}x}, \tag{3.43}$$

$$\hat{u}_{u/d} = \frac{1}{\bar{\rho}\bar{c}} \left(\hat{p}^{+}_{u/d} e^{-ik^{+}x} - \hat{p}^{-}_{u/d} e^{ik^{-}x} \right), \tag{3.44}$$

where $k^{\pm} = \omega/(\bar{c} \pm \bar{u})$ represent the complex wavenumber of the wave traveling in upstream or downstream direction. The complex pressure and velocity amplitudes $\hat{p}_{u/d}$ and $\hat{u}_{u/d}$, upstream and downstream of the configuration under investigations, are solutions of the LNSEs. As these are

field variables, they are averaged over cross-section planes. A least-squares Levenberg-Marquardt algorithm is then used to retrieve the complex pressure amplitudes $\hat{p}_u^+$, $\hat{p}_u^-$, $\hat{p}_d^+$ and $\hat{p}_d^-$ for both acoustic states (Levenberg, 1944; Marquardt, 1963). With all pressure amplitudes known, four equations may be formulated for the four unknown coefficients

$$\begin{pmatrix} T^+(\omega) & R^-(\omega) \\ R^+(\omega) & T^-(\omega) \end{pmatrix} = \begin{pmatrix} \hat{p}_{d,I}^+ & \hat{p}_{d,II}^+ \\ \hat{p}_{u,I}^+ & \hat{p}_{u,II}^+ \end{pmatrix} \begin{pmatrix} \hat{p}_{u,I}^- & \hat{p}_{u,II}^- \\ \hat{p}_{d,I}^- & \hat{p}_{d,II}^- \end{pmatrix}^{-1}. \tag{3.45}$$

The results are generally insensitive to the specific location of the acoustic source. Only prerequisite is that it is not located to close to the region of interest and does not overlap with regions where the complex pressure and velocity amplitudes $\hat{p}_{u/d}$ and $\hat{u}_{u/d}$ are extracted.

3.3.6 Eigenvalue Problem

The matrices may also be assembled in a different way, if the frequency dependent terms are first shifted to the RHS, which results in

$$\nabla \cdot \left(\bar{\mathbf{u}}\hat{\phi}\right) + \sigma\hat{\phi} - \nu\Delta\hat{\phi} - s_\phi = i\omega\hat{\phi}, \tag{3.46}$$

for the general convection-diffusion-reaction equation. Such equations may then be again discretized and assembled to a global matrix representation. The resulting problem is of eigenvalue type and can be formulated as: find pulsations $\omega \in \mathbb{C}$ and eigenvectors $\mathcal{V} \in \mathbb{C}$ which satisfy the fluid dynamic as well as boundary conditions, such that

$$\mathbf{A}\mathcal{V} = i\omega\mathcal{V}. \tag{3.47}$$

For the LNSEs, the eigenvectors $\mathcal{V}$ contain the unknown coefficients $\hat{\rho}_A$, $\hat{\mathbf{u}}_A$ and $\hat{p}_A$. Note that matrix $\mathbf{A}$ is not a function of the pulsation ω. For thermoacoustic problems, however, the situation is changed as soon as the unsteady effect of the flame is incorporated into the source term s_p. Then, matrix $\mathbf{A}$ does indeed depend non-linearly on the pulsation ω, see Section 2.6, and the problem may not be solved directly. An intuitive solution to treat the non-linear source term is introduced by Nicoud et al. (2007) in case of the Helmholtz equation, who propose the use of an iterative algorithm. The method works as such, if k denotes the current iterative step, the global

matrix $\mathbf{A}$ is simply evaluated at the last iteration step with a known ω_{k-1}. Following these authors, the iterative algorithm works as follows:

- Determine first eigenfrequencies $\omega_0^1, \omega_0^2, \ldots$ without acoustic-flame coupling by solving Eq. (3.47) with $\hat{\dot{q}}_V = 0$.
- Select the i-th frequency, ω_0^i.
- Set $\omega_k = \omega_0^i$ with $k = 1$ and $\hat{\dot{q}}_V \neq 0$.
- Solve $\mathbf{A}(\omega_{k-1})\mathcal{V} = i\omega_k\mathcal{V}$.
- Assess the error $\epsilon = |\omega_k - \omega_{k-1}|/|\omega_0|$.
- Return to step four and perform a finite number of iterations on k until ϵ is small enough.
- Repeat the algorithm until all necessary frequencies are found by returning to step two.

Solving this equation system yields a set of complex eigenpairs $(\omega, \mathcal{V})$. The eigenfrequency at a pulsation ω contains two main parts

$$\omega = \omega_r + i\omega_i, \tag{3.48}$$

a real part ω_r which determines the frequency of pulsation and an imaginary part ω_i which determines the respective growth or decay rate $\exp(-\omega_i t)$ (cp. to Eq. (2.12)). If a pulsation grows or decays in time depends on the respective sign of ω_i. The eigenvector $\mathcal{V}$ belonging to a certain pulsation ω, describes the characteristic distribution of fluctuating quantities throughout the computational domain. Generally, the iterative solution algorithm is found to converge within a number of three to four iterations k for a single eigenfrequency of investigation.

4 Solution of Large Linear Systems

In the beginning of this chapter, the two main problem formulations resulting from the finite element discretization of the LNSEs in Chapter 3 are shortly summarized. The first is of eigenvalue type, where $\omega \in \mathbb{C}$ is complex and not known a priori. This means finding the complex eigenpairs of pulsations ω and eigenvectors $\mathcal{V}$ which satisfy the given constraints and fluid dynamic conditions inside the computational domain

$$\mathbf{A}\mathcal{V} = i\omega\mathcal{V}, \tag{4.1}$$

where the purely real operator matrix $\mathbf{A} \in \mathbb{R}^{n\times n}$ is of size n and $\mathcal{V} \in \mathbb{C}^n$ is a discrete eigenvector containing the unknown nodal values $(\hat{\rho}_A, \hat{\mathbf{u}}_A, \hat{p}_A)$ for each finite element.

The second problem set can be formulated if $\omega \in \mathbb{R}$ is explicitly prescribed. Then, the problem reduces to a simple inversion of the complex matrix $\mathbf{A} \in \mathbb{C}^{n\times n}$,

$$\mathbf{A}\mathbf{x} = \mathbf{b}, \tag{4.2}$$

which can be solved using either direct or iterative methods described in Sections 4.2-4.4. For both problem sets the matrix $\mathbf{A}$ is typically non-hermitian (non-symmetric for real matrices) and indefinite for classical convection transport equations as the LNSEs and LEEs are. This has a strong impact on the selection of an appropriate iterative solver. Some of the iterative routines are based on a projection of the original problem into a so-called Krylov subspace. The construction of such a subspace is the main operation of the eigenvalue problem, which is therefore discussed first.

As most problems in reality have three dimensional geometries and flow conditions, the use of iterative solvers becomes indispensable. Until now, no iterative routine has been proposed in the literature to solve the LNSEs in an efficient way. Therefore, this chapter designs three different iterative algorithms for this purpose. First, the basic theory of direct and iterative

schemes is introduced. The introduction is followed by an explanation of preconditioning techniques which are used to accelerate iterative algorithms. Finally, based on the theory, three different combinations of iterative algorithm and preconditioner technique are selected and their performance is compared on a generic combustor configuration.

4.1 Eigenvalue Solvers

Three algorithms exist for solving the eigenvalue problem of Eq. (4.1). For hermitian matrices the Lanczos algorithm (Lanczos, 1950) is generally used. However, typical fluid dynamic transport equations are generally non-hermitian and therefore subspace methods like the Arnoldi method (Arnoldi, 1951) or Jacobi-Davidson method (Sleijpen and Van der Vorst, 1996; Sleijpen et al., 1996) have to be used instead. In the specific case of the Helmholtz equation Eq. (2.25), it is shown that the Jacobi-Davidson method is globally more efficient than the Arnoldi algorithm (Sensiau et al., 2008), i.e. it requires a lower amount of iterations to converge. The differences are, however, insignificant and both methods share nearly similar solution capabilities. Therefore, the Arnoldi algorithm is chosen in the present thesis to solve the eigenvalue problem defined by the LNSEs and Helmholtz equation, respectively.

4.1.1 Arnoldi Algorithm

Discretization of three dimensional combustion chamber geometries using a finite element procedure of Section 3 may result in large numbers of degrees of freedom and equivalently large system matrices $\mathbf{A}$. Consequently, these matrices have also large numbers of eigenvalues. However, in thermoacoustic applications we are mainly interested in a subset of the first few eigenfrequencies. At such low frequencies it is believed that the system is more susceptible to the coupling of acoustic waves with the heat release rate of the flame. Therefore, solving for the complete spectrum of eigenfrequencies is unnecessary and would involve high computational costs.

General idea behind the Arnoldi algorithm is to solve an eigenvalue problem of much smaller dimension m, which accurately approximates the first few eigenvalues of the original matrix $\mathbf{A} \in \mathbb{C}^{n \times n}$ where $m << n$. This smaller matrix is called a upper Hessenberg matrix $\mathbf{H} \in \mathbb{C}^{m \times m}$. It is constructed by performing a projection of the original system onto a so-called Krylov subspace. This subspace spans matrix-vector products of the first powers of a matrix $\mathbf{A}$ and a vector $\mathbf{r}_0 = \mathbf{b} - \mathbf{A}\mathbf{x}_0$ (Saad, 2010)

$$K_m = span\left\{\mathbf{r}_0, \mathbf{A}\mathbf{r}_0, \mathbf{A}^2\mathbf{r}_0, \ldots, \mathbf{A}^{m-1}\mathbf{r}_0\right\}. \tag{4.3}$$

The dimensions of the subspace is explicitly given by the value m. The Arnoldi algorithm then iteratively calculates the orthogonal vectors $\mathbf{q}_n$ which span the Krylov subspace as well as the individual matrix coefficients h_{ij} using a so-called modified Gram-Schmidt (MGS) procedure. The vectors are summarized in the matrix $\mathbf{Q}_{n,m+1} = (\mathbf{q}_1; \ldots; \mathbf{q}_{m+1})$ and the individual matrix coefficients h_{ij} in a non-square Hessenberg matrix $\mathbf{H}_{m+1,m}$ to obtain the following form

$$\mathbf{A}\mathbf{Q}_{n,m} = \mathbf{Q}_{n,m+1}\mathbf{H}_{m+1,m} \tag{4.4}$$

A square upper Hessenberg matrix $\mathbf{H}_{m,m}$ can now be obtained by removing the last line of $\mathbf{H}_{m+1,m}$. Then, the relation Eq. (4.4) may be reformulated in terms of a square Hessenberg matrix $\mathbf{H}_{m,m}$

$$\mathbf{A}\mathbf{Q}_{n,m} = \mathbf{Q}_{n,m}\mathbf{H}_{m,m} + h_{m+1,m}\mathbf{q}_{m+1}\mathbf{e}_m^T \tag{4.5}$$

with $\mathbf{e}_m^T$ being the unity vector. Herein, the last term on the right hand side describes the residual of this process. The eigenvalues and eigenvectors of the resulting square Hessenberg matrix may then be computed with the help of direct or iterative methods explained in following Sections 4.2-4.3. The reduced eigenvalue problem to be solved is of an equivalent form to Eq. (4.1)

$$\mathbf{H}_{m,m}\mathbf{y}_i^m = \lambda_i \mathbf{y}_i^m, \tag{4.6}$$

where λ_i are the eigenvalues of the square Hessenberg matrix $\mathbf{H}_{m,m}$ and $\mathbf{y}_i^m$ their corresponding eigenvectors. The time and memory consuming task of calculating the eigenpairs of the original matrix $\mathbf{A}$ of size $n \times n$ is circumvented by the computations of the eigenvalues of a much smaller matrix $\mathbf{H}_{m,m}$ with m dimensions. Whether an eigenpair of the Hessenberg

matrix $(\lambda_i, \mathbf{y}_i^m)$ is a good approximation of the original matrix $\mathbf{A}$ $(\omega_i, \mathcal{V}_i)$ can be assessed by the following relation

$$||(\mathbf{A} - \lambda_i \mathbf{I})\, \mathbf{u}_i^m||_2 = h_{m+1,m} \left|\mathbf{e}_m^T \mathbf{y}_i^m\right|. \tag{4.7}$$

where $\mathbf{u}_i^m = \mathbf{Q}_{n,m}\mathbf{y}_i^m$ is an approximation of the actual eigenvector $\mathcal{V}_i$ of $\mathbf{A}$ and $\mathbf{I}$ the unitary matrix. If the norm of right hand side of Eq. (4.7) is smaller than a certain threshold value, the routine is stopped. It is important to note that the original system matrix $\mathbf{A}$ appears only in the form of matrix-vector products in the Arnoldi iteration.

There are two main problems associated with the Arnoldi method: The first is the choice of subspace dimension m. Sensiau et al. (2008) show in case of the Helmholtz equation Eq. (2.25) that the Arnoldi algorithm is insensitive to the choice of m after having reached a certain magnitude of about 50. The second problem is related to a fairly large Krylov subspace. In this case the MGS may produces Arnoldi vectors that are not orthogonal to machine precision, leading to spurious eigenvalues (Åkervik, 2008). Explicit re-orthogonalization of the basis set in this case becomes preferable, like e.g. done with the DKGS method introduced by Daniel et al. (1976). However, the re-orthogonalization is not implemented into the current COMSOL version.

4.1.2 Shift and Invert Method

The Arnoldi algorithm can determine the very large eigenfrequencies or those very close to zero. However, sometimes intermediate or slightly higher eigenvalues are of interest. This can be achieved by applying the Arnoldi algorithm on a so-called shifted and inverted form of the original problem Eq. (4.1). Therein, the problem is reformulated as

$$[\mathbf{A} - i\sigma\mathbf{I}]^{-1}\, \mathcal{V} = i(\omega - \sigma)^{-1}\mathcal{V} = i\mu\mathcal{V} \tag{4.8}$$

wherein σ is the target value in the region of interest, $\mathbf{I}$ denotes the unity matrix and μ is the eigenvalue of the shifted problem. Instead of system matrix $\mathbf{A}$ the eigenvalues of $[\mathbf{A} - i\sigma\mathbf{I}]^{-1}$ are now sought for. A major difference to the standard Arnoldi algorithm is that matrix vector products

of $[\mathbf{A} - i\sigma\mathbf{I}]^{-1}\,\mathbf{q}_n$ instead of $\mathbf{A}\mathbf{q}_n$ are calculated which requires the use of a direct or iterative procedure to invert the matrix $[\mathbf{A} - i\sigma\mathbf{I}]$. The way this is done in the current framework is explained in the following sections.

This thesis employes a parallel implementation of the shift and invert method available in the ARPACK library (Lehoucq et al., 1998). Also consult the same publication for a more thorough explanation of the introduced methods.

4.2 Direct Solvers

In this section it is shown how to solve the linear matrix system of LNSEs of Eq. (4.2), viz. $\mathbf{A}\mathbf{x} = \mathbf{b}$, or the matrix inversion in Eq. (4.8) as part of a shift and invert eigenvalue routine. The class of direct solvers are characterized by providing the exact solution of a linear system of equations after a finite number of iteration steps (when neglecting round-off errors). Their main disadvantages are related to the fact that on the one hand the system matrix $\mathbf{A}$ must be available and can not be implicitly calculated, while on the other hand, the complete matrix needs to be inverted. Such methods suffer from excessive fill-in and unacceptable computer work, growing with the problem size $\mathcal{O}(n^3)$ (Trefethen and Bau, 1997).

Direct methods and latest developments are described in a review article of George and Liu (1981). In the present thesis the two main direct solution methods of LU and QR factorization will be introduced. It has to be noted that variants of the factorization methods have been developed which better cope with large system matrices and account for their band structure. These are, e.g. the MUMPS (Amestoy et al., 2001) or PARADISO solvers (Schenk and Gärtner, 2004) provided in the software package COMSOL Multiphysics. To further reduce internal memory usage, all solvers include out-of-core capabilities, i.e. storing parts of the matrix on the computer hard disc.

In the current framework, only small two dimensional problems are generally solved using direct methodologies, providing a good trade-off between accuracy, robustness and computational time in these cases.

4.2.1 LU Factorization

The LU factorization method decomposes the system matrix $\mathbf{A}$ into the product of a lower and upper triangular matrix, $\mathbf{L}$ and $\mathbf{U}$ respectively. The individual matrix elements l_{ij} and u_{ij} of matrices $\mathbf{L}$ and $\mathbf{U}$ are computed by means of a conventional elimination algorithm. One finally obtains

$$\mathbf{A} = \mathbf{LU}. \tag{4.9}$$

When the factorization is completed, the solution vector $\mathbf{x}_n$ is computed in two sequential steps:

$$\begin{aligned} \mathbf{LU}\mathbf{x}_n &= \mathbf{b}, && (4.10)\\ \mathbf{L}\mathbf{y}_n &= \mathbf{b}, \quad \text{for unknown } \mathbf{y}_n, && (4.11)\\ \mathbf{U}\mathbf{x}_n &= \mathbf{y}_n, \quad \text{for unknown } \mathbf{x}_n. && (4.12) \end{aligned}$$

Eq. (4.11) is solved for $\mathbf{y}_n$ using forward substitution, while Eq. (4.12) is solved for the unknown solution vector $\mathbf{x}_n$ using backward substitution.
$\mathbf{A}$ is typically a band structured matrix. In this case $\mathbf{L}$ and $\mathbf{U}$ are also band structured matrices with the same bandwidth of matrix $\mathbf{A}$. However, as $\mathbf{A}$ is sparse along these bands, this is not the case for $\mathbf{L}$ and $\mathbf{U}$ which bands are generally completely filled. This requires an increased memory space and represents the main drawback of this direct methodology.

4.2.2 QR Factorization

The main advantage of the QR compared to the LU factorization method is that the Euclidian norm is conserved for the unitary transformation (Meister, 2011) and the equation set can easily be solved since $\mathbf{Q}^* = \mathbf{Q}^{-1}$. The subscript $.^*$ denotes the hermitian transposed. Let $\mathbf{Q} \in \mathbb{C}^{n\times n}$ be an orthonormal unitary matrix while $\mathbf{R} \in \mathbb{C}^{n\times n}$ is the upper right triangular matrix, then it follows

$$\mathbf{A} = \mathbf{QR}. \tag{4.13}$$

The decomposition of $\mathbf{A}$ can be performed using Gram-Schmidt method or using the algorithms of Givens and Housholder. After decomposition, the solution vector is calculated as follows

$$\mathbf{QRx}_n = \mathbf{b}, \tag{4.14}$$
$$\mathbf{Qy}_n = \mathbf{b}, \quad \text{for unknown } \mathbf{y}_n, \tag{4.15}$$
$$\mathbf{Rx}_n = \mathbf{y}_n, \quad \text{for unknown } \mathbf{x}_n. \tag{4.16}$$

The process of computing the factorizations $\mathbf{LU}$ or $\mathbf{QR}$ is the most expensive part in terms of computational costs. For the LU factorization Golub and Van Loan (1996) and Duff et al. (1986) give estimates of computational costs (or number of flops) $\mathcal{O}(n^{3/2})$ for two dimensional problems and $\mathcal{O}(n^{5/2})$ for three dimensional problems. The costs may increase however significantly when not taking into account the sparse character of the matrix $\mathcal{O}(n^4)$ for two dimensional problems and $\mathcal{O}(n^7)$ for three dimensional problems (Schäfer, 1999). The high demand in memory as well as computational resources limits the applicability of direct solution methods to relatively small cases.

4.3 Iterative Solvers

When large sparse matrices $\mathbf{A}$ are involved, direct solvers face limitations in memory and processing time. As direct solvers can generally not make advantage of the sparse structure of system matrices, iterative schemes become more interesting. For three dimensional problems such iterative schemes become indispensable. Unlike direct solvers, the class of iterative solvers may only provide the approximate solution of a discretized problem. Another drawback of iterative solvers is their lack in robustness, when compared to direct solvers.

Most simplistic representatives of iterative schemes are the Jacobi, Gauß-Seidel and the successive over relaxation techniques. These algorithms are, however, mostly inefficient (Schäfer, 1999). Therefore, a different class of Krylov subspace solvers has been developed. The most famous representative is the Conjugate-Gradient (CG) method developed by Hestenes and Stiefel (1952). It typically involves only one matrix vector multiplication per iteration step and is therefore highly efficient. The algorithm, however,

is only applicable to hermitian and positive definite matrix systems and breaks down in the presence of non-hermitian systems like the ones considered in the present analysis. Later, the method was then extended to cope with non-hermitian and indefinite systems. Bi-CG (Fletcher, 1975) and BiCGstab (van der Vorst, 1992) have been developed for this purpose. However, both iterative solvers do not satisfy optimality condition in the sense that the residual is not minimized and convergence is irregular (Bi-CG) or may break down before an exact solution is calculated (Meister, 2011). This low level in robustness is also observed in the course of the present study when solving the LNSEs, where the solution algorithm would converge for some frequencies but not for others. Compared to Bi-CG and BiCGstab, the GMRES algorithm developed by Saad and Schultz (1986) satisfies optimality condition and provides high robustness. This comes at the cost of an increased usage of memory space. In terms of work per iteration step all introduced Krylov subspace methods perform relatively similar (van der Vorst, 2009). Another class of promising algorithms is represented through the development of multi-resolution methods (Hackbusch, 1985; Wesseling, 1992). These may be directly applied to perform matrix inversion or may serve as preconditioners for solution algorithms like GMRES (Wienands et al., 2000). Latter potential is exploited in this thesis.

For the challenging task of computing solutions of the LNSEs or LEEs, a suitable solver must be capable to cope with strongly changing flow fields, different mesh resolutions as well as different frequencies of investigations. Therefore, robustness of the solution algorithm plays the most important role for the explicit choice of iterative scheme for the present area of application. First, some available solvers are discussed in more detail. Then, suitable combinations of solvers and preconditioners are selected from the literature to solve the LNSEs. Their individual performance is then compared for a generic combustor model.

4.3.1 Jacobi, Gauß-Seidel and SOR

Generally Jacobi, Gauß-Seidel and successive over relaxation (SOR) methods are the most classical iterative solvers. They belong to the group of so-called splitting methods. The linear system is expanded by the addition

of $\mathbf{Bx} - \mathbf{Bx}$ to the problem of Eq. (4.2) for matrix inversion problems and of Eq. (4.8) for eigenvalue problems, respectively, yielding

$$\mathbf{Bx} - \mathbf{Bx} + \mathbf{Ax} = \mathbf{b}. \tag{4.17}$$

which directly leads to the general iteration rule for step $k+1$

$$\mathbf{Bx}^{k+1} - \mathbf{Bx}^{k} + \mathbf{Ax}^{k} = \mathbf{b}, \tag{4.18}$$

$$\mathbf{x}^{k+1} = \mathbf{B}^{-1}(\mathbf{B} - \mathbf{A})\mathbf{x}^{k} + \mathbf{B}^{-1}\mathbf{b}. \tag{4.19}$$

The convergence rate of this algorithm is now governed by the characteristics of matrix $\mathbf{M} = \mathbf{B}^{-1}(\mathbf{B} - \mathbf{A})$ instead of $\mathbf{A}$. As matrix $\mathbf{A}$ is fixed a priori, the choice of the arbitrary matrix $\mathbf{B}$ can be exploited to positively influence the rate of convergence. An optimal choice of matrix $\mathbf{B}$ requires it to minimize $\mathbf{M}$. In the specific case of $\mathbf{B} = \mathbf{A}$, the solution would be achieved within a single iteration step $k = 1$, see Eq. (4.19). Secondly, matrix $\mathbf{B}$ must be easily invertible. This can be achieved by subscribing $\mathbf{B} = \mathbf{I}$. However, these two requirements can not be fulfilled conjointly. A pragmatic solution to such conflicting requirements is to subscribe only parts of $\mathbf{A}$ to matrix $\mathbf{B}$, viz.

$$\mathbf{A} = \mathbf{A}_L + \mathbf{A}_D + \mathbf{A}_U, \tag{4.20}$$

where $\mathbf{A}_L$ is a matrix containing the lower part below the diagonal, $\mathbf{A}_D$ contains only the diagonal and $\mathbf{A}_U$ includes the upper half of matrix $\mathbf{A}$. By the explicit choice of matrix $\mathbf{B}$, three splitting methods may be derived:

$$\mathbf{B} = \mathbf{A}_D, \qquad \text{Jacobi (JAC)} \tag{4.21}$$

$$\mathbf{B} = \mathbf{A}_D + \mathbf{A}_L, \qquad \text{Gauß-Seidel (GS)} \tag{4.22}$$

$$\mathbf{B} = \frac{\mathbf{A}_D + \omega_{SOR}\mathbf{A}_L}{\omega_{SOR}}, \quad \text{SOR} \tag{4.23}$$

where the parameter ω_{SOR} introduces a certain relaxation to the Gauß-Seidel algorithm. For SOR to converge, the relaxation parameter must fulfill $\omega_{SOR} \in (0, 2)$. Its optimal value ω_{opt} for general convection-diffusion problems can not be derived explicitly. On simple model problems it can be shown that the computational time may be reduced significantly using the SOR compared to the Gauß-Seidel method when choosing the relaxation parameter ω_{SOR} between $[1, 2)$. It is important to note that this is not necessarily the case when the SOR technique is used as a preconditioner

for the here presented LNSEs system. If $\omega_{SOR} < 1$ is chosen, SOR is also refereed to successive under relaxation (SUR) method.

Computational costs of the Gauß-Seidel and Jacobi method are estimated in Schäfer (1999) and feature an order of $\mathcal{O}(n^4)$ for two dimensional and $\mathcal{O}(n^5)$ for three dimensional problems. The asymptotic convergence behavior may be decreased by an order of magnitude when considering the SOR method (Axelsson, 1996; Schäfer, 1999). This class of iterative solver shows high robustness. However, with increasing degrees of freedom the iteration costs still increase disproportionately according to Schäfer (1999).

4.3.2 Generalized Minimal Residuals (GMRES)

The Generalized Minimal Residual approach (GMRES) of Saad and Schultz (1986) is an extension of the conjugate gradients (CG) method of Hestenes and Stiefel (1952) to non-hermitian systems. Latter property is common to general convection-diffusion equations in fluid dynamic applications. The algorithm is based on an approximation of the linear problem $\mathbf{Ax} = \mathbf{b}$ at each iteration k by a vector $\mathbf{x}_k$ that minimizes the residual norm $\mathcal{R}$ of Eq. (4.2), i.e.

$$\min||\mathcal{R}|| = \min||\mathbf{Ax}_k - \mathbf{b}||. \tag{4.24}$$

At every k-th iteration, the vector $\mathbf{x}_k$ may be expressed through $\mathbf{x}_k = \mathbf{Q}_k\mathbf{y}$. GMRES uses the Arnoldi method to generate a basis of orthogonal vectors of $\mathbf{Q}_k$. Substitution into relation Eq. (4.24) yields

$$\min||\mathcal{R}|| = \min||\mathbf{AQ}_k\mathbf{y} - \mathbf{b}||. \tag{4.25}$$

Next the relation of Eq. (4.4) is applied to obtain

$$\min||\mathcal{R}|| = \min||\mathbf{Q}_{k+1}\mathbf{H}_k\mathbf{y} - \mathbf{b}||. \tag{4.26}$$

Multiplication with $\mathbf{Q}^*_{k+1}$ on the right side and usage of the knowledge that $\mathbf{Q}^*_{k+1}\mathbf{b} = ||\mathbf{b}||\mathbf{e}_1$ with $\mathbf{e}_1 = (1, 0, 0, ...)$, yields the final problem formulation: find a vector $\mathbf{y}$ that minimizes

$$\min||\mathcal{R}|| = \min||\mathbf{H}_k\mathbf{y} - ||\mathbf{b}||\mathbf{e}_1||. \tag{4.27}$$

The solution vector is then explicitly calculated through $\mathbf{x}_k = \mathbf{Q}_k\mathbf{y}$. The size of the problem to be solved at each k-th iteration, is given by the Hessenberg matrix $\mathbf{H}_k$ which is of size $(k+1, k)$.

GMRES's main disadvantage is the higher memory consumption connected with the storage of the Krylov subspace basis vectors. The number of stored vectors increases by one with every iteration and each vector is of problem size n. In order to avoid this excessive storage, the algorithm can be restarted after l iterations steps. This algorithm is referred to as restarted GMRES(l). Now, l can be conveniently be chosen according to the available memory resources. Various numerical experiments have shown that $l =$ 10-50 is a suitable choice. Main disadvantage of this restarting procedure is, however, that after having performed l iterations, GMRES(l) may face stagnation.

GMRES is an optimal solution algorithm and always features a monotonically decreasing convergence behavior, but its rate of convergence significantly depends on the choice of preconditioner, see e.g. Meister (1998). Estimating the computational costs therefore becomes difficult. For the very specific case of the CG methods, van der Vorst (2009) shows that CG scales with $\mathcal{O}(n^{3/2})$ for two dimensional problems and $\mathcal{O}(n^{4/3})$ for three dimensional problems. From his consideration it is directly obvious that Krylov subspace methods may rather be disadvantageous to solve two dimensional problems. However, for three dimensional problems their capabilities are unquestioned and with choice of a suitable preconditioner may even yield scales of up to $\mathcal{O}(n^{7/6})$, see e.g. Axelsson (1996); Gustafsson (1978).

4.3.3 Flexible Generalized Minimal Residuals (FGMRES)

The Flexible Generalized Minimal Residual (FGMRES) is a modification of the GMRES algorithm to handle different types of preconditioners more flexibly (Saad, 1993). Instead of Eq. (4.2) the right preconditioned system reads

$$\mathbf{A}\mathbf{P}_R^{-1}\mathbf{y} = \mathbf{b}, \tag{4.28}$$

where $\mathbf{P}_R$ denotes a right preconditioning matrix and $\mathbf{x} = \mathbf{P}_R^{-1}\mathbf{b}$. Performing the operation $\mathbf{A}\mathbf{P}_R^{-1}$ is straightforward using the GMRES algorithm.

However, to retrieve the solution vector $\mathbf{x}$ the matrix vector operation $\mathbf{P}_R^{-1}\mathbf{y}$ has to be evaluated. This operation is saved using the FGMRES method at the expense of storing m intermediate vectors $\mathbf{P}_R^{-1}\mathbf{q}_k$ per m steps. Thus, the memory costs increase slightly using FGMRES, which is not favorable for most applications. However, in some situations, the preconditioning matrix is not known explicitly and may change in every iteration step (Saad, 2000). In the context of finite elements, the benefits of an FGMRES have been pointed out by Tezduyar et al. (1991).

4.3.4 Multiresolution Methods

Multiresolution methods (Brandt, 1973; Fedorenko, 1964) can also be used to solve linear equations systems, but are also frequently used to speed up the convergence rate of numerical solution algorithms, e.g. for the Navier-Stokes equations (Arnone et al., 1995; Brandt, 1981). Their main advantage is that their performance and memory storage scales linearly with the degrees of freedom $\mathcal{O}(n)$ (Wesseling, 1992). To achieve such convergence rates, however, requires understanding and careful design of all solver components. Statements on the convergence behavior of multiresolution methods are provided for example in Hackbusch (1985, 1993).

This class of method is based on the general idea that the numerical error is distributed smoothly among the grid points. A hierarchy of different mesh structures is generated and the problem is solved using direct solvers of Section 4.2 on the coarsest mesh. Due to the insufficient numerical resolution, the error produced by the direct solver has different wavenumber components which obscure the physical solution. As it is the general idea of the method, high wavenumber components of the error are thought to be unphysical and are filtered out by performing a number of smoothing operations. Multigrid methods provide a vast framework and only a brief introduction to the subject is presented here.

4.3.4.1 Geometric Two-Grid Method (GTG)

Consider a linear system of the discretization order l, where the element size h^l changes according to

$$\Omega^l = \left\{ jh_l | j = 1, ..., 2^{l+1} - 1 \right\}. \tag{4.29}$$

Then, the linear problem to solve on the l-th grid layer is written as

$$\mathbf{A}^l \mathbf{x}^l = \mathbf{b}^l. \tag{4.30}$$

The essential principle of the method is to approximate the smooth (long wavelength) part of the error on coarser grids. The non-smooth part (small wavelength) is reduced by a small number of iterations with a basic iterative method, e.g. using splitting methods, on the fine grid (Wesseling, 1992). After a certain amount of iterations of the two-grid algorithm, an approximation of the solution vector $\mathbf{x}^l$ is computed. In the first step of the next iteration, a number of $\nu_1 \geq 0$ pre-smoothing operations is performed for the model problem on the fine grid, Eq. (4.30) using the introduced splitting methods (Sec. 4.3.1) of the general form,

$$\mathbf{x}^l_{\nu_1+1} = \mathbf{M}(\omega)\mathbf{x}^l_{\nu_1} + \mathbf{N}(\omega)\mathbf{b} \qquad \text{for} \qquad \nu_1 = 0, 1, 2.... \tag{4.31}$$

In a next step, the defect $\mathbf{d}^l = \mathbf{A}^l\mathbf{x}^l - \mathbf{b}^l$ is computed for the fine mesh Ω^l and is projected onto the coarser mesh Ω^{l-1} performing a so-called restriction operation

$$\mathbf{d}^{l-1} = \mathbf{R}_l^{l-1}\mathbf{d}^l \text{ where } \quad \mathbf{R}_l^{l-1} : \mathbb{C}^{n_l} \to \mathbb{C}^{n_{l-1}}, \mathbf{R} \in \mathbb{R}^{n_{l-1}, n_l} \tag{4.32}$$

On the coarser grid the error $\mathbf{e}^{l-1}$ is computed solving the resulting equation system

$$\mathbf{A}^{l-1}\mathbf{e}^{l-1} = \mathbf{d}^{l-1}, \tag{4.33}$$

directly. For this task the algorithms introduced in Section 4.2 are used. Depending on the size of the coarse mesh this operation is computationally cheap to obtain. Interpolation, or so-called prolongation, on the finer mesh yields the unknown error $\mathbf{e}^l$ on the fine mesh Ω^l

$$\mathbf{e}^l = \mathbf{P}_{l-1}^l \mathbf{e}^{l-1} \text{ where } \quad \mathbf{P}_{l-1}^l : \mathbb{C}^{n_{l-1}} \to \mathbb{C}^{n_l}, \mathbf{P} \in \mathbb{R}^{n_l, n_{l-1}} \tag{4.34}$$

with which a new defect $\mathbf{d}^{l,new}$ and solution vector $\mathbf{x}^{l,new}$ can be computed from $\mathbf{A}^l\mathbf{e}^l = \mathbf{d}^{l,new}$. A number of $\nu_2 \geq 0$ post-smoothing iterations of similar type of Eq. (4.31) may be performed. For pre- and post-smoothing iterations the relaxation parameter ω inherits a different functionality compared to its usage in iterative schemes of Section 4.3.1. It is employed as a kind of calibration parameter for a 'quasi' low-pass filter, ideally canceling all high wavenumber components of the error.

4.3.4.2 Geometric Multi-Grid Methods (GMG)

Obviously, the two-grid can be recursively applied to some coarser grid with m number of different grid layers. In general this may lead to very efficient iterative routine since instead of Eq. (4.33), a much coarser problem

$$\mathbf{A}_{l-m}\mathbf{e}^{l-m} = \mathbf{d}^{l-m}, \tag{4.35}$$

is solved for $\mathbf{e}^{l-m}$ directly. This extends the GTG method to the Geometrical Multigrid Method (GMG). One iteration of the GMG method is called a cycle. The exact structure of the cycle depends on a parameter γ, which denotes the number of two-grid iterations at each intermediate stage. The case of $\gamma = 1$, the GMG performs a so-called V-cycle, while $\gamma = 2$ and $\gamma = 3$ are called a W-cycle and a F-cycle, respectively. Most common cycles found in the literature are the V- and W-cycle. The explicitly choice of cycle, however, does not have a significant influence on the convergence behavior as Schäfer (1999) notes. For indefinite systems, multigrid methods may become inefficient, as it is shown in the case of the Helmholtz equation by Hackbusch (1978). In some cases even a diverging behavior of the iterative solution algorithm could be observed. This is the reason why GMG methods are not applied directly as a solution algorithm to solve the present set of LNSEs. However, this class of solver has high capabilities for accelerating iterative routines.

4.4 Preconditioners

Depending on the physical problem (i.e. transport equations) solved, the numerical methodology (e.g. finite volume, finite element) and the individual discretization applied, each system matrix $\mathbf{A}$ has its own structure and

characteristics. To iterative routines this structure is highly important and determines whether an iterative routine convergence at all, or if so, its individual rate of convergence. Certain measures may be defined which provide an estimate of convergence rate. One is the condition number $\kappa(\mathbf{A})$ of a regular matrix $\mathbf{A} \in \mathbb{C}^{n \times n}$,

$$\kappa(A) = ||A||_a ||A^{-1}||_a, \tag{4.36}$$

where $||.||_a$ is defined as the a-th matrix norm. Low condition numbers implicate that a reducing residuum reduces the error norm equivalently. On the contrary, a high condition number indicates that the norm of the error may not necessarily be reduced with reducing residuum. In this case we generally refer to an ill-conditioned system matrix. An other important measure is the spectral radius of $\mathbf{A}$. It is defined as the maximum eigenvalue λ of $\mathbf{A}$, i.e.

$$\rho(\mathbf{A}) = \max\{|\lambda| \lambda \in \sigma(\mathbf{A})\} \tag{4.37}$$

where $\sigma(\mathbf{A})$ denotes the spectrum of $\mathbf{A}$. In the case of splitting methods it can be shown that as long as $\rho(\mathbf{A}) < 1$, convergence is ensured, see e.g. Meister (2011); Schäfer (1999), and the smaller the value $\rho(\mathbf{A})$, the higher are the convergence rates reached.

In case a system matrix is $\mathbf{A}$ ill-conditioned, i.e. high $\kappa(\mathbf{A})$ and $\rho(\mathbf{A}) \gg 1$, a precondition matrix $\mathbf{P}_L$ may be multiplied to both sides of the system of Eq. (4.2)

$$\mathbf{P}_L \mathbf{A}\mathbf{x} = \mathbf{P}_L \mathbf{b}. \tag{4.38}$$

Now, the convergence rate does not depend on the properties of matrix $\mathbf{A}$ but on the properties of matrix $\mathbf{P}_L\mathbf{A}$ with $\kappa(\mathbf{P_L A}) < \kappa(\mathbf{A})$. The solution of the system, however, remains unchanged. In the above form, the preconditioning is called left preconditioning which is denoted by the index L. Similarly a right preconditioning exists, but as Saad (2000) notes both techniques yield similar acceleration. In the following, only left preconditioning is considered therefore.

Main aim of the preconditioning is to define a matrix $\mathbf{P}_L$ which is simple to calculate, uses low memory space, its inverse is easily formed and for which $\mathbf{P}_L\mathbf{A}$ approximates a unitary matrix. If $\mathbf{P}_L\mathbf{A} = \mathbf{I}$, only one iteration is needed to produce the solution. Multiple algorithms have been designed for this task and are mainly based on the classical solution algorithms:

- Jacobi, Gauß-Seidel or SOR
- Gradient algorithms (GMRES, FGMRES)
- Geometric Multi-Grid Methods

For this purpose the original solution algorithms of Section 4.3 are modified in order to construct a matrix $\mathbf{P}_L$. Details on how these algorithm are integrated in a global solution procedure of Section 4.3 is out of scope for the present analysis but can be extracted from the specific literature on this field, e.g. in Saad (2000); van der Vorst (2009); Wienands et al. (2000). It is important to note that the complete preconditioning matrix $\mathbf{P}_L$ is not necessarily known by an efficient preconditioner, only its implicit effect on $\mathbf{A}$ needs to be calculated.

Scaling of the primitive variables represents the simplest form of preconditioning. It is justified through the different orders in magnitude of the solution variables. For example when solving LNSEs, pressure and velocity variables may have a difference in magnitude of the order of four and it becomes advantageous to introduce new solution variables denoted by a superscript $.^*$

$$\hat{\rho}^* = \hat{\rho}/\rho_{ref}, \qquad \hat{\mathbf{u}}^* = \hat{\mathbf{u}}/c_{ref}, \qquad \hat{p}^* = \hat{p}/p_{ref}. \tag{4.39}$$

where ρ_{ref}, c_{ref} and p_{ref} are selected mean flow quantities from a given point in the domain. This methods disadvantage is that only a small increase in convergence rate is generally observed (Meister, 1998). Nevertheless, due to its simplicity the scaling is introduced to the present LNSEs solver.

4.5 Convergence Analysis

Main aim of this section is the design of an efficient solver to cope with the large system matrices using LNSEs. This procedure includes the choice of a suitable linear solver, in a so-called inner iteration, as well as an acceleration technique (preconditioner) in an outer iteration cycle. The proposed methods must be able to solve typical flow configurations of combustion chambers with Mach numbers up to $Ma \approx 0.3$, high temperature and velocity gradients.

For low-frequency applications using the finite element discretized LNSEs, molecular viscosity has a negligible effect on the acoustic propagation, see Appendix A. Matrix **A** therefore becomes generally ill-conditioned for the application of interest. Using LEEs the situation is significantly worsened, due to the unavailability of any diffusive term, yielding $Pe^e \to \infty$. Based on these considerations, a single tetrahedra element is analyzed first. It is discretized in finite space to identify parameters influencing the structure of the system matrix **A** and therewith its possible convergence behavior. In a next step, three different linear algorithms are proposed to solve the LNSEs in an efficient way. These are mainly based on the considerations above and preliminary tests. Open parameters will be discussed and optimized for a generic combustion chamber flow to yield fast and robust solution algorithms. In a last step, the performance of all three defined algorithms will be compared against each other and the most suitable one is identified.

4.5.1 Single Finite Element Analysis

At first, we assemble the system matrix $\mathbf{A}^e$ for a single tetrahedra finite element arbitrarily located in three dimensional space. Such an element is shown in Fig. 4.1 with its local distribution of nodes. By reducing the overall system matrix **A** to a single finite element $\mathbf{A^e}$, we may analyze the basic mathematical character of the set of acoustic governing equations and give approximations of the convergence behavior. LEEs are chosen

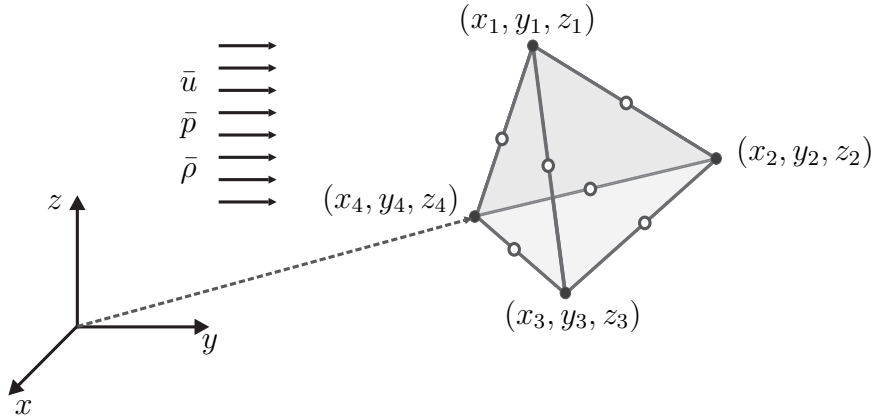

Figure 4.1: Single tetrahedra finite element located in three dimensional space. Distribution of nodes of linear element are shown by the filled symbols. For second order elements, the unfilled nodes are additionally considered.

here as representative of the most 'conservative' case and since they are more frequently used in the fields of aero- and thermoacoustics. Of course, similar conclusions may be drawn for the LNSEs as well. Dependencies of the convergence behavior on e.g. frequency and velocity gradients in the mean flow field are identified. Moreover, the effect of finite element stabilization methods on the system matrix structure is discussed.

The parameter used to characterize the convergence behavior is the condition number $\kappa(\mathbf{A})$ of Eq. (4.36). Consider a single tetrahedron finite element, Fig. 4.1, with its nodes located arbitrarily in three dimensional space. It is subjected to a certain mean flow which satisfies conservation of mass, momentum and energy. LEEs are discretized on this element using the Bubnov-Galerkin finite element approach with piecewise linear test functions to simplify the derivation. Scaling of the primitive variables, introduced in Eq. (4.39), is also performed. Transformation into parameter space using a Jacobian transform yields the final form of the element system matrix $\mathbf{A^e}$. Its characteristics is analyzed next.

In the first case, the frequency dependance is analyzed for a constant baseline flow having zero velocity gradients. Fig. 4.2 (left) shows a distinct characteristic upon frequency. The condition number drastically increases at low frequencies, indicating possible difficulties when considering low frequency oscillations. Above a frequency of around 500Hz the condition number reaches a constant level.

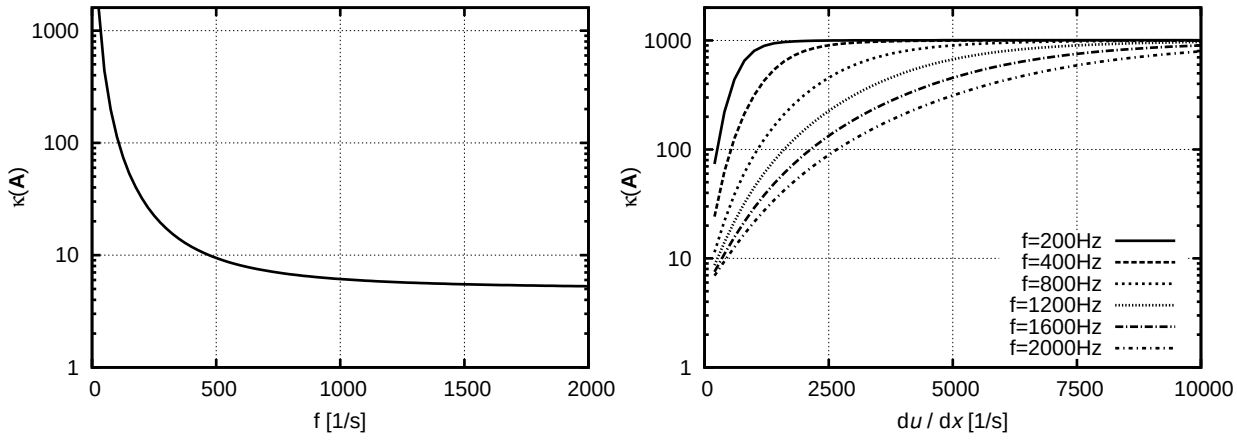

Figure 4.2: Influence of frequency f and velocity gradients du_x/dx on the condition number $\kappa(\mathbf{A^e})$ of a single finite element stiffness matrix.

In Fig. 4.2 (right) we observe a strong dependance of $\kappa(\mathbf{A}^e)$ upon the velocity gradient. Increasing the axial velocity gradient negatively influences the condition number. The influence is stronger for lower frequencies which are also displayed in the same figure. The high condition numbers reached highlights the need of SFEMs as well as suitable combination of a solution algorithm and preconditioning techniques. In the course of the study, contributions of the GLS term of Eqs. (3.35)-(3.37) were also introduced into the element matrix. A direct effect is that the symmetry of the element system matrix increases, due to the symmetric structure of the GLS terms.

Of course, the condition number also depends on the specific quality of the tetrahedra element and the incidence of the flow velocity. In the presented case a well shaped tetrahedra element has been selected. Decreasing the element quality, decreases the condition number accordingly. Another influencing factor is the domain size (depending on number of elements and the order of interpolation functions), which may also lead to a significant decrease in the condition number. Therefore, it has to be noted that the study of condition numbers of the system matrix of a single element is not able to provide estimates of condition numbers of real physical problems. The only aim of this section was to identify influencing factors and possible dependancies.

4.5.2 Solution Procedures

In practical problems, acoustic fields over a wide range of frequencies are of interest. For every discrete pulsation ω the matrix inversion problem of Eq. (4.2) has to be solved once. The frequency dependance of the condition number already indicates possible difficulties, especially in the low frequency limit. Furthermore, the analysis has confirmed the mathematical nature of the assembled system matrix of LEEs, being indefinite and non-hermitian. If one can not rely on the special properties of matrix $\mathbf{A}$, Krylov subspace methods are the most suitable choice (Saad, 2000).

In the following, the generic combustion chamber problem is introduced first. This problem will be used to 'calibrate' free parameters of the solution algorithms and to compare their performance against each other later on. Note that the same generic problem will be used in Section 6.1 to validate

the accuracy of the LNSEs solution procedure as a whole and a much more elaborate discussion is found therein. Here, the discussion is confined to create a basic understanding of the test case.

The generic premixed combustor is composed of a simple tube having constant cross section, see Fig. 4.3. A fully premixed reactive mixture enters from the inlet and is burnt in the flame region located in the middle of the duct leading to a temperature jump of $\bar{T}_h/\bar{T}_c = 4$. The burnt gases are accelerated and leave the combustor at its outlet. Acoustically this problem is considered by exciting the inlet by prescribing velocity fluctuations $\hat{u}_x = 1$. The outlet is considered to fully transmit acoustic waves which is achieved by prescription of an impedance boundary condition, Eq. (2.38).

Temperatures are assumed to be constant in the upstream and downstream duct, while the temperature level is raised over the flame region by prescribing a hyperbolic tangent profile. All other mean flow quantities can then be calculated as a function of inlet Mach number, density and pressure and satisfy continuity of mass, momentum and energy. The main advantage of

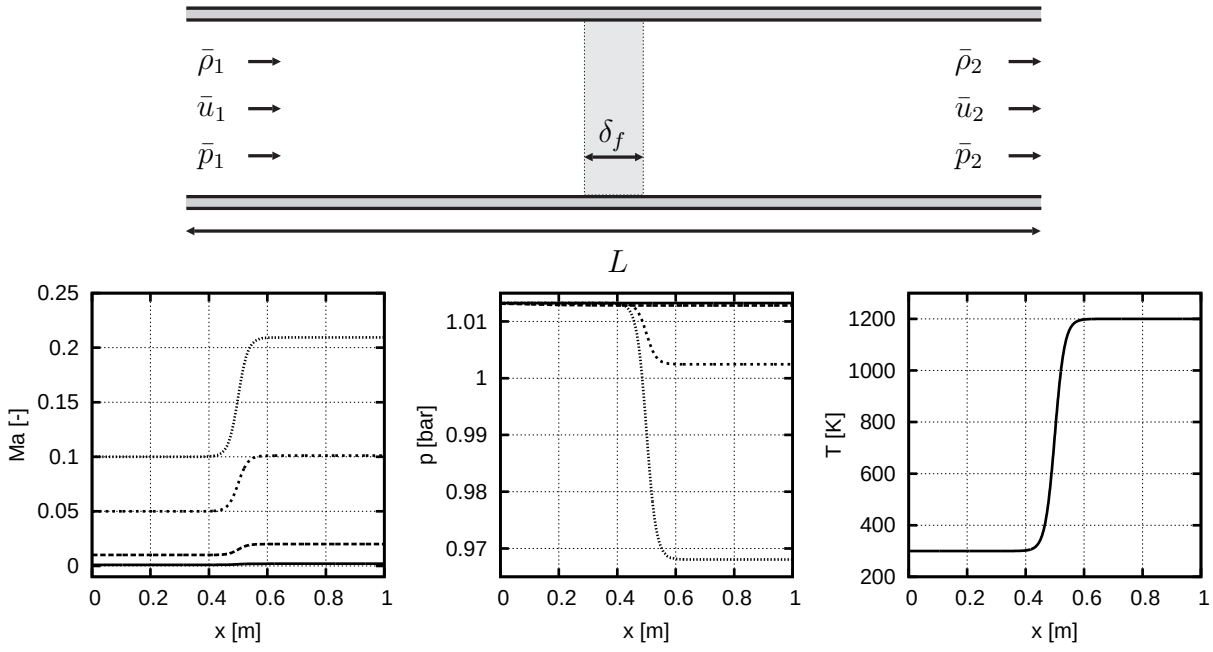

Figure 4.3: Quasi one dimensional model combustor of length L, shaded area represents flame region separating fresh to burnt gas side. Figures below show the axial mean Mach number distribution as well as associated pressure and temperature distribution for the inlet Mach numbers of Ma =0,0.01,0.05 and 0.1.

this test case is that many different parameters may be studied, e.g. inlet Mach number Ma_{in} or frequency f. Semi-analytical solutions can be derived from a one dimensional consideration of the LEEs to which the numerically obtained solutions are compared.

For an iterative scheme to converge, a linear solver needs to be coupled with an appropriate preconditioner. This thesis proposes three different algorithms to solve LNSEs or LEEs in frequency space:

- **FGMRES-GMRES(SOR)**: A similar form of this algorithm has already been used to solve the elliptic Helmholtz equation (Silva, 2011). It is based on the choice of FGMRES as linear solver which flexibly incorporates an GMRES preconditioner in the outer iteration loop. In the present implementation the GMRES preconditioner is itself preconditioned by a SOR splitting method. The method is based on the considerations of Section 4.3.1. This additional step may accelerate the solution process considerably. However, the method needs careful calibration of the SOR relaxation parameter ω_{SOR}. For the given model problem this parameter is varied for different frequencies and inlet Mach numbers in Fig. 4.4. It can be seen that the lower the frequency the smaller the band is in which acceptable iteration numbers are reached to converge to an error of $\epsilon = 0.01$. Moreover, the graphs illustrate that with increasing inlet Mach number, the choice of ω_{SOR} must decrease. A suitable range for this parameter would be between $0.2 \leq \omega_{SOR} \leq 0.4$.
- **GMRES-GMG**: Like FGMRES, GMRES satisfies the optimality condition and therefore represents a highly robust method. Here, it is used in an inner iteration cycle. When used as linear solver for the LEEs, the multigrid method proves not to converge fully satisfactory. Certain error frequencies may not be reduced sufficient enough and the convergence behavior becomes strongly dependent on the selected parameters. However, when employed as preconditioner for GMRES, the GMG method shows its high capabilities. Recently, different authors have already proposed GMG methods to accelerate Krylov subspace methods (Wienands et al., 2000; Zubair et al., 2007). This potential is exploited by the use of GMG as a preconditioner for this solver configuration.

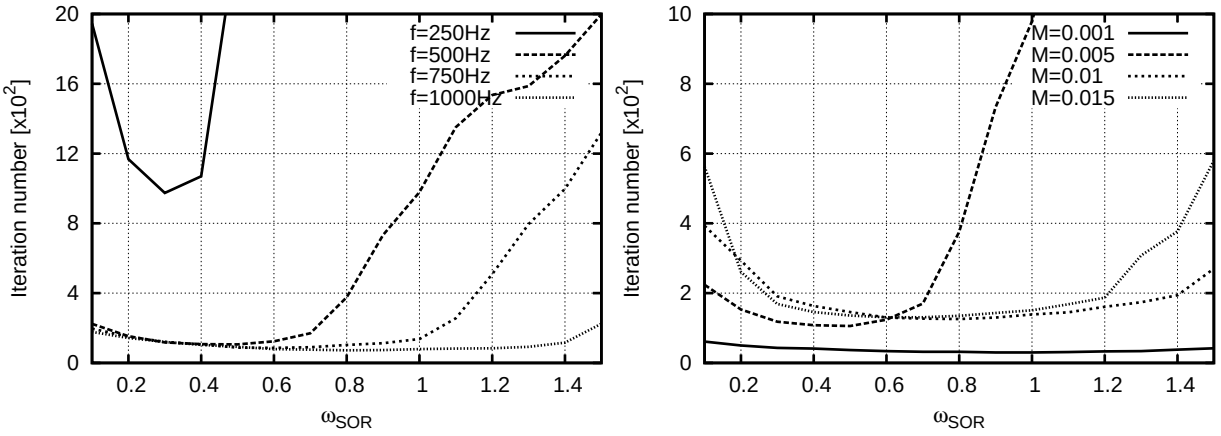

Figure 4.4: Iteration number compared to the explicit choice of ω_{SOR} for the FGMRES-GMRES-SSOR(ω_{SOR}) solution algorithm: dependance on frequency for an inlet $Ma = 0.01$ (left), dependance on inlet Mach number at a frequency $f = 500$Hz (right).

For multigrid preconditioners many open variables exist and must be specified. These include the number of discretization levels, the type of cycle (V-, F-, or W-cycle), the number of pre- and post smoothing iterations (ν_1, ν_2) and the relaxation parameter ω_{SOR}. Latter value is employed as a filter to dampen small wavelength components. The success of the GMRES-GMG procedure mainly depends on the choice of ω_{SOR}. Therefore, it is optimized for the model combustor problem. Fig. 4.5 shows the variation of iteration numbers depending on the specific choice of ω_{SOR}. At first sight it is clear that the iteration number is relatively insensitive to the explicit choice of ω_{SOR}, except for low frequencies. This makes the method more robust compared to the formally introduced FGMRES-GMRES algorithm. According to Wienands et al. (2000), the amount of pre- and post-smoothing iterations is to be chosen such that $\nu_1 \leq \nu_2$ when employing GMG as preconditioner.

- **BiCGstab-GMG**: Although BiCGstab may break down before an exact solution is calculated, the method requires significant less memory and is less expensive in terms of work per iteration compared to the GMRES algorithm (van der Vorst, 2009). It is therefore selected as a third alternative. The reduced memory consumption is ascribed to the fact that BiCGstab does not need to store subspace vectors.

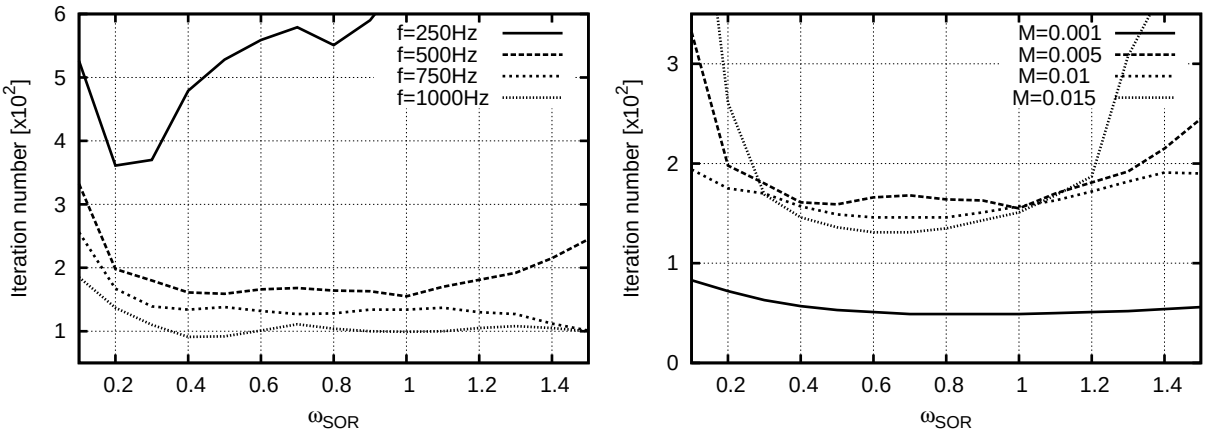

Figure 4.5: Iteration number compared to the explicit choice of ω_{SOR} of the pre- and post smoothing iterants of the GMRES-GMG solution algorithm: dependance on frequency for an inlet $Ma = 0.01$ (left), dependance on inlet Mach number at a frequency $f = 500$Hz (right).

All preconditioning parameters behave similarly to the GMRES-GMG algorithm and are therefore chosen equivalently.

For the sake of clarity of the solver formulations, the linear solution algorithm is always mentioned in first place while preconditioners used are listed thereafter. With respect to Fig. 4.4 and 4.5, note that the different algorithms may not be compared against each other, since the number of iterations is only a relative measure of the speed of convergence. The comparison of the three different iterative solvers on the generic combustion chamber is shown in the next section in terms of computational time.

4.5.3 Performance Comparison

In order to compare the performance of the three different iterative algorithms, the CPU-seconds are compared to reach a convergent solution. The numerical error ϵ for all three algorithms is estimated as

$$|\epsilon| = \sqrt{\frac{1}{n}\sum_{i=1}^{n}\left(\frac{|\mathbf{b}-\mathbf{A}\mathbf{x}_i|}{\max\left(|\mathbf{x}_i|, S_i\right)}\right)^2}, \quad \text{where} \quad S_i = 0.1\frac{1}{n}\sum_{i=1}^{n}|\mathbf{x}_i|, \tag{4.40}$$

where the subscript i denotes the iteration number. A converged solution is reached when $\epsilon = 0.001$ is established. The benchmark problem of Fig. 4.3 is chosen in the following.

Fig. 4.6 shows the performance of the three algorithms versus frequency at an inlet Mach number of $Ma = 0.05$. The BiCGstab-GMG algorithm shows a strong frequency dependance and does not converge for frequencies below $f \lesssim 750\,\mathrm{Hz}$. At higher frequencies BiCGstab-GMG does converge, however, slightly slower than the other two considered algorithms. BiCGstab-GMG also showed to be very sensitive in respect to the explicit choice of free parameters. The FGMRES-GMRES algorithm shows a lower dependency upon frequency. Only in the very narrow band below $f < 400\,\mathrm{Hz}$ the time to obtain a convergent solution increases. In this band of frequencies, however, thermoacoustic instabilities are generally suspected and a numerical routine must be able to retrieve acoustic solutions in this limit. Consuming higher amounts of computational time in this range is therefore undesirable. Here, the GMRES-GMG algorithm shows its potential of providing constant convergence speeds over the complete frequency range.

A similar behavior for the GMRES-GMG algorithm is found when changing the inlet Mach number of the configuration for a constant frequency of 500 Hz (Fig. 4.6). As illustrated in Fig. 4.3, the mean velocity gradient over the flame zone then changes equivalently with inlet Mach number. The GMRES-GMG algorithm shows a very robust behavior with a relatively constant convergence speed over the complete Mach number range. FGMRES-

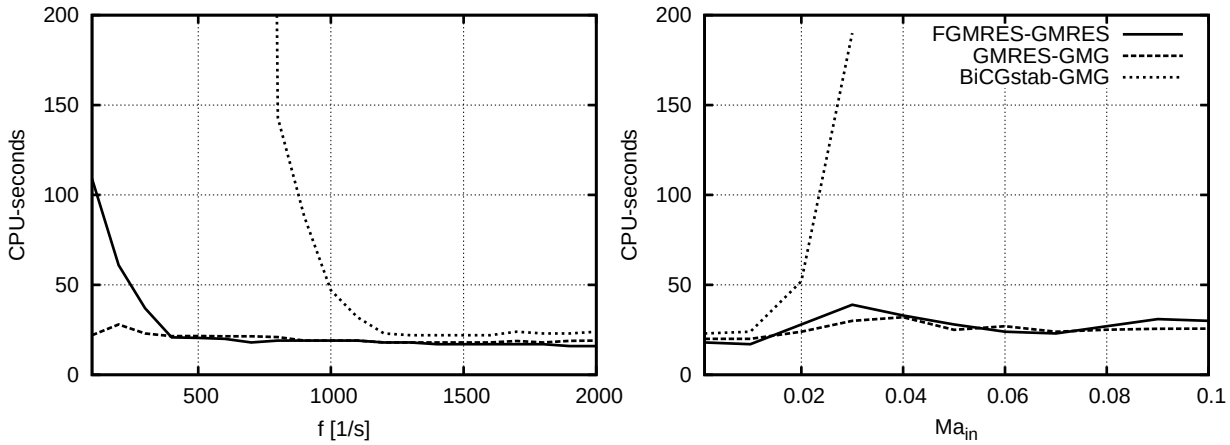

Figure 4.6: Performance comparison in CPU-seconds of three different iterative algorithms: FGMRES-GMRES, GMRES-GMG and BiCGstab-GMG for the generic combustor problem. Left: Variation of frequency at an inlet Mach number of $Ma = 0.05$; Right: Variation of inlet Mach number at a frequency of $f = 500$Hz.

GMRES performs equally well. On the other hand, the BiCGstab-GMG algorithm only showed converging behavior for very low Mach numbers.

From the considerations, the GMRES-GMG algorithm is chosen as iterative solver for three dimensional problem sets of this thesis as it provides constantly high convergence speed independent of frequency and velocity distributions. For complex geometries, the GMG preconditioner may not be able to represent the configuration's geometry sufficiently enough on the coarsest grid. In such cases, FGMRES-GMRES provides with a suitable alternative. The BiCGstab-GMG may be a suitable choice when considering low Mach number/high frequency applications, as the memory consumption is lower than in the aforementioned algorithms.

5 Prediction of Acoustic Scattering Behavior

Combustion chamber flows generally have a complex dynamic and feature a large diversity of different flow configurations. In technical devices, the flow coming from a feeding system is generally contracted in swirler channels of an injector nozzle and a swirling fluid motion is imposed. The flow then expands into a combustion chamber experiencing an abrupt change in area. A strong shear layer is formed separating an inner from an outer recirculation zone. Due to the significant radial momentum of the jets the shear layer may impinge onto the combustion chamber walls.

As the different flow configurations are diverse, so are the acoustic flow interactions: Acoustic waves interact with vortical structures in close proximity of flow separation edges leading to attenuation or amplification processes of the acoustic energy. Shear layers may also refract sound and influence the scattering process into higher order modes (Ribner, 1964). Vortical structures traveling inside the shear layers may be deformed when impinging onto walls, causing a certain feedback to the acoustic field. For high Reynolds-number flows, acoustic waves may also interact with turbulent fluctuations (Howe, 1984).

A combustor flow field may be subdivided into its different components. Each component may then be studied individually in order to generate reliable statements on the suitability of LNSEs to predict acoustic interactions in realistic combustion chamber configurations. This approach is followed in this section. First, a simple area expansion is considered which mainly features damping of acoustic waves. Then, a flow contraction in an orifice is analyzed, where energy is also transferred from the vortical to the acoustic modes for certain frequency ranges, leading to amplification of sound. Swirler vane channels may be thought of as representatives of such a configuration. Both aforementioned problems have in common that the vortices separate in a -more or less- free shear layer. This is not the case for a grazing

flow in a T-joint, the third test case considered. There, vortical structures impinge onto confining walls and may provide an acoustic feedback. For this test case aeroacoustic interactions are strongest. Finally, the last test integrates the individual problems into one computation: A complex swirled combustion chamber flow is simulated including an industrial combustion injector developed by Avio S.p.A.[1] The complexity of the acoustic analysis increases with every configuration.

Main aim of this section is to study the effect of acoustic-vortex interactions and the resulting implications on the acoustic losses. The solution procedure of Section 3.3.5, which solves the matrix inversion problem of Eq. (4.2) twice for each frequency, is applied to determine the complex scattering coefficients of the different flow configurations mentioned. Coupling with entropy waves is not considered herein, assuming isentropic behavior of all fluctuating components, viz. $\hat{p} = \bar{c}^2\hat{\rho}$. Governing equations, stabilization schemes and wave extraction procedure are implemented in the flexible finite element package COMSOL Multiphysics (2010).

5.1 Area Expansion

The first configuration studied is an area expansion depicted in Fig 5.1. Its geometry consists of two pipe segments which are co-axially connected, having an upstream diameter of d_u and a downstream diameter of d_d. The upstream pipe has a length of l_u, while the length of the downstream pipe is l_d. The area ratio $A_r = 0.35$ is selected to resemble the experimental measurements of Ronneberger (1987). The measurements are utilized to

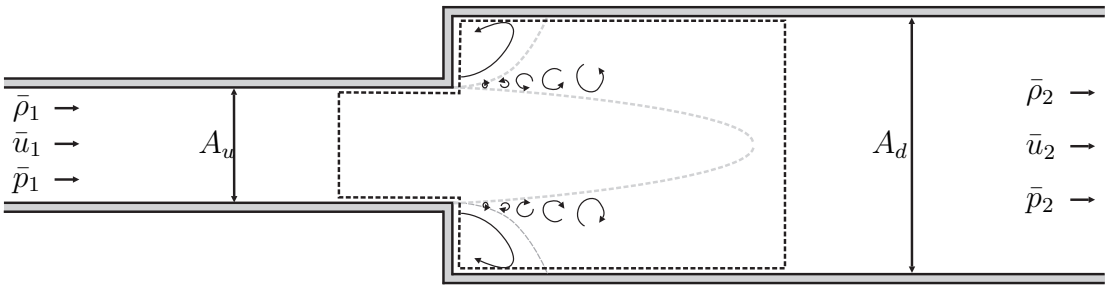

Figure 5.1: Schematic presentation of geometry and flow conditions of the area expansion of the experimental set up of Ronneberger (1987).

[1] http://www.aviogroup.com/

validate the present method. Table 5.1 gathers the main characteristics of this test case.

Acoustic phenomena involved are the scattering process of plane waves into higher order modes at the area expansion, refraction of sound in the expanding shear layer and the attenuation of sound generated through acoustic-vorticity interactions. Latter effect results from the triggering process of vortical structures by acoustic fluctuations at the trailing edge. At small Strouhal numbers ($St < 0.25$) the shear layer features instability (see Michalke, 1965), leading to aeroacoustic interactions.

The area expansion is used to study two main effects: First, the capability of the LNSEs is demonstrated to capture acoustic-flow coupling and the mode scattering effects. Secondly, the test case is used to study the influence of the acoustic boundary layer. Some authors in the literature believe that acoustic-flow interaction processes are significantly influenced by the effect of the acoustic boundary layer Kierkegaard et al. (2012a,b). If so, the mesh refinement of wall boundaries would exceed the ones encountered in typical CFD simulations where the boundary is fully resolved. This is due to the fact that the acoustic boundary layer (already at moderate frequencies, see Eq. (2.50)), becomes an order of magnitude smaller than the fluid dynamic boundary layer. With the unavailability of wall models incorporating the effect of the acoustic boundary layer, this requirement would not be desirable and would restrict the use of LNSEs to at most small scale problems for

Table 5.1: Geometrical and physical operating conditions of the sudden area expansion Ronneberger (1987).

Description	Variable	CFD/CAA
upstream pipe diameter	d_u	0.05 m
downstream pipe diameter	d_d	0.085 m
upstream pipe length	l_u	0.5 m
downstream pipe length	l_d	0.7 m
area ratio	A_u/A_d	0.35
Mach number at inlet	Ma	0.2
Reynolds number at inlet	Re	1.88×10^5
kinematic viscosity	ν	1.55×10^{-5} m^2 s^{-1}

the near future. Therefore, two computations with different boundary layer resolutions are performed. The first uses the LNSEs incorporating the effect of molecular viscosity and the second uses the non-viscous counterpart, the LEEs, where the acoustic boundary layer is not resolved.

In order to design the different mesh configurations for the simulations using LNSEs and LEEs, one has to be aware of the different length scales involved in aeroacoustic problems. Resolving only the acoustic wavelength λ_a is not sufficient. In order to capture the main acoustic-flow interaction processes, resolution of the vortical length scale is necessary as well. It is roughly an order of magnitude smaller for low Mach number configurations $\lambda_v = Ma\lambda_a$. As vortical structures originate from the trailing edge and propagate inside the shear layer until they are dissolved, this region is significantly refined to capture the vorticity length scale in the complete frequency range of interest. The resolution of the uniform flow in the upstream and downstream ducts, where generally only acoustic waves travel, is dedicated to sound waves with shortest wavelength or the highest frequency. The shortest wavelength considered at f =5100 Hz is resolved by a minimum of 15 cells. These considerations are common to both LNSEs and LEEs resolutions. However, for the LNSEs a different upstream near wall refinement is chosen. Up to a Strouhal number of $St < 0.25$, after which aero-acoustic interactions theoretically vanish, the acoustic boundary layer is resolved by at least four cells. In case that the acoustic boundary layer contributes significantly to the aeroacoustic interactions, differences in the computations with LEEs must be seen up to $St < 0.25$. For the LEEs, only the hydrodynamic boundary layer is resolved by four cells. Beginning from the smallest cell located directly at the edge of the area expansion, the grids grow in axial and radial direction with an element growth of 2%. Rectangular elements are chosen in conjunction with second order Lagrangian interpolation functions. The different mesh refinements result in overall 900k and 350k degrees of freedom for the LNSEs and LEEs computations, respectively.

In order to establish a well-posed mathematical problem, two inlet boundary conditions need to be defined in two dimensional space. Zero reflecting acoustic impedance boundaries are subscribed for the acoustic characteristic, Eq. (2.38) with $Z = 1$, while vorticity perturbations are assumed to vanish, setting the velocity components parallel to the inlet to zero, viz. $\hat{\mathbf{u}}_{||} = 0$. At the domain outlet, only a boundary condition for the upstream

reflected wave needs to be imposed, as vorticity perturbations are simply convected out of the domain. Similarly to the inlet, this is done by imposing zero reflections using an impedance boundary condition. The only difference between LNSEs and LEEs computation is the definition of the wall boundary. As the effect of the acoustic boundary layer is estimated in the following simulations, consequently acoustic no-slip wall boundaries are ascribed for the LNSEs in the upstream duct $\hat{\mathbf{u}} = 0$. For LEEs, slip boundaries are ascribed instead, Eq. (2.51). To reduce the computational effort, the LNSEs and LEEs are formulated in a cylindrical coordinate system (see Appendix B.2) and a symmetry boundary is chosen for the center axis. Any symmetry line or plane does not permit the presence of acoustic fluxes and friction forces yielding the symmetry boundary condition,

$$\mathbf{n} \cdot \hat{\mathbf{u}} = 0; \qquad \frac{\partial \hat{\mathbf{u}}_{||}}{\partial \mathbf{n}} = 0. \tag{5.1}$$

For this test case also the influence of the finite element stabilization scheme is assessed as well. It is found that the GLS scheme performes slightly better compared to the SUPG scheme in case of the LNSEs. GLS is able to reduces the numerical error by overall 1% compared to the experimental data. However, when LEEs are employed, SUPG and GLS produce similar orders of accuracy. For consistency, the following simulations are performed using the GLS stabilization scheme using a stabilization parameter defined in Eq. (3.38) using $\alpha = 0.1$.

Main focus of this section is to validate the prediction capabilities of the LNSEs and LEEs solely, errors stemming from the mean flow field computations are undesired and minimized by restricting the modeling to the subgrid turbulent scales. Thus, a well validated LES simulation is time averaged to produce the mean flow fields. This is done within the flow solver AVBP developed from CERFACS (Schoenefeld and Rudgyard, 1999). The same mesh consisting of block-structured hexahedra elements and boundary conditions as described by Föller and Polifke (2012) are utilized. For boundary layers, the applied wall model switches between logarithmic and linear law depending on the value of y^+. On average a $y^+ = 35$ is achieved. To produce the mean flow fields, overall 0.026 s are time averaged while the time step satisfies a Courant-Friedrich-Levi

number (CFL) of 0.7. Subgrid turbulent scales are modeled using a Wall Attached Layer Eddy model developed by Nicoud and Ducros (1999).

5.1.1 Scattering Matrix

The procedure described in Section 3.3.5 is used to compute the scattering matrix of the area expansion. LNSEs and LEEs are solved in a cylindrical coordinate system and two simultaneous simulations are performed exciting the area expansion once from upstream and once from downstream direction to retrieve all scattering matrix coefficients. Acoustic forcing is implemented by inserting the source vector

$$\mathbf{s_u} = \left(-\cosh\left(\frac{x - x_s}{\delta_s}\right) - 1, 0 \right)^T \tag{5.2}$$

into the finite element procedure of Eq. (3.2), where δ_s defines the thickness of the region of the excitation source and x_s its axial location. Outside of the excitation region, the source term is set to zero. The resulting scattering matrix is plotted versus the upstream Helmholtz number

$$He = \frac{\omega d_u}{2\bar{c}}, \tag{5.3}$$

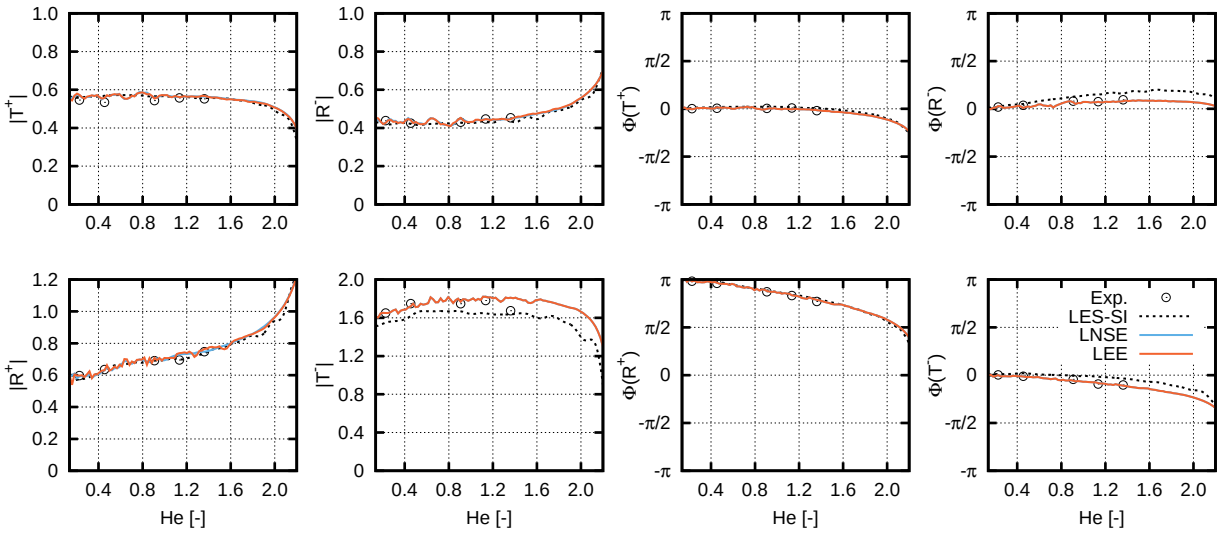

Figure 5.2: Amplitude and phase of scattering matrix coefficients of a sudden area expansion at $Ma = 0.2$. Results of LNSEs and LEEs with experimental data of Ronneberger (1987).

in Fig. 5.2. Amplitudes and phases are resolved with a frequency step of 50 Hz up to the first cut-on frequency of the first non planar mode at $He_{\text{cut-on}} = 2.2$. In comparison to the experimental results of Ronneberger (1987), both equation sets, viz. LNSEs and LEEs, accurately capture the scattering behavior of the sudden area expansion. Increasing reflection and decreasing transmission coefficients amplitudes are observed. Characteristic inflection points in $|R^+|$ at about $He = 0.3$ and 0.6 are captured with high accuracy. The phase behavior is equally well predicted.

Direct comparison of LNSEs and LEEs shows nearly no deviation in the results. Scattering coefficients predicted with LNSEs show only a slightly smoother trend. This is attributed to the stronger vorticity perturbations produced by the LEEs ansatz, due to the absence of viscosity. Larger amplitudes of vorticity in the wave extraction region increase the error of the least-square algorithm. In the LNSEs, viscous effects contribute to the suppression of vorticity waves and thus possibly reduce the fitting error. Nevertheless, the similarity in the results between LNSEs and LEEs, may lead to the preliminary conclusion that the coupling mechanism between acoustic waves and the hydrodynamic mode is not strongly influenced by molecular viscosity of the acoustic boundary layer in this particular case. As it will be shown, this is also not the case for other configurations like a single hole orifice. The strong similarity in the results, considering the very different mesh resolution, also proves that grid independence is established.

Fig. 5.2 also compares the current approach to an LES/system-identification ansatz of Föller and Polifke (2012) yielding the same order of accuracy. Föller and Polifke (2012) argued that the linearized method neglects two main aeroacoustic interaction effects: The scattering of sound into turbulence as well as the reverse effect of the acoustic on the fluid dynamic field. Although LNSEs and LEEs do neglect such effects, they do not seem highly pronounced for this very test case. Both linearized equation sets are able to capture the scattering matrix elements for the sudden area expansion with high accuracy.

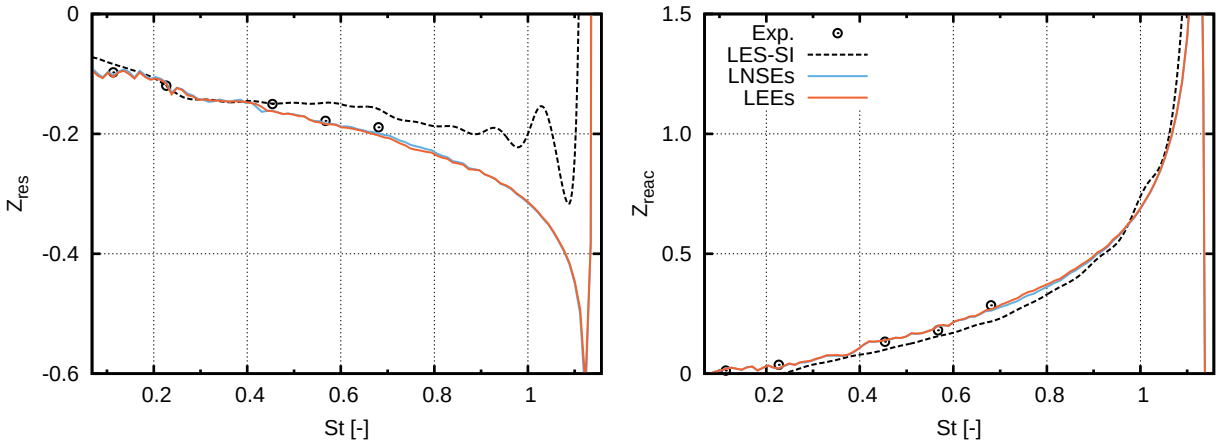

Figure 5.3: Acoustic resistance Z_{res} and reactance Z_{reac} of a sudden area expansion at $Ma = 0.2$. Results of LNSEs and LEEs with experimental data of Ronneberger (1987) and results achieved by the LES/SI approach Föller and Polifke (2012).

5.1.2 Acoustic Impedance

In this section the results of the acoustic impedance are shown to demonstrate the capabilities of the optimized hybrid approach to capture the acoustic flow interaction process and mode scattering mechanism in detail. First, the analytic representation of the lumped impedance is introduced from various publications (Föller and Polifke, 2012; Karal, 1953; Morse and Ingard, 1987; Peat, 1988)

$$Z = \frac{\hat{p}_u - \hat{p}_d}{\bar{\rho}\bar{c}\hat{u}_u} = Z_{\text{res}} + \mathrm{i}Z_{\text{reac}}. \tag{5.4}$$

Its real part is called resistance Z_{res}, whereas its imaginary part is generally referred to as reactance Z_{reac}. The resistance contains inertial information about the damping behavior of the system. The reactance describes the scattering process and temporal storage of acoustic energy in evanescent higher-order modes. When the acoustic energy from the higher order modes is back-scattered into the plane wave mode, a phase shift is introduced. Fig. 5.3 plots the evolution of the resistance and reactance versus the non dimensional Strouhal number

$$St = \frac{\omega\theta}{\bar{c}Ma}, \tag{5.5}$$

where θ is the boundary layer thickness in the upstream pipe close to the separation edge. Boij and Nilsson (2006) estimate this thickness to be 10 %

of the upstream pipe radius r_u. The Strouhal number represents the ratio of time scales between the acoustic and mean flow field. If the time-scales are approximately of the same order, then most-likely acoustic-flow interactions appear.

Ronneberger's measurements are in excellent agreement with the results obtained through the linearized equations. In the following, the discussion of the results is split into three Strouhal number ranges. According to the differentiation made in Föller and Polifke (2012) these ranges are associated to three different physical phenomena which lead to the observed impedance behavior.

In the low Strouhal number range ($St \leq 0.25$), Föller and Polifke (2012) observe an initially constant resistance, which then gradually changes to a lower level. This observation is confirmed by the linearized approach. At about $St = 0.25$ the resistance becomes constant again. Throughout the low Strouhal number range, the reactance remains mostly constant. This characteristic behavior observed is associated with the hydrodynamic instability of the shear layer, which is triggered by the impinging acoustic waves. Interaction causes an energy transfer from the acoustic to the vortical mode, which results in a loss of acoustic energy or equivalently in an increase of resistance (Boij and Nilsson, 2003, 2006). According to Michalke (1965) the shear layer features instability only up to a Strouhal number of $St \leq 0.25$ after which it reaches a stable state. Thus, after passing this point, the interaction is supposed to vanish, which is confirmed by a nearly constant resistance.

The second range between $0.25 \leq St \leq 0.4$ is characterized by constant levels of resistance as well as an increasing reactance. The underlying acoustic phenomenon can be associated to the well known end-correction at pipe discontinuities (see Section 2.7.1.2 for elaboration). As the reactance features a constant slope, this indicates a constant end-correction in this frequency range.

In the higher Strouhal number range $St \geq 0.4$, more acoustic energy is scattered from the plane wave mode into higher order duct modes at the area expansion. As the frequency approaches the cut-on frequency, higher order modes are allowed to propagate through longer distances in the downstream duct, leading to a delayed back-scattering process into the plane wave mode.

This behavior is characterized by an increasing reactance. The results shown in Fig. 5.3 prove the capability of LNSEs as well as LEEs to capture the physics with similar accuracy for all three Strouhal number ranges.

5.2 Orifice

In the second test case, the current approach is used to determine the scattering coefficients of a single hole orifice schematically shown in Fig. 5.4. The geometry consists of a constant area duct with diameter d which is intersected by a sharp edged orifice with a hole diameter of d_o and thickness t. The duct section upstream of the orifice has a length of l_u, whereas the length of the downstream duct is l_d. The geometry and inlet flow velocity ($\bar{u}_0 = 9\text{m/s}$) are selected to allow comparison with the experimental measurements of Testud et al. (2009). Table 5.2 gathers the main characteristics of this test case. Compared to the area expansion, which features only attenuation of sound, the flow inside an orifice may cause net amplification of acoustic energy. This feature is analyzed in this section.

Despite the geometric simplicity of an orifice, strong acoustic-flow interactions can be observed: The flow reaching the orifice is contracted to a central jet and a shear layer is formed between the expanding flow and the outer recirculation zones. In regions of flow separation, acoustic waves trigger vortical modes in the flow field which are then convected downstream inside the shear layer. For certain frequency ranges, the shear layer amplifies the vortical structures (Michalke, 1965). This process may lead to a net amplification of the acoustic energy if the vortical energy is fed back into the acoustic mode by aeroacoustic interactions. If this type of amplification occurs at frequencies which correspond to resonance frequencies of the com-

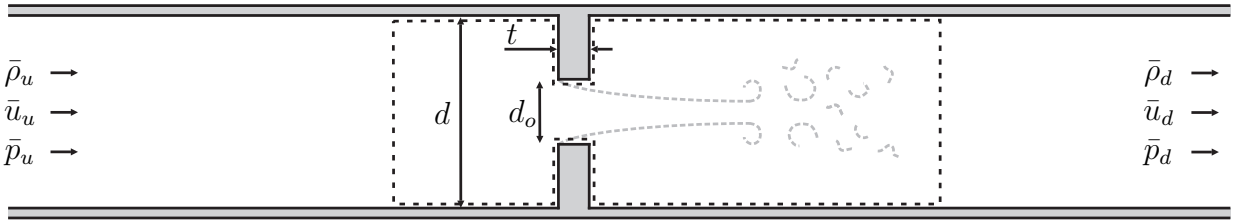

Figure 5.4: Schematic presentation of geometry and flow conditions of single hole orifice of experimental set up of Testud et al. (2009).

plete system, a resonant feedback loop is created, yielding large amplitude oscillations (Rockwell and Naudascher, 1979). Latter phenomenon is called whistling and is a completely non-linear phenomenon. However, it can also be studied by means of a linear analysis (Testud et al., 2009).

Acoustic fields for a discrete number of frequencies are calculated using LNSEs and LEEs formulated in a cylindrical coordinate system. A GLS Petrov-Galerkin approach is applied for finite element stabilization using the τ_{stab} parameter of Eq. (3.38). As shown previously for the sudden area expansion the viscous acoustic boundary layer has negligible influence on the scattering behavior of the acoustic element. It is therefore neglected subsequently and not resolved numerically. Eq. (2.51) is applied to all solid walls. All other domain boundaries are chosen analogously to the area expansion test case. At the axis of rotation again a symmetry boundary is assigned to reduce the computational effort.

Due to the smaller dimensions of this test case the two dimensional acoustic mesh consists only of roughly 4.200 rectangular elements which are discretized using second order Langragian test functions. Overall, this leads to 120.000 degrees of freedom. The orifice $d_o/2 \times t$ is discretized by 15×5 cells respectively. Element growth rates in upstream and downstream direction do not exceed 1 percent, resulting in a highly uniform grid distribution. The resulting system matrix is efficiently solved using the direct LU factorization method for large system matrices called MUMPS. For a single

Table 5.2: Geometrical and physical operating conditions of the single hole orifice Testud et al. (2009).

Description	Variable	CFD/CAA
pipe diameter	d	$0.03\,\mathrm{m}$
orifice hole diameter	d_o	$0.015\,\mathrm{m}$
orifice thickness	t	$0.005\,\mathrm{m}$
upstream pipe length	l_u	$0.15\,\mathrm{m}$
downstream pipe length	l_d	$0.36\,\mathrm{m}$
Mach number at inlet	Ma	0.026
Reynolds number at inlet	Re	1.8×10^4
kinematic viscosity	ν	$1.55{\times}10^{-5}\,\mathrm{m^2\ s^{-1}}$

matrix inversion the computational time required by the direct algorithm is approximately 12 seconds using a single core processor. In the same way as for the sudden area expansion, regions of wave extraction are chosen upstream $-0.09\,\mathrm{m} \leq x \leq -0.03\,\mathrm{m}$ and $0.15\,\mathrm{m} \leq x \leq 0.85\,\mathrm{m}$ downstream of the orifice outlet plane ($x = 0\,\mathrm{m}$).

The mean flow field is calculated performing a time average over LES solutions. Subgrid scale model, discretization schemes and CFL number are chosen equally to the described simulation of Section 5.1. The mesh of Lacombe et al. (2011) is adopted for the present computations. It is significantly refined around the orifice's leading and trailing edges. Main aim of the employed discretization is to capture the correct flow angle of the flow contraction at the upstream edge, the separation point and the shear layer expansion inside the orifice. It is believed that these parameters strongly influence the acoustic-flow interaction processes at an orifice configuration. The fine discretization employed yielded a total number of 5.5 million cells. Overall, 0.3 s are time averaged to produce the mean flow field. A time step was chosen to satisfy CFL< 0.7 for the flow field computations.

5.2.1 Scattering Matrix

For a discrete number of frequencies $f = 200-5100\,\mathrm{Hz}$ with a frequency step of $\Delta f = 50$ Hz, the results of the scattering matrix coefficients are shown in Fig. 5.5. The results are plotted versus the orifice Strouhal number

$$St = \frac{\omega t}{2\pi \bar{u}_o}, \tag{5.6}$$

wherein, $\bar{u}_o = \bar{u}_0 (d/d_o)^2$ describes the flow velocity through the orifice. Again, high agreement in the complete frequency range between the predicted scattering matrix coefficients of the LNSEs or LEEs and the experimental measurements is observed.

In the low frequency limit, amplitudes of the reflection coefficients predicted by the linearized equations are about constant, whereas the experimental results show a slight negative slope. After a drop, the reflection coefficients increase sharply around $St = 0.25$. Similarly, amplitude transmission coefficients increase and reach a maximum at about the same Strouhal number.

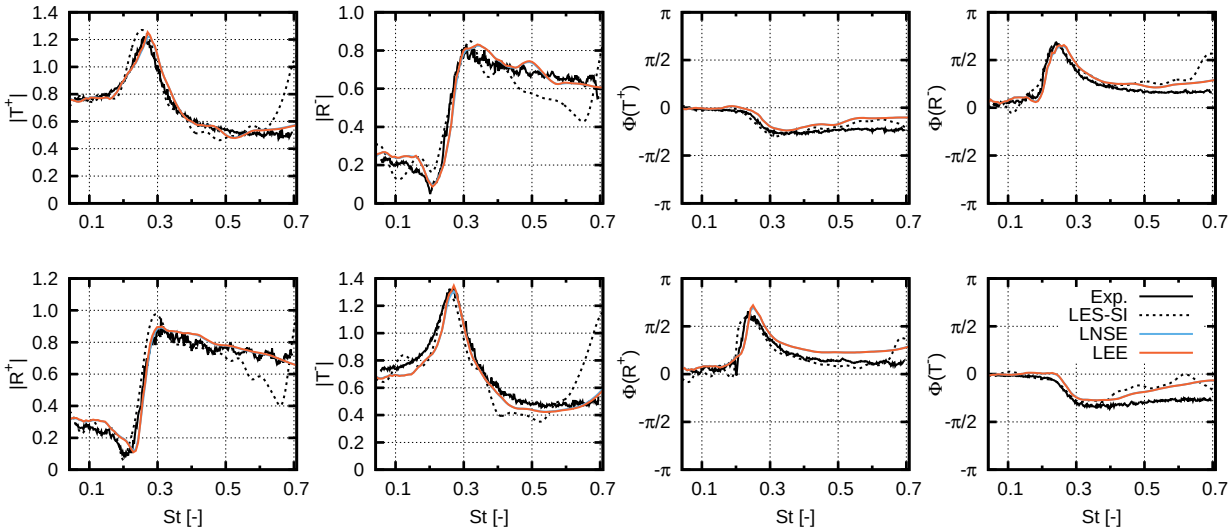

Figure 5.5: Amplitude and phase of scattering matrix coefficients of an orifice ($\bar{u}$ =9 m s^{-1}). Results of LNSEs and LEEs with experimental data of Testud et al. (2009) and results achieved by the LES/SI approach Lacombe et al. (2011).

In this frequency range, strong aeroacoustic interaction leads to the amplification of acoustic waves resulting in transmission coefficients much larger than unity. At higher Strouhal numbers ($St > 0.4$), the shear layer stabilizes again, leading to decreasing transmission and reflection coefficients.

LNSEs and LEEs are both able to capture all acoustic flow interaction processes in the studied Strouhal number range in trend as well as in frequency. Predicted amplitudes and phases are nearly identical for both linearized equation sets and are in excellent agreement with the measurements for all scattering matrix coefficients. Only some deviations to the experimental data is observed for higher Strouhal numbers.

A comparison to the LES/SI approach of Lacombe et al. (2011) shows that the scattering behavior of the test case is predicted with higher accuracy by the LNSEs and LEEs. At higher Strouhal numbers ($St > 0.5$), the LES/SI approach predicts a higher order mode. Its appearance, however, is not in agreement with the experiments and results of the LNSEs and LEEs simulations. A possible explanation may be the under prediction of the inflow velocity in the LES/SI computations by 0.2 m s^{-1} yielding a mean flow velocity of $\bar{u}_0 = 8.8$ m s^{-1}. However, the results should still scale with Strouhal number which was adapted accordingly for the LES/SI representation in Fig. 5.5. A more recent publications with corrected inflow

velocity still shows the appearance of this higher order acoustic mode (see Lacombe et al., 2013).

5.2.2 Whistling Criterion

As described above, orifices may be subjected to a phenomenon called whistling. Although, this is a completely non-linear effect its onset may be predicted by a linear approach such as the LNSEs. Whistling results from a shear layer instability at the orifice which amplifies acoustic waves and may lead to self-sustained oscillations in pipe-networks, such as ventilation or supply systems. Aurégan and Starobinski (1999) derived a criterion to determine the frequency regions where whistling may potentially occur. The criterion can be formulated as follows: calculate the minimum and maximum eigenvalue $(\xi_{\min}, \xi_{\max})$ of,

$$\xi = \mathbf{I} - \mathrm{eig}(\mathbf{S}_e^* \mathbf{S}_e) \qquad \text{with} \qquad \mathbf{S}_e = \begin{pmatrix} T^+(\omega) & \frac{1+Ma}{1-Ma} R^-(\omega) \\ \frac{1-Ma}{1+Ma} R^+(\omega) & T^-(\omega) \end{pmatrix}, \quad (5.7)$$

where $\mathbf{I}$ is the identity matrix and $\mathbf{S}_e$ the scattering matrix in terms of exergy and the superscript * denotes the hermitian transpose. The obtained eigenvalues define the margins of the ratio of dissipated acoustic power $(P_{in} - P_{out})$ to the incident acoustic power P_{in}, i.e.

$$\xi_{min} \leq \frac{P_{in} - P_{out}}{P_{in}} \leq \xi_{max}. \quad (5.8)$$

The authors distinguish between three different cases:

- $\xi_{min} \geq 0$ and $\xi_{max} > 0$, the system damps acoustic energy and the outgoing acoustic power is lower than the incoming acoustic power,
- $\xi_{min} < 0$ and $\xi_{max} = 0$, the system amplifies acoustic energy and the outgoing power may exceed the incoming acoustic power,
- $\xi_{min} = 0$ and $\xi_{max} = 0$, the element is energetically neutral and neither amplifies nor damps acoustic waves.

The whistling potential of the orifice is characterized for a broad range of frequencies in Fig. 5.6. Three distinct regions can be identified. At low

Strouhal numbers ($St < 0.2$), $\xi_{\min} \approx 0$ and the orifice dissipates acoustic energy. Both, LNSEs and LEEs are in good agreement with the measurements.

The second range between $0.2 \leq St \leq 0.4$ is characterized by negative values of $\xi_{\min}$ which exhibit a minimum at $St \approx 0.28$. Here, acoustic sound is potentially produced by the orifice, which leads to a net amplification of incident acoustic waves. LNSEs and LEEs predict the whistling mode at slightly higher Strouhal numbers. The magnitude of the eigenvalues is captured with quantitative accuracy by LNSEs but not by the LEEs. Here, a first discrepancy between the two linearized models is observed: Although showing qualitative agreement, the LEEs do not coincide with the results of the LNSEs. A slightly lower $\xi_{\min}$ is predicted, indicating that more sound is produced than physically observed. This behavior is attributed to the missing molecular viscosity in the LEEs, which inevitably leads to a stronger growth of the vortical structures and therewith to a stronger aeroacoustic coupling. The behavior found is believed to be unique to linearized sets of equations and will be explained in more detail in the next section of the T-joint where interactions are found to be stronger.

Similar to the case of the area expansion, a resolution of the acoustic boundary layer does not seem important to capture the main aero-acoustic effects of an orifice. A numerical edge-to-edge instability observed by Kierkegaard

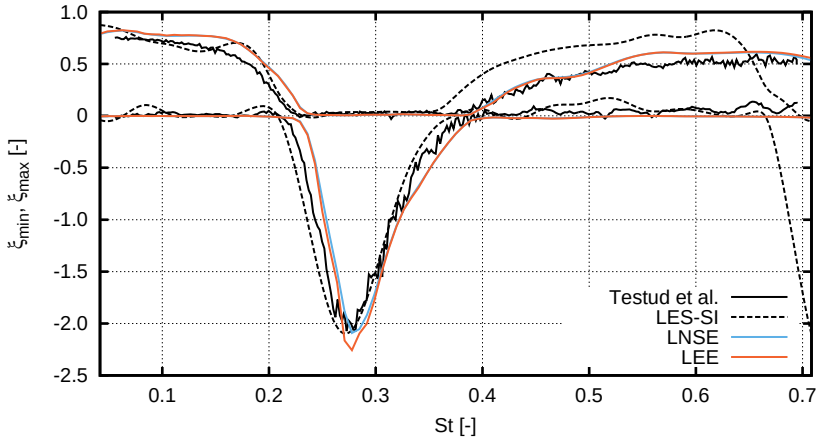

Figure 5.6: Minimum and maximum eigenvalues ($\xi_{\min}$ $\xi_{\max}$) of the eigenvalue problem in Eq. (5.7). Results of LNSEs and LEEs with experimental data of Testud et al. (2009) and results achieved by the LES/SI approach Lacombe et al. (2011).

et al. (2012a), when slip wall boundary conditions are subscribed to the orifice walls, is not observed in the present study. In the third range ($St > 0.4$) the orifice again potentially dissipates acoustic energy.

This section successfully illustrates that the LNSEs as well as LEEs are able to capture basic sound attenuation as well as amplification processes with slight differences in accuracy. In regions close to the frequency of instability of a shear layer, where maximum amplification of incident acoustic waves occurs, LEEs are shown to slightly over predict the acoustic-flow coupling processes.

5.3 T-Joint

A grazing flow in a T-joint is the third validation test case for which the LNSEs are solved. This configuration features a flow through a main pipe to which a side branch is attached perpendicular to the central axis of the main pipe. Unlike in an area expansion or an orifice, the shear layer which separates at the trailing edge of the upstream pipe intersection does not evolve freely. Instead it expands until it reaches the downstream edge. In a grazing flow configuration the shear layer separates the stagnant medium in the side branch from the mean flow inside the pipe.

Similarly to the single hole orifice, this configuration may exhibit energy transfer to or from the acoustic field, depending on the Strouhal number considered. Consequently, incident acoustic waves are either amplified or

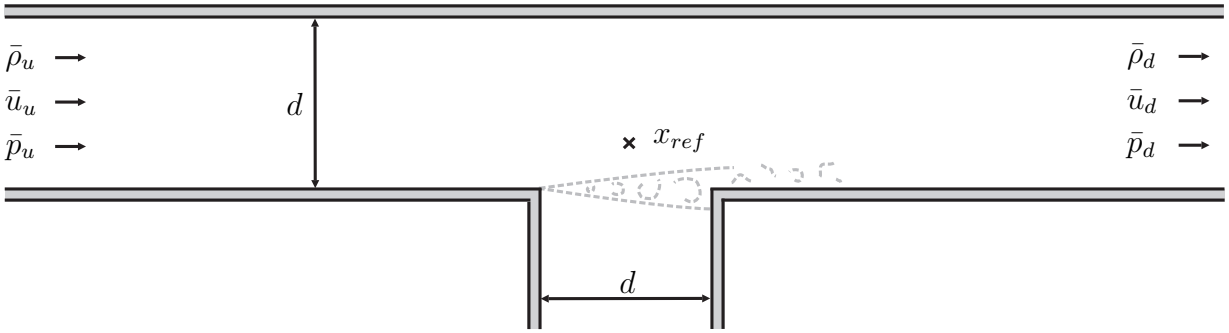

Figure 5.7: Schematic presentation of geometry and flow conditions of grazing flow in a T-joint experimentally measured by Karlsson and Åbom (2010).

attenuated. The mechanism behind this acoustic-flow coupling may be described by a feedback loop of the following chain of events:

- the acoustic field excites the shear layer at the upstream edge of the T-joint, where the flow separates. Instability of the shear layer leads to the generation of vortical disturbances,
- the disturbances are convected through the shear layer and interact with the acoustic field, resulting in a transfer of acoustic energy from the flow field into the acoustic field, and vice versa,
- the additional sound produced through aeroacoustic interactions propagates to the upstream edge, the most receptive area for the shear layer instability, creating a certain feedback loop.

The concept of the feedback loop is very similar to the one observed in low Mach number flows over deep cavities (Rockwell, 1983) or Helmholtz resonators. Under resonance conditions, e.g. in pipe systems, this process may also lead to the phenomenon of whistling already explained for the orifice configuration.

In order to analyze the acoustic scattering behavior of a T-joint, the theory for the determination of scattering coefficients of acoustic two-ports of Section 3.3.5 must be extended to acoustic three-ports. The scattering matrix of an acoustic three-port is defined by

$$\begin{pmatrix} \hat{p}_u^- \\ \hat{p}_s^- \\ \hat{p}_d^+ \end{pmatrix} = \begin{pmatrix} R_u & T_{s,u} & T_{d,u} \\ T_{u,s} & R_s & T_{d,s} \\ T_{u,d} & T_{s,d} & R_d \end{pmatrix} \begin{pmatrix} \hat{p}_u^+ \\ \hat{p}_s^+ \\ \hat{p}_d^- \end{pmatrix} \tag{5.9}$$

where R's denote the reflection coefficients and T's describe the transmission coefficients from one branch to the other. The direction of acoustic transmission is included in the respective subscripts: The first index $\{u/d/s\}$ defines the point of origin of an acoustic wave to be transmitted, while the second subscript defines the direction in which the acoustic wave is transmitted. $\hat{p}_{u/d/s}^{+/-}$ defines the complex pressure wave amplitudes in the upstream branch (subscript u), downstream branch (subscript d) or side branch (subscript s), traveling either in downstream $+$ or upstream direction $-$.

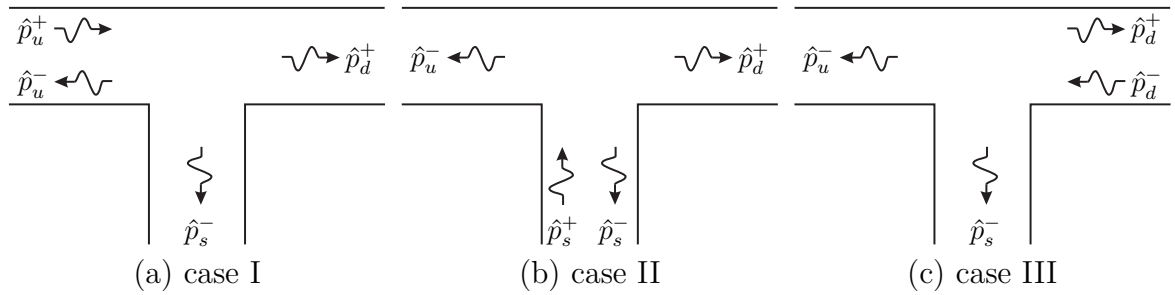

Figure 5.8: Different acoustic excitation cases of the T-joint and location of complex pressure amplitudes. Case I, case II and case III denote excitation from upstream, side and downstream branch, respectively.

In order to obtain all unknown scattering matrix coefficients of Eq. (5.9) three instead of formerly two independent acoustic states need to be defined. This is done by performing three acoustic simulations for each discrete angular frequency ω, as shown in Fig. 5.8. In the first simulation, the T-joint is numerically excited from the upstream branch (case I) by introducing a forcing function of Eq. (5.2), in the linearized momentum equation in x-direction. Other contributions to the forcing vector are chosen to be zero in this case. In a second and third case, case II and III, the T-joint is excited from the side branch direction and from the downstream direction, respectively. Following this routine provides nine equations for the nine unknown scattering matrix coefficients of an acoustic three-port.

5.3.1 Configuration

The T-joint consists of two pipe segments of equal diameter d. Both intersect each other in an angle of 90 degrees. The main pipe has a length of l_m while the side branch pipe section is l_s long. The edge geometry at the intersection of both pipes has a strong impact onto the aeroacoustic behavior, see e.g. Bruggeman et al. (1991) and Kooijman et al. (2008). Here, in this thesis, a sharped edge T-joint is considered.

The flow enters the main pipe with an average Mach number of 0.1 and forms a turbulent shear layer $Re \sim \mathcal{O}(10^5)$ at the pipe intersection which impinges onto the downstream edge. Tab. 5.3 summarizes the geometric

Table 5.3: Geometrical and physical operating conditions of the T-junction Karlsson and Åbom (2010) for the LES and LNSEs computations.

Description	Variable	LES/LNSEs
pipe diameter	d	$0.033\,\mathrm{m}$
main pipe length	l_m	$0.364\,\mathrm{m}$
sidebranch pipe length	l_s	$0.172\,\mathrm{m}$
ambient pressure	$\bar{p}$	$101\,325\,\mathrm{m}$
ambient temperature	$\bar{T}$	$298.15\,\mathrm{K}$
speed of sound	$\bar{c}$	$346.18\,\mathrm{m\ s^{-1}}$
kinematic viscosity	ν	$1.568 \times 10^{-5}\mathrm{m^2\ s^{-1}}$
Mach number at inlet	Ma	0.1
Reynolds number at inlet	Re	6×10^4

and operating conditions. The numerical results are compared to the experimental data of Karlsson and Åbom (2010). The configurations differ in the duct diameter $d < d_{\mathrm{exp}} = 0.057\mathrm{m}$. While the Strouhal number and the Mach number show similarity, the Reynolds number of the simulation is 58 percent smaller than in the experiment. Föller et al. (2010b) argue that this discrepancy has little influence on the momentum thickness of the shear layer and that the data collapses well with Strouhal number.

5.3.2 Large Eddy Simulation of Flow Field

In the context of cavity noise prediction, Slimon et al. (1998) highlight the importance of the turbulence model. In order to accurately predict the fluid dynamics of the T-joint, LES is used within the flow solver AVBP (Schoenefeld and Rudgyard, 1999). Series of data are time-averaged to produce the mean flow field, which is input to the acoustic solver. At this point it is noted that also Reynolds-averaged Navier-Stokes turbulence closures can be used under some limitations (Tam et al., 1995). However, in order to clearly validate the accuracy of LNSEs a much higher effort is undertaken in correctly predicting the mean flow field and shear layer dynamics.

The domain Ω is discretized using the same mesh configuration which is described in detail by Föller et al. (2010b). Overall, five million hexahedral cells are used. The spatial and temporal derivatives are approximated using a second-order Lax-Wendroff scheme and an explicit Euler scheme, respectively. Time marching is performed with a CFL number satisfying CFL<0.7.

The choice of subgrid scale model has a significant effect on the dynamics of the shear layer and the near-wall structures (see Fureby and Grinstein, 2002). The results of Bogey and Bailly (2005), using a dynamic Smagorinsky model, suggest that this subgrid scale model is overly diffusive and artificially decreases the Reynolds number. Therefore, again the effect of the unresolved scales is modeled via the WALE approach by Nicoud and Ducros (1999), which should better represent boundary and shear layers.

For the inflow velocity boundary condition turbulent profiles, experimentally measured by Zagarola and Smits (1998), are prescribed. A velocity inlet is also assumed for the side branch boundary with a bias flow velocity set to zero. Walls are adiabatic and no-slip conditions are used. The fluid dynamic boundary layer is fully resolved below dimensionless radii of the pipe section of $r^+ \approx 5$. At the outflow boundary of the main pipe a pressure outlet is applied. Fig. 5.9 shows the result of the time averaged LES over 0.3 s axial flow velocity distribution.

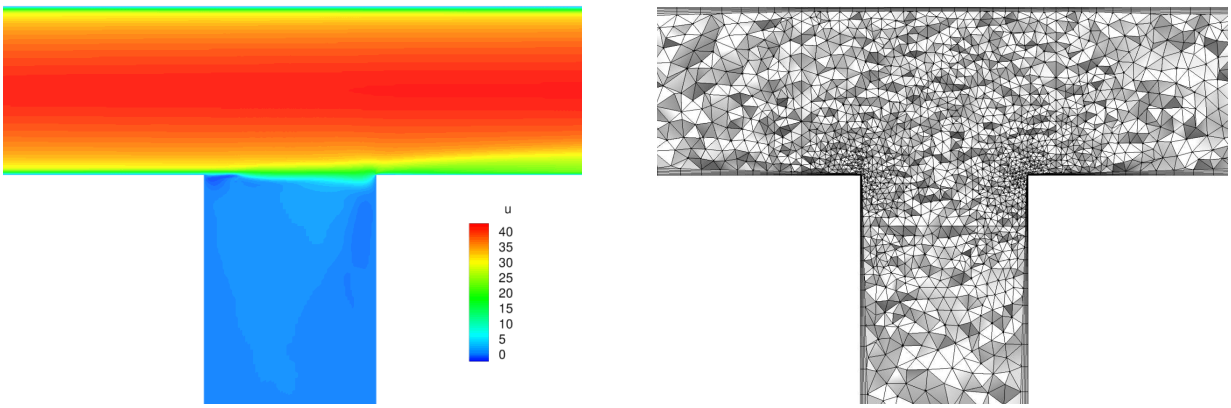

Figure 5.9: Inputs to the acoustic LNSEs solver, left: mean axial velocity $\bar{u}_x$ of grazing T-joint flow, right: unstructured acoustic mesh consisting of tetrahedral and hexahedral finite elements.

5.3.3 Scattering Matrix

The LNSEs are solved up to 3000 Hz using a discrete frequency step of Δf =100 Hz. Geometry and flow conditions are highly three dimensional and the LNSEs are therefore formulated in a Cartesian coordinate system in three dimensional space. The computational domain Ω is discretized using approximately 280.000 tetrahedral and hexahedral elements and second order Lagrangian interpolation functions, yielding a total number of 2.1 million degrees of freedom N_{dofs}. Four layers of hexahedral elements are used to discretize the fluid dynamic boundary layer. Regions of separation edges at the intersection of main and side branch are rigorously refined in order to capture the flow separation accurately. The acoustic mesh is displayed in Fig. 5.9. The GLS- stabilization finite element scheme is employed. However, test runs using the SUPG approach have shown similarly accurate results. The resulting large system matrix is inverted for discrete frequencies, using the proposed Krylov subspace solver GMRES-GMG of Section 4.5.2.

The result of the scattering matrix is plotted versus the Strouhal number defined in Karlsson and Åbom (2010), providing best comparability between experimental and numerical configuration,

$$St = \frac{f d_{\text{eff}}}{u_{\text{vc}}}, \tag{5.10}$$

where u_{vc} is the convective velocity of the shear layer disturbance and approximated as $0.45 Ma\bar{c}$, and $d_{\text{eff}} = \pi/4$ is the effective diameter of the joint.

Results of the amplitudes of scattering matrix coefficients, Eq. (5.9), as well as the respective arguments are illustrated in Fig. 5.10 and 5.11. The results can be differentiated in three different Strouhal number ranges. For small Strouhal numbers $St < 0.5$, all coefficients tend to a quasi-stationary response. This corresponds to the operability region of devices such as Helmholtz-resonators, where the area of intersection is of much smaller dimension compared to the main duct. The LNSEs manage to capture this trend with relatively high accuracy.

For $0.5 < St < 2.5$, hydrodynamically unstable modes appear inside the flow at integer multiples of the Strouhal number (Karlsson and Åbom,

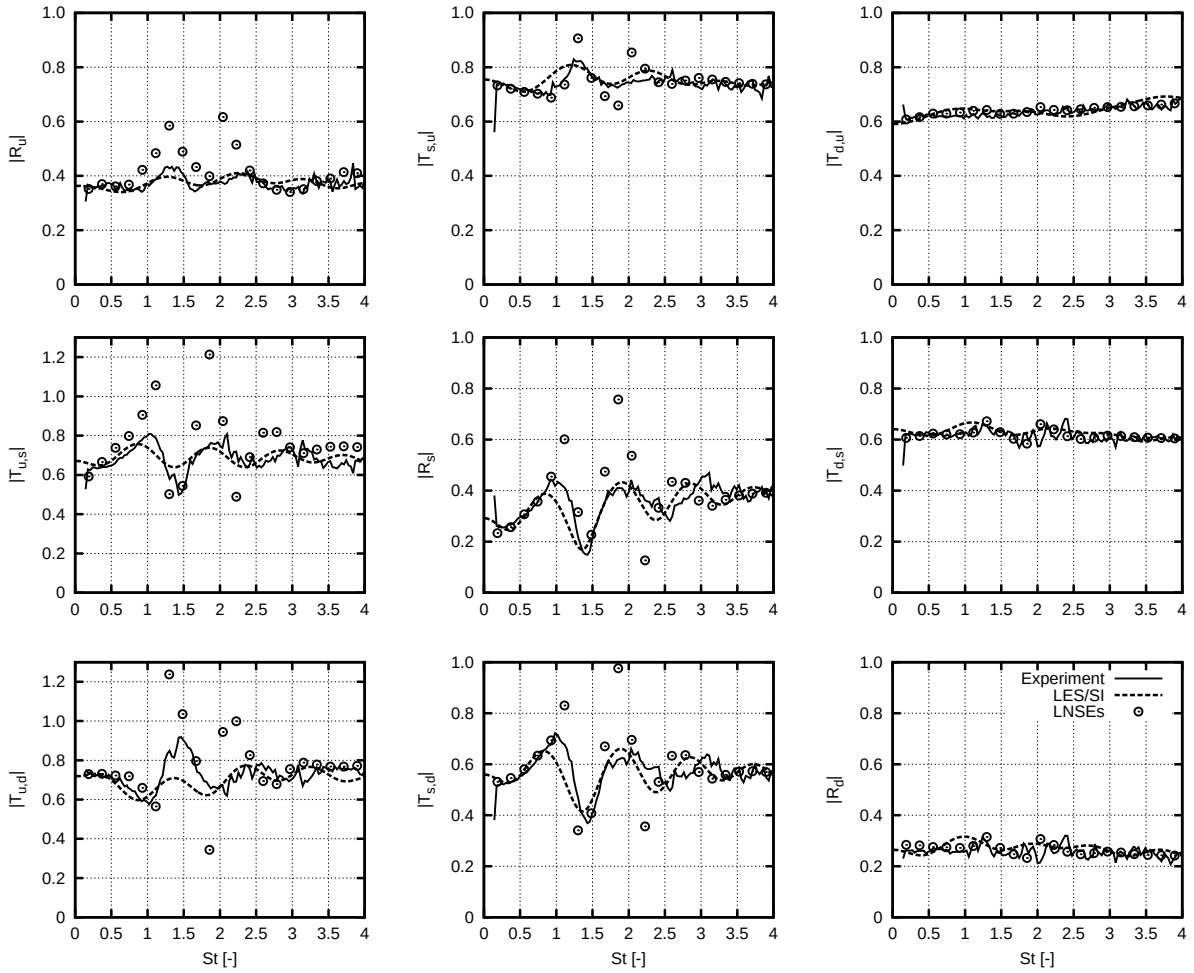

Figure 5.10: Amplitudes of scattering matrix coefficients, Eq. (5.9), of a sharp edged T-joint at $Ma = 0.1$ versus Strouhal number. Results of LNSEs are compared to the experimental data of Karlsson and Åbom (2010) and to the results of the LES/SI approach of Föller et al. (2010b).

2010; Meissner, 2002) and the reflection and transmission coefficients show a highly oscillatory behavior. Bruggeman (1987) shows that this is related to the position of the vortex during the acoustic cycle and the explicit distribution of vorticity. In order to describe the obtained results more thoroughly, we differentiate between the three cases of excitation from upstream ($R_u, T_{u,s}, T_{u,d}$), from the side branch ($T_{s,u}, R_s, T_{s,d}$) and from downstream ($T_{d,u}, T_{d,s}, R_d$) direction. In the first and second case scattering matrix coefficients exhibit a strong frequency dependance, whereas in the case of downstream excitation no pronounced dependance is observed. The mechanism leading to this effect is the same for upstream and side branch excitation cases and is explained by the above described feedback loop. However, the

situation is different when exciting from downstream direction: Acoustic waves are already scattered at the downstream edge and reach the upstream separation edge only indirectly, leading to smaller triggering of the hydrodynamic instabilities and thus lower aeroacoustic interactions. Using a model for the vortex distribution derived by Bruggeman (1987) and Howe's model of Eq. (2.58), a model for the limiting Strouhal numbers, for which the high reflection and transmission coefficients are observed may be derived following Meissner (2002):

$$St + \tan^{-1}\left(\frac{1}{St}\right) = 2n\pi \pm \frac{\pi}{2}, \tag{5.11}$$

where n is a certain mode number which is defined as the ratio of the convective travel time, τ, of the vortices from one edge to the other and the acoustic oscillation period T. The travel time can be approximated by $\tau = d/\bar{u}$. Indeed for this Strouhal number range, this relatively simple formula very well describes the ranges for which self-sustained oscillations may occur.

The LNSEs clearly manage to predict the oscillatory trend of scattering and transmission coefficients of the T-joint correctly. Especially, the frequencies of the amplification and attenuation of acoustic sound are captured by the linear approach, taking the discrepancies in the mean flow field into consideration. However, the finite magnitudes reached by the experiment are significantly over predicted, especially of the upstream and side branch excitation cases. The linear model predicts a stronger aeroacoustic interaction which is unphysical. This can be explained through following hypothesis: In general, shear layers feature two different flow regimes. After separation, a laminar shear layer is formed, which may itself be subdivided in a stable and a potentially unstable region. In latter region small disturbances may be exponentially amplified. After a critical Reynolds number is reached a laminar-turbulent transition takes place and a fully turbulent region follows (Schlichting et al., 2006). A purely linear approach based on the LNSEs is able to describe the triggering process and exponential growth of the Kelvin-Helmholtz instability correctly, however as second order effects like turbulence are only incorporated through the mean flow field, the transition into the turbulence regime is not captured correctly. After having reached this transition point vortical structures will still be partially allowed to grow, whereas in reality the growth of such structures

is bounded by turbulence effects. Thus, if aeroacoustic interactions are not confined to the region of laminar shear layer growth but extend into the region of the turbulent shear layer, the acoustic interaction with vortical structures will be over predicted by the linearized Navier-Stokes equations due to the stronger vortex structures. That aeroacoustic interactions are taking place in the complete cross-section is most likely the case for the T-joint (see Bruggeman, 1987; Hofmans, 1998).

This reasoning also provides an explanation for the fact that aeroacoustic interactions in an area expansion and an orifice were predicted with higher accuracy. There, most probably, the aeroacoustic interactions are confined to the laminar regime of linear growth of Kelvin Helmholtz instabilities, where the LNSEs are still valid and most accurate. This finding is supported by many authors, who state that the aeroacoustic interactions, e.g. for the area expansion, happen in close proximity to the separation edge (Boij and Nilsson, 2003, 2006). This may also explain the deviations between LNSEs and LEEs for the orifice configuration of Section 5.2. Although nearly full agreement is observed in the complete frequency range, at Strouhal numbers where the highest aeroacoustic interaction was observed, LEEs over predict the sound generation through flow coupling. As LNSEs include viscous effects, growth of vortical structures is partially bounded by laminar viscosity which may extend the range of validity of the approach. This will enable the LNSEs to better describe the interaction phenomena, but only to some limited extend. Viscosity may have an effect on the growth of vortical structures already in a laminar flow regime. Thus, in order to improve aeroacoustic predictions in Strouhal number ranges where Kelvin-Helmholtz instabilities occur it is slightly more advantageous to consider LNSEs instead of LEEs.

In the region beyond $St > 2.5$, the oscillatory behavior decays significantly and again a quasi-stationary response can be observed. In this region, the vortices interact multiple times with acoustic waves during their convection time to the downstream edge and acoustic cancellation effects become significant. Magnitude as well as trend are captured with relatively good agreement by the LNSEs.

Phase angles of the reflection coefficients are shown in Fig. 5.11. Despite of the large disagreement in magnitudes of scattering coefficients at the fre-

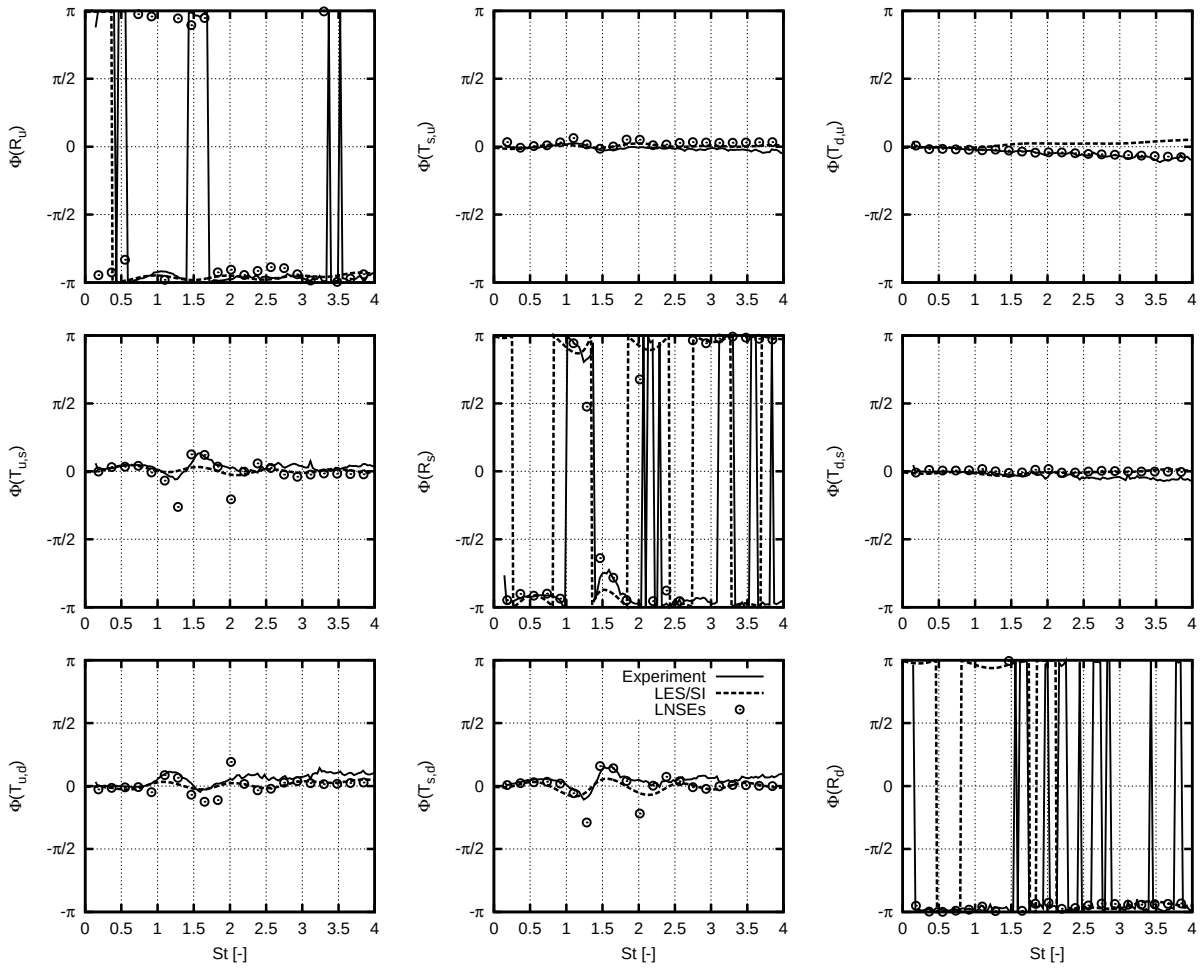

Figure 5.11: Phase angles of scattering matrix coefficients, Eq. (5.9), of a sharp edged T-joint at $Ma = 0.1$ versus Strouhal number. Results of LNSEs are compared to the experimental data of Karlsson and Åbom (2010) and to the results of the LES/SI approach of Föller et al. (2010b).

quencies where hydrodynamic instabilities appear the respective arguments are captured by the LNSEs with higher agreement in the complete frequency range. Phase angles are close to values of 0 or $\pm\pi$ and vary in regions where strong acoustic flow coupling occurs. Generally, a phase shift can be observed when maxima and minima of the respective scattering coefficient amplitudes are reached. Solely points of discrete maxima and minima are again over predicted.

A comparison with the LES/SI technique of Föller et al. (2010b) shows that the higher order approach yields much more accurate results in this case. Especially magnitudes of reflection and transmission coefficients are captured in higher detail than the linear models. This shows that when the turbulence effect on the vortical scales is captured correctly, also the magnitude of the coefficients can be captured.

5.3.4 Acoustic Power Conservation

Karlsson and Åbom (2010) show that amplification or attenuation effects can be studied by observing the averaged power ratios $\langle W \rangle_i$ of outgoing to ingoing acoustic power for each reflection or transmission coefficient. These can be calculated from the passive scattering matrix data, Eq. (5.9),

$$\begin{pmatrix} \frac{\langle W\rangle_{\hat{p}_u^-}}{\langle W\rangle_{\hat{p}_u^+}} & \frac{\langle W\rangle_{\hat{p}_u^-}}{\langle W\rangle_{\hat{p}_s^+}} & \frac{\langle W\rangle_{\hat{p}_u^-}}{\langle W\rangle_{\hat{p}_d^-}} \\ \frac{\langle W\rangle_{\hat{p}_s^-}}{\langle W\rangle_{\hat{p}_u^+}} & \frac{\langle W\rangle_{\hat{p}_s^-}}{\langle W\rangle_{\hat{p}_s^+}} & \frac{\langle W\rangle_{\hat{p}_s^-}}{\langle W\rangle_{\hat{p}_d^-}} \\ \frac{\langle W\rangle_{\hat{p}_d^+}}{\langle W\rangle_{\hat{p}_u^+}} & \frac{\langle W\rangle_{\hat{p}_d^+}}{\langle W\rangle_{\hat{p}_s^+}} & \frac{\langle W\rangle_{\hat{p}_d^+}}{\langle W\rangle_{\hat{p}_d^-}} \end{pmatrix} = \begin{pmatrix} \frac{(1-M)^2}{(1+M)^2}|R_u|^2 & (1-M)^2|T_{s,u}|^2 & |T_{d,u}|^2 \\ \frac{1}{(1+M)^2}|T_{u,s}|^2 & |R_s|^2 & \frac{1}{(1-M)^2}|T_{d,s}|^2 \\ |T_{u,d}|^2 & (1+M)^2|T_{s,d}|^2 & \frac{(1+M)^2}{(1-M)^2}|R_d|^2 \end{pmatrix}. \tag{5.12}$$

As the Mach number is included into the expressions, the convective effect of the mean flow on the wave propagation is taken into account. To analyze whether acoustic energy is absorbed or produced, the power ratios of the specific scattering matrix can be summed up, assuming boundary reflection coefficients at $\partial\Omega_Z$ to be zero. These are defined as the power ratios which are based on the same ingoing acoustic waves $\hat{p}_u^+$, $\hat{p}_s^+$ or $\hat{p}_d^-$:

$$\left.\frac{\langle W\rangle_{out}}{\langle W\rangle_{in}}\right|_I = \frac{\langle W\rangle_{\hat{p}_u^-}}{\langle W\rangle_{\hat{p}_u^+}} + \frac{\langle W\rangle_{\hat{p}_s^-}}{\langle W\rangle_{\hat{p}_u^+}} + \frac{\langle W\rangle_{\hat{p}_d^+}}{\langle W\rangle_{\hat{p}_u^+}}, \tag{5.13}$$

$$\left.\frac{\langle W\rangle_{out}}{\langle W\rangle_{in}}\right|_{II} = \frac{\langle W\rangle_{\hat{p}_u^-}}{\langle W\rangle_{\hat{p}_s^+}} + \frac{\langle W\rangle_{\hat{p}_s^-}}{\langle W\rangle_{\hat{p}_s^+}} + \frac{\langle W\rangle_{\hat{p}_d^+}}{\langle W\rangle_{\hat{p}_s^+}}, \tag{5.14}$$

$$\left.\frac{\langle W\rangle_{out}}{\langle W\rangle_{in}}\right|_{III} = \frac{\langle W\rangle_{\hat{p}_u^-}}{\langle W\rangle_{\hat{p}_d^-}} + \frac{\langle W\rangle_{\hat{p}_s^-}}{\langle W\rangle_{\hat{p}_d^-}} + \frac{\langle W\rangle_{\hat{p}_d^+}}{\langle W\rangle_{\hat{p}_d^-}}. \tag{5.15}$$

In case a sum exceeds unity, energy of the vortical mode is transferred to the acoustic mode and hence more acoustic power is emitted from the

system than is introduced. Values below unity indicate acoustic energy absorption. The assumption of low acoustic reflection is valid for the current computations, as the acoustic reflection coefficients do not exceed an value of $R \leq 0.02$. Thus, the sum over the power ratios of a certain excitation case represent the acoustic power absorbed or produced well.

Figure 5.12 shows the computed acoustic power ratios of Eqs. (5.13)-(5.15) which correspond to the different excitation case I-III. The LNSEs predict a significant overproduction for incident acoustic wave amplitudes $\hat{p}_u^+$ and two maxima are predicted instead of one in the experiments. The sum of power ratios for an acoustic wave amplitude $\hat{p}_s^+$ (case II) exhibits a slightly higher agreement with the experiments. Generally, the frequency ranges for which acoustic energy amplification ($P_s > 1$) or acoustic energy attenuation ($P_s < 1$) is present are predicted correctly by the LNSEs. However, the magnitudes of the acoustic power ratios are significantly over or under predicted indicating an overly amplifying or dissipating behavior of the LNSEs. This supports the fact that most probably the vortex strength is over predicted and therewith the interaction described through the integral in Eq. (2.58). The best agreement is again reached for case III.

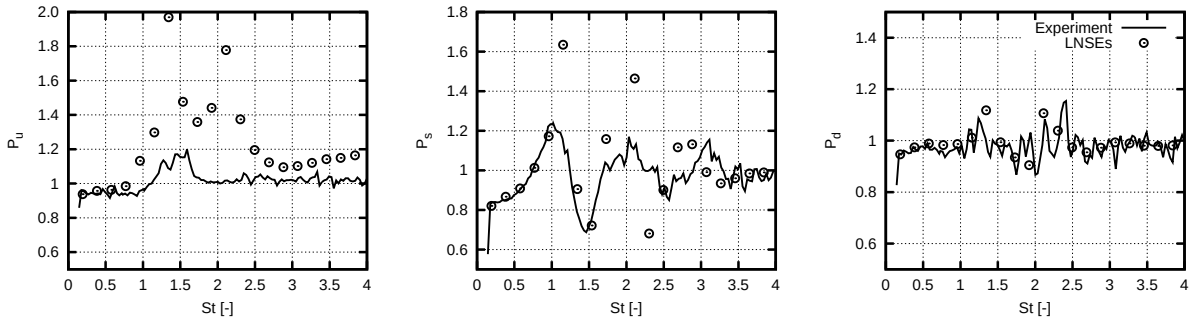

Figure 5.12: Sums of acoustic power ratios, Eq. (5.13)-(5.15) of a sharp edged T-joint at $M = 0.1$ versus Strouhal number. Results of LNSEs are compared to the experimental data of Karlsson and Åbom (2010).

5.4 Non-Reactive Swirler Nozzle

Chapter 5 is structured in a way to increase the understanding of the underlying acoustic-flow interaction phenomena step by step, considering validation test cases with increasing complexity. This consequently leads to

the study of acoustic interaction processes with a three dimensional and highly complex flow field created by an industrial injection system. The configuration includes an area expansion where the fluid discharges into the combustion chamber. It includes flow contractions such as the orifice configuration, e.g. the swirler vane channels, and due to the strong radial momentum of the swirling fluid motion vortices may impinge onto wall surfaces providing a possible acoustic feedback.

The swirl nozzle is mounted at the end of a circular plenum with diameter d_u and length l_u. The nozzle connects the plenum to the combustion chamber (CC), which is square in cross-section. It has a total axial length of l_d and side wall length of l_c. The nozzle investigated is a partially evaporation rapid mixing (PERM) injection system, developed by Avio S.p.A. (see e.g. Marinov et al. (2010)). In detail, it consists of two co-rotating swirl channels and a centered injector. As the fluid passes through the nozzle circumferential momentum is imposed. At its exit, the flow expands into the combustion chamber and inner and outer recirculation zones are formed. Fig. 5.14 illustrates the complexity of geometry and flow conditions.

The chosen test conditions correspond to two different inlet flow temperatures at a constant air mass flow rate. In the first Case A, ambient air temperatures are used. Then the air is preheated in Case B to more realistic engine inlet conditions of $\bar{T}_{in} = 573.15\,\mathrm{K}$. Consequently, inlet Mach and Reynolds number vary with the inlet temperature. The geometrical and flow conditions are gathered in Tab. 5.4.

The mean flow fields necessary for the acoustic analysis are supplied using a standard k-ϵ turbulence closure model proposed by Launder and Spald-

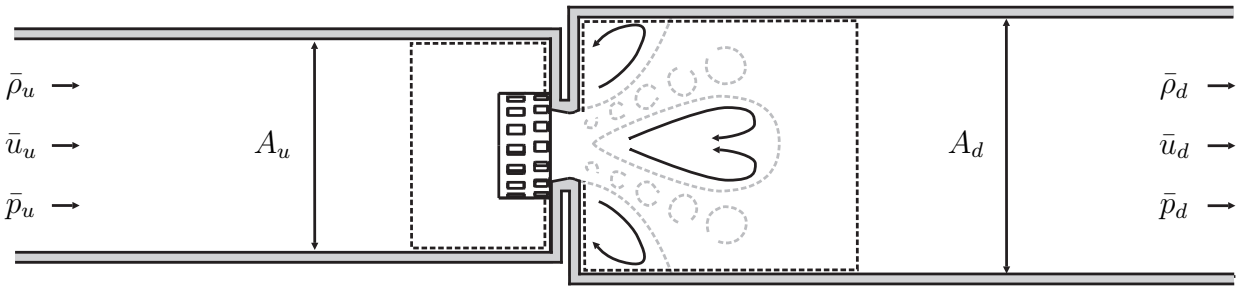

Figure 5.13: Schematic presentation of the geometry and flow conditions of the atmospheric pressure test rig including an industrial swirl nozzle, inner and outer recirculation zones are also shown.

Table 5.4: Geometrical and physical operating conditions of the non-reactive swirl injector flow.

Description	Variable	Case A	Case B
upstream pipe diameter	d_u	0.1245 m	
downstream edge length	l_d	0.15 m	
upstream pipe length	l_u	1.34 m	
downstream length	l_d	0.890 m	
inlet temperature	$\bar{T}_{in}$	293.15 K	573.15 K
Mach number at inlet	Ma_{in}	0.007	0.01
Reynolds number at inlet	Re_{in}	1.96×10^4	1.22×10^4
kinematic viscosity	ν	$1.55{\times}10^{-5}\,\mathrm{m^2\ s^{-1}}$	$5.012{\times}10^{-5}\,\mathrm{m^2\ s^{-1}}$

ing (1972). All free calibration constants are chosen accordingly. The use of k-ϵ models in aeroacoustic applications is not new and has been applied to study scattering matrices of generic configurations (Kierkegaard et al., 2012a,b) but also e.g. for the prediction of jet noise problems or outlet impedances (Bailly et al., 1996; Jörg et al., 2013; Khavaran et al., 1994). The unstructured computational mesh comprises overall 1.8 million elements. Tetrahedral elements are used to discretize the complex features of the swirl nozzle while hexahedra elements are used for the nozzle exit as well as the combustion chamber and plenum sections. Special care is taken for discretization of the shear layer separation point at the atomizer lip, its expansion and the outer diameter of the nozzle diffusor. Second order upwind schemes are employed for the momentum and energy equation.

For the fluid dynamic simulations a mass flow is prescribed at the inlet while at the outlet an ambient pressure level is imposed. Parameters of turbulence production k and dissipation ϵ at the inlet are simply calculated by assuming turbulence levels and a length scale. However, due to the long plenum section turbulence parameters are able to develop until they reach the injector nozzle. The influence of the wall is incorporated through the definition of wall functions for the momentum and energy equation. For the simulations with preheated air, the plenum walls are believed to be adiabatic due to their insulation. The combustor walls, however, are air cooled and are therefore assumed non-adiabatic by prescribing a constant wall temperature. Its specific value is determined iteratively until the sim-

ulated outlet combustor temperature is equivalent to its measured value. It was believed that the axial impedance distribution along the combustion chamber may have an influence on the acoustic scattering behavior.

Using the mean flow fields from the RANS computations, the LNSEs defined in a cartesian coordinate system are solved for a discrete frequency range of 25-800 Hz with a resolution of Δf =25 Hz. The computational domain is discretized using roughly 230.000 tetrahedral elements while second order Lagrangian test functions are selected. Regions of flow separation and shear layer expansion are refined as shown in Fig. 5.15. A GLS- finite element stabilization technique introduced by Franca et al. (1992) is chosen for the presented test case in order to better account for reactive terms in the LNSEs. In terms of degrees of freedom (N_{dofs}), the acoustic mesh comprises only a fraction of 30 percent of N_{dofs} compared to the RANS computation. Grid independence is ensured by varying the grid size for a single frequency.

Acoustic boundary conditions are chosen equally to all aforementioned validation test cases. Due to the large size of the system matrix, the developed GMRES-GMG algorithm is used herein to solve the resulting linear set of LNSEs for every distinct frequency. The algorithm is highly efficient and additionally allows parallelization yielding computation times of around 30 minutes per frequency. This time span comprises the solution of one matrix inversion problem. The simulations are performed on a desktop machine using overall eight cores.

The same flow fields computed in this section will be used in the following Chapter 6 to analyze the eigenfrequencies of the combustion chamber flow under non-reactive conditions.

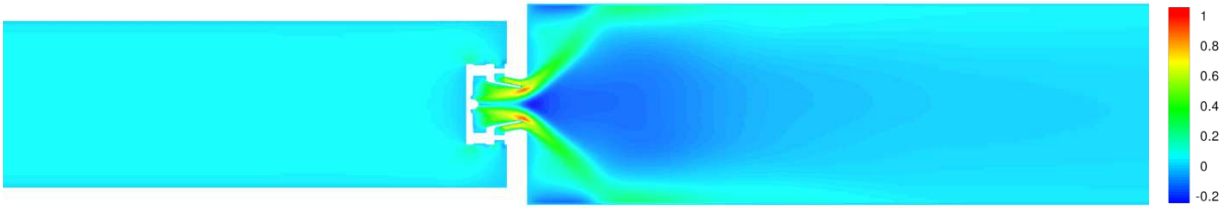

Figure 5.14: Normalized mean axial flow velocity field $\bar{u}/\bar{u}_{max}$ of mean flow field computations of Case A at ambient inflow temperatures.

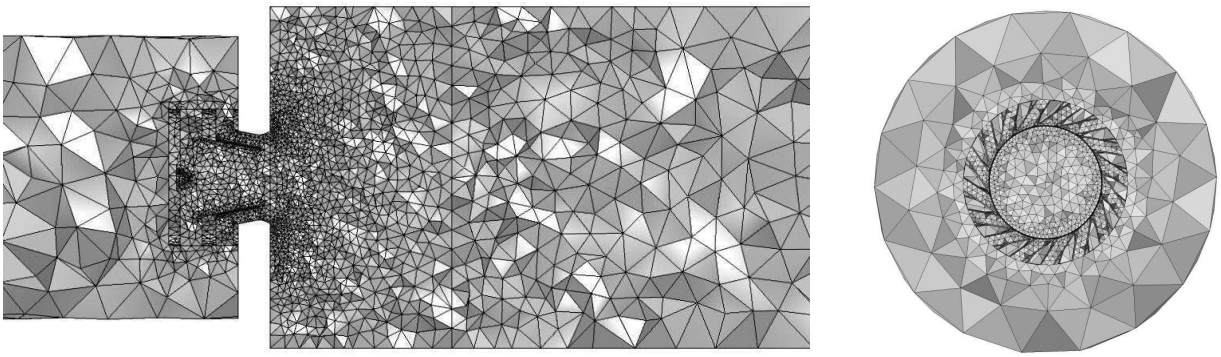

Figure 5.15: Three dimensional unstructured grid of the non-reactive combustion chamber flow configuration used for the acoustic computations, slice through the mid plane (left) and view on the discretization close to the nozzle outlet (right).

5.4.1 Experimental Measurements

The experimental measurements are performed at the atmospheric combustion test rig originally designed by Eckstein (2004). A detailed description of the main components can be found therein. In a later study the same test rig is used for the measurements of flame transfer matrices (Alemela, 2009). It has been found that the FTFs measured at a single combustion chamber test rig are not comparable to the FTFs measured at an annular combustion chamber (Fanaca et al., 2010). In order to meet scalability of the FTFs, the authors propose a design rule for the area expansion. Therefore, a new combustion chamber having a greater cross section is designed fulfilling the general guideline proposed. In the course of the present study this configuration is optimized for the measurement of scattering matrices.

The two-source method, introduced by Munjal and Doige (1990b), is applied to determine the experimental scattering matrices. The technique works very similarly to the numerical simulations performed using LNSEs and requires two independent acoustic states in order to construct a scattering matrix. This is achieved by harmonically exciting the inlet air flow using a siren configuration. A fraction of around 35 percent of the inlet air mass flow is excited, whereas the other fraction bypasses the siren. Then, the pulsating air flows through a 1.2 m long plenum section. At three consecutive locations along the duct, air temperatures are measured. A series of three dynamic pressure transducers of type PCB-J106B are mounted about

$8d$ away from the injector configuration where d denotes the outlet diameter of the nozzle. The pressure transducer distances from one another are chosen non-uniformly following the general guideline of Bodén and Abom (1986). After the air passes through the swirl nozzle, the flow expands into a square combustion chamber. Windows on either side allow visual access. About $10d$ further downstream of the combustion chamber inlet plane, a second series of three dynamic pressure transducers is positioned. Their consecutive distances are chosen irregularly in accordance with the upstream measurement section. At the outlet of the downstream measurement section a perforated screen is mounted yielding reflection coefficients of about $R \approx 0.6$ for the considered frequency range. An exhaust gas system collects the air mass flow at the outlet.

The second acoustic state is constructed by mounting a siren to the downstream end of the combustion chamber. It periodically injects fresh air in the circumference direction. When the downstream siren is employed the upstream siren is solely bypassed. To ensure linear behavior of the scattering matrix coefficients, it is verified that the velocity fluctuations at the nozzle outlet do not exceed $|\hat{u}_{ref}|/\bar{c} < 0.1$. This is done by extrapolating the acoustic signals measured in the downstream combustion chamber section to the nozzle outlet. Acquisition times are chosen to be of 12 s per frequency at a sampling rate of 16 kHz to ensure statistical convergence. Calibration of the pressure transducers is performed before and after measurements.

The frequency range considered in the experiments is 100-800 Hz. It is noted that the experimental measurements face limitations in the low frequency limit. This is due to high reflection coefficients at inlet and outlet boundaries ($R \sim 1$). Then, the two acoustic states become linearly dependant and the two-source method breaks down. Moreover, due to the special characteristic of the considered spray atomizer nozzle only low amounts of acoustic energy are transmitted to the upstream and downstream sections, respectively. Considering the high turbulent noise levels of the flow the signal to noise ratio may degrade. This is especially of a concern when exciting with the downstream siren which has a low acoustic power. The high frequency limit is bounded by the operability range of the available infrastructure.

5.4.2 Scattering Matrix

For a broad range of frequencies up to 800 Hz, the results of the scattering matrix coefficients are shown in Fig. 5.16. Amplitudes and phases are plotted against frequency f. Blue and red symbols denote the conditions of Case A and Case B respectively. In the low frequency limit $f \to 0$, the transmission and reflection amplitudes seem to tend towards similar values for both excitation cases. Between $0\,\text{Hz} < f < 200\,\text{Hz}$ in the cold flow Case A and between $0\,\text{Hz} < f < 400\,\text{Hz}$ in Case B, the amplitude scattering coefficients show distinct Strouhal number characteristics which are a result of acoustic-flow interaction processes. Beyond that ($f > 200\,\text{Hz}$ and $f > 400\,\text{Hz}$, respectively), the transmission coefficients T^+ and T^- decrease and the reflection coefficients R^+ and R^- increase steadily for both considered cases showing a quasi-steady trend.

The scattering matrix coefficient phases Φ are also shown in Fig. 5.16. There, a similar characteristic is observed: A sharp frequency shift at a distinct frequency. In the region before the shift we observe constant phase levels. In the region after the shift, phases for the reflection $\Phi(R)$ and transmission coefficients $\Phi(T)$ show a steady growing or decreasing trend.

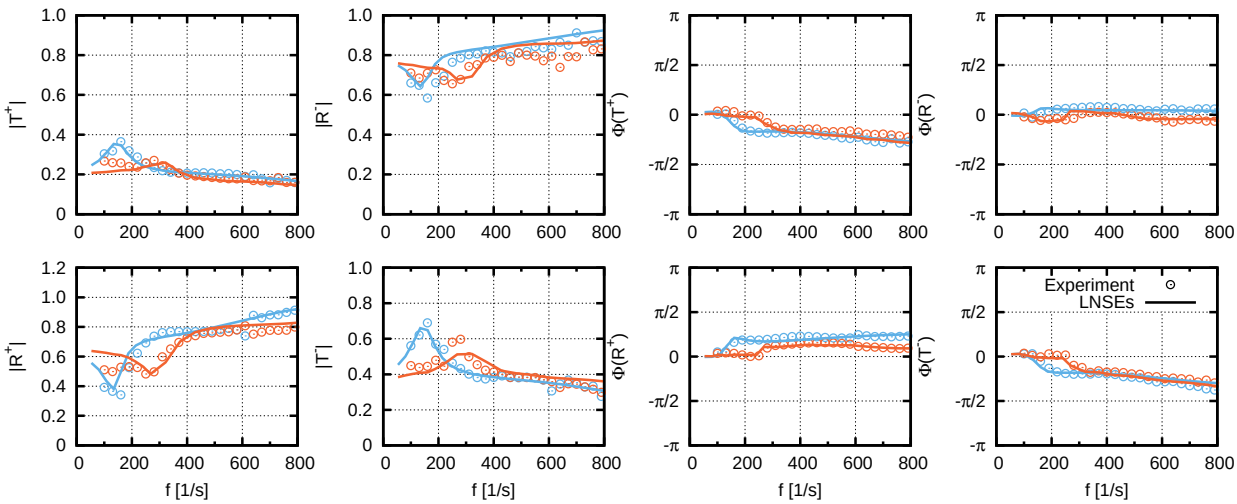

Figure 5.16: Scattering matrix coefficients of non-reactive confined swirling flow at atmospheric (—) and elevated inlet temperatures (—), experiments are plotted in comparison to the result of LNSEs, amplitudes of scattering matrix coefficients (left) and their respective arguments (right).

The comparison of the LNSEs results with the experimental data clearly demonstrates that the approach accurately captures the acoustic scattering behavior of a flow field generated by an industrial injection system. Acoustic-flow interaction phenomena in the low frequency range as well as constantly increasing and decreasing amplitudes are captured with relatively high accuracy. Phase shifts of the reflected and transmitted planar waves are equally well predicted. Small discrepancies are observed predicting the location of peaks for the reflection amplitudes. This is attributed to inaccuracies in the fluid dynamic field.

Acoustic-flow interaction processes are further illustrated in Fig. 5.17 for three distinct frequencies of 150 Hz, 400 Hz and 800 Hz of the cold flow Case A. The first chosen frequency corresponds to the range where acoustic-flow interactions seem to be more pronounced. Fields of pressure and velocity

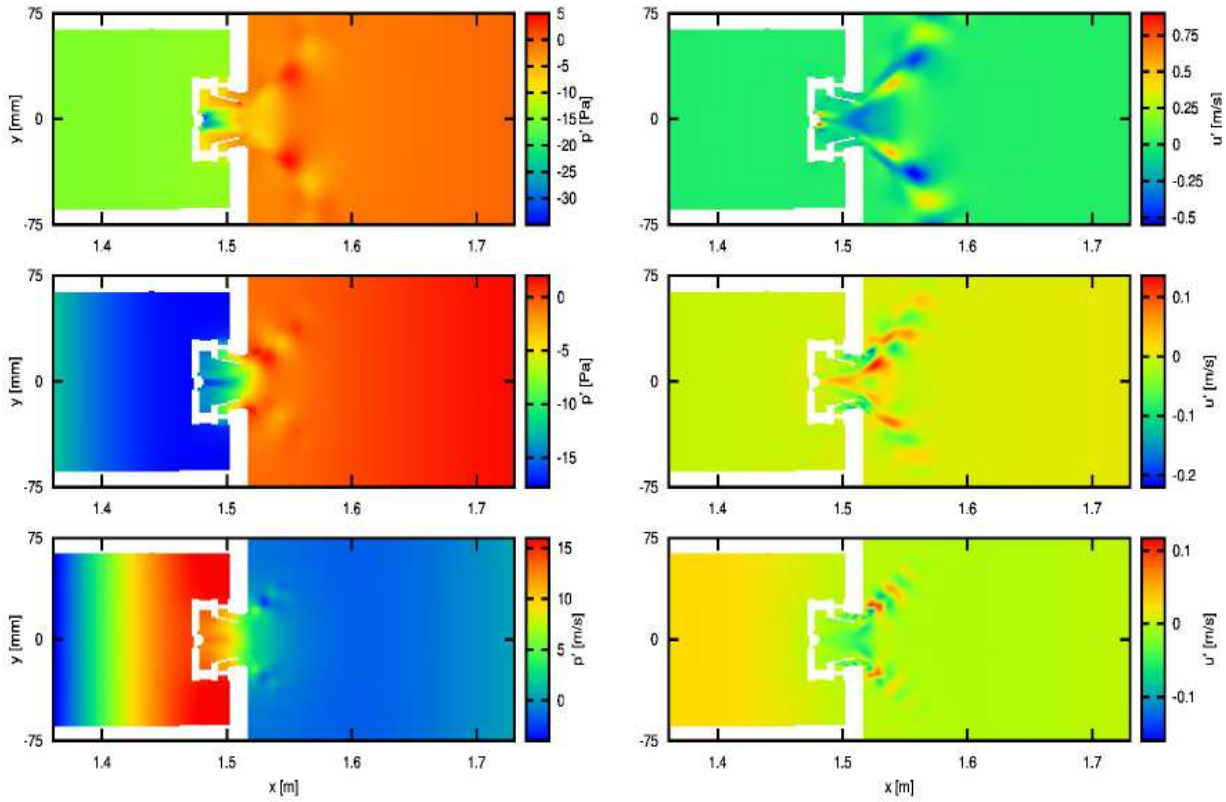

Figure 5.17: Acoustic fields of perturbed pressure p' (left) and velocity u'_x (right) at different frequencies of upstream excitation f =150 Hz, 400 Hz and 800 Hz from top to bottom, respectively.

fluctuations are shown in the left and right column, respectively. For all three frequencies it is clearly visible how vortical structures are excited in the burner mouth and travel along the shear layer. These vortical structures impinge onto the combustion chamber walls for low frequencies. By comparison of the magnitudes of the velocity fluctuations at the three frequencies it can be observed that highest vorticity amplitudes are reached for the 150 Hz case, which is exactly the frequency where strong variations in the scattering matrix coefficients are observed. Thus, in the small frequency range higher acoustic-flow interactions are observed. In the next section the effect of these vortical structures on the acoustic loss generation potential is shown.

It is interesting to note that despite the fact that RANS models tend to misspredict swirling flows with high radial pressure gradients, the acoustic scattering behavior using RANS computed mean flow fields is captured with relatively high accuracy by the LNSEs. Many publications, see e.g. Boij and Nilsson (2006); Munt (1977), suggest that the important acoustic-flow interaction phenomena happen in close proximity of flow separation edges (for an area expansion). As our employed RANS model uses calibration constants measured for flow separation cases, we may assume that this phenomenon is captured in relatively high detail by the turbulence model.

5.4.3 Acoustic Loss Margins

As already described, the scattering matrix contains valuable information of the system's potential damping behavior. A method to access this information from the already known scattering matrix coefficients has been introduced for the orifice configuration in Section 5.2.2 and is based on the ideas of Aurégan and Starobinski (1999). The experimental and numerical data is post-processed to obtain the values of ξ_{min} and ξ_{max} which define the margins of dissipated acoustic power to incident acoustic power, see Eq. (5.8).

The values ξ_{min} and ξ_{max} are plotted in Fig. 5.18 over frequency for both flow conditions investigated. In the complete frequency range solely acoustic damping is observed which is confirmed by positive values of ξ_{max} and a ξ_{min} close to zero. At low frequencies, ξ_{max} shows a relatively constant trend.

However, between 150 Hz $\leq f \leq$ 300 Hz for case A and 300 Hz $\leq f \leq$ 450 Hz for case B, values of ξ_{max} abruptly start to decrease and a constant negative slope is observed. The slope of the curve then changes again towards higher frequencies. For the frequency range considered, the swirl nozzle behaves very similar to an orifice configuration shown in Fig. 5.6 in the sense that both configurations damp acoustic waves in the low frequency limit.

LNSEs manage to accurately predict the margins ξ_{min}, ξ_{max} in magnitude as well as trend for both Cases A and B. Solely a slightly lower ξ_{min} is observed compared to the experiments. If the additional information about the damping potential is considered when observing Fig. 5.17, it is evident that highest magnitudes of vortical structures (at 150 Hz) transfer to high amounts of acoustic damping potential.

The severe misprediction of frequency regions of strong acoustic-flow coupling, found for the T-joint case, cannot be observed for the injection system flow field. The scattering matrix of Fig. 5.16 and damping potential of Fig. 5.18 illustrate this statement convincingly. As it seems, the aeroacoustic interactions take place in flow regimes of the shear layer which may be purely described by the linear model. Thus, the aeroacoustic feedback loop described in Section 5.3 is indeed represented correctly. However, the configuration does not exhibit strong Kelvin-Helmholtz instabilities as observed in the cases of the orifice and the T-joint. A similarity which is shared with

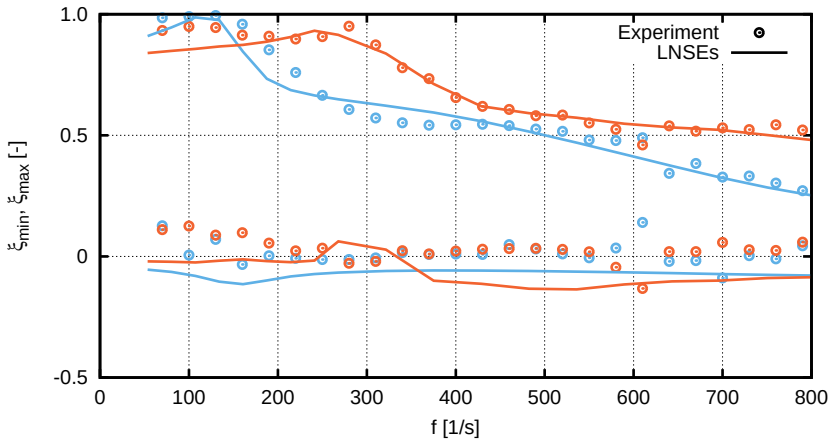

Figure 5.18: System's damping potentiality (ξ_{min}, ξ_{max}) plotted against frequency, experiments are compared to the results the LNSEs computations for the two cases of ambient inlet temperatures (—) and elevated temperatures (—).

the area expansion test case. In the frequency range considered, both systems purely damp acoustic energy and a high agreement with experimental data is achieved.

The high amounts of acoustic loss potential observed in the low-frequency regime stresses the fact that numerical models incorporating the conversion process between acoustic and vortical structures are essential to reliably predict low frequency instabilities. Similarly, information about acoustic losses is generally needed to predict magnitudes of saturation amplitudes, as flame saturation occurs when the energy input of the flame is in balance with acoustic field and boundary losses.

5.5 Concluding Remarks

A hybrid method, a combination of a flow simulation including an appropriate turbulence closure and the frequency space LNSEs approach, is shown to be capable to determine the scattering matrix coefficients of a set of different flow configurations. It has been found that the acoustic loss mechanisms are captured in detail by the presented method. Such a method may be used in conjunction with a network modeling approach in order to assess certain network elements at relatively low costs compared to an experimental approach or a compressible LES. As it is shown in the case of the injection system, these elements may feature highly complex geometries and flow conditions which may not be accessible to analytical modeling.

However, the applicability limits of the LNSEs and LEEs approach are also shown in the case of the T-joint. There, it is illustrated that if strong Kelvin-Helmholtz instabilities appear in certain frequency bands, the linearized model approach fails to predicting the finite magnitudes of the scattering matrix coefficients observed in the experiments. Following the hypothesis made, the region of vortex formation and propagation through a stable laminar shear layer are well described, but in regions where the laminar shear layer gets unstable and promotes the growth of Kelvin-Helmholtz instabilities is not captured physically. The LNSEs predict an exponential growth of such flow instabilities only bounded by laminar viscosity. Thus, if the aeroacoustic interaction expands into this range, where non-linear phenom-

ena (like turbulence) limit the growth of disturbances, then the linear model will suffer from inaccuracies leading to an overly excessive prediction of the interactions between flow field and acoustic waves. The stronger the growth of Kelvin-Helmholtz instabilities, i.e. the more unstable such instabilities are, the earlier the point is reached where non-linear saturation mechanisms set in.

This finding inevitably leads to the discussion of the validity of the linear assumptions made. As found by Davis and Holland (2004) for practical applications, linear and non-linear models for the acoustic wave propagation in a duct only have negligible differences for amplitudes of 10% of the static pressure. Thus, even if the excitation signals in the experiments are not fully harmonic (e.g. for siren configurations), this may not explain differences in the results obtained. Also, in the configurations studied the authors largely estimated the influence of excitation amplitude on the scattering behavior and found the configurations to be fully in the linear regime (see Karlsson and Åbom (2010); Ronneberger (1987); Testud et al. (2009)). Therefore, we have to expect a localized non-linear behavior in the fluctuating field especially in the description of the growth of vortical disturbances which can be captured in the experiments but not with the current linearized approach. As shown, this behavior will depend on the particular case considered and, thus, is difficult to handle in a general fashion. Expansion of the approach to incorporate turbulence effects e.g. of Föller and Polifke (2012), however, will complicate the analysis and increase the computational costs significantly.

6 Global Stability Analysis

Although the isentropic assumption is not valid for multidimensional flow fields, see Eq. (2.11), the above studies have shown that the introduced errors are negligible for isothermal flow configurations. However, as soon as the heat release has an unsteady component ($\hat{q} \neq 0$) or a mean entropy gradient is present inside the flow ($\nabla \bar{s} \backsimeq c_p \nabla \bar{T}/\bar{T}$) the isentropic assumption is violated.

The main aim of this thesis is to address combustion instabilities. This necessitates not only a detailed analysis of the acoustic-vortical interaction processes, but must also include the description of acoustic-entropy coupling (Dowling, 1995; Nicoud and Wieczorek, 2009). This process is linked to an energy transfer from the acoustic to the entropy mode, leading to attenuation of combustor modes. Therefore, to take this interaction process into account, the isentropic assumption is discarded and the full set of LNSEs including the linearized energy equation are solved.

The reverse effect of energy transfer from the entropy spots back to the acoustic field is not considered in this thesis. This phenomenon is generally caused by acceleration of entropy spots inside the downstream vane passage (Cumpsty and Marble, 1977; Marble and Candel, 1977). The contribution of this effect to the thermoacoustic feedback loop as well as related noise emissions is subject to discussions in the literature (Polifke et al., 2001; Sattelmayer, 2003), as well as experimental (Bake et al., 2009) and numerical investigations (Leyko et al., 2009).

In this chapter the second methodology, presented in Section 3.3.6, of the eigenvalue analysis using LNSEs is validated. Since the unsteady behavior of the flame is now included, the solution algorithm requires not only the knowledge of the mean flow field, but also a model for the unsteady flame behavior, i.e. for $\hat{\dot{q}}_V$. In the presented test cases this is done by means of an analytical model or by incorporating an experimentally measured FTF function.

Note that when assuming non-isentropic wave propagation the grid requirement changes slightly. After coupling with the flame, entropy waves are generated which are convected downstream. These have similar wavelength as the vortical structures but, compared to the acoustic wavelength, are much shorter $\lambda_s = Ma\lambda_a$. However, unlike vortical structures which dissolve relatively quickly in expanding shear layers, this type of fluctuation is convected along larger distances throughout the combustor. Then, especially at small Mach numbers, the combustion chamber needs to be significantly refined.

The Helmholtz equation represents the zero Mach number limit when predicting stability of combustion systems. Using this scalar equation, a quadratic eigenvalue problem may be defined which can be solved using the same iterative routine as in Section 3.3.6. It is a kind of state-of-the art tool to predict thermoacoustic instabilities for complex three dimensional combustion chamber configurations (Gullaud and Nicoud, 2012; Nicoud et al., 2007; Selle et al., 2006). Here, it will be used to highlight differences to the developed LNSEs tool which takes mean flow effects into account. Details on the routine and finite element treatment are shown and explained in Appendix E.

6.1 Generic Premixed Combustion Chamber

A simple premixed combustor which is frequently used in the thermoacoustic society to validate network models is discussed next (Dowling, 1995). Its main advantage is that a huge number of different influencing parameters can be studied which are essential for the development of thermoacoustic tools like the one presented in this thesis.

As it will be shown a semi-analytical solution of the form of the matrix Eq. (2.30) can be retrieved. This dispersion relation is derived without taking viscous effects into account. Thus, in order to be consistent with the semi-analytical solution the LEEs are solved instead of LNSEs. This step is only performed for reasons of formality and simulations using LNSEs yield approximately the same results.

6.1.1 Configuration

The configuration considered is depicted in Fig. 6.1 and is a one dimensional duct of length L and constant cross section. The fresh gas in the left duct is separated from the hot gas by a thin flame sheet of thickness δ_f located in the middle of the duct. It is assumed that the flame causes a temperature jump from the hot-to-fresh gas side of $\bar{T}_d/\bar{T}_u$.

If assuming that the fresh gas enters the domain from the left boundary at a specific state, it is possible to derive equations representing the mean flow field in the complete generic combustion chamber. Doing so, we assume the static temperature to vary along both duct segments and in the anisentropic flame region in form of a hyperbolic tangent function, similar to Wieczorek and Nicoud (2010)

$$\bar{T}(x) = \frac{\bar{T}_d + \bar{T}_u}{2} + \frac{\bar{T}_d - \bar{T}_u}{2} \tanh\left(2\frac{x - x_f}{\delta_f/2}\right), \tag{6.1}$$

where x_f defines the mid point of the flame region. Then, the mean flow field may be calculated by assuming conservation of mass, momentum, and total temperature, i.e.

$$\bar{\rho}\bar{u} = \text{const.}, \tag{6.2}$$

$$\bar{p} + \bar{\rho}\bar{u}^2 = \text{const.}, \tag{6.3}$$

$$\bar{q} = c_p \bar{\rho}\bar{u}\frac{d\bar{T}_t}{dx}, \tag{6.4}$$

where $\bar{T}_t = \bar{T} + \bar{u}^2/(2c_p)$. The mean flow is then entirely defined by the choice of inlet parameters, i.e. static pressure $\bar{p}_u$, static temperature $\bar{T}_u$ and Mach-number Ma_u. Dowling (1995) proposed this configuration to study

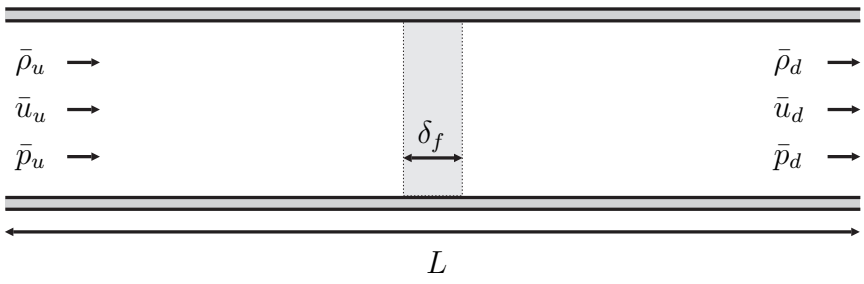

Figure 6.1: Quasi one dimensional model combustor of length L, shaded area represents flame region separating fresh to burnt gas sides.

the effect of the mean flow on combustion instabilities, while Nicoud and Wieczorek (2009) have extensively studied the configuration using one and two dimensional LEEs.

6.1.2 Semi-Analytical Model

A semi-analytical solution may be derived when assuming the flame sheet to be infinitely thin (Dowling, 1995). Then the flow in the upstream (index u) and downstream (index d) duct segments can be assumed to be uniform and isentropic. Thus, with constant velocity and temperature distribution along the two duct elements the acoustic solution of pressure, velocity and entropy waves are described by

$$\hat{p}(x) = \hat{p}^{+}e^{-ik^{+}x} + \hat{p}^{-}e^{ik^{-}x}, \tag{6.5}$$

$$\hat{u}(x) = \frac{1}{\bar{\rho}\bar{c}}\left(\hat{p}^{+}e^{-ik^{+}x} - \hat{p}^{-}e^{ik^{-}x}\right), \tag{6.6}$$

$$\hat{s}(x) = \hat{s}^{+}e^{-ik_c x}, \tag{6.7}$$

where $k_c = \omega/\bar{u}$ is the complex wavenumber of the convected entropy fluctuations $\hat{s}^{+}$ and $k^{\pm} = \omega/\bar{c}(1 \pm M)$ the respective complex wavenumber of the acoustic pressure waves traveling in upstream ($\hat{p}^{+}e^{-ik^{+}x}$) or downstream ($\hat{p}^{-}e^{ik^{-}x}$) direction. Note that entropy fluctuations may only be convected with the mean flow and, thus, have only one wave component.

The flame region cannot be considered as isentropic and jump conditions on both sides of the infinitely thin flame need to be derived. Integrating conservation of mass, momentum and total energy over the limits $x_f - \epsilon$ and $x_f + \epsilon$, where $\epsilon \to 0$ and performing a linearization one obtains:

$$\bar{\rho}\hat{u} + \hat{\rho}\bar{u} = 0, \tag{6.8}$$

$$\hat{p} + \hat{\rho}\bar{u}^2 + 2\bar{\rho}\bar{u}\hat{u} = 0, \tag{6.9}$$

$$\left(c_p\bar{T} + \frac{1}{2}\bar{u}^2\right)(\bar{\rho}\hat{u} + \hat{\rho}\bar{u}) + \bar{\rho}\bar{u}\left(c_p\hat{T} + \bar{u}\hat{u}\right) = \hat{\dot{Q}}, \tag{6.10}$$

where $Q(t) = \hat{\dot{Q}}\exp(i\omega t)$. At the upstream ($x = 0$) and downstream ($x = L$) boundary, general impedance boundary conditions are imposed $\hat{p} - \bar{\rho}\bar{c}Z_{u/d}\hat{u}_i n_i = 0$, see Eq. (2.38). Substitution of the solutions Eqs. (6.5)-(6.7) in the jump conditions of Eqs. (6.8)-(6.10), taking into account the

relations of Eqs. (2.16) and (2.17) and assuming that no entropy wave enters the domain through its inlet, leads together with the two impedance boundary conditions to the following compact matrix notation:

$$\mathbf{S}(\omega)\mathbf{P} = 0. \tag{6.11}$$

Herein, $\mathbf{P} = (\hat{p}_u^+ \ \hat{p}_u^- \ \hat{p}_d^+ \ \hat{p}_d^- \ \frac{\rho_d c_d^2}{c_p}\hat{s}^+ e^{ik_c x})^T$ is the unknown solution vector and $\mathbf{S}(\omega)$ a coefficient matrix containing,

$$\mathbf{S}(\omega) = \left[\begin{array}{ccc|cc} (1-Z_u) & (1+Z_u) & 0 & 0 & 0 \\ (1+M_u)e^{-ik_u^+ L/2} & (M_u-1)e^{ik_u^- L/2} & -\frac{\bar{c}_u}{\bar{c}_d}(1+M_d)e^{-ik_d^+ x} & \frac{\bar{c}_u}{\bar{c}_d}(1-M_d)e^{ik_d^- x} & M_d\frac{\bar{c}_u}{\bar{c}_d} \\ (1+M_u)^2 e^{-ik_u^+ L/2} & (M_u-1)^2 e^{ik_u^- L/2} & -(1+M_d)^2 e^{-ik_d^+ x} & (1-M_d)^2 e^{ik_d^- x} & M_d^2 \\ S_{31} & S_{32} & S_{33} & S_{34} & M_d^3/2 \\ 0 & 0 & (1-Z_d)e^{-ik_d^+ L} & (1+Z_d)e^{ik_d^- L} & 0 \end{array}\right] \tag{6.12}$$

where,

$$S_{31} = \frac{\bar{c}_u}{\bar{c}_d}\left((1+M_u)\left[M_u + \frac{1}{\kappa-1} + \frac{1}{2}M_u^2\right] + \frac{\hat{\dot{Q}}}{\kappa\bar{p}}\right)e^{-ik_u^+ x}, \tag{6.13}$$

$$S_{32} = \frac{\bar{c}_u}{\bar{c}_d}\left((1-M_u)\left[M_u - \frac{1}{\kappa-1} - \frac{1}{2}M_u^2\right] - \frac{\hat{\dot{Q}}}{\kappa\bar{p}}\right)e^{ik_u^- x}, \tag{6.14}$$

$$S_{33} = -(1+M_d)\left[M_d + \frac{1}{\kappa-1} + \frac{1}{2}M_d^2\right]e^{-ik_d^+ x}, \tag{6.15}$$

$$S_{34} = -(1-M_d)\left[M_d - \frac{1}{\kappa-1} - \frac{1}{2}M_d^2\right]e^{ik_d^- x}. \tag{6.16}$$

Solutions of the Eq. (6.11) can be obtained when requiring the matrix $\mathbf{S}(\omega)$ to be singular. Thus, a dispersion relation $\det\mathbf{S}(\omega) = 0$ is obtained of which the complex roots are the semi-analytical eigenvalues. The iterative procedure of Polifke (2003) is then used to solve for the discrete eigenvalues.

6.1.3 Steady Heat Release Rate ($\hat{\dot{q}}_V = 0$)

First, the heat release is assumed to be steady and thus no source of heat release fluctuations is present inside the domain ($\hat{\dot{q}}_V = 0$). The parameters of the problem are L =1 m, $\bar{T}_u$ =300 K, $\bar{T}_d$ =1200 K, $\bar{p}_u$ =101 320 Pa and for the flame sheet a thickness $\delta_f = 0.04L$ and a position $x_f = 0.5L$ are chosen analogously for all considered cases herein.

Before comparing the results, it is stressed that one may expect differences between the semi-analytical solution Eq. (6.11) and the LEEs computations for one main reason: In the simulations the flame front is not infinitely thin as in the semi-analytical model. It is at least as thick as the size of the finite element in this region. The finite element mesh is shown in Fig. 6.2 and consists of 15.000 triangular elements which are refined in the flame zone. The two dimensional LEEs are solved using a SUPG finite element stabilization technique.

In first instance, simple acoustic boundary conditions are chosen setting velocity fluctuations $\hat{u}_x = 0$ at the inlet while at the outlet pressure fluctuations vanish $\hat{p} = 0$ (case 1). For the two dimensional LEEs formulation it is further assumed that entropy as well as vorticity fluctuations vanish at the domain inlet assuming $\hat{s} = 0$ and $\hat{u}_{||} = 0$, respectively. For the upper and lower wall boundaries, slip conditions are prescribed for the velocity fluctuations. The first four eigenmodes for this case are shown in the left graph in Fig.6.3. If the mean flow is at rest ($Ma_u = 0$) no coupling of acoustic and entropy waves occurs and thus, no amplification or attenuation is generated. The frequencies are purely real, which is captured by the Helmholtz equation and LEEs and is in good agreement with the analytical solution: 135.4 Hz, 347.2 Hz, 558.8 Hz, 829.8 Hz for the first four modes, respectively.

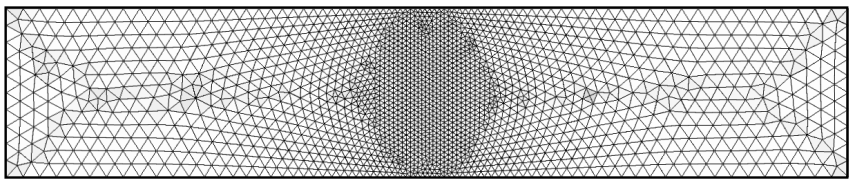

Figure 6.2: Finite element mesh of generic premixed combustor configuration using triangular elements.

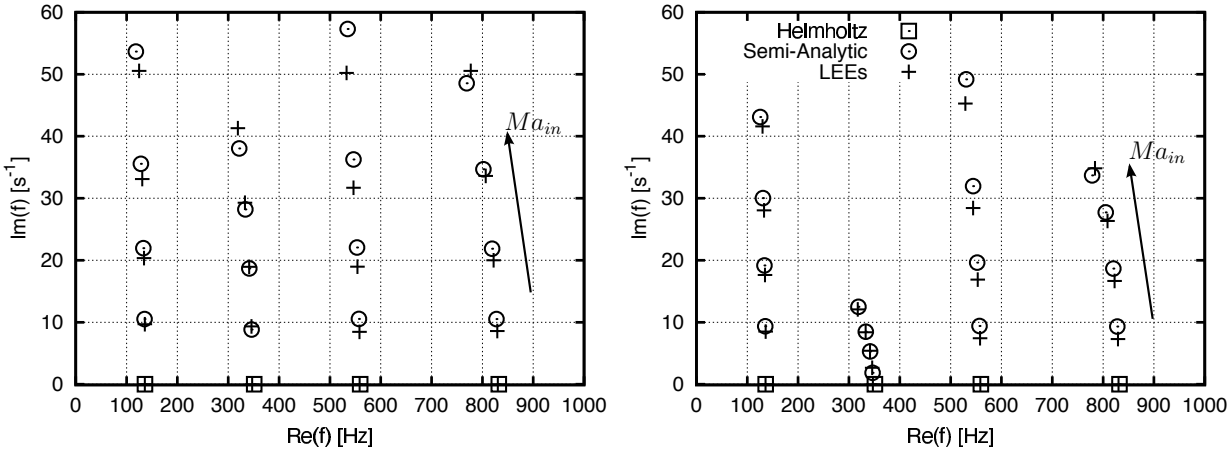

Figure 6.3: Evolution of the first four eigenmodes for a steady flame ($\hat{\dot{q}}_V = 0$) of the academic configuration of Fig. 6.1. For each mode the inlet Mach number is varied from $Ma_u = 0 - 0.16$ with an increment of 0.04. Arrows indicate direction of increasing inlet Mach number. Semi-analytical results are plotted against LEEs and the solution of the Helmholtz equation; Left: boundary conditions of case 1; Right: boundary conditions of case 2.

As soon as $Ma_u > 0$, mean flow effects become significant and even for small Mach numbers of 0.04 the imaginary part of the eigenmode is positive. Hence, the eigenmodes decay exponentially with $\mathfrak{R}(\exp(i\omega t))$. If the inlet Mach number is further increased, the imaginary part increases simultaneously more and more. Highest damping rates are obtained for $Ma_u = 0.16$ where the imaginary party yields: $53\,\mathrm{s}^{-1}$, $38\,\mathrm{s}^{-1}$, $57\,\mathrm{s}^{-1}$, $48\,\mathrm{s}^{-1}$ for the first four modes, respectively. A shift in real frequency can also be observed which is non negligible for the second and forth mode, $-24\,\mathrm{Hz}$ and $-58\,\mathrm{Hz}$, respectively. The LEEs tend to under or over-estimates the solution obtained from the semi-analytical solution. However, considering the infinite thickness of the flame, assumed to derive the semi-analytical solution, these differences are small. It has been verified that the results of the LEEs converge towards the semi-analytical result when further decreasing the flame thickness. Note that for all Mach numbers considered the eigenvalues of the Helmholtz solution remain purely real, as the equations is based on the assumption of a quiescent medium ($\bar{u} \backsimeq 0$). Thus, the Helmholtz equation does completely neglect any damping generated in this configuration.

The damping observed for case 1 originates from two effects: First, acoustic waves trigger entropy waves in the steady flame region which are convected

out of the domain. This coupling process is described by Eq. (2.11). Secondly, acoustic energy is radiated out of the domain since the boundary conditions formerly chosen permit an acoustic energy flux when a flow is present. Thus, in order to estimate the attenuation from acoustic-entropy coupling only, a different set of boundary conditions is prescribed to in- and outlet zeroing the acoustic energy flux in presence of a mean flow (case 2). This is achieved by correcting the above boundaries for convective flow effects, by choosing $\hat{u} + \bar{u}/(\kappa\bar{p})\hat{u} = 0$ and $\hat{p} + \bar{\rho}\bar{u}\hat{u} = 0$ for the in- and outlet, respectively. Compared to the first case, the damping rates at $Ma_u = 0.16$ slightly decrease for mode one, three and four: $43\,\mathrm{s}^{-1}$, $49\,\mathrm{s}^{-1}$, $34\,\mathrm{s}^{-1}$. The impact is significantly higher on the second mode: $12\,\mathrm{s}^{-1}$. However, this effect can be explained through a velocity node in the flame region which reduces the acoustic-entropy coupling. The shift towards lower real parts of the eigenvalues is observed in this case as well. Agreement between LEEs and analytical solution is found to be good while the error for the Helmholtz equation increases significantly with Ma_u and can reach in maximum about 47 Hz for the real and $45\,\mathrm{s}^{-1}$ for the imaginary part of the frequency.

6.1.4 Unsteady Heat Release Rate ($\hat{\dot{q}}_V \neq 0$)

Now, unsteady combustion is included in the considerations by introducing the global n-τ model into the dispersion relation of Eq. (6.11) for the semi-analytical model

$$\hat{\dot{Q}} = \frac{\kappa\bar{p}}{\kappa - 1} n e^{i\omega\tau}\hat{u}, \tag{6.17}$$

at the location $x = x_f$. For the LEEs a local formulation of the n-τ model is introduced to model the heat release rate per unit volume of the finite flame region

$$\hat{\dot{q}}_V = \frac{q_t}{\bar{u}_b} n_l(\mathbf{x}) e^{i\omega\tau_l}\hat{u}(x_{ref}), \text{ with } \quad n_l(\mathbf{x}) = \frac{\kappa\bar{p}}{\kappa - 1}\frac{\bar{u}_b}{q_t}\frac{n}{\delta_f}. \tag{6.18}$$

When employing the Helmholtz Eq. (2.25), the relation in Eq. (2.22) provides a direct link between velocity and pressure fluctuations. Transformation into frequency space needs to be performed additionally using Eq. (2.12).

In order to validate the LEEs for the unsteady flame case, two different values of interaction index are considered, viz. $n = 1$ and $n = 3$, corresponding to a small and large amplitude of the flame response, respectively. The time delay is chosen to mimic typical combustor conditions τ =0.4 ms and the simplified set of inlet and outlet boundary conditions is chosen (case 1), viz. $\hat{u} = 0$ and $\hat{p} = 0$ for inlet and outlet, respectively. Again, we expect differences in the results for the in Section 6.1.3 mentioned reason, but also because the reference point for the flame model is chosen directly upstream of the flame region ($x = 0.48L$) in order to be consistent with the idea of the n-τ model. Unlike for the semi-analytical model it cannot be chosen directly at $x_{ref} = L/2$.

When the amplitude of the flame is small $n = 1$, Fig. 6.4 left shows the results obtained with the semi-analytical model for $Ma_u = 0 - 0.16$ and two solutions of the LEEs for zero and $Ma_u = 0.16$ inlet conditions. At zero Mach number the agreement between semi-analytical solution and LEEs is excellent for all four modes. Mode one and four are already stable at this zero Mach number limit, while mode two is marginally stable ($\Im(f) = 0$) and mode three shows a clearly unstable characteristic ($\Im(f) < 0$). If a mean flow is introduced, this has a stabilizing effect on all four modes considered. At the $Ma_u = 0.16$ limit, all modes show a stable behavior. This trend is accurately predicted by the LEEs model. Note that also the shift in frequency is captured with good agreement.

When the amplitude of the flame response is high $n = 3$, Fig. 6.4 right shows that mode three is generally more amplified at zero mean flow conditions. Compared to the small amplitude response of the flame case, a much higher inlet Mach number must be reached in order to stabilize the mode ($Ma_u > 0.1$). For the other modes, a similar behavior is observed as for $n = 1$. LEEs manage to predict the trend correctly but deviations at $Ma_u = 0.16$ are higher than before. However, overall a good agreement is achieved for both conditions.

Next, the impact of the flame parameters on the combustor eigenmodes is studied. When a flame model of n-τ type is introduced to the equations the situation becomes complex. In this case, the Helmholtz equation will predict eigenmodes which are either stable or unstable, depending on the phase relationship between pressure and heat release fluctuations Eq. (1.1).

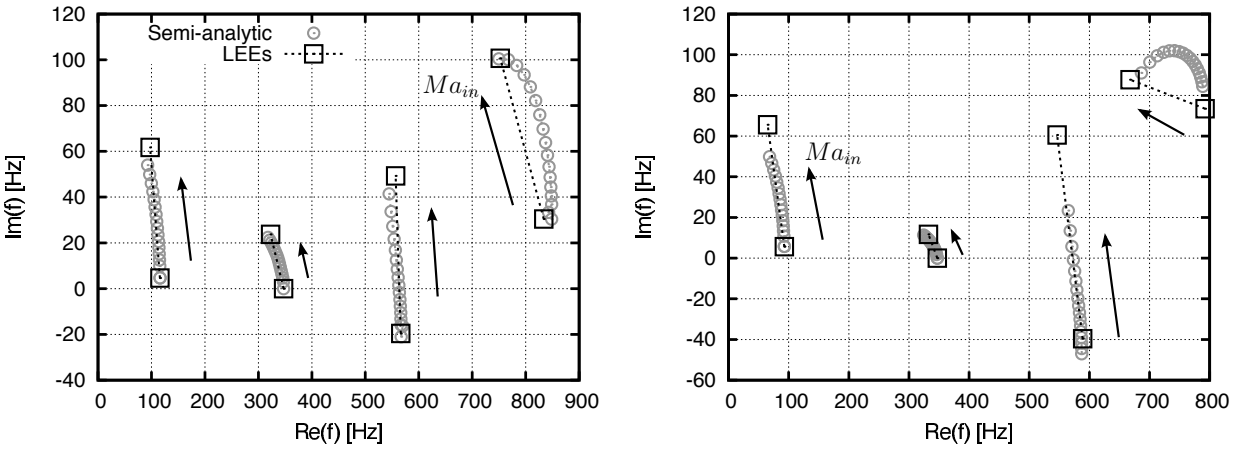

Figure 6.4: Evolution of the first four eigenmodes for an unsteady flame ($\hat{q}_V \neq 0$, τ =4 ms) of the academic configuration of Fig. 6.1 for different values of the mean flow inlet Mach number Ma_u. Semi-analytical results are varied $Ma_u = 0 - 0.16$. LEEs only display $Ma_u = 0$ and $Ma_u = 0.16$ results. Arrows indicate direction of increasing Mach number. Left: small amplitude response $n = 1$; Right: high amplitude response $n = 3$.

Influence of damping is not accounted for due to the nature of the equation. A parametric study is conducted for the first two modes to highlight the differences between the quiescent assumption and LEEs. The interaction index n and the time delay τ are varied from 0, 1, 2, ..., 7 and 0, 0.2, 0.4, ..., 3 ms, respectively. This study is performed by retrieving solely solutions from the LEEs and Helmholtz equation.

A subtle way to compare the differences in frequency prediction between the Helmholtz equation and the LEEs is shown in Nicoud and Wieczorek (2009). Their presentation is adopted herein and the resulting figure is shown in Fig. 6.5 for the first and second eigenmode. The graph displays the frequency shifts between solutions of the LEEs at $Ma_u = 0.16$ and Helmholtz equation (i.e. $Ma_u = 0$) for each value of the flame response (n and τ) and thus provides information of the error in frequency $\mathfrak{R}(f)$ and growth rate $\Im(f)$ made by assuming a medium at rest.

It is directly evident that a method based on the quiescent medium assumption, like the Helmholtz equation, is not able to predict the frequencies incorporating mean flow effects. Indeed, the frequency change depends strongly on the acoustic-flame coupling (values of n and τ). The shift in real frequency for both modes is always negative and yields up to -70 Hz and -180 Hz for the first and second mode, respectively. This result is

consistent with the findings of Section 6.1.3 but shows a stronger trend. Although the first mode is only stabilized by the presence of a mean flow, the shift in imaginary frequency of the second mode can either be positive or negative. Thus, including a mean flow may stabilize this particular mode e.g. for $n \leq 1$ or destabilize it e.g. for $n > 1$ and $\tau > 1\,\text{ms}$. Summarizing the results yields that frequencies of instabilities can hardly be guessed when assuming a zero mean flow. Depending on the acoustic-flame coupling and acoustic boundary conditions an error is introduced. Including a mean flow may yield a stabilizing effect but can similarly also turn into a stronger forcing of thermoacoustic instabilities. Moreover, the achieved results suggest that inclusion of acoustic interaction effects with entropy waves is recommendable in many cases.

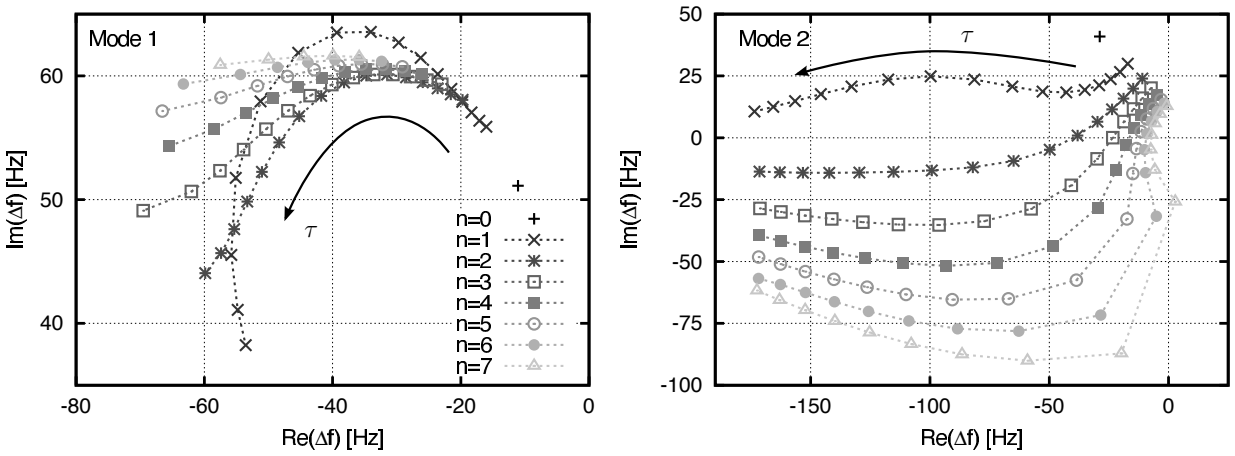

Figure 6.5: Difference in real and imaginary part of first and second eigenmode predicted by LEEs ($Ma_u = 0.16$) and Helmholtz equation ($Ma_u = 0$), frequency shifts are plotted as a function of interaction index n while the values of the time delays are varied along the curves from $\tau = 0$ to 3 ms. Arrows indicate the direction of increasing τ. Left: First eigenmode; Right: Second eigenmode.

6.2 Two-Phase Flow Combustion Instabilities

From the validated test cases one may conclude that acoustic-vorticity coupling of Chapter 5 is equally important as acoustic-entropy coupling of Section 6.1. It has been shown that both effects generally damp combustion instabilities in the low frequency limit, although -under some limitations- the reverse effect of amplification may also occur. Up until now the effects

have been considered separately. This is changed in the following section as both coupling processes and their effect on eigenfrequencies will be considered conjointly.

The validation test case is the same atmospheric combustion chamber already used in section 5.4 to validate the scattering matrices of a non-reactive swirled combustion chamber flow. Now, the eigenfrequencies of the configuration are considered under reactive conditions by introducing a kerosene mass flow to the centered injector of the injector nozzle. Liquid film breakup, atomization and evaporation processes then lead to the generation of a reactive mixture which burns along the shear layers between the recirculating zones. The test rig is modified to perform experiments with self-excitation by establishing a thermoacoustic feedback loop. This is achieved by introducing a subsonic nozzle at the downstream boundary of the combustor.

In order to increase confidence in the robustness and accuracy of the presented method, the approach to the full reactive combustion chamber is subdivided into four consecutive steps. First, the eigenmodes are considered under zero mean flow conditions. Then, in the second case, a constant mean flow is introduced at atmospheric temperatures. The mean flow velocity is then increased by preheating the inlet air, in the third test case, but keeping the air mass flow constant. Finally, in the last step the influence of the flame is introduced. The complexity increases with every validation test case considered.

This section is structured as follows: First, the atmospheric pressure test rig is illustrated. Then, the measurement equipment and methods are briefly discussed. Measurements mainly comprise the evaluation of the eigenfrequencies of the combustion chamber. This is achieved by performing acoustic damping measurements yielding real and imaginary parts of the eigenfrequencies. However, to provide all necessary data for validation purposes the acoustic boundary conditions need to be provided, as well as a FTF for the reactive case.

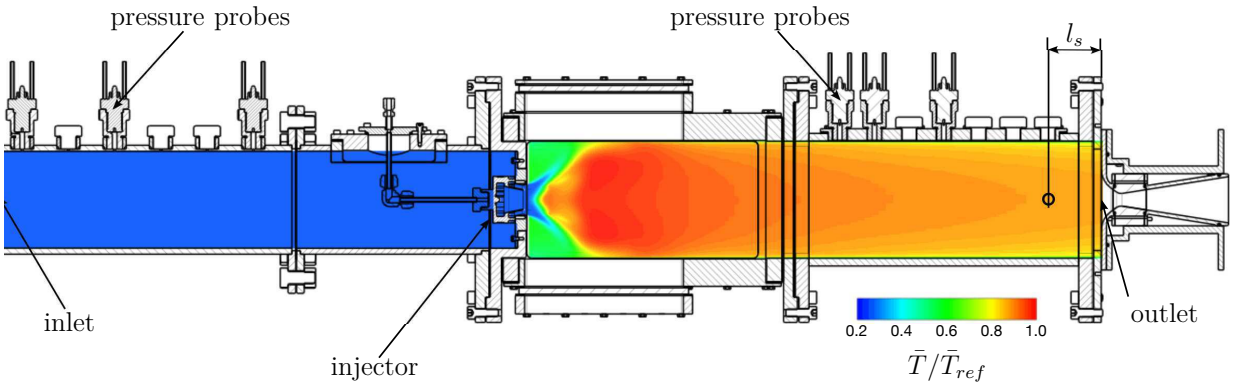

Figure 6.6: Atmospheric pressure test rig including parts of the plenum section, the injector nozzle, combustion chamber and convergent-divergent nozzle of Case D. Field shows the dimensionless temperature distribution computed using RANS model and PDF transported mixture fraction approach.

6.2.1 Experimental Configuration and Measurements

The atmospheric test rig is shown in Fig. 6.6 with its characteristic mean temperature distribution for the reactive case. The upstream plenum section has the same length $l_u = 1.34\,\mathrm{m}$ as for the scattering matrix measurements of Section 5.4. Downstream of the injector nozzle, the combustion chamber expands to a length $l_d = 0.73\,\mathrm{m}$ which comprises a window section allowing optical access and a measurement section. At the end of the combustor two different boundary conditions are mounted for the present validation measurements. For cases with no reaction a perforated screen is used. In the case including reaction a converging-diverging nozzle is mounted providing high amounts of acoustic reflection. The critical section of the nozzle has a diameter $d_n = 16\,\mathrm{mm}$. Unlike the scattering matrix measurements of Section 5.4, no downstream siren is present.

First the operating condition for the experimental validation case are determined. In order to show the capability of the numerical method to discriminate between stable and unstable combustor operation, the combustor needs to feature a self-excited unstable operating condition. However, in case of instability the flame saturates and its flame transfer function, being in the non-linear regime, cannot be measured. Thus, in this case the LNSEs and Helmholtz equation remain mathematically unclosed. In order to resolve this conflict, an operating condition must be chosen which is acoustically stable to provide the FTF as well as acoustically unstable to provide the eigenfrequency of instability. This is realized by mounting a

low and a high reflecting boundary condition to the downstream end of the combustion chamber. Latter condition may close the thermoacoustic feedback loop leading to a combustor instability. These two different conditions are represented by a perforated screen and an accelerated nozzle flow.

For both boundary conditions the air ratio and air mass flow is ramped up and down while recording time series of the pressure signal. After Fourier transformation the maximum pressure amplitudes of the frequency spectrum are summarized in Fig. 6.7 for both boundaries. Low pressure amplitude levels are observed for the complete operability range when employing a perforated screen at the combustor outlet (Fig. 6.7 left). Only at the lean extinction limit slightly higher pressure levels are reached. This illustrates that a flame transfer function may be measured in the complete operability range displayed, except at the lean extinction limit. Now, the nozzle is mounted and the time series at each operating point are again post processed to determine the maximum pressure amplitudes displayed in the right Fig. 6.7. Again, slightly higher pulsations are observed at the lean extinction limit at high λ. However, significant pressure amplitudes of around 260 Pa are reached at high thermal powers, i.e. high air mass flow and low air ratio, which indicates the presence of a thermoacoustic instability.

From these considerations the validation test case is defined at $m_{air} = 45\,\mathrm{g\,s^{-1}}$ and at an air ratio of $\lambda = 1.6$. On the one hand, a FTF can be measured at these conditions using a perforated screen at the outlet

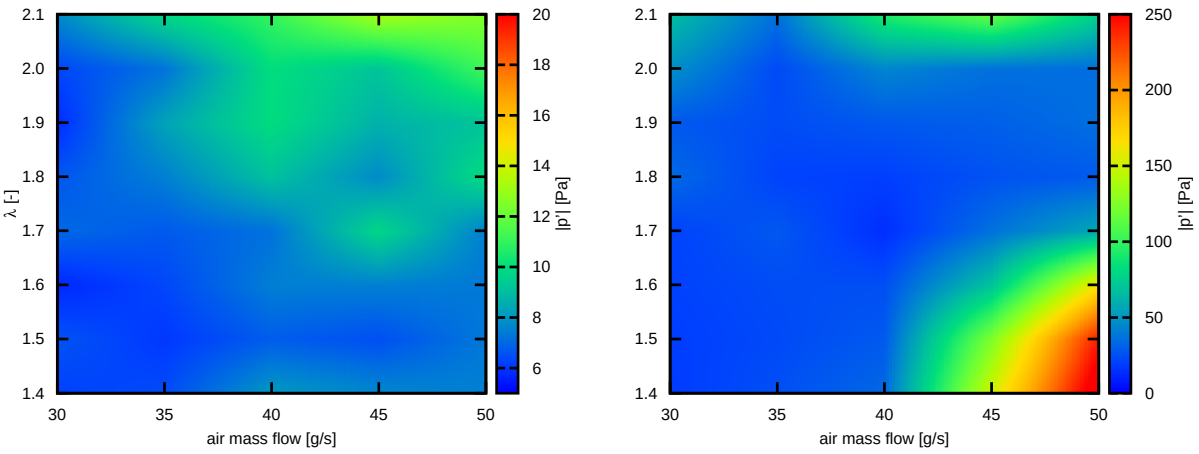

Figure 6.7: Contour of pressure amplitude in the combustion chamber varying air mass flow and air ratio for two different boundary conditions at the outlet: a low-reflecting perforated screen (left) and a subsonic nozzle (right).

(Fig. 6.7 left). On the other hand, a self-excited thermoacoustic instability is observed when using a convergent-divergent nozzle (Fig. 6.7 right). The instability causes pressure amplitude levels of around 130 Pa.

As already explained above, the reactive combustor test case is highly complex as it integrates a variety of different interaction effects. To allow for a better understanding of the problem and its associated mean flow effects, the problem is subdivided into a number of different steps with increasing complexity. First, the combustion chamber modes are considered under zero flow conditions in a Case A. Then, a mass flow $m_{air} = 45\,\mathrm{g\ s^{-1}}$ is prescribed to the combustor inlet in Case B. The same inlet air mass flow of Case B is then preheated to temperatures of $\bar{T}_{in} = 573\,\mathrm{K}$ in the next Case C. Air preheating results in an approximate doubling of the maximum velocity reached in the swirl injector exit plane. In the final Case D, a kerosene mass flow is supplied to the centered injector of the swirler and a steady flame establishes. Only in this case, a convergent-divergent nozzle is mounted at the combustion chamber exit. For all other cases a perforated screen is employed. All operating conditions are summarized in Tab. 6.1.

Table 6.1: Operating conditions of atmospheric pressure test rig of the four investigated Cases A, B, C and D. Downstream boundary condition is specified according to PS: perforated screen; NOZ: convergent-divergent nozzle.

Parameters		Case A	Case B	Case C	Case D
$\dot{m}_{air}$	[g/s]	0	45	45	45
T_{in}	[K]	293	293	573	573
λ	[-]	-	-	-	1.6
DS boundary	[-]	PS	PS	PS	NOZ

6.2.1.1 Acoustic Damping Measurements

Generally only the real part of the eigenfrequencies of combustor modes are provided for experimental test cases found in the literature. Determination of the decay or growth rates of eigenmodes is far more complex. However, recently Wagner et al. (2013) have proposed a method to determine the decay rates ω_i of a given combustor configuration. Their technique is applied

to the current atmospheric combustion test rig to provide not only the real part of the eigenfrequencies but also their respective decay rate. This information allows a better validation of LNSEs and Helmholtz solvers.

For all different cases investigated the siren of Kathan et al. (2010) is connected to the downstream part of the combustion chamber having a circular port with a diameter of $d_s = 0.012\,\mathrm{m}$. The siren intake is located $l_s = 60\,\mathrm{mm}$ away from the outlet section. Its exact location is depicted in Fig. 6.6. The siren can be operated under two different conditions: Providing a continuous excitation signal at distinct frequencies, or, exciting the test rig for an amount of nine excitation periods T. In this time span a certain saturation amplitude is reached. After $9T$, acoustic excitation is stopped for $45T$ and the pressure levels decay exponentially with a respective decay rate of $\exp(-\omega_i t)$ (cp. to Eq. (3.48)). This specific siren operation is realized by perforating the rotating disc of the siren by an amount of nine perforations (compared to 54 perforations for continuous excitation).

The continuous siren operation is used to identify the pressure amplitude spectra of the combustion test rig in order to determine the approximate locations of the eigenfrequencies. Then, in a next step, the second siren disc is mounted and the test rig is excited periodically for $9T$ at the approximate eigenfrequencies of combustion chamber. The transient pressure signals are recorded using piezo transducers located in the plenum and combustion chamber section with a sampling rate of 20 kHz. A Gibbs sampler is used which calculates the probability distributions of frequency and damping rates using a Monte-Carlo type of method. In this thesis the JAGS algorithm available online is used (Plummer, 2012). Wagner et al. (2013) have found this approach to be highly robust compared to other methods commonly found in literature.

Damping coefficients measured for the four cases of investigation are shown in Tab. 6.2 for eigenmodes up to 1000 Hz. Damping rates reached for the zero mean flow case are relatively low compared to the cases with mean flow except for the frequency at 730 Hz which is fully conform with the previous results. The damping reached for the zero mean flow case must result entirely from the acoustic energy transmission at the inlet and outlet boundaries. In case of a thermoacoustic instability where acoustic amplitudes exponentially grow in time (i.e. negative values of ω_i), the measurement

Table 6.2: Eigenfrequencies and damping rates of combustion chamber test rig including and excluding mean flow in the non-reactive case.

Description			Frequency	Damping Rate
$\dot{m}_{air}$ [g/s]	T_{in}[K]	λ [-]	f [Hz]	$\omega_i/2\pi$ [s^{-1}]
0	293	-	125	40
			292.8	47
			499.5	50
			730	110
			954	62
45	293	-	164	40
			288	130
			496	160
			737	170
			957	110
45	573	-	165	-
			290	48
			605	210
			973	150
45	573	1.6	90.9	4.7

technique loses its validity and only the frequencies of oscillations may be retrieved from the pressure time series.

6.2.1.2 Acoustic Boundary Characterization

In order to provide all necessary data for LNSEs validation, the acoustic boundary conditions at inflow and outflow need to be available for all cases considered. The boundary's impedance Eq. (2.38) governs the acoustic energy flux out of the system and therefore contributes to the overall combustor damping. Inlet and outlet impedances are determined by measuring the acoustic reflection coefficients at the same operating conditions but in a separate experiment. At the inlet of the plenum a stationary siren naturally provides a perforated screen. Measurement of the acoustic reflection coefficients of such boundaries is straightforward and well known in the existing

literature. The reflection behavior for the siren intake are displayed for the first three measurement conditions in Fig. 6.8. Similarly, the downstream reflection coefficient of the perforated screen is determined for the cases A, B and C and is displayed below in the same Fig. 6.8.

For Case D the same inlet boundary conditions are used for the LNSEs as in Case C. At the outlet, the nozzle mimics the presence of the first vane passage of the turbine. Due to a low signal-to-noise ratio in case of a thermoacoustic instability, measurement of the reflection coefficient becomes difficult. Therefore, the reflection coefficient is obtained from acoustic theory using an one dimensional formulation of the LEEs (Lamarque and Poinsot, 2008). The routine is described in detail in Appendix F and is implemented into Matlab. Amplitude and phase of the resulting reflection

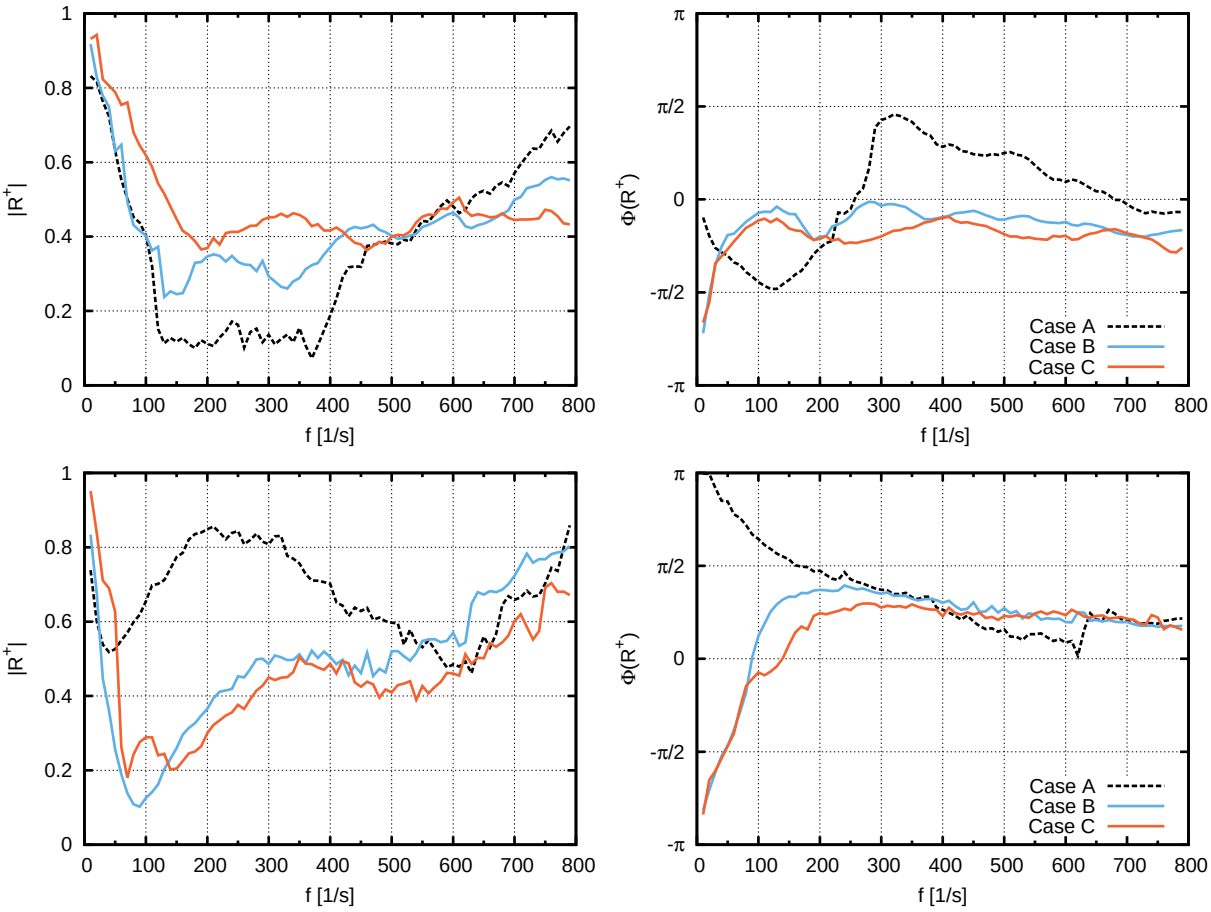

Figure 6.8: Amplitudes and phases of the reflection coefficients at the upstream R^+ and downstream R^- boundary for operation Cases A, B and C. Top: Upstream boundary, Bottom: Downstream boundary.

coefficient for the specific nozzle mounted at the combustor exit are shown in Fig. 6.9.

6.2.1.3 Spray Flame Transfer Function

For the reactive Case D, the flame transfer function of the spray flame produced by the injection system is measured additionally. This FTF needs to be provided to the numerical LNSEs eigenvalue solver in order to provide a model for the unsteady heat release rate $\hat{\dot{q}}_V(\omega)$. This is done by performing the measurement routine described in Section 2.6.2 and assessing the transfer matrices of the two acoustic states with and without flame. A perforated screen is mounted to the combustor exit ensuring low acoustic reflection coefficients and a stable flame operation. Fig. 6.10 shows the result of the measured FTF. The temperature $\bar{T}_h$, which is necessary to close Eq. (2.37), is chosen from the incompressible flow simulations. Averaging this temperature over a plane just downstream of the flame yields $\bar{T}_h = 2020\,\mathrm{K}$.

The FTF shows a very similar characteristic to gaseous flames (cp. with Alemela, 2009; Lieuwen and Yang, 2005). A frequency step of 10 Hz is used during the experiments. Roughness in the representation of the FTF are due to a degraded signal to noise ratio, especially when employing the downstream siren. For this excitation state, the pressure amplitudes reached

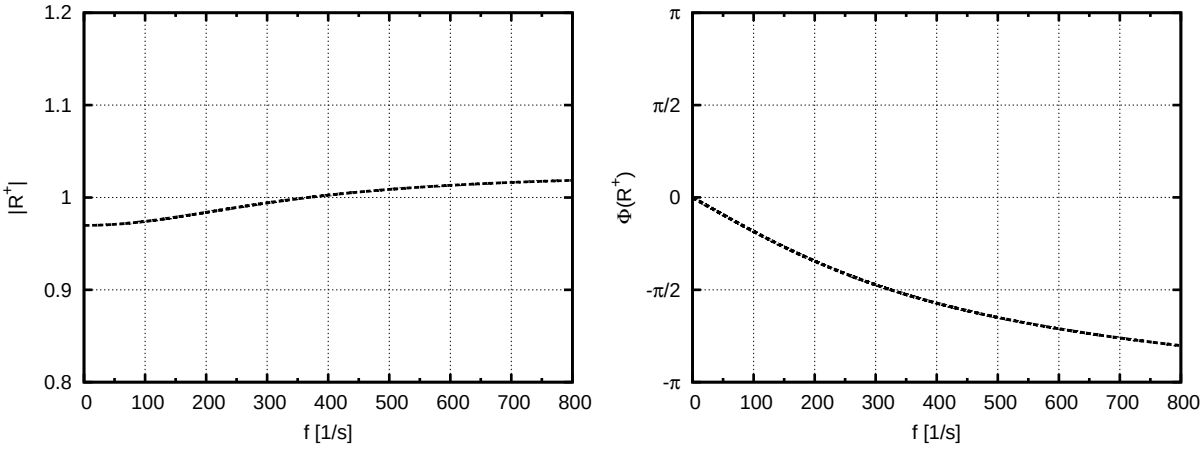

Figure 6.9: Amplitude and phase of frequency dependent reflection coefficient of the subsonic nozzle mounted downstream of the combustion chamber of Case D. Prediction is performed using the numerical routine of Appendix F.

in the combustion chamber are already relatively low. When the acoustic signals are transmitted to the upstream plenum section via the swirl injector, the amplitudes are further decreased due to the low transmission coefficients of the injector (see $|T^-|$ in Fig. 5.16).

6.2.2 Mean Flow Computations

The non-reactive flow configurations (Case A, B and C) are calculated using the same specifications as in Section 5.4. For the reactive calculation (Case D) only the mesh is slightly refined in the flame region yielding a total amount of 1.9 million elements. Instead of the standard k-ϵ turbulence closure model, a modified version called renormalized group (RNG) k-ϵ model is employed. The method is proposed by Yakhot et al. (1992) and is based on their theory derived in Yakhot and Orszag (1986). For Case D, the fields of unknown variables are initialized by prescribing the flow fields computed in the preheated Case C. Then, in a next step, kerosene droplets are injected into the combustion chamber and in a last step the flame is ignited. Chemical reaction is modeled in terms of a PDF transported mixture fraction variable approach with a total number of 30 species considered. The numerical computations were also verified by performing simulations with an eddy dissipation concept model yielding similar results.

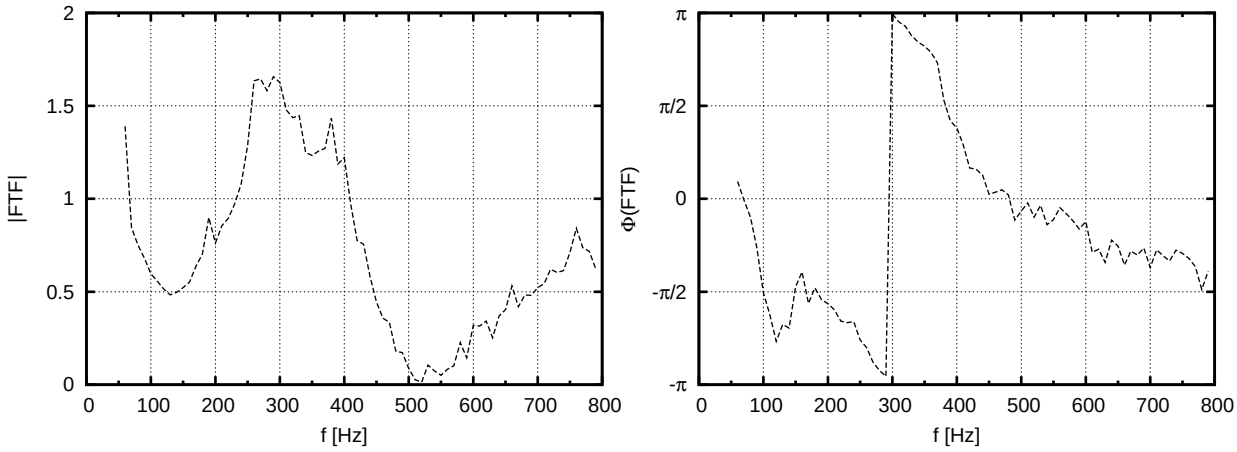

Figure 6.10: Amplitude and phase of flame transfer function measured at the operating conditions of Case D ($\lambda = 1.6$, $m_{air} = 45$ g/s) using a two-source microphone technique.

Liquid kerosene is injected by prescribing a characteristic droplet diameter and respective mass flow rate at the end of the atomizer lip. Droplet diameters are determined experimentally by Avio S.p.A. and are provided to the numerical computation. All droplets are transported through the computational domain until they fully evaporate using a Lagrangian approach. Heat flux through the combustor walls becomes non-negligible in this case and is accounted for by prescribing constant temperature to all combustor walls. The wall temperatures are varied iteratively, similarly to the procedure of Section 5.4.

6.2.3 Non-Reactive Flow ($\bar{\dot{q}}_V = \hat{\dot{q}}_V = 0$)

For the acoustic simulations of the three different cases without acoustic-flame coupling ($\bar{\dot{q}}_V = \hat{\dot{q}}_V = 0$, Case A, B and C) the frequency dependent impedance boundary conditions of Fig. 6.8 are subscribed to inlet and outlet boundaries. Additionally, velocity fluctuations parallel to the inlet are assumed to be zero, i.e. zeroing vorticity fluctuations,

$$\hat{\mathbf{u}}_{||} = 0. \tag{6.19}$$

Entropy fluctuations vanish by subscribing Eq. (2.45). At solid walls slip conditions of Eq. (2.51) and vanishing gradients of pressure and density fluctuations of Eq. (2.53) are chosen.

Using the Helmholtz equation, only one condition needs to be imposed on each boundary. For mass flow inlet and outlet the same frequency dependent impedance boundary conditions are used as subscribed for the LNSEs. Velocity amplitudes for the zero mean flow assumption become directly coupled to pressure amplitudes $i\omega\hat{\mathbf{u}} = -\nabla\hat{p}/\bar{\rho}$ (in Eq. (2.22)). A homogenous Neumann condition results when injecting this expression into the slip boundary condition of Eq. (2.51) (see also Eq. (E.4)).

We expect deviations of the numerical computations compared to the experimental data for the following reasons: (1) The siren introduces an additional mass flux to the system which may lead to a short-term change in the acoustic flow state and boundary conditions. (2) The siren is connected via a tube to the combustion chamber (diameter $d = 12\,\mathrm{mm}$ and length $l = 1.5\,\mathrm{m}$). Strictly speaking, the experimental and numerical setup are not

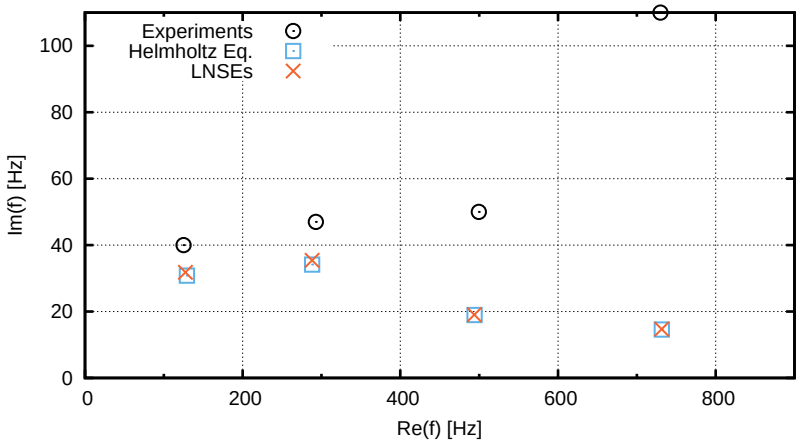

Figure 6.11: Combustor eigenmodes of quiescent operating condition of Case A. Results of real and imaginary part of eigenfrequencies, i.e. $\Re(f)$ and $\Im(f)$, are plotted of experiments, Helmholtz equation and LNSEs.

the same as the siren supply tube is neglected in the numerical computations. (3) Furthermore, in the zero mean flow case (Case A) the assessment of the boundary reflection coefficients $R^{\pm}$ is done by introducing a 8 g/s mass flow rate. Otherwise, performing reflection coefficient measurements employing sirens would be infeasible. (4) Damping generated through structure vibration or small slits and holes in the configuration is not accounted for in the numerical simulations. However, the combustor walls are at least 100 mm thick and, thus, the influence of structural vibrations is assumed to be of low order.

For the quiescent conditions of Case A the LNSEs reduce to the system of Eqs. (2.21)-(2.23), apart from the diffusion term, and should yield very similar eigenmodes compared to the Helmholtz equation. This is indeed the case, as shown by the results plotted in Fig. 6.11. For all four modes both models coincide. Higher mode damping is predicted at low magnitudes of reflection coefficients (modes one and two) while lower amounts of mode damping are observed for frequency regions characterized through higher reflection coefficients at domain boundaries (modes three and four), see Fig. 6.8. Results obtained with LNSEs and Helmholtz equation are fully in line with these considerations: With the unavailability of acoustic-flow coupling in Case A, the only contributor to acoustic damping $\Im(f)$ should be the acoustic energy flux through the domain boundaries, which is governed by their acoustic impedances. Therefore, if the correct impedances are prescribed to the simulation, then, experimental results and simulations

should not deviate from one another. However, differences in the results are observed which increase with frequency. As mentioned above the differences may be explained through the measurement of acoustic boundary conditions: To operate the sirens a finite mass flow had to be introduced. Thus, the impedances do not represent quiescent conditions. The very strong deviation of mode four at 730 Hz can not be explained through this consideration. Even when artificially decreasing the boundary reflection coefficients in the Helmholtz computations to values below $R < 0.1$ the experimental measured damping rate could not be reached. The deviation can only be explained through differences in the geometric configuration. It must be noted that also eigenmodes inside the plenum section exist which are not plotted.

The frequencies associated with the first four modes found in the experimental campaign of Case B and Case C are gathered in the left and right graph of Fig. 6.12, respectively. Tab. 6.3 and Tab. 6.4 show the errors made by the respective acoustic model. A set of longitudinal acoustic modes is found in the combustor. All modes are significantly damped for both cases as part of the acoustic energy leaves the domain through the boundaries but also -and most importantly- acoustic-flow coupling sets in. This is conform with the findings of Section 5.4. It is evident that the acoustic-flow coupling must contribute significantly to the damping rates reached when comparing the experimental values to the solutions of the Helmholtz equation. As

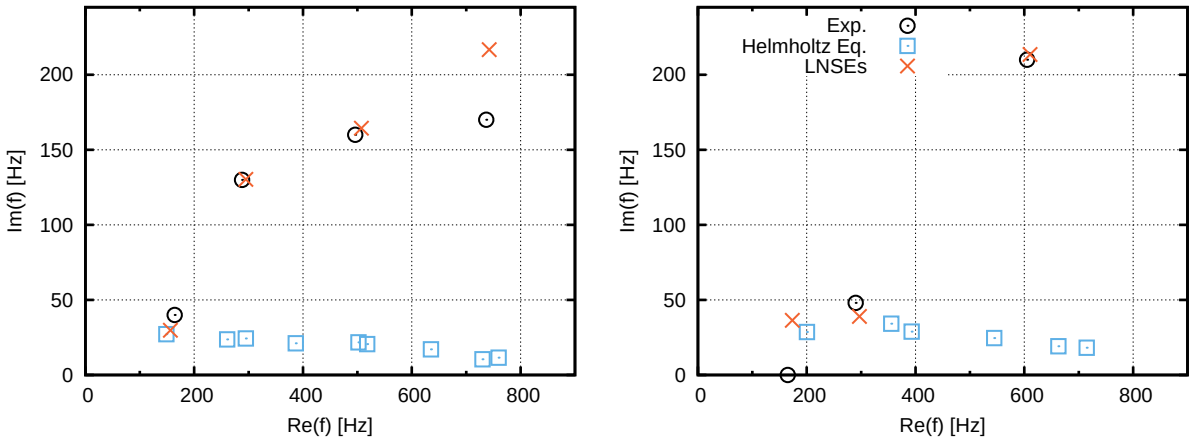

Figure 6.12: Combustor eigenmodes of ambient and preheated operating conditions of Case B (left) and Case C (right), respectively. Results of real and imaginary part of eigenfrequencies, i.e. $\Re(f)$ and $\Im(f)$, are plotted of experiments, Helmholtz equation and LNSEs.

explained, the Helmholtz equation solely incorporates the influence of the damping generated at the acoustic boundaries. Especially at frequencies $f > 250\,\mathrm{Hz}$, the contribution of acoustic-flow interactions is remarkably high. This fact emphasizes the importance of acoustic-flow interaction processes on combustor damping.

Table 6.3: Experimental measured eigenfrequencies of case B of combustion chamber test rig and error of made by LNSEs and Helmholtz code.

Mode	Experiments		LNSEs		Helmholtz Eq.	
	$\Re(f)$ [Hz]	$\Im(f)$ [1/s]	$\epsilon(\Re(f))$ [%]	$\epsilon(\Im(f))$ [%]	$\epsilon(\Re(f))$ [%]	$\epsilon(\Im(f))$ [%]
1	164	40	4.8	25.5	9.3	32.0
2	288	130	2.4	0.2	2.4	81.3
3	496	160	2.3	2.7	1.2	86.4
4	737	170	0.7	27.4	1.0	93.9

At ambient inflow temperatures (Case B), a lower amount of damping is measured for the first mode. With increasing mode number the damping increases significantly and reaches values of up to $170\,\mathrm{s}^{-1}$ for mode four. Overall, the agreement with the LNSEs is very good with respect to frequency and damping rates as shown in Tab. 6.3. Similarly to Case A, highest deviation is observed for the fourth acoustic mode. Currently, the origin of the deviations cannot be explained.

When considering the quiescent approximation of the eigenmodes using a Helmholtz equation, the frequencies of the respective modes are captured with relatively high agreement, cp. Tab. 6.3. However, the inability of the model to account for mean flow effects results in a significant under prediction of the combustor damping. For modes one, two and three the differences in damping rates are $106\,\mathrm{s}^{-1}$, $139\,\mathrm{s}^{-1}$ and $160\,\mathrm{s}^{-1}$, respectively. If the presence of a flame is incorporated into the Helmholtz equation, probably only small amounts of energy input by the flame are enough to balance the acoustic losses. Thus, a Helmholtz solver will tendentiously find a combustion chamber to be more unstable when operated under reactive conditions.

For the Helmholtz equation also eigenmodes pulsating inside the plenum section are determined. These modes have not been determined experimen-

Table 6.4: Experimental measured eigenfrequencies of case C of combustion chamber test rig and error of made by LNSEs and Helmholtz equation.

Mode	Experiments		LNSEs		Helmholtz Eq.	
	$\Re(f)$ [Hz]	$\Im(f)$ [1/s]	$\epsilon(\Re(f))$ [%]	$\epsilon(\Im(f))$ [%]	$\epsilon(\Re(f))$ [%]	$\epsilon(\Im(f))$ [%]
1	165	-	5.0	-	21.2	-
2	290	48	2.4	18.7	22.5	28.7
3	605	210	1.0	1.7	9.5	90.9

tally. Their presence is explained through the high amounts of acoustic reflections and low amounts of acoustic transmissions featured by the injector nozzle. This leads to a partially decoupling of modes in the plenum section and modes observed inside the combustion chamber. Using the LNSEs the presence of plenum modes can be observed as well. However, because of the increased computational costs only the experimental determined combustor modes are searched for.

When the inlet air is preheated (Case C) the flow velocity through the rig nearly doubles. In this case, a higher impact on the frequencies of oscillations is expected (Tab. 6.4). Rather low amounts of damping are reached for low mode numbers. Experimentally the damping rate for the first mode could not be evaluated as the statistical error is large and the resulting exponential fit shows low agreement with the pressure time series. However, LNSEs predict a low damping rate in this frequency range which is of similar order to the second acoustic mode observed. As LNSEs damping predictions are of similar order of the Helmholtz equation, acoustic-flow coupling must have an insignificant effect in the low frequency regime. The agreement reached between LNSEs and the experimental data is again high, as seen from the corresponding Fig. 6.12. As the damping reached for the first two modes is of the order of the acoustic losses through the boundaries, the Helmholtz equation performs well in predicting the damping for mode one and two. However, as soon as acoustic-flow coupling becomes predominant it fails in providing the correct magnitude as it can be observed for mode three. Interestingly, another deficiency of the Helmholtz equation can be observed: with an increase in flow velocity also the real parts of the frequencies are mispredicted by about 21%, 22% and 9% for modes one, two and three, respectively.

The eigenvalue simulations of this section show an irregular convergence behavior. This is related to the fact that experimentally measured boundary conditions (or FTF in the next section) are employed. All measurements are performed with a frequency step of 10 Hz and the results are not smooth on a local scale, due to measurement errors. If the eigenvalue linearization point surpasses an integer multiple of 10 Hz the eigenmodes are found to experience a stronger shift in frequency leading to problems in the convergence behavior of the iterative routine. The convergence criterium after which the iterative routine of Section 3.3.6 is ended, is therefore chosen to be more nonrestrictive $\epsilon = 2\pi 10\,\mathrm{Hz}/|\omega_0|$. In future, such problems can be overcome by either employing higher order interpolation schemes or by approximating the measured data with sufficiently smooth models. With this convergence criterion chosen, the eigenvalue would converge within a number of two to three iterations.

6.2.4 Unsteady Heat Release Rate ($\hat{\dot{q}}_V \neq 0$)

Solving the LNSEs as in the preceding section means finding the eigenmodes of the combustor, taking into account mean flow effects and acoustic losses through the boundaries but neglecting steady and unsteady effects of the flame. When addressing thermoacoustic problems, however, the ultimate objective is to discriminate between unstable and stable combustor operation which requires the inclusion of a flame response. This is the goal of the current section which treats the reactive Case D by accounting for the acoustic-flame coupling incorporating the experimentally measured FTF of Fig. 6.10 into the LNSEs formulation.

The FTF is included numerically by reformulating it as a local n-τ model using Eq. (2.36) and Eq. (2.34). A flame sheet over the complete combustor cross section with thickness $\delta_f = 0.01\,\mathrm{m}$ is inserted into the region of highest rate of reaction at $x_f = 0.073\,\mathrm{m}$ as depicted in Fig. 6.13. The kinetic rate of reaction is obtained, performing an area average of the simulations using an eddy dissipation model. Parameters of global $n(\omega)$ and $\tau(\omega)$ are considered frequency dependent and are interpolated for every iteration step from the experimentally measured data of Fig. 6.10. For interpolation the pulsation ω_{k-1} of a previous iteration $(k-1)$ is used following the iterative routine of Section 3.3.6.

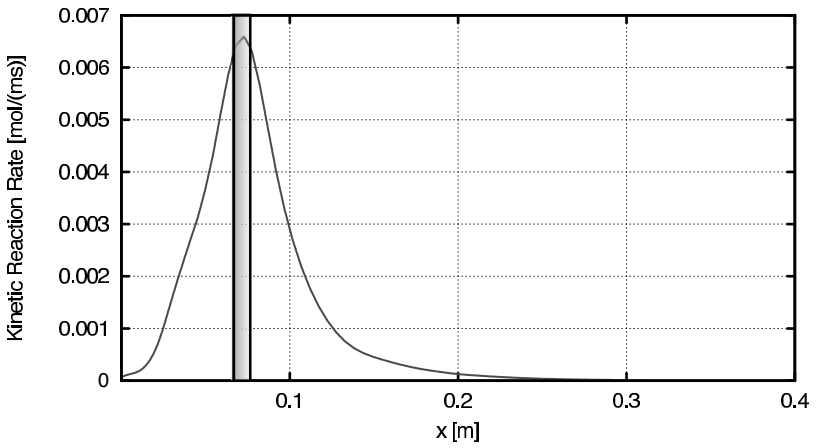

Figure 6.13: Kinetic rate of reaction averaged radially over space. Results from three dimensional steady reactive combustion simulation using an eddy dissipation concept model. Shaded area shows finite thickness and axial location of the unsteady combustion model in the acoustic simulations.

The frequency spectrum at the operating point is illustrated in Fig. 6.14 and shows two sharp peaks at frequencies of 95.4 Hz and 510.9 Hz reaching pressure amplitudes of 129.4 Pa and 21.5 Pa, respectively. From the amplitudes reached it is concluded that the first eigenmode is most likely unstable. Pressure levels reached for the second mode at 510.9 Hz are of the order of the background noise levels and therefore the mode is considered to be in the stable regime. At this particular frequency the FTF also shows a low source strength, cp. Fig. 6.10 left.

Overall, two simulations are performed: One in which the steady effect of the flame through the mean temperature field is accounted but neglecting any unsteady effects ($\hat{\dot{q}}_V \neq 0$). And another one in which the acoustic-flame coupling is incorporated and the combustor may feature instability ($\hat{\dot{q}}_V \neq 0$). This is done for both simulation tools (Helmholtz and LNSEs). However, using the Helmholtz equation all eigenfrequencies between 50 Hz-800 Hz are predicted while using the LNSEs it is focused on the two modes of interest.

For the cases including and excluding an unsteady heat release rate the modes predicted by the LNSEs and Helmholtz equation are plotted in Fig. 6.15, left and right, respectively. For the unstable mode at 90 Hz, it can be observed that the LNSEs correctly predict a shift from the stable ($\Im(f) > 0$) to the unstable regime ($\Im(f) < 0$) when the unsteady effect of the flame is included. An instability is predicted at 97 Hz and corresponds

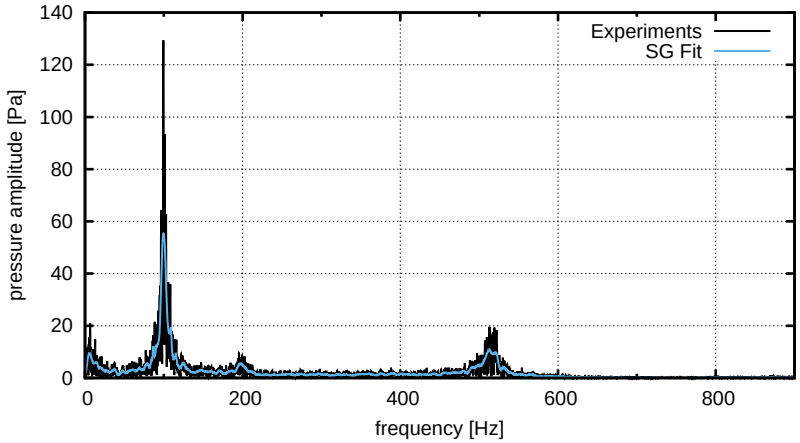

Figure 6.14: Pressure amplitude spectrum of combustion chamber operated under acoustically unstable conditions of Case D. Pure acoustic signal and data fit using a Savitzky-Golay filter.

to the quarter wave mode in the combustion chamber. Interestingly, it is often believed that low frequency instabilities are caused by entropy coupling. The feedback mechanism of accelerated entropy spots is, however, not accounted for and thus, the low frequency of instability must originate from mean flow effects. In the present framework the instability can be explained by the fact that the mean flow may introduce large shifts to the frequency of oscillations. The difference in frequency compared to the first stable mode of the Helmholtz equation ($\bar{\mathbf{u}} = 0$) is $-67\,\mathrm{Hz}$. Such shifts to lower values in frequency have already been observed in the earlier sections. The Helmholtz equation, however, finds the first mode to be in the fully stable regime. A prediction not supported by the experiments.

The second mode observed in the frequency spectrum of Fig. 6.14 at 510 Hz is found to be stable by the LNSEs tool but is predicted as unstable using the Helmholtz equation. Here, again, the difference in frequency is $-36\,\mathrm{Hz}$, when including the mean flow. This shift in frequency is most probably responsible for the stable mode prediction by the LNSEs. When looking at Fig. 6.10 in this range the flame shows almost no acoustic response. Artificially increasing the flame response, however, would directly yield an unstable mode for the LNSEs as well.

For both acoustic modes considered, the LNSEs manage to capture the frequency of instability and is able to correctly discriminate between stable and unstable combustor operation. LNSEs results are conform with the ex-

perimental findings. When neglecting mean flow effects using the Helmholtz equation a completely different acoustic mode is found to be unstable and the instability at 90 Hz is not predicted at all.

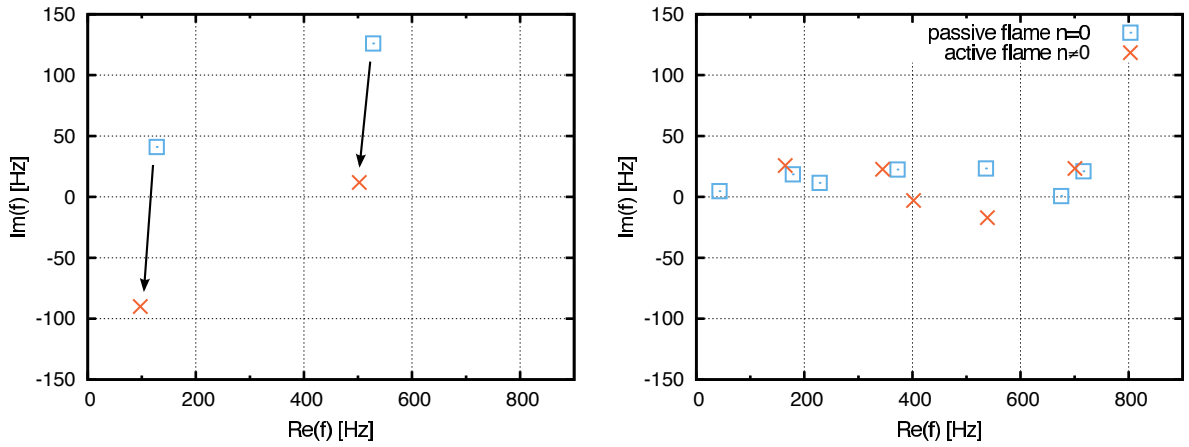

Figure 6.15: Acoustic modes of LNSEs (left) and Helmholtz equation (right) for the atmospheric pressure test rig including combustion (Case D). Modes including the stationary effect of the flame (passive flame, $\hat{\dot{q}}_V = 0$) are plotted as well as the modes associated with unsteady combustion (active flame, $\hat{\dot{q}}_V \neq 0$).

6.3 Concluding Remarks

In this chapter a global stability analysis of combustion chambers was performed using LNSEs. Two configurations were studied: a generic premixed combustor configuration and an experimental single combustor test rig employing an industrial injection system developed by Avio S.p.A.

For both considered cases including a mean flow field without any unsteadiness in the reaction yields a stabilizing effect of the combustion chamber eigenmodes, cp. to Figs. 6.3 and 6.12. As the experimental combustion chamber solely damps acoustic waves (cp. Fig. 5.18), coupling of acoustic with entropy or vorticity modes leads to a stabilizing effect of the combustor eigenmodes. This stabilizing effect of the mean flow field can also be observed when including the effect of the unsteady flame, see e.g. Figs. 6.4 and 6.5 left. However, as shown by the Figs. 6.5 right and 6.15 including a mean flow and unsteadiness of reaction may also lead to a destabilizing effect on the combustor eigenmodes. Moreover, the mean flow field significantly al-

ters the frequencies of instability and therewith the acoustic coupling with the flame.

The LNSEs are able to assess the stabilizing, but also destabilizing effect of the mean flow field onto the combustion chamber modes with relatively high accuracy in frequency as well as in growth rate. As the Helmholtz equation is derived on basis of a quiescent assumption, it does not include the mean flow effect on combustion instabilities. Consequently, the damping or attenuation of combustion chamber modes, i.e. $\Im(f)$, is continuously misspredicted using the Helmholtz equation. For cases with lower mean flow speed and no reaction, the Helmholtz equation, however, manages to predict the frequencies $\Re(f)$ of the combustor modes with similar accuracy than the LNSEs. However, as soon as the flow speed is approximately doubled by preheating the inlet air at constant mass flow, also the frequencies exhibit errors much greater than those predicted using the LNSEs. Finally, when unsteady reaction was included the Helmholtz equation predicted an unstable mode which was found to be stable in the experiments and a stable mode which was found to exhibit instability. Therefore, the Helmholtz equation may only provide with rough approximations of the modes of instability and great care needs to be taken when higher flow velocities are reached within a combustion chamber.

When performing an eigenvalue analysis using the LNSEs, the eigenvalues were found to exhibit small shifts in frequencies and were not easily traceable by the iterative routine. To increase robustness of the methodology, the following three steps are proposed for future investigations:

- Representation of experimentally measured boundary conditions and flame FTF by smoothened curves, using e.g. a Savitzky-Golay filter performing a local polynomial regression or theoretical models.

- For all regions in the field, the local density of the fluid dynamic data points must be considerably higher than the density of the computational nodes of the acoustic simulation. Otherwise, interpolation may cause inaccurate representations of fluid dynamic boundary and shear layer profiles. If by chance, interpolation artificially causes a point of inflection in the representation of the mean flow distribution, this would inevitably lead to the promotion of local hydrodynamic instabili-

ties. From the incompressible fluid dynamic theory of Michalke (1965) it is well known that an inflection point in the flow field causes the appearance of such flow instabilities.

- Great care needs to be taken to represent shear layers emitting from leading or trailing edges of any configuration in the acoustic simulation. This requires a relatively fine resolution of such regions in the fluid dynamic simulations.

This observed sensitivity was also observable for the Helmholtz equation, but was more pronounced when using the LNSEs. The simulation of the scattering matrices of Chapter 5 did not show such sensitivities.

7 Conclusion

Two different numerical solvers are presented in this thesis which solve for the acoustic fields or eigenfrequencies and eigenmodes of multidimensional flow configurations employing complex impedances and active or passive flames. They are based on the linearized Navier-Stokes equations which account for the propagation of three types of disturbances (acoustic, vorticity and entropy). Interaction between the different disturbances leads to a transfer of energy from one to the other and allows to capture acoustic attenuation and amplification processes. Different stabilized finite element procedures are introduced which may be interpreted as methods modeling the effect of the unresolved subgrid scales. The schemes provide finite element stabilization with lowest amounts of numerical diffusion and preserve the order of accuracy of the interpolating functions. After finite element discretization, large system matrices may arise in three dimensional space. In order to solve such large problem sets, different iterative solvers are designed. The Krylov subspace method of GMRES used in conjunction with a geometric multigrid acceleration technique has proven to yield best convergence rates and is relative insensitive to variations in frequency and flow field. This technique has been applied either to invert the system matrix or to accelerate the shift and invert formulation of the Arnoldi algorithm. The resulting solvers are tested on a large variety of different flow configurations.

At first, only coupling of acoustic waves with coherent vortical structures are considered. The LNSEs manage to capture accurately the main acoustic flow interaction processes for the different flow configurations of an area expansion, an orifice and an industrial aeroengine injection system. Comparisons of scattering matrices as well as acoustic energy balances illustrate the quality of the approach and justify all assumptions made. Interestingly, at frequencies where strong fluid dynamic instabilities are present in the flow (only observed in case of a T-joint) deviations occur and the aeroacoustic interaction is significantly over predicted. This effect is attributed to the over prediction of the growth rate of vortical structures which are

convectively transported downstream. Larger growth leads to stronger vortical disturbances and consequently to stronger acoustic-flow interactions. This over prediction, results from an insufficient inclusion of the effect of turbulence which provides a certain physical bound to the coherent vortex growth. This issue can be resolved even in this purely linear framework and future work will be dedicated to this subject.

When a flame is absent, predicting the eigenmodes of a combustion chamber configuration using LNSEs, the presence of the flow generally leads to a significant increase of acoustic damping. Main contributor is the swirling flow produced by the injection system at which multiple shear layers are formed and discharge into the combustion chamber. In addition, acoustic entropy interactions with a stationary flame may further increase the acoustic loss process. For certain frequencies the damping reached by these mechanisms seems to be of much higher order than the damping introduced through perforated screens (cp. Gullaud and Nicoud, 2012). But not only the damping is changed, also the frequencies of oscillations experience a shift in maximum of about $-50\,\mathrm{Hz}$ when the influence of the flow is accounted for. When a flame is introduced, the mean flow can have a stabilizing but also -on the contrary- a destabilizing effect on the thermoacoustic modes. Depending on the characteristics of the flame, even the frequency of oscillations can be shifted by $-150\,\mathrm{Hz}$ for the generic premixed combustor case and of about $-67\,\mathrm{Hz}$ for the experimental test case compared to the zero mean flow case. This may have a drastic effect on the acoustic coupling process with the flame. A method neglecting the mean flow field will hardly be capable of predicting the eigenmodes and stability of the system correctly. However, for the case with lower flow speeds inside the combustor it is still believed that, e.g., a Helmholtz equation is still able to provide relatively accurate results.

The method proposed is very general and has considerable potential to complement current state-of-the-art thermoacoustic and aeroacoustic analysis in the near future. On the one hand, LNSEs can be used to support low-order lumped network model approaches by supplying scattering or transfer matrices of complex flow configurations. If a mean flow field is available, the routine may provide scattering matrices within a few hours until up to a day (depending on the frequency range and frequency resolution). On the other hand, it can be used to verify the existence and stability of eigen-

modes computed by a network model approach or a Helmholtz code. Using this higher order tool, the gap between lower order approaches and an high fidelity LES can be filled.

Despite the method's high potential, there are still some problems involved. As the determination of scattering matrices proved to be highly robust, the problems are mainly associated with the thermoacoustic eigenmode analysis. One problem concerns the observed sensitivity of the eigenmodes to irregularities in boundary conditions and mean flow representation. Another problem is associated with the prediction of a multitude of eigenmodes mostly located at low frequencies which contain physical as well as spurious modes. In such cases, discrimination between physical and unphysical solution becomes difficult. A solution followed in this thesis is to run a Helmholtz solver computation beforehand and to feed the resulting eigenfrequencies as starting values to the LNSEs solver. Also, a re-orthogonalization of eigenvectors, as proposed in Section 4.1.1, may become favorable. In order to extend the current approach to larger systems, the issue of code parallelization must also be considered. At the moment, this cannot be sufficiently realized by Comsol Multiphysics which is inefficient in large parts and is only capable to provide a solid starting ground.

Possibilities of further research employing the developed schemes are multifold. Here, only two of them are mentioned: Inclusion of entropy waves and their coupling in an accelerated flow in downstream turbine vane passage, which possibly leads to low frequency instabilities, can be studied. Experimental tests are readily available in the literature, see. e.g. the papers by Zukoski and Auerbach (1976) and Bake et al. (2009). Furthermore, the here proposed method can be employed to study fluid dynamic instabilities and their respective source regions, the so-called wave-maker region (see Oberleithner et al., 2012). In this case, it is probably advisable to introduce the incompressible assumption before linearizing the equations.

APPENDIX

A Influence of Viscosity on Acoustic Wave Propagation

Derivations in this section are partially based on the lecture series given by Prof. Sujith at the Technical University of Munich in 2011. The section estimates the importance of viscosity for wave propagation problems. Assuming purely one dimensional wave propagation and a medium at rest $\bar{u} = 0$, the linearized equation of momentum yields

$$\frac{\partial u'}{\partial t} = -\frac{1}{\bar{\rho}}\frac{\partial p'}{\partial x} + \nu\frac{\partial^2 u'}{\partial x^2}. \tag{A.1}$$

The equation may be made non dimensional by substituting dimensionless variables into the equation:

$$t^* = \frac{t}{\tau_a}, \quad x^* = \frac{x}{\lambda}, \quad p'^* = \frac{p'}{p_{ref}}, \quad u'^* = \frac{u'}{p_{ref}/\left(\bar{\rho}\bar{c}\right)}, \tag{A.2}$$

using a characteristic acoustic length scale λ_a and time scale τ_a. Substitution, multiplication with $p_{ref}/\bar{\rho}\bar{c}$, and rearrangement of the terms yields

$$\frac{\partial u'^*}{\partial t^*} = -\frac{\partial p'^*}{\partial x^*} + \frac{\Lambda}{2\lambda_a}\frac{\partial^2 u'^*}{\partial (x^*)^2}, \tag{A.3}$$

with the acoustic time and length scale related by $\tau = 1/f = \lambda_a/c$ and viscosity defined as $\nu = c\Lambda/2$ where Λ defines the molecule's mean free path length. Thus, viscosity becomes only important if the coefficient of the viscous term is of the order

$$\frac{\Lambda}{\lambda_a} \sim 1. \tag{A.4}$$

The magnitude of the molecule's free path length is generally of the order $\mathcal{O}(10^{-8}\text{m})$. Thus, only if λ_a is sufficiently small, i.e. the frequency is high, molecular viscosity becomes important for acoustic wave propagation. This is for example the case when computing the noise audible in the far field of

jet engines where high frequency components travel along large distances. Note, however, that any acoustic flow interactions stemming from convective or reactive terms were eliminated for the derivation. The effect of viscosity is much more important for the convectively transported vortical and entropy modes which have much lower length scales $\lambda_v \approx \lambda_s \approx Ma\ \lambda_a$. Thus, the effect of viscosity on aeroacoustic interactions may be much more important to thermoacoustic stability analysis.

B Forms of Transport Equations

B.1 Forms of Energy Conservation Equation

The conservation of energy equation, Eq. (2.3), may be written in very different forms. The present study choses pressure to be the primitive variable to represent energy conservation. This choice is motivated through the fact that the pressure variable can easily be determined experimentally at surfaces and is a conservation variable. Other forms of the energy equation found in literature (e.g. Nicoud and Wieczorek (2009)) employ the entropy variable. However, as entropy is not conserved and can not be measured directly it is not chosen for the present approach. Next, the energy equation is derived in terms of pressure variable starting from its formulation in terms of total energy E,

$$\frac{DE}{Dt} = \frac{\partial u_i \tau_{ij}}{\partial x_j} - \frac{\partial p u_i}{\partial x_i} + \rho f_i u_i - \frac{\partial \dot{q}_i}{\partial x_i}. \tag{B.1}$$

From the Fourier's law for thermal heat conduction q_i is defined as

$$\dot{q}_i = -\lambda \frac{\partial T}{\partial x_i}. \tag{B.2}$$

Substitution of enthalpy $h = e + p/\rho$ then yields

$$\rho \frac{Dh}{Dt} = \frac{Dp}{Dt} + \tau_{ij} \frac{\partial u_i}{\partial x_j} - \frac{\partial q_i}{\partial x_i}. \tag{B.3}$$

Using the equations of state $p = \rho R T$ and $h = c_p T$ and assuming constant c_p and ratio of specific heats κ finally yields

$$\frac{\partial p}{\partial t} + u_i \frac{\partial p}{\partial x_i} + p\kappa \frac{\partial u_i}{\partial x_i} = (\kappa - 1) \left[\dot{q}_V + \tau_{ij} \frac{\partial u_i}{\partial x_j} \right]. \tag{B.4}$$

Note that the conservation of mass equation, Eq. (2.1), was used to derive this equation. Equally, the energy equation can be written in terms of entropy variable s using the entropy formulation of Eq. (2.6) which leads to

$$\frac{Ds}{Dt} = \frac{R}{p}\left(\dot{q}_V + \tau_{ij}\frac{\partial u_i}{\partial x_j}\right). \tag{B.5}$$

B.2 Cylindrical Coordinate System

Often it is advantageous to formulate the transport equations in a cylindrical coordinate system. This is especially the case when considering configurations which are symmetric with respect to the axis of rotation. Then, the transport equations may be formulated in two dimensional space but represent the configuration in a quasi three dimensional manner. Conversion between a Cartesian and a cylindrical coordinate system is done through

$$x = r\cos\theta, \tag{B.6}$$
$$y = r\sin\theta, \tag{B.7}$$
$$z = z, \tag{B.8}$$

where r is the radius and θ defines an angle. The continuity equation then writes

$$\frac{\partial \rho}{\partial t} + \frac{1}{r}\frac{\partial}{\partial r}(\rho r u_r) + \frac{1}{r}\frac{\partial}{\partial \theta}(\rho u_\theta) + \frac{\partial}{\partial z}(\rho u_z) = 0, \tag{B.9}$$

the momentum transport equations equally yields

$$\begin{aligned}\rho\left(\frac{\partial u_r}{\partial t} + u_r\frac{\partial u_r}{\partial r} + \frac{u_\theta}{r}\frac{\partial u_r}{\partial \theta} + u_z\frac{\partial u_r}{\partial z} - \frac{u_\theta^2}{r}\right) &= -\frac{\partial p}{\partial r} \\ &+ \left[\frac{1}{r}\frac{\partial}{\partial r}(r\tau_{rr}) + \frac{1}{r}\frac{\partial}{\partial \theta}\tau_{\theta r} + \frac{\partial}{\partial z}\tau_{zr} - \frac{\tau_{\theta\theta}}{r}\right] + \rho g_r,\end{aligned} \tag{B.10}$$

$$\begin{aligned}\rho\left(\frac{\partial u_\theta}{\partial t} + u_r\frac{\partial u_\theta}{\partial r} + \frac{u_\theta}{r}\frac{\partial u_\theta}{\partial \theta} + u_z\frac{\partial u_\theta}{\partial z} + \frac{u_r u_\theta}{r}\right) &= -\frac{1}{r}\frac{\partial p}{\partial \theta} \\ &+ \left[\frac{1}{r^2}\frac{\partial}{\partial r}(r^2\tau_{r\theta}) + \frac{1}{r}\frac{\partial}{\partial \theta}\tau_{\theta\theta} + \frac{\partial}{\partial z}\tau_{z\theta}\right] + \rho g_\theta,\end{aligned} \tag{B.11}$$

$$\begin{aligned}\rho\left(\frac{\partial u_z}{\partial t} + u_r\frac{\partial u_z}{\partial r} + \frac{u_\theta}{r}\frac{\partial u_z}{\partial \theta} + u_z\frac{\partial u_z}{\partial z}\right) &= -\frac{\partial p}{\partial z} \\ &+ \left[\frac{1}{r}\frac{\partial}{\partial r}(r\tau_{rz}) + \frac{1}{r}\frac{\partial}{\partial \theta}\tau_{\theta z} + \frac{\partial}{\partial z}\tau_{zz}\right] + \rho g_z.\end{aligned} \tag{B.12}$$

and finally the energy equation using the pressure variable formulation,

$$\begin{aligned}\frac{\partial p}{\partial t}+u_r\frac{\partial p}{\partial r}+u_\theta\frac{1}{r}\frac{\partial p}{\partial \theta}+u_z\frac{\partial p}{\partial z}+p\kappa\left(\frac{1}{r}\frac{\partial}{\partial r}(ru_r)+\frac{1}{r}\frac{\partial u_\theta}{\partial \theta}+\frac{\partial u_z}{\partial z}\right)=\\ +(\kappa-1)\,\dot{q}_V+(\kappa-1)\left[\tau_{rr}\frac{\partial u_r}{\partial r}+\tau_{r\theta}\left(\frac{1}{r}\frac{\partial u_r}{\partial \theta}-\frac{u_\theta}{r}\right)+\tau_{rz}\frac{\partial u_r}{\partial z}\right.\\ \left.+\tau_{\theta r}\frac{\partial u_\theta}{\partial r}+\tau_{\theta\theta}\left(\frac{1}{r}\frac{\partial u_\theta}{\partial \theta}-\frac{u_r}{r}\right)+\tau_{\theta z}\frac{\partial u_\theta}{\partial z}+\tau_{zr}\frac{\partial u_z}{\partial r}+\tau_{z\theta}\left(\frac{1}{r}\frac{\partial u_z}{\partial \theta}\right)+\tau_{zz}\frac{\partial u_z}{\partial z}\right].\end{aligned} \tag{B.13}$$

The components of the viscous stress tensor are now defined as,

$$\tau_{rr} = \mu\left[2\frac{\partial u_r}{\partial r}-\frac{2}{3}\left(\frac{1}{r}\frac{\partial}{\partial r}(ru_r)+\frac{1}{r}\frac{\partial u_\theta}{\partial \theta}+\frac{\partial u_z}{\partial z}\right)\right], \tag{B.14}$$

$$\tau_{\theta\theta} = \mu\left[2\left(\frac{1}{r}\frac{\partial u_\theta}{\partial \theta}+\frac{u_r}{r}\right)-\frac{2}{3}\left(\frac{1}{r}\frac{\partial}{\partial r}(ru_r)+\frac{1}{r}\frac{\partial u_\theta}{\partial \theta}+\frac{\partial u_z}{\partial z}\right)\right], \tag{B.15}$$

$$\tau_{zz} = \mu\left[2\frac{\partial u_z}{\partial z}-\frac{2}{3}\left(\frac{1}{r}\frac{\partial}{\partial r}(ru_r)+\frac{1}{r}\frac{\partial u_\theta}{\partial \theta}+\frac{\partial u_z}{\partial z}\right)\right] \tag{B.16}$$

$$\tau_{r\theta} = \tau_{\theta r}=\mu\left[r\frac{\partial}{\partial r}\left(\frac{u_\theta}{r}\right)+\frac{1}{r}\frac{\partial u_r}{\partial \theta}\right], \tag{B.17}$$

$$\tau_{\theta z} = \tau_{z\theta}=\mu\left(\frac{1}{r}\frac{\partial u_z}{\partial \theta}+\frac{\partial u_\theta}{\partial z}\right), \tag{B.18}$$

$$\tau_{zr} = \tau_{rz}=\mu\left(\frac{\partial u_r}{\partial z}+\frac{\partial u_z}{\partial r}\right), \tag{B.19}$$

Next, the problem is reduced to two dimensions using $u_\theta = 0$ and assuming rotational symmetry along $r = 0$ and $\partial/\partial\theta = 0$,

$$\frac{\partial \rho}{\partial t}+\frac{1}{r}\frac{\partial}{\partial r}\left(\rho r u_r\right)+\frac{\partial}{\partial z}\left(\rho u_z\right)=0, \tag{B.20}$$

$$\begin{aligned}\rho\left(\frac{\partial u_r}{\partial t}+u_r\frac{\partial u_r}{\partial r}+u_z\frac{\partial u_r}{\partial z}\right)=-\frac{\partial p}{\partial r}\\ +\mu\left[\frac{\partial^2 u_r}{\partial z^2}+\frac{4}{3}\frac{\partial^2 u_r}{\partial r^2}+\frac{1}{3}\frac{\partial^2 u_z}{\partial z\partial r}+\frac{4}{3r}\frac{\partial u_r}{\partial r}-\frac{4}{3r^2}u_r\right]+\rho g_r,\end{aligned} \tag{B.21}$$

$$\rho\left(\frac{\partial u_z}{\partial t}+u_r\frac{\partial u_z}{\partial r}+u_z\frac{\partial u_z}{\partial z}\right)=-\frac{\partial p}{\partial z}$$
$$+\mu\left[\frac{\partial^2 u_z}{\partial r^2}+\frac{4}{3}\frac{\partial^2 u_z}{\partial z^2}+\frac{1}{3}\frac{\partial^2 u_r}{\partial z\partial r}+\frac{1}{3r}\frac{\partial u_r}{\partial z}+\frac{1}{r}\frac{\partial u_z}{\partial r}\right]+\rho g_z, \tag{B.22}$$

$$\frac{\partial p}{\partial t}+u_r\frac{\partial p}{\partial r}+u_z\frac{\partial p}{\partial z}+p\kappa\left(\frac{1}{r}\frac{\partial}{\partial r}(ru_r)+\frac{\partial u_z}{\partial z}\right)=(\kappa-1)\,\dot{q}_V$$
$$+(\kappa-1)\left[\tau_{rr}\frac{\partial u_r}{\partial r}+\tau_{rz}\frac{\partial u_r}{\partial z}+\tau_{zr}\frac{\partial u_z}{\partial r}+\tau_{zz}\frac{\partial u_z}{\partial z}\right]. \tag{B.23}$$

The equations can be linearized in the same way as described in Chapter 2. In order to keep the formulation more compact we introduce the index notation again $i,j=(r,z)$. Linearization leads to

$$\frac{\partial \rho'}{\partial t}+\bar{\rho}\frac{\partial u_i'}{\partial x_i}+\rho'\frac{\partial \bar{u}_i}{\partial x_i}+\bar{u}_i\frac{\partial \rho'}{\partial x_i}+u_i'\frac{\partial \bar{\rho}}{\partial x_i}+\frac{\bar{\rho}u_r'}{r}+\frac{\bar{u}_r\rho'}{r}=0 \tag{B.24}$$

$$\frac{\partial u_r'}{\partial t}+\bar{u}_j\frac{\partial u_r'}{\partial x_j}+u_j'\frac{\partial \bar{u}_r}{\partial x_j}+\frac{1}{\bar{\rho}}\frac{\partial \hat{p}}{\partial r}-\frac{\hat{\rho}}{\bar{\rho}^2}\frac{\partial \bar{p}}{\partial r}=$$
$$\mu\left[\frac{\partial^2 u_r'}{\partial z^2}+\frac{4}{3}\frac{\partial^2 u_r'}{\partial r^2}+\frac{1}{3}\frac{\partial^2 u_z'}{\partial r\partial z}+\frac{4}{3r}\frac{\partial u_r'}{\partial r}-\frac{4}{3r^2}u_r'\right]+\rho' g_r \tag{B.25}$$

$$\frac{\partial u_z'}{\partial t}+\bar{u}_j\frac{\partial u_z'}{\partial x_j}+u_j'\frac{\partial \bar{u}_z}{\partial x_j}+\frac{1}{\bar{\rho}}\frac{\partial \hat{p}}{\partial z}-\frac{\hat{\rho}}{\bar{\rho}^2}\frac{\partial \bar{p}}{\partial z}=$$
$$\mu\left[\frac{\partial^2 u_z'}{\partial r^2}+\frac{4}{3}\frac{\partial^2 u_z'}{\partial z^2}+\frac{1}{3}\frac{\partial^2 u_r'}{\partial z\partial r}+\frac{1}{3r}\frac{\partial u_r'}{\partial z}+\frac{1}{r}\frac{\partial u_z'}{\partial r}\right]+\rho' g_z. \tag{B.26}$$

B.3 Matrix notation of LNSEs

Eqs. (2.8)-(2.10) can also be written in compact matrix form notation which may allow for a simpler differentiation between the individual terms (convection, diffusion, reaction) contributing to the acoustic problem. Using the general variable $\phi=(\hat{\rho},\hat{u}_x,\hat{u}_y,\hat{u}_z,\hat{p})^T$, all five linearized equations of mass, momentum and energy can be written in form of

$$i\omega\phi+\frac{\partial \mathbf{A}_i\phi}{\partial x_i}+\mathbf{C}\phi-\mathbf{D}\phi=\mathbf{f}_s, \tag{B.27}$$

for a cylindrical coordinate system. x_i is the coordinate vector and is specified through $x_i=(r,z)$. Matrices $\mathbf{A}_i$, $\mathbf{C}$ and $\mathbf{D}$ are the convective matrices

in the i-th direction, the reactive matrix and the diffusive matrix. $\mathbf{f}_s$ is a source vector. The constant coefficient convective matrices $\mathbf{A}_i$ writes

$$\mathbf{A}_x = \begin{pmatrix} \bar{u}_x & \bar{\rho} & 0 & 0 & 0 \\ 0 & \bar{u}_x & 0 & 0 & 1/\bar{\rho} \\ 0 & 0 & \bar{u}_z & 0 & 0 \\ 0 & 0 & 0 & \bar{u}_x & 0 \\ 0 & \kappa\bar{p} & 0 & 0 & \bar{u}_x \end{pmatrix}, \mathbf{A}_y = \begin{pmatrix} \bar{u}_y & 0 & \bar{\rho} & 0 & 0 \\ 0 & \bar{u}_y & 0 & 0 & 0 \\ 0 & 0 & \bar{u}_y & 0 & 1/\bar{\rho} \\ 0 & 0 & 0 & \bar{u}_y & 0 \\ 0 & 0 & \kappa\bar{p} & 0 & \bar{u}_y \end{pmatrix}, \tag{B.28}$$

$$\mathbf{A}_z = \begin{pmatrix} \bar{u}_z & 0 & 0 & \bar{\rho} & 0 \\ 0 & \bar{u}_z & 0 & 0 & 0 \\ 0 & 0 & \bar{u}_z & 0 & 0 \\ 0 & 0 & 0 & \bar{u}_z & 1/\bar{\rho} \\ 0 & 0 & 0 & \kappa\bar{p} & \bar{u}_z \end{pmatrix}, \tag{B.29}$$

while the reactive matrix reads

$$\mathbf{C} = \begin{pmatrix} 0 & 0 & 0 & \dots \\ -\frac{1}{\bar{\rho}^2}\frac{\partial\bar{p}}{\partial x_1} & -\left(\frac{\partial\bar{u}_2}{\partial x_2}+\frac{\partial\bar{u}_3}{\partial x_3}\right) & \frac{\partial\bar{u}_1}{\partial x_2} & \dots \\ -\frac{1}{\bar{\rho}^2}\frac{\partial\bar{p}}{\partial x_2} & \frac{\partial\bar{u}_2}{\partial x_1} & -\left(\frac{\partial\bar{u}_1}{\partial x_1}+\frac{\partial\bar{u}_3}{\partial x_3}\right) & \dots \\ -\frac{1}{\bar{\rho}^2}\frac{\partial\bar{p}}{\partial x_3} & \frac{\partial\bar{u}_3}{\partial x_1} & \frac{\partial\bar{u}_3}{\partial x_2} & \dots \\ 0 & (1-\kappa)\frac{\partial\bar{p}}{\partial x_1} & (1-\kappa)\frac{\partial\bar{p}}{\partial x_2} & \dots \end{pmatrix}$$
$$\begin{pmatrix} \dots & 0 & 0 \\ \dots & \frac{\partial\bar{u}_1}{\partial x_3} & \frac{1}{\bar{\rho}^2}\frac{\partial\bar{\rho}}{\partial x_1} \\ \dots & \frac{\partial\bar{u}_2}{\partial x_3} & \frac{1}{\bar{\rho}^2}\frac{\partial\bar{\rho}}{\partial x_2} \\ \dots & -\left(\frac{\partial\bar{u}_1}{\partial x_1}+\frac{\partial\bar{u}_2}{\partial x_2}\right) & \frac{1}{\bar{\rho}^2}\frac{\partial\bar{\rho}}{\partial x_2} \\ \dots & (1-\kappa)\frac{\partial\bar{p}}{\partial x_3} & (\kappa-1)\left(\frac{\partial\bar{u}_1}{\partial x_1}+\frac{\partial\bar{u}_2}{\partial x_2}+\frac{\partial\bar{u}_3}{\partial x_3}\right) \end{pmatrix}. \tag{B.30}$$

Making use of the Schwarz's law of continuous second derivatives and changing differentiation order, the diffusive matrix yields

$$\mathbf{D} = \nu \begin{pmatrix} 0 & 0 & 0 & 0 & 0 \\ 0 & \frac{4}{3}\frac{\partial^2}{\partial x_1^2}+\frac{\partial^2}{\partial x_2^2}+\frac{\partial^2}{\partial x_3^2} & \frac{1}{3}\frac{\partial^2}{\partial x_1\partial x_2} & \frac{1}{3}\frac{\partial^2}{\partial x_1\partial x_3} & 0 \\ 0 & \frac{1}{3}\frac{\partial^2}{\partial x_1\partial x_2} & \frac{\partial^2}{\partial x_1^2}+\frac{4}{3}\frac{\partial^2}{\partial x_2^2}+\frac{\partial^2}{\partial x_3^2} & \frac{1}{3}\frac{\partial^2}{\partial x_2\partial x_3} & 0 \\ 0 & \frac{1}{3}\frac{\partial^2}{\partial x_1\partial x_3} & \frac{1}{3}\frac{\partial^2}{\partial x_2\partial x_3} & \frac{\partial^2}{\partial x_1^2}+\frac{\partial^2}{\partial x_2^2}+\frac{4}{3}\frac{\partial^2}{\partial x_3^2} & 0 \\ 0 & 0 & 0 & 0 & 0 \end{pmatrix} \tag{B.31}$$

Finally, the source vector defined for thermoacoustic problems is defined as

$$\mathbf{f_s} = \begin{pmatrix} 0 \\ 0 \\ 0 \\ 0 \\ (\kappa - 1)\, \dot{q}'_V \end{pmatrix}. \tag{B.32}$$

C Acoustic Energy

The conservation of acoustic energy can be written in differential form. It states that the temporal change of acoustic energy in a system plus the acoustic energy flux out of the boundaries is equal to the acoustic sources inside the system.

$$\frac{\partial E}{\partial t} + \frac{\partial I_i}{\partial x_i} = S, \tag{C.1}$$

by integration over a domain Ω and applying the gaussian divergence theorem one obtains

$$\int_\Omega \frac{\partial E}{\partial t} \; d\Omega + \int_\Gamma I_i n_i \; d\Gamma = \int_\Omega D \; d\Omega. \tag{C.2}$$

C.1 Acoustic Energy in a Quiescent Medium

Considering a fluid without motion $\bar{u}_i = 0$, and hence $\bar{p} = const.$ and assuming $\bar{\rho} = const.$, the differential equation describing the external energy of an acoustic system can be calculated from the momentum equation, Eq. (2.9), times perturbations of mass flow $u_i' \bar{\rho}$ yielding

$$\frac{\partial}{\partial t}\left(\frac{\bar{\rho} u_i'^2}{2}\right) + u_i' \frac{\partial p'}{\partial x_i} = 0. \tag{C.3}$$

The internal energy is expressed by the linearized Euler energy equation, Eq. (2.24), multiplied by $p'/(\bar{\rho}\bar{c}^2)$ which leads to

$$\frac{\partial}{\partial t}\left(\frac{p'^2}{2\bar{\rho}\bar{c}^2}\right) + p' \frac{\partial u_i'}{\partial x_i} = \frac{\kappa - 1}{\bar{\rho}\bar{c}^2} p' \dot{q}_V'. \tag{C.4}$$

The total overall energy, composed of internal and external energy, is obtained by a simple addition of Eq. (C.3) and Eq. (C.4), yielding

$$\underbrace{\frac{\partial}{\partial t}\left(\frac{p'^2}{2\bar{\rho}\bar{c}^2} + \frac{\bar{\rho} u_i'^2}{2}\right)}_{E} + \frac{\partial}{\partial x_i} \underbrace{(p' u_i')}_{I_i} = \underbrace{\frac{\kappa - 1}{\bar{\rho}\bar{c}^2} p' \dot{q}_V'}_{S}. \tag{C.5}$$

Note that the total energy E of the system consists of two terms. One resembles the kinetic energy of the system $E_{kin} = p'^2/2\bar{\rho}\bar{c}^2$. The other can be interpreted as the amount of energy needed for an isentropic compression of an ideal gas and hence defines the potential energy of the system. One can clarify this consideration by a simple consideration, if

$$E_{pot} = -\frac{1}{\bar{V}} \int_{\bar{V}}^{V} p \, dV, \tag{C.6}$$

defines the potential energy of a given system. Its differential volume can be rewritten as

$$dV = \frac{\bar{V}}{\bar{v}} dv, \tag{C.7}$$

where $v = 1/\rho$. Applying the isentropic change of state

$$v = \bar{p}^{1/\kappa} p^{-1/\kappa} \bar{v}, \tag{C.8}$$

and linearizing the equation of the state around $\bar{p}$

$$\left.\frac{dv}{dp}\right|_{p=\bar{p}} = \bar{p}^{1/\kappa} \frac{-1}{\kappa} \bar{p}^{-1/\kappa-1} \bar{v} = -\frac{\bar{v}}{\kappa \bar{p}}, \tag{C.9}$$

finally leads to

$$E_{pot} = -\frac{1}{\bar{V}} \int_{0}^{V} p \frac{\bar{V}}{\bar{v}} \, dv = -\frac{1}{\bar{V}} \int_{0}^{p'} p \frac{\bar{V}}{\bar{v}} \frac{-\bar{v}}{\kappa \bar{p}} \, dp = \frac{p'^2}{2\bar{c}^2 \bar{\rho}}. \tag{C.10}$$

Assuming that the acoustic flux over the boundaries I_i is zero, the total energy inside the system is directly proportional to the source term S. In this case if $S > 0$, the acoustic energy of the system increases, i.e. $\partial E/\partial t > 0$, and the system becomes unstable. This condition is known as the Rayleigh criterion of Eq. (1.1).

C.2 Acoustic Energy in an Isentropic Medium

To retrieve the acoustic energy from an isentropic medium is somewhat more complex as acoustic-flow coupling becomes important. For the sake of clarity only the derivation is shortly explained next: Starting point is

the multiplication of the linearized mass equation, Eq. (2.21), linearized Navier-Stokes momentum equation, Eq. (2.22), and the linearized energy equation, Eq. (2.23), with $\bar{u}_j u'_j$, $u'_i\bar{\rho} + \bar{u}_i\rho'$ and $p'/(\kappa\bar{p})$, respectively. Influence of viscosity is neglected ($\lambda = \nu = 0$). Adding the linearized mass equation to the linearized momentum and energy equations, making use of the isentropic relation, Eq. (2.18), and performing some math one finally obtains the energy equation sorted in the form of Eq. (C.1):

$$\begin{aligned}\frac{\partial}{\partial t}\underbrace{\left(\frac{\bar{\rho}u_i'^2}{2} + \bar{u}_i\frac{\bar{\rho}}{\bar{p}\kappa}p'u'_i + \frac{1}{2\kappa\bar{p}}p'^2\right)}_{E} + \frac{\partial}{\partial x_i}\underbrace{\left(u'_ip' + \frac{p'^2\bar{u}_i}{\bar{p}\kappa} + u'_j\bar{\rho}u'_i\bar{u}_j + \frac{p'}{\bar{p}\kappa}\bar{u}_j\bar{\rho}\bar{u}_iu'_j\right)}_{I_i} \\ = \underbrace{\frac{\kappa-1}{\kappa\bar{p}}p'\dot{q}'_V + \left(\bar{\rho}\frac{\partial u'_j}{\partial x_i} - \frac{\bar{\rho}p'}{\bar{p}\kappa}\frac{\partial\bar{u}_j}{\partial x_i}\right)\left(\bar{u}_iu'_j + u'_i\bar{u}_j\right)}_{S}.\end{aligned} \tag{C.11}$$

The contributions to the source term S can be interpreted as fluctuating heat release and vorticity. Note that steady-state conservation of mass, momentum and adiabatic energy was used for the derivation.

$$\bar{u}_i\frac{\partial\bar{\rho}}{\partial x_i} = -\bar{\rho}\frac{\partial\bar{u}_i}{\partial x_i}, \tag{C.12}$$

$$\bar{u}_j\frac{\partial\bar{u}_i}{\partial x_j} = -\frac{1}{\bar{\rho}}\frac{\partial\bar{p}}{\partial x_i}, \tag{C.13}$$

$$\bar{u}_i\frac{\partial\bar{p}}{\partial x_i} = -\kappa\bar{p}\frac{\partial\bar{u}_i}{\partial x_i}. \tag{C.14}$$

C.3 Stability Considerations of Acoustic Energy

The growth or damping rate of the acoustic energy α can also be evaluated from the energy balance of a given system. By assuming that the amplitudes of harmonic fluctuations slowly change with time

$$p' = \mathrm{Re}\left[\hat{p}(x)e^{i\omega t}\right], \quad u'_i = \mathrm{Re}\left[\hat{u}_i(x)e^{i\omega t}\right], \quad \dot{q}'_V = \mathrm{Re}\left[\hat{\dot{q}}_V(x)e^{i\omega t}\right], \tag{C.15}$$

and substituting this ansatz into the acoustic energy balance equations Eq. (C.5) or Eq. (C.11) leads to the following equation for α

$$\alpha = \frac{\mathscr{S} - \mathscr{I}_i}{2\mathscr{E}}. \tag{C.16}$$

$\mathscr{E}$ is a measure of the overall acoustic energy content of a combustion system, $\mathscr{I}_i$ is the acoustic flux leaving the combustor and $\mathscr{S}$ defines the volume averaged source term, precisely speaking

$$\mathscr{E} = \int_{\Omega} E \; d\Omega, \qquad \mathscr{I}_i = \int_{\partial\Omega} I_i n_i \; d\Gamma, \qquad \mathscr{S} = \int_{\Omega} S \; d\Omega. \tag{C.17}$$

Thus, the growth rate of acoustic energy α can be evaluated as the difference between the combustion source term $\mathscr{S}$ and the acoustic losses at the boundaries $\mathscr{I}_i$. Instability for a given pulsation ω occures if the growth rate exceeds values greater then one ($\alpha > 1$), which is equivalent in writing

$$\mathscr{I}_i > \mathscr{S}. \tag{C.18}$$

Whether these functions grow or decay in time for a given pulsation ω will determine the stability of the system.

D Additional LNSEs Validation Testcases

Other than the test cases considered in Chapters 5-6 additional validation cases were considered in order to generate a thorough understanding of the underlying physical phenomena. Apart from very generic one dimensional axial flow configurations, which are not mentioned herein, two different cases investigating aeroacoustic interactions are considered. These comprise a generic one dimensional shear layer which promotes the growth of a Kelvin-Helmholtz instability at a certain pulsation ω and an open pipe termination where a jet issues in a quiescent atmosphere. For the first test case an analytical solution exists, while for the second test case experimental data is available.

D.1 Radiation and Refraction in Two Dimensional Shear Layer

The first problem considered deals with the prediction of radiation and refraction of sound through a two dimensional shear layer (Morris and Agarwal, 2004). A time-harmonic acoustic energy source is located inside a two dimensional jet. It may be thought of as an acoustic source arising from turbulent jet noise. All acoustic waves the source generates are radiated and refracted by the jet shear layer. An hydrodynamic instability wave is triggered by the acoustic source which is convected downstream by the mean flow.

In combustion chamber flows general multiple shear layers are present, e.g. the flow expansion out of the swirl injection system or at the emitting jets from air dilution holes or perforated screens. Therefore, the problem is solved to prove the LEE capability (or LNSE) to capture the mean flow effects of refraction and convection of sound waves by shear layers. In

a confined combustion chamber environment refraction and scattering of sound may result in phase shifts for the longitudinal wave propagation which may alter the thermoacoustic feedback loop.

The baseline flow is parallel $\bar{u}_2 = 0$ and the unidirectional sheared flow is described through a Gaussian function

$$\bar{u}_1(y) = \begin{cases} \bar{u}_0 \exp\left[-\ln(2)\left(y/b - h/b\right)^2\right] & y \geq h \\ \bar{u}_0 & 0 \leq y \leq h \end{cases}, \tag{D.1}$$

while the density relation is deduced from the Crocco-Busemann relation

$$\frac{\bar{\rho}_0}{\bar{\rho}(y)} = \frac{\bar{T}_\infty}{\bar{T}_0} - \left(\frac{\bar{T}_\infty}{\bar{T}_0} - 1\right)\frac{\bar{u}(y)}{\bar{u}_0} + \frac{\kappa - 1}{2} M_0^2 \frac{\bar{u}(y)}{\bar{u}_0}\left(1 - \frac{\bar{u}(y)}{\bar{u}_0}\right) \tag{D.2}$$

where the subscripts $'0'$ define the values at the center axis of the jet. The time-harmonic acoustic source term is given by

$$f = A \exp\left[-\left(B_x x^2 + B_y y^2\right)\right]. \tag{D.3}$$

The problems parameters are $M_0 = 0.789$, $T_0 = 600\,\mathrm{K}$, $T_\infty = 300\,\mathrm{K}$, $R = 287\,\mathrm{m^2\ K^{-1}\ s^{-2}}$, $\kappa = 1.4$, $b = 1.3$, $A = 10^{-3}\mathrm{kg\ m^{-2}\ s^{-3}}$, $B_x = 0.04\log(2)\mathrm{m}^{-2}$, $B_y = 0.32\log(2)\mathrm{m}^{-2}$. The mean pressure is constant $\bar{p} = \bar{p}_\infty = 103\,330\,\mathrm{kg\ m^{-1}\ s^{-2}}$. The Strouhal number is $St = 0.087$ based on the center jet velocity $\bar{u}_0$ and the jet diameter $2b$. At a pulsation $\omega_0 = 76\,\mathrm{rad\ s^{-1}}$ the acoustic source triggers a hydrodynamic instability. This is the pulsation for which the LEEs are solved.

The computational domain expands from $[x_{min}, x_{max}] \times [y_{min}, y_{max}] = [-250, 225] \times [0, 100]$ and contains a physical domain and a buffer zone. The purpose of a buffer zone is to avoid acoustic reflections from computational boundaries by the introduction of acoustic damping. Here, acoustic waves decay exponentially by prescribing an artificial imaginary part to the otherwise purely real frequency f. At $y = 0$ a symmetry boundary is placed. The computational mesh uses rectangular elements 99×45. Near the acoustic source, at the origin of the problem, the mesh is clustered in x and y direction in order to better resolve the mean flow and the acoustic source. This problem corresponds to the Problem 1 of Category 4 in the 4th CAA Workshop on Benchmark Problems (Morris and Agarwal, 2004).

D.1.1 Analytical Solution

The numerical generated solution is compared to the analytic solution provided by Agarwal et al. (2004). Starting with the frequency space formulation of the LEEs, the authors reduce the system of equations to a single third-order partial differential equation. Its third order differential operator is the well-known Lilley wave operator. By applying a Fourier transform in streamwise x-direction the Lilley operator is reduced to a second order ordinary differential Rayleigh operator. After integration of the Rayleigh equation in the cross-stream direction and inverse Fourier transform in x-direction the final solution is obtained.

D.1.2 Unstable Hydrodynamic Solution

When predicting acoustic propagation phenomena in a shear layer using LEEs, the shear layer will exhibit instability at a certain frequency. Many authors claim that these instabilities are non-physical. However, this requires a more differentiated consideration: The occurrence of a hydrodynamic instability is completely physical but its unbounded growth is not, since in reality it is suppressed by viscosity and non-linear effects. In fact, every shear layer with inflection points exhibits instability at certain frequencies (cp. Michalke, 1965). In this sense, it may be advantageous to include viscosity by employing the LNSEs instead of the non-viscous LEEs, since LNSEs reduce the growth of vortical scales by including the influence of viscosity. To be consistent with the analytical solution which was derived for a non-viscous flow, only the LEEs are considered.

The unstable solution of the LEEs is presented in Fig. D.1 and compared to its respective analytical solution. The LNSEs are solved using 3rd order Lagrangian finite elements and a SUPG finite element scheme. An hydrodynamic instability is triggered in close proximity of the acoustic source and is convected in downstream direction, obscuring the acoustic solution in this area. Its wavelength is much smaller compared to the wavelength of the corresponding acoustic signal. The existence and spatial growth of the instability at the distinct pulsation $\omega = 76\,\mathrm{s}^{-1}$ is accurately captured by the LEEs solver.

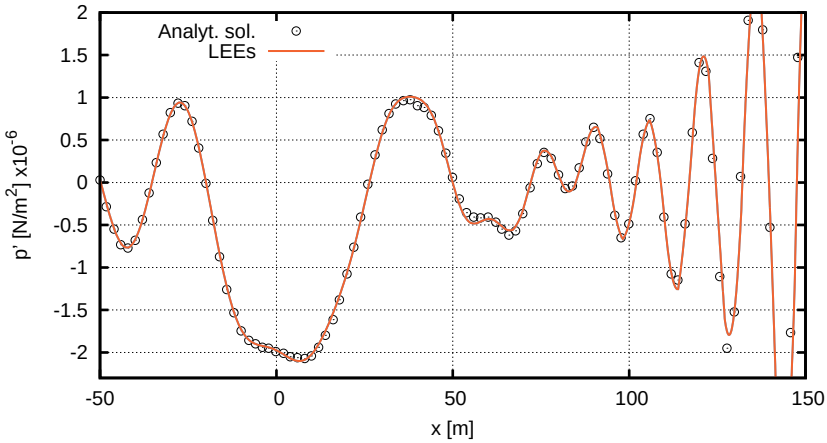

Figure D.1: Fluctuating pressure distribution in the physical domain along line $y = 15$. Acoustic solution contains a hydrodynamic instability wave. Comparison of LEE computation and analytic solution.

D.1.3 Purely Acoustic Solution

In many aeroacoustic applications the triggering of a Kelvin-Helmholtz instability is not desired, since the fluid dynamic instability wave obscures the acoustic solution (as seen in Fig. D.1). For such applications, it is a main aim to retrieve a clear picture of the acoustic wave propagation phenomena in the computational domain. To suppress the triggering of the instability wave in the LEEs, Rao and Morris (2006) have used a SUPG finite element stabilization technique in conjunction with a buffer layer at the domain boundaries. The authors argue that with fine tuning of the SUPG scheme, buffer layer region as well as the numerical mesh employed, the hydrodynamically unstable component of the solution may be extracted.

It was tried to replicate their results by employing the same technique and approximately the same discretization scheme and order but did not succeed directly. In the current investigations their proposed technique was not found robust in extracting the instability wave from the solution. However, a solution solely based on the acoustic waves could finally be obtained mostly by means of calibrating the buffer layer and mesh by trial and error. Fig. D.2 shows that the predicted solution captures the analytically stable solution. Therefore, it is concluded that the radiation and refraction of sound through a shear layer is predicted by the LEEs quite accurately. The two dimensional acoustic field is plotted in Fig. D.3. It shows the typical silence region in the wake of the jet.

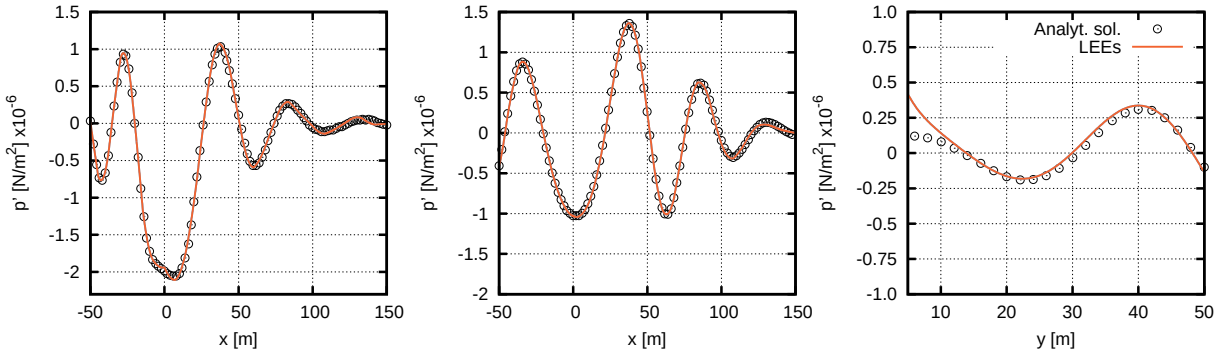

Figure D.2: Fluctuating pressure distribution p' along line $y = 15$ (left), $y = 50$ (middle) and $x = 100$ (right) of purely acoustic solution, Comparison of LEE computation and analytic solution.

The picture drawn from the aforementioned publication of Rao and Morris (2006) may implicate that the SUPG technique is a highly diffusive scheme. This is not the case. It is believed that the explicit distribution of mesh elements, order of shape functions and buffer layer lead to the suppression of the instability wave. Explicitly the mesh resolution in the source region governs the presence of the instability wave. This argumentation is supported by the fact that by switching off the SUPG finite element stabilization scheme for the hydrodynamically stable solution, the solution is not altered and does not change into the unstable regime of Section D.1.2.

The purely acoustic solution is retrieved in order to study the prediction capabilities of LEEs for sound radiation and refraction in a jet flow. It is believed that by suppressing the instability wave, main aeroacoustic interaction effects cannot be captured accurately as acoustic waves may not interact with vortical structures. This effect was found to be a main driver of acoustic losses inside a multidimensional flow field.

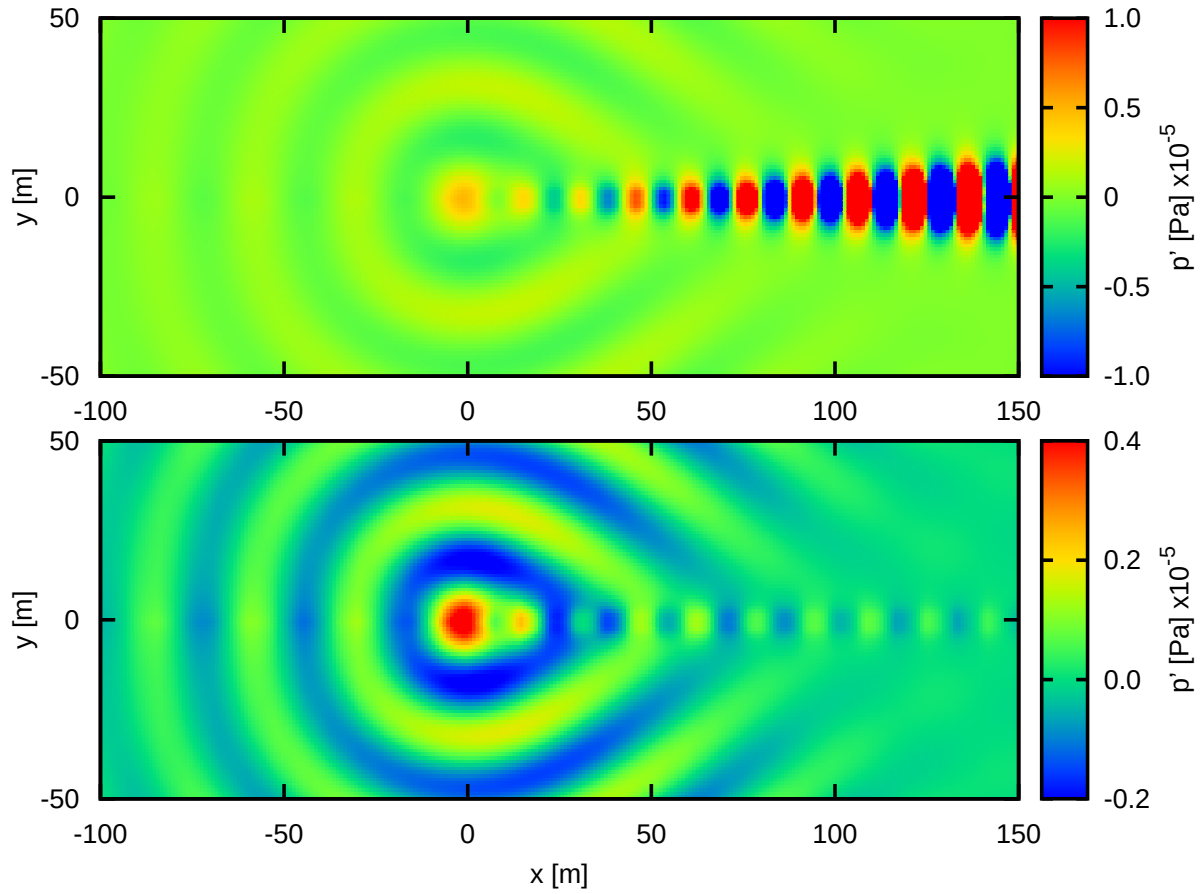

Figure D.3: Acoustic field of fluctuating pressure including the hydrodynamic instability wave (upper graph) and absence of an instability wave (lower graph) of the mean flow. Solution of the LEEs for the benchmark problem one of category four in (Morris and Agarwal, 2004).

D.2 Acoustic Reflection of an Open Pipe Termination

In the second additional test case the LNSE procedure described in Section 3.3.5 is modified to determine the reflection coefficient of an open pipe termination. For this case a variety of experimentally measured cold flow configurations and analytical models exist for which the present technique can be validated. However, as this case can be interpreted as the outlet of a gas turbine, the jet temperatures are generally significantly elevated compared to atmosphere. For this conditions little-to-non validation data exists so far. Therefore the LNSEs technique is used to get into the range of higher temperature ratios of $\bar{T}_{jet}/\bar{T}_{\infty}$ and to assess the reflection coefficient of a pipe termination with different temperature ratios. This is done in the

publication of Jörg et al. (2013) and is not further illustrated herein. There, also deviations to the existing theory by Munt (1977) are assessed.

E Helmholtz Solver

E.1 Governing Equation

For a medium at rest the LNSEs reduce to a single wave or Helmholtz equation in time, Eq. (2.24), and frequency domain, Eq. (2.25), respectively. These type of equations were already derived in Section 2.4 but are recalled herein for sake of completeness. As the mean flow is assumed to vanish only acoustic waves propagate, while vorticity and entropy waves do not propagate. The wave equation incorporating a heat release source term writes,

$$\frac{1}{\bar{c}^2}\frac{\partial^2 p'}{\partial t^2} - \bar{\rho}\frac{\partial}{\partial x_i}\left(\frac{1}{\bar{\rho}}\frac{\partial p'}{\partial x_i}\right) = \frac{(\kappa-1)}{\bar{c}^2}\frac{\partial \dot{q}'_V}{\partial t}, \tag{E.1}$$

where the RHS source term is frequently modeled as a function of a time delayed velocity fluctuation at a reference point in the burner mouth. It requires the knowledge about of the time history of acoustic states at that position. This is not favorable and complicates the treatment considerably. Moreover, the treatment of impedance boundary conditions becomes more complicated and therefore it is advantageous to introduce the harmonic assumption, transforming the wave equation into frequency space,

$$-\frac{\omega^2}{\bar{c}^2}\hat{p} - \bar{\rho}\frac{\partial}{\partial x_i}\left(\frac{1}{\bar{\rho}}\frac{\partial \hat{p}}{\partial x_i}\right) = i\omega\frac{\kappa-1}{\bar{c}^2}\hat{\dot{q}}_V. \tag{E.2}$$

Using the linearized momentum Eq. (2.22) and the flame model, Eq. (2.34), the volumetric heat source translates to

$$\hat{\dot{q}}_V = \frac{\bar{\dot{q}}_V}{i\omega\bar{\rho}(x_{ref})} n_l(x_i) e^{-i\omega\tau_l(x_i)} \frac{\partial \hat{p}(x_{ref})}{\partial x_i} n_{i,ref}. \tag{E.3}$$

E.2 Boundary Conditions

The boundary conditions derived in Section 2.7 for the LNSEs are also valid for the wave- and Helmholtz equation when assuming a flow at rest. These conditions include velocity fluctuations as unknown variables. However, in the Helmholtz equation velocity fluctuations are not primitive variables which are solved. They are rather directly coupled to the pressure fluctuations through Eq. (2.22). This requires to reformulate the important boundary conditions and has implications on the finite element method described later. Since only one scalar equations is solved, only one condition needs to be imposed on every boundary of the computational domain. For a solid, non-moving wall at which velocity fluctuations vanish $\hat{u}_i = 0$, use of Eq. (2.22) translates the boundary condition from a Dirichlet to a Neumann type, i.e.

$$\frac{\partial \hat{p}}{\partial x_i} n_i = 0, \qquad \text{on } \partial\Omega_N. \tag{E.4}$$

This boundary is also frequently used as a fully reflecting inlet at which velocity fluctuations vanish. The condition can also be imposed at a silencing chamber, where the velocity of the flow is strictly imposed. At open outlets, where the outer pressure is imposed strongly onto the flow domain, pressure fluctuations vanish. In case of a vanishing mean flow, this yields a fully reflecting boundary condition,

$$\hat{p} = 0, \qquad \text{on } \partial\Omega_D. \tag{E.5}$$

In the most general case of a complex reduced impedance $Z = \hat{p}/\bar{\rho}\bar{c}\hat{u}_i n_i$ the boundary condition translates to a Robin type of condition for the acoustic pressure,

$$\frac{\partial \hat{p}}{\partial x_i} n_i + \frac{i\omega}{\bar{c}Z}\hat{p} = 0, \qquad \text{on } \partial\Omega_Z. \tag{E.6}$$

Note that a treatment of the impedance boundary becomes non-trivial in time space, since the second term on the LHS transforms to a time derivative of the fluctuating pressure and thus the time history of pressure fluctuations at the boundary must be known for every frequency component of fluctuations. Together with the boundary conditions on $\partial\Omega = \partial\Omega_D \cup \partial\Omega_N \cup \partial\Omega_Z$ and heat release rate fluctuations of Eq. (2.34), Eq. (E.2) defines a nonlinear quadratic eigenvalue problem.

E.3 Finite Element Treatment

Eq. (E.2) can be spatially discretized and transformed into a finite element eigenvalue problem using a finite element procedure. Consider a spatial domain $\Omega \in \mathbb{R}$ with a piecewise smooth boundary $\partial\Omega$. N_e defines the number of finite elements Ω_i ($i \in 1...N_e$), N_v the number of vertices v_k ($k \in 1...N_n$) of which N_D elements are located on $\partial\Omega_D$. Without any loss in generality we may integrate the Helmholtz equation over the entire domain Ω and multiply it with a test function w_j, yielding

$$-\int_\Omega \frac{\partial}{\partial x_i}\left(\frac{1}{\bar{\rho}}\frac{\partial \hat{p}}{\partial x_i}\right) w_j \; d\Omega - \int_\Omega \frac{\omega^2}{\bar{c}^2\bar{\rho}}\hat{p}w_j \; d\Omega = 0. \tag{E.7}$$

The weak formulation of the problem is obtained by integrating the first term by parts and making use of Eqs. (E.4)-(E.6),

$$\int_\Omega \frac{1}{\bar{\rho}}\frac{\partial \hat{p}}{\partial x_i}\frac{\partial w_j}{\partial x_i} \; d\Omega - i\omega \int_{\partial\Omega_Z} \frac{1}{\bar{\rho}\bar{c}Z}\hat{p}w_j \; d\Omega_Z - \omega^2 \int_\Omega \frac{1}{\bar{c}^2\bar{\rho}}\hat{p}w_j \; d\Omega = 0. \tag{E.8}$$

Note that only the impedance boundary contributes to the boundary integral on the LHS, since $\hat{p} = 0$ for all $x \in \partial\Omega_D$ as well as $\nabla\hat{p} \cdot n = 0$ on $x \in \partial\Omega_N$. For the following derivation we consider linear finite elements where φ_k denotes the piecewise linear shape function for each node v_k. It is equal to one directly at node v_k and is zero for all $v_{j\neq k}$. Next, we approximate the complex unknown function $\hat{p}(x)$ by

$$\hat{p}(x) = \sum_{k=1}^{N} \hat{p}_k \varphi_k(x), \tag{E.9}$$

which directly satisfies the homogenous Dirichlet boundary condition on $\partial\Omega_D$. Following a Bubnov-Galerkin approach with weighting functions chosen equivalently to the solution variable approximations, yields

$$\sum_{k=1}^{N} \hat{p}_k \int_\Omega \frac{1}{\bar{\rho}}\frac{\partial \varphi_k}{\partial x_i}\frac{\partial \varphi_j}{\partial x_i} dx - \sum_{k=1}^{N} \hat{p}_k \int_{\partial\Omega_Z} \frac{\partial \varphi_k}{\partial x_i}\varphi_j n_i d\gamma - \omega^2 \sum_{k=1}^{N} \hat{p}_k \int_\Omega \frac{1}{\bar{\rho}\bar{c}^2}\varphi_k\varphi_j dx = 0, \tag{E.10}$$

coefficients $\hat{p}_k$ become constant and independent of space. Thus, they are extracted from the integral. Introducing the symmetric matrices

$$\mathbf{K}_{kj} = \int_\Omega \frac{1}{\bar{\rho}}\frac{\partial \varphi_k}{\partial x_i}\frac{\partial \varphi_j}{\partial x_i} \; dx, \quad \mathbf{D}_{kj} = -\int_{\partial\Omega_Z} \frac{i}{\bar{\rho}\bar{c}Z}\varphi_k\varphi_j \; d\gamma, \quad \mathbf{E}_{kj} = -\int_\Omega \frac{1}{\bar{c}^2\bar{\rho}}\varphi_k\varphi_j \; dx, \tag{E.11}$$

which are of size $N \times N$ we may rewrite Eq. (E.10) for the discrete acoustic problem

$$\omega^2 \mathbf{E}_{kj}\mathbf{P} + \omega \mathbf{D}_{kj}(\omega)\mathbf{P} + \mathbf{K}_{kj}\mathbf{P} = 0, \tag{E.12}$$

where $\mathbf{P}$ contains a number of N complex coefficients $\hat{p}_k$. Matrix $\mathbf{E}$ and $\mathbf{K}$ are completely real whereas $\mathbf{D}$ is complex except for the particular case of an purely imaginary impedance Z. Solving the homogeneous Eq. (E.12) means finding the characteristic eigenfrequencies and eigenmodes of the burner geometry, taking into account the flame by its mean temperature field but neglecting its unsteady effect. Because the coupling of acoustics and flame is not accounted for, there is no possibility to discriminate between unstable and stable operation conditions. As the flame acts as a source of acoustic energy an extra term needs to be introduced to the RHS:

$$\mathbf{S}_{kj} = -\int_{\Omega} \frac{\kappa - 1}{\bar{\rho}\bar{c}^2} \frac{\bar{\dot{q}}_V}{\bar{\rho}_{ref}\bar{u}_{ref}} n_l(x_i) e^{-i\omega\tau_l x_i} \varphi_j \frac{\partial}{\partial x_i} \varphi_k(x_{ref}) n_{ref} dx. \tag{E.13}$$

Note that $\mathbf{S}$ depends non-linearly on the pulsation ω and is not hermitian. The non-linearity originates from the assumption that the unsteady heat release is a function of a time delayed velocity perturbation, which converts into an exponential term in frequency space. Finally, the full discretized thermoacoustic eigenvalue problem writes

$$\omega^2 \mathbf{E}_{kj}\mathbf{P} + \omega \mathbf{D}_{kj}(\omega)\mathbf{P} + \mathbf{K}_{kj}\mathbf{P} = \mathbf{S}_{kj}(\omega)\mathbf{P}. \tag{E.14}$$

In fact, Eq. (E.10) can not easily be converted into a linear eigenvalue problem since it still depends quadratically on the pulsation ω and contains an exponential term in N. However, the first non-linearity can be resolved by introducing a new column vector

$$\mathbf{P}_\omega = \omega \mathbf{P} \tag{E.15}$$

and rewrite Eq. (E.14) as

$$\omega \mathbf{E}_{kj} P_\omega + \mathbf{D}_{kj}(\omega)\mathbf{P}_\omega + \mathbf{K}_{kj}\mathbf{P} = \mathbf{S}_{kj}(\omega)\mathbf{P} \tag{E.16}$$

Both equations, Eq. (E.15) and Eq. (E.16), can then be transformed into the following matrix form,

$$\begin{bmatrix} 0 & -\mathbf{I} \\ \mathbf{K} & \mathbf{D} \end{bmatrix} \begin{bmatrix} \mathbf{P} \\ \mathbf{P}_\omega \end{bmatrix} = \omega \begin{bmatrix} \mathbf{I} & 0 \\ 0 & \mathbf{E} \end{bmatrix} \begin{bmatrix} \mathbf{P} \\ \mathbf{P}_\omega \end{bmatrix} \tag{E.17}$$

where $\mathbf{I}$ defines the unitary matrix. If the impedance Z in matrix $\mathbf{D}$ does not depend on the pulsation and $\mathbf{S}_{kj}(\omega) = 0$, this matrix system is a linear eigenvalue problem and may be solved for the eigenfrequencies and corresponding eigenmodes $(\omega, \mathbf{P})$. The obtained solution accounts for the boundary conditions and can provide relevant information about the shape and frequency of the first few combustor modes. However, the non-linearity in N needs to be resolved in order to account for unsteady flames. This can be done by introduction of an iterative technique of Nicoud et al. (2007): If ω_k is the eigenfrequency at the k-th iteration, then matrix $\mathbf{D}$ including the impedance and matrix $\mathbf{S}$ including the flame coupling are assumed to be functions of the ω_{k-1} of the last iteration step, and thus become constant coefficient matrices. The quadratic eigenvalue problem is then defined through

$$\omega_k \mathbf{E}_{kj} \mathbf{P}_\omega + \mathbf{D}_{kj}(\omega_{k-1}) \mathbf{P}_\omega + \left[\mathbf{K}_{kj} - \mathbf{S}_{kj}(\omega_{k-1})\right] \mathbf{P} = 0. \tag{E.18}$$

Initialization for ω_0 is naturally done by calculation of the modes with an acoustically passive flame. This routine is implemented in this thesis around the finite element package COMSOL Multiphysics which solves the eigenvalue problem using an Arnoldi method available in the ARPACK-library (Lehoucq et al., 1998). Iterative updating of the linearization point leads to rapid convergence: For the real part of the eigenfrequency convergence is reached within four iterations while six iterations are generally needed for convergence of the eigenfrequencies imaginary part.

E.4 Validation Cases

Several test cases are selected to illustrate the potential of the method to account for complex impedance boundary conditions as well as non-isothermal active flames ($\hat{\dot{q}}_V \neq 0$). The major difficulty arising from the thermoacoustic problem given by Eq. (E.2) or Eq. (E.18) originates from the strong non-linearity of the source term with respect to the pulsation ω. Therefore, in a first step, the purely acoustic problem is considered by neglecting the influence of the unsteady flame, viz. $\hat{\dot{q}}_V = 0$. All test cases presented herein allow for a detailed comparison to available analytical or semi-analytical solutions.

E.4.1 Isothermal Rectangular Cavity

In this test case the capability of the Helmholtz code is assessed to account for complex valued impedances at domain boundaries. The computational domain is a rectangular cavity of length $L = 0.4\,\mathrm{m}$ and height $h = 0.1\,\mathrm{m}$ and the speed of sound inside the cavity is $\bar{c} = 450\,\mathrm{m\ s^{-1}}$. The domain is discretized using a uniform distribution of 600 triangular finite elements.

Two sets of boundary conditions are considered in the following. At first, the side edge is subjected to an impedance boundary, admitting a set of longitudinal modes. In the second configuration, a complex impedance is imposed to the top edge yielding a set of two dimensional or transversal modes. Both configurations and their respective boundary conditions are shown in Fig. E.1.

E.4.1.1 One Dimensional Modes

A homogeneous Neumann boundary condition Eq. (E.4) is subscribed to top, bottom and left boundaries, whereas a complex impedance of type

$$Z = Z_r + iZ_i \tag{E.19}$$

is imposed at the right boundary (see Fig. E.1 left). A set of one dimensional or longitudinal modes are solutions to this configuration. In case of a purely reactive impedance, viz. $Z = iZ_i$ with $Z_i \in \mathbb{R}$ the eigenfrequencies are given by

$$f_n = n\frac{\bar{c}}{2L} + \frac{\bar{c}}{2\pi L}\arctan\left(\frac{-i}{Z}\right), \qquad n \in \mathbb{N}, \tag{E.20}$$

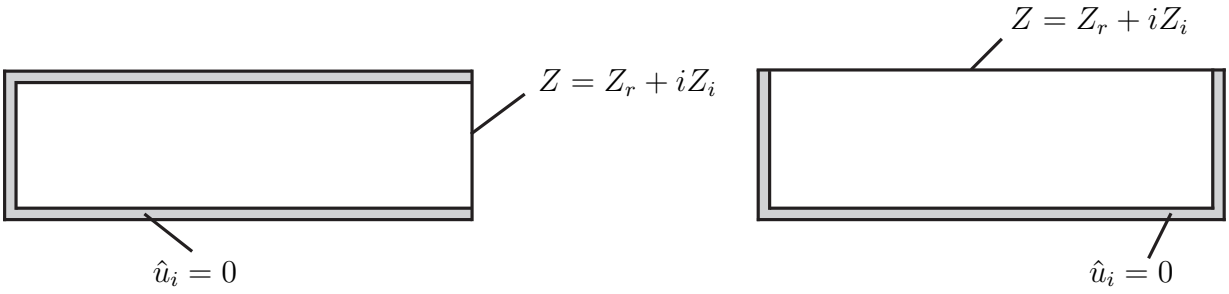

Figure E.1: Isothermal rectangular cavity supporting a number of longitudinal modes (left) and a number of transversal modes (right).

and are purely real. n defines the mode index. In this case the acoustic flux at the boundary is zero and the eigenmodes are marginally stable ($\Im(f) = 0$). If, on the other hand, a purely resistive impedance is selected, viz. $Z = Z_r$ with $Z_r \in \mathbb{R}$, the eigenfrequencies are complex valued and equal to

$$f_n = n\frac{\bar{c}}{2L} - i\frac{\bar{c}}{4\pi L}\ln\left(\frac{Z_r+1}{Z_r-1}\right), \qquad n \in \mathbb{N}. \tag{E.21}$$

If $Z_r < 0$ the acoustic flux at the boundary is positive and the eigenmode is unstable ($\Im(f) < 0$). If, on the other hand, $Z_r > 0$ the eigenmode becomes stable as the acoustic flux is negative transporting acoustic energy out of the computational domain. However, the eigenfrequencies imaginary part is independent of the mode index n. Furthermore, if $|Z_r| > 1$, viz. $(Z_r + 1)/(Z_r - 1) > 1$ the real part of f is a multiple of the half-wave mode $\bar{c}/2L$, whereas if $|Z_r| < 1$, viz. $(Z_r + 1)/(Z_r - 1) < 1$, the frequencies real part is of quarter wave mode shape, see Nicoud et al. (2007). Fig. E.2 illustrates that the solutions of the Helmholtz equation are in full agreement with the analytical findings.

E.4.1.2 Two Dimensional Modes

The following configuration admits a set of two dimensional modes. Homogeneous Neumann boundary conditions are subscribed to left, bottom and right edges, whereas a complex impedance ($Z = Z_r + iZ_i$) is imposed to the top boundary of the computational domain (see Fig. E.1 right). Solutions of the eigenmodes can be deduced from the dispersion relation

$$e^{2jk_yh}\left(k_y - \frac{k}{Z}\right) - \left(k_y + \frac{k}{Z}\right) = 0, \text{ with } k_y = \sqrt{k^2 - \left(\frac{n\pi}{L}\right)^2}, \quad n \in \mathbb{N}, \tag{E.22}$$

with a wavenumber $k = \omega/\bar{c}$. Similarly to the considerations above, if the impedance is purely reactive, viz. $Z = iZ_i$ with $Z_i \in \mathbb{R}$ the acoustic flux at the boundaries is zero and consequently the wave number k is real. In case of a purely resistive impedance $Z = Z_r$ with $Z_r \in \mathbb{R}$ the acoustic flux can be positive or negative depending on the mode index and both real and imaginary part of the eigenfrequencies depend on Z_r. For both considered cases and mode numbers, analytical solution, Eq. (E.22) and numerical results show high agreement (see Fig. E.3).

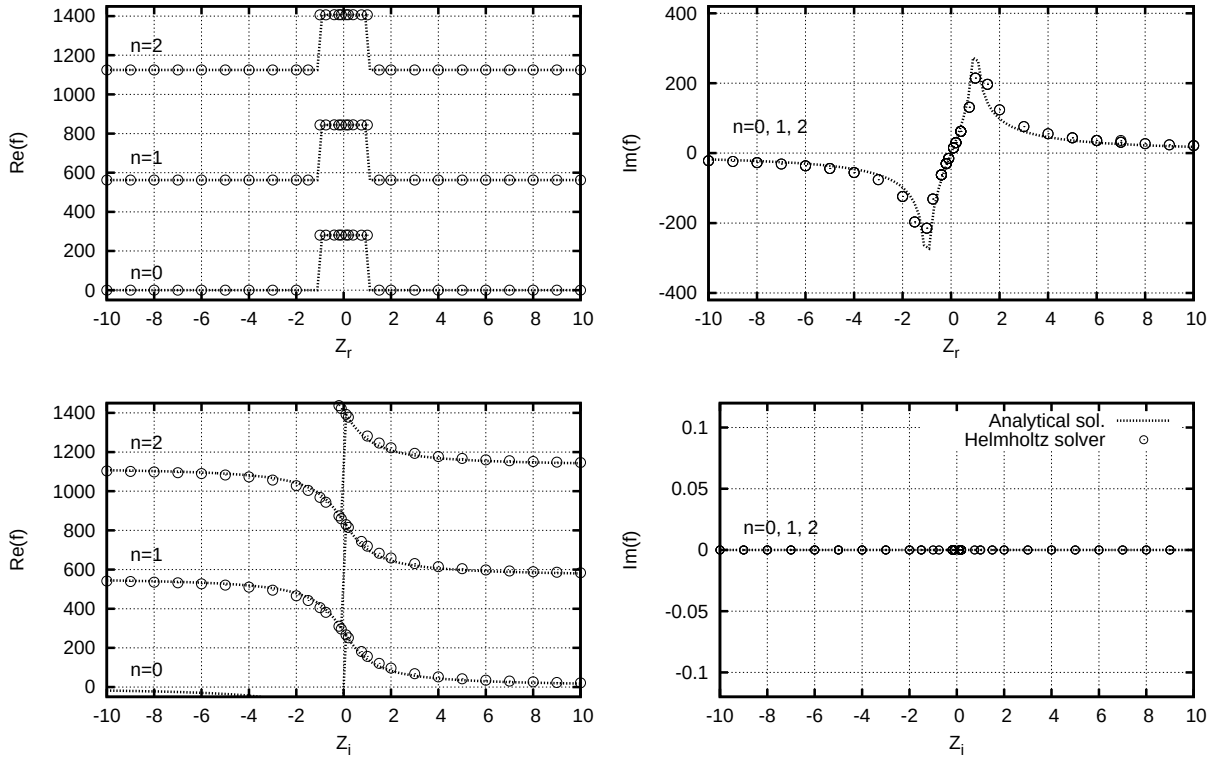

Figure E.2: Complex eigenvalues of one dimensional longitudinal modes in a cavity depending on the complex impedance $Z = Z_r + iZ_i$, value n indicates the different eigenmodes of the configuration.

E.4.2 One Dimensional Combustor

In this case the capability of the Helmholtz solver is tested to account for the influence of acoustically active flames. The configuration is quasi one dimensional and consists of a straight duct of length $L = 0.5\,\mathrm{m}$ and constant cross section $h = 0.1\,\mathrm{m}$. A reactive mixture enters the duct from the left boundary and is burnt in an infinitely thin flame sheet located in the middle of the duct, see Fig. 6.1. Its unsteady effect is modeled via the n-τ model Crocco (1951, 1952). After reaction, the burnt gas leaves the domain at the right boundary. The temperature ratio from burnt to unburnt mixture is chosen as $\bar{T}_2/\bar{T}_1 = 4$ to resemble engine conditions.

A semi-analytical solution can be obtained by considering linear wave propagation in both ducts sections, up- and downstream of the flame, see

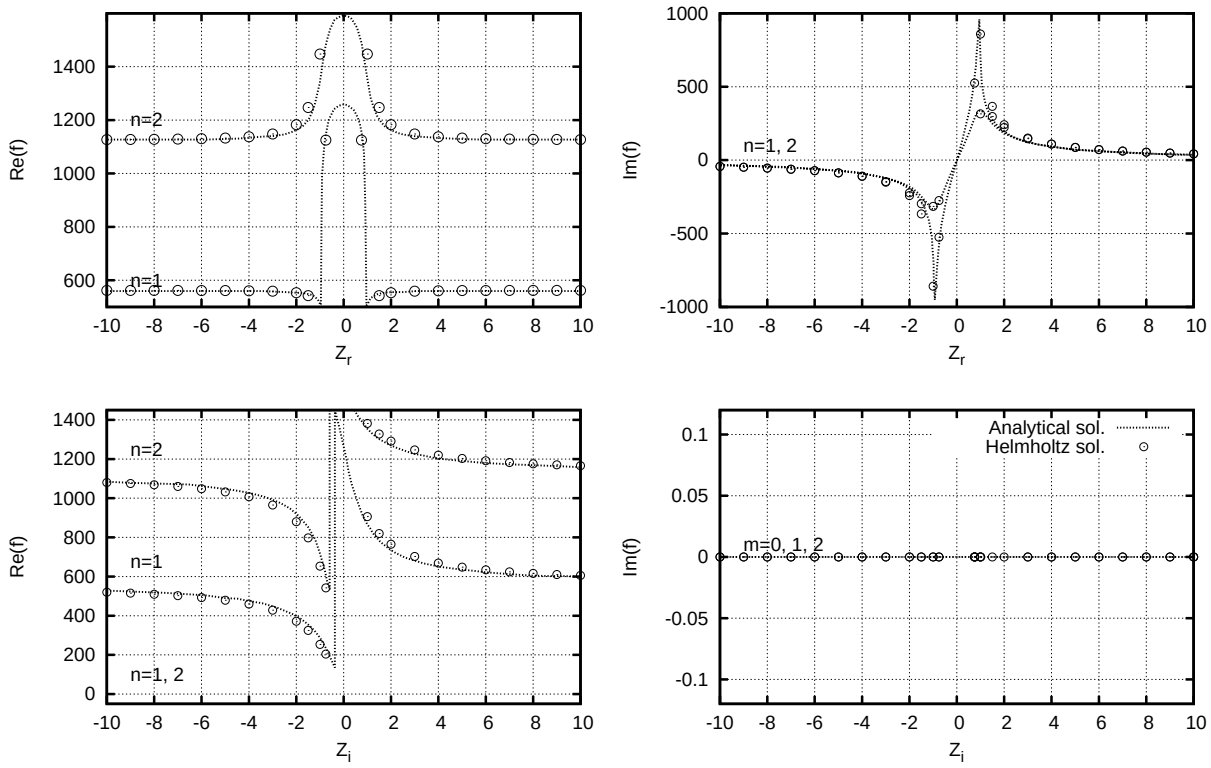

Figure E.3: Complex eigenvalues of two dimensional modes in a cavity depending on the complex impedance $Z = Z_r + iZ_i$, top: purely real (resistive) impedance, bottom: purely imaginary (reactive) impedance.

Eqs. (3.43) and (3.44). At the interface of both ducts, jump relations are defined from pressure continuity, i.e.

$$\hat{p}_1\left(x = l_1\right) = \hat{p}_2\left(x = 0\right), \tag{E.23}$$

and conservation of mass,

$$A_2\hat{u}_2 = A_1\hat{u}_1 + \frac{\kappa - 1}{\kappa\bar{p}}\hat{\dot{q}}_V, \tag{E.24}$$

where the indices 1 and 2 define the states of the reactive mixture and the burnt gases. We derive the semi-analytical solution for the general case of different duct lengths l_1 and l_2 and different cross sections A_1 and A_2.
For the unsteady heat release rate $\hat{\dot{q}}_V$ a n-τ model is chosen

$$\frac{\kappa - 1}{\kappa\bar{p}}\hat{\dot{q}}_V = A_1 n e^{-i\omega\tau}. \tag{E.25}$$

At the inlet ($x_1 = 0$) the velocity fluctuations are assumed to vanish, viz. $\hat{u} = 0$. At the outlet ($x = l_1 + l_2$) the fluid discharges into atmosphere and

an acoustic open boundary is prescribed, viz. $\hat{p} = 0$. Using the definitions of reflection coefficients, these boundaries can be expressed as

$$R_1 = \frac{\hat{p}_1^+}{\hat{p}_1^-} = 1, \tag{E.26}$$

$$R_2 = \frac{\hat{p}_2^+}{\hat{p}_2^-} e^{-2ik_2 l_2} = -1. \tag{E.27}$$

Applying Eq. (3.43) and Eq. (3.44) on the jump relations, Eq. (E.23) and (E.24) and introducing the n-τ model Eq. (E.25) yields

$$\hat{p}_1^+ e^{-ik_1 l_1} + \hat{p}_1^- e^{ik_1 l_1} = \hat{p}_2^+ + \hat{p}_2^-, \tag{E.28}$$

$$\Gamma\left(1 + ne^{-i\omega\tau}\right)\left(\hat{p}_1^+ e^{-ik_1 l_1} - \hat{p}_1^- e^{ik_1 l_1}\right) = \hat{p}_2^+ - \hat{p}_2^-, \tag{E.29}$$

where $\Gamma = A_1\bar{\rho}_2\bar{c}_2/A_2\bar{\rho}_1\bar{c}_1$ is a dimensionless coefficient which reduces to the ratio of impedances when both ducts have constant cross section. Using the jump relations Eqs. (E.28) and (E.29) and the boundary conditions Eqs. (E.26) and (E.26) a matrix $\mathbf{S}$ of the type

$$\mathbf{S}(\omega)\mathbf{P} = 0, \tag{E.30}$$

can be constructed, where $\mathbf{P}$ defines the vector of unknown complex pressure amplitudes, viz. $\mathbf{P} = (\hat{p}_1^+, \hat{p}_1^-, \hat{p}_2^+, \hat{p}_2^-)$. Then, matrix $\mathbf{S}$ is of the form

$$\mathbf{S} = \begin{bmatrix} 1 & -1 & 0 & 0 \\ \frac{1}{2}\left(1 + \Gamma\left(1 + ne^{-i\omega\tau}\right)\right)e^{-ik_1 l_1} & \frac{1}{2}\left(1 - \Gamma\left(1 + ne^{-i\omega\tau}\right)\right)e^{ik_1 l_1} & -1 & 0 \\ \frac{1}{2}\left(1 - \Gamma\left(1 + ne^{-i\omega\tau}\right)\right)e^{-ik_1 l_1} & \frac{1}{2}\left(1 + \Gamma\left(1 + ne^{-i\omega\tau}\right)\right)e^{ik_1 l_1} & 0 & -1 \\ 0 & 0 & e^{-2ik_2 l_2} & 1 \end{bmatrix} \tag{E.31}$$

Requiring matrix $\mathbf{S}$ to be singular $\det(\mathbf{S}) = 0$, yields a dispersion relation for the unknown eigenfrequencies ω and eigenvectors $\mathbf{P}$ of the problem. However, the characteristic equation cannot be solved explicitly for the eigenfunctions ω_n. Instead, numerical route finding has to be applied (see Polifke, 2003).

For the case of $l_1 = l_2$ and $A_1 = A_2$ the semi-analytical solution is calculated for two different values of the interaction index n, viz. $n = 0.01$ and $n = 5$ corresponding to small and high amplitude flame response respectively. The time-lag $\tau = 10^{-4}$s is selected in accordance with Nicoud et al. (2007) leading to a set of stable and unstable modes. The unstructured mesh used

for the Helmholtz algorithm consists of 17.500 triangular finite elements which are refined in the flame region located in the middle of the duct.

Deviations from the semi-analytical solution can be expected for two reasons (Benoit and Nicoud, 2005): First, the flame thickness of the semi-analytical model is assumed to be infinitely thin. This can not be realized in the finite element Helmholtz computation, where the flame thickness is at least as thick as the typical cell size in the flame region. In the present simulation it is set to $\delta_f = 0.001\,\mathrm{m}$. Secondly, as the flame has finite thickness the reference point of the flame model can not be placed directly at $L/2$, since it belongs to the reactive mixture gas side.

In the following, the exact eigenfrequencies are compared in Fig. E.4 with the numerical results obtained from the iterative algorithm described in Sec. 3.3.6. In the case of small amplitude response of the flame ($n = 0.01$), the iterative Helmholtz solver is in good agreement with the analytical findings. The first and fourth mode are found to be stable, while the third mode is amplified by the unsteady flame. Mode two is neither stable nor unstable since a velocity node is located in the flame region. When an steady flame is considered, i.e. $\hat{\dot{q}} = 0$ (or $n = 0$), all four modes are marginally stable, as no acoustic energy is transported in nor out of the system and the acoustic source function of the flame is zero.

A high flame response by the flame ($n = 5$) leaves the second mode unchanged, while the first and fourth mode are more damped. Fig. E.4 shows that the third mode is unstable and acoustically forced by the flame. Compared to the case with $n = 0.01$ the frequencies $\Re(f)$ of the eigenmodes deviate more strongly from the marginally stable solution without unsteady acoustic/flame interaction. Generally, it can also be observed that the prediction error increases with increasing frequency.

E.4.3 Two Dimensional Combustor

The generic combustor test case with constant cross section introduced above can be modified to incorporate an area change $A_2/A_1 = 2$ at the flame location $L/2$. Temperature, speed of sound and density distribution as well as all boundary conditions remain unchanged. The semi-analytic model of Eq. (E.31) is used by modification of the dimensionless coefficient

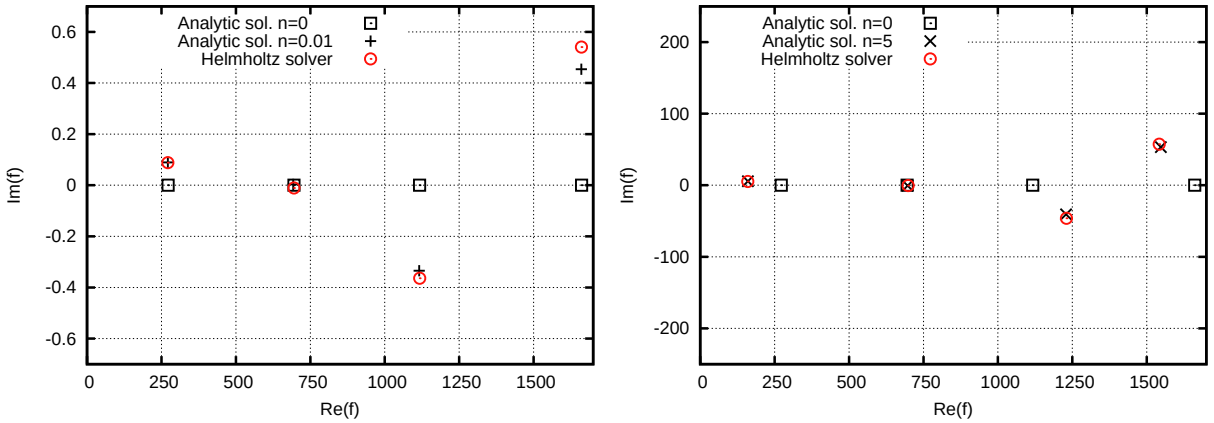

Figure E.4: First four eigenfrequencies of the generic model combustor with constant cross section. Simulation results are compared to the semi-analytic solution for small amplitude $n = 0.01$ (left) and high amplitude flame response $n = 5$ (right). Figures include location of modes with steady flame operation $n = 0$.

Γ to calculate the semi-analytical reference data. Kaufmann et al. (2002) solve this case analytically for the limiting $n \to 0$.

Similarly to the constant cross section combustor of Section E.4.2, differences are excepted in the simulation to originate from the finite thickness of the flame sheet and the location of the reference point. To minimize these inequalities an unstructured mesh is considered with 12.000 second order triangular finite elements. These are refined in the region of the area jump. A fame thickness of $\delta_f = 0.001\,\mathrm{m}$ is chosen which expands from $0.25\,\mathrm{m} \leq x \leq 0.251\,\mathrm{m}$. The reference point x_{ref} is located upstream of the flame $x = 0.2495\,\mathrm{m}$.

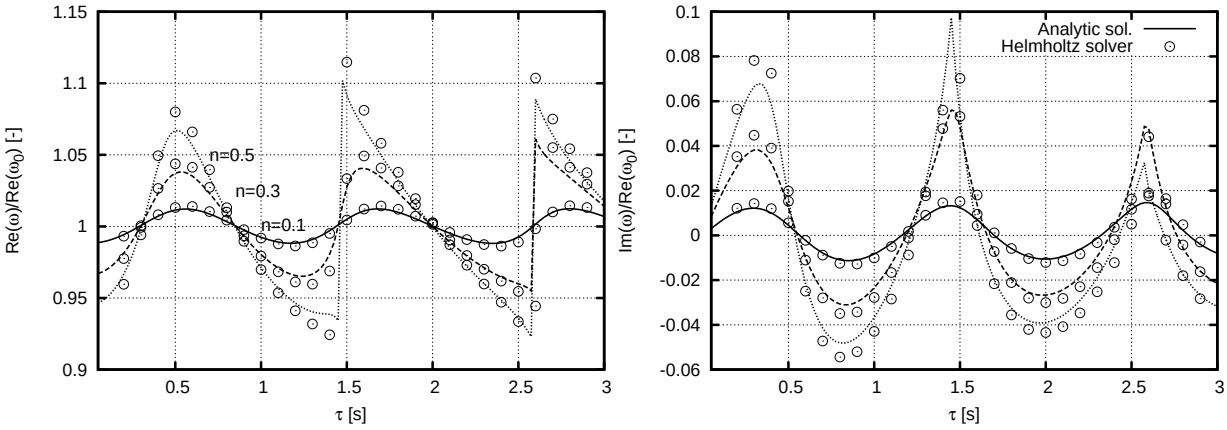

Figure E.5: Evolution of first eigenfrequency of a two dimensional combustion chamber as a function of interaction index $n = 0.1, 0.3$ and 0.5 and time delay τ.

The test case is used to study the detailed influence of the flame model parameters n and τ on the frequency and stability of the first eigenfrequency. Fig. E.5 compares the result of the semi-analytical solution and of the numerical prediction. Three ranges of instability $0.5\,\mathrm{s} \lesssim \tau \lesssim 1.25\,\mathrm{s}$, $1.6\,\mathrm{s} \lesssim \tau \lesssim 2.4\,\mathrm{s}$ and $2.7\,\mathrm{s} \lesssim \tau \lesssim 3\,\mathrm{s}$ exist. These ranges are relatively insensitive to the specific choice of amplitude of the flame response, viz. n. Latter variable solely augments the magnitude of damping or excitation by the flame. Generally, the stabilizing/destabilizing effect of the unsteady flame is captured with high agreement by the numerical method. Small deviations are observed with increasing interaction index n.

F One Dimensional Impedance LEE Solver

Predicting thermoacoustic instabilities in combustion chambers generally requires exact knowledge of the acoustic boundary conditions up- and downstream of the combustion chamber, respectively. At the entrance a diffusor decelerates the air flow to lower Mach numbers while at the exit the exhaust gas is accelerated in the downstream first turbine stage. The flow states inside the diffusor or nozzle depend on the operating conditions: While a diffusor is generally subsonic and thus unchoked, a nozzle operates under subsonic but also transonic conditions. It may thus be choked zeroing any mass flow fluctuations.

For an acoustic stability analysis two alternatives exist: One may either incorporate these elements fully into the numerical computation or impose complex impedances at its inlets and outlets which account for the complex reflection behavior of diffusor or nozzle elements. When employing the Helmholtz equation, the first alternative is not realizable, since the Helmholtz equation is derived for a zero baseline flow and loses its validity for higher Mach numbers. Thus, imposing the complex impedance representing mean flow effects is the only suitable choice. In case a stability analysis is carried out using the LNSEs or LEEs both alternatives are possible. However, when discretizing diffusor inlets or nozzle outlets, vortical and acoustic length scales become of the same order of magnitude ($\lambda_a = Ma\ \lambda_v$) and the numerical resolution must drastically increase. Under these circumstances, subscribing complex impedances at in- or outlets becomes advantageous in terms of numerical resources. Thus, analytical models or low-order numerical tools are required to predict the impedance behavior of combustion chamber diffusors and nozzles.

Many analytical models exist assessing the acoustic reflection behavior of such elements, see e.g. Mani (1981); Marble and Candel (1977) and Moase et al. (2007). In such models, generally an assumption about compactness

of the acoustic element or the specific velocity distribution is introduced. When the geometry becomes more complex a suitable alternative is to discretize the LEEs in one dimensional space. In this case no further assumption needs to be introduced. Recently, this procedure is introduced in a finite difference context by Lamarque and Poinsot (2008). Their routine is implemented into Matlab in this thesis, enabling the assessment of the unknown acoustic impedances of diffusers and nozzle flows. In the following, the approach is introduced and then validated against test cases with analytical solution or experimental data available.

F.1 Calculation of Mean Flow Distribution

Fields of mean density, velocity and pressure, viz. $(\bar{\rho}, \bar{u}, \bar{p})$ can be calculated from basic gas dynamic theory (Spurk and Aksel, 2006). With the inlet area A at $x = 0$ and the inlet Mach number known, the critical section A^* can be calculated from,

$$\frac{A(x)}{A^*} = \frac{1}{Ma^2}\left[\frac{2}{\kappa+1}\left(1+\frac{\kappa-1}{2}Ma^2\right)\right]^{(\kappa+1)/(\kappa-1)}. \tag{F.1}$$

When A^* is determined, the axial Mach number distribution is calculated from the same relation for any given axial distribution of $A(x)$. All other mean quantities can then be obtained from the isentropic relations using the respective total values at the inlet,

$$\frac{p_t}{p(x)} = \left(\frac{T_t}{T(x)}\right)^{\kappa/(\kappa-1)} = \left(\frac{\kappa-1}{2}Ma^2+1\right)^{\kappa/(\kappa-1)}, \tag{F.2}$$

$$\frac{\rho_t}{\rho(x)} = \left(\frac{T_t}{T(x)}\right)^{1/(\kappa-1)} = \left(\frac{\kappa-1}{2}Ma^2+1\right)^{1/(\kappa-1)}, \tag{F.3}$$

and $\bar{u}(x) = Ma\,\bar{c}$. The one dimensional mean flow computation is validated for a subsonic flow through a convergent-divergent nozzle of Section F.4. All inlet parameters are given therein. Fig. F.1 compares the result of a computational fluid dynamic simulation which is area averaged (Myrczik, 2006) and the one dimensional numerical solution of Eqs. (F.1)-(F.2). The one dimensional solution captures the flow profile through the nozzle very well.

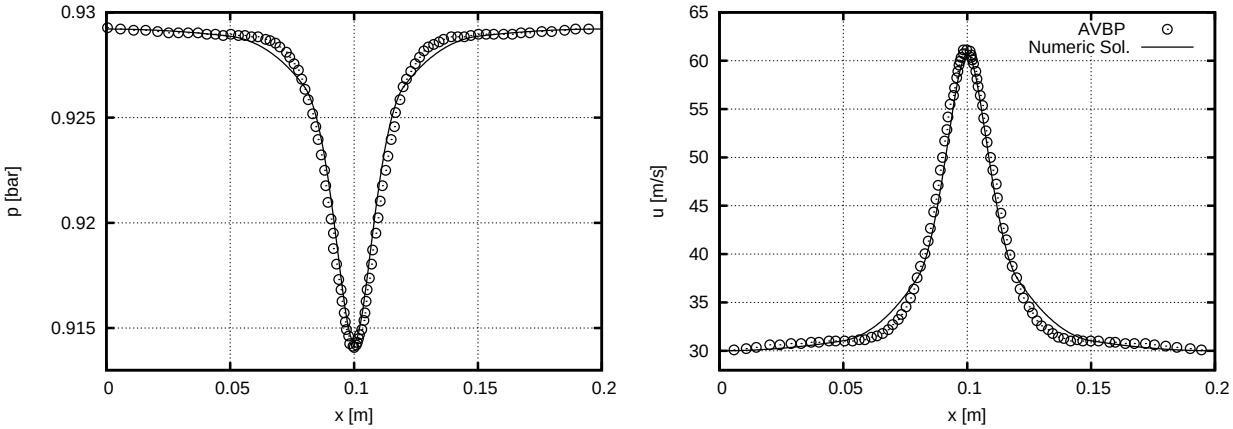

Figure F.1: Pressure and velocity distribution computed with a two dimensional flow solver AVBP (Myrczik, 2006) and results from the one dimensional approach for a subsonic flow through a diffusor.

F.2 Finite Difference LEEs Solver

Basis of the finite difference solver are the one dimensional LEEs formulated in frequency space. Existence of entropy waves is excluded and the gas is considered perfect with constant decomposition and heat capacities. With these assumptions, the quasi one dimensional LEEs are written (cp. to Marble and Candel, 1977):

$$\frac{\partial}{\partial t}\left(\frac{\rho'}{\bar{\rho}}\right) + \bar{u}\frac{\partial}{\partial x}\left(\frac{\rho'}{\bar{\rho}} + \frac{u'}{\bar{u}}\right) = 0, \tag{F.4}$$

$$\frac{\partial}{\partial t}\left(\frac{u'}{\bar{u}}\right) + \bar{u}\frac{\partial}{\partial x}\left(\frac{u'}{\bar{u}}\right) + \left(\frac{\rho'}{\bar{\rho}} + 2\frac{u'}{\bar{u}}\right)\frac{d\bar{u}}{dx} - \frac{p'}{\bar{p}}\frac{d\bar{u}}{dx} + \frac{\bar{p}}{\bar{\rho}\bar{u}}\frac{\partial}{\partial x}\left(\frac{p'}{\bar{p}}\right) = 0, \tag{F.5}$$

$$\left(\frac{\partial}{\partial t} + \bar{u}\frac{\partial}{\partial x}\right)\left(\frac{p'}{\bar{p}} - \kappa\frac{\rho'}{\bar{\rho}}\right) = \left(\frac{\partial}{\partial t} + \bar{u}\frac{\partial}{\partial x}\right)\left(\frac{s'}{c_v}\right) = 0. \tag{F.6}$$

Assuming harmonic oscillations of all fluctuating quantities,

$$\frac{p'}{\bar{p}} = \varphi(x)e^{i\omega t}, \qquad \frac{u'}{\bar{u}} = \nu(x)e^{i\omega t}, \qquad \frac{\rho'}{\bar{\rho}} = \delta(x)e^{i\omega t}, \tag{F.7}$$

and substitution into Eqs. (F.4)-(F.6) leads to a set of differential equations

$$i\omega\varphi + \bar{u}\frac{d\varphi}{dx} + \kappa\bar{u}\frac{d\nu}{dx} = 0, \tag{F.8}$$

$$\kappa\left(i\omega + 2\frac{d\bar{u}}{dx}\right)\nu + \left(\frac{1}{Ma^2} - 1\right)\bar{u}\frac{d\varphi}{dx} + \left[(1-\kappa)\frac{d\bar{u}}{dx} - i\omega\right]\varphi = 0, \tag{F.9}$$

which may be discretized in space to form a matrix system

$$S_i \begin{pmatrix} \varphi_i \\ \nu_i \end{pmatrix} = \begin{pmatrix} \varphi_{i-1} \\ \nu_{i-1} \end{pmatrix}, \tag{F.10}$$

where S_i is a 2×2 system matrix depending on mean flow properties, speed of sound and frequency. In terms or reduced variables, the impedance at every axial location inside the nozzle is then calculated from

$$Z = \frac{1}{\bar{\rho} c} \frac{p'}{u'} = \frac{1}{\kappa Ma} \frac{\varphi}{\nu}. \tag{F.11}$$

However, before the impedance may be calculated, a numerical boundary conditions needs to be prescribed at a certain location inside the diffusor or nozzle. Choked conditions represent an exception from this rule, since an analytical boundary condition can be derived from the linearized momentum equation Eq. (F.9) by substituting $Ma^* = 1$, yielding a throat impedance of

$$Z^* = \frac{1}{\kappa Ma} \frac{\varphi^*}{\nu^*} = \frac{2 \left.\frac{d\bar{u}}{dx}\right|^* + i\omega}{(\kappa - 1) \left.\frac{d\bar{u}}{dx}\right|^* + i\omega}. \tag{F.12}$$

When the diffusor or nozzle is not choked the situation is different. For this case up- or downstream impedances at the compressor exit or at the turbine inlet, respectively, must be known. As this information is generally not available simplified pressure outlet $\hat{p} = 0$, viz. $Z = 0$, or zero velocity fluctuations $\hat{u} = 0$, viz. $Z = \infty$, must be prescribed. At lower flow Mach numbers the unknown impedance represents the main source of error.

F.3 Cylindrical Duct Impedance

The finite difference code is validated for a straight duct, where an analytical solution exists. The duct has a length $L = 0.2\,\mathrm{m}$ and a constant speed of sound $\bar{c} = 334.6\,\mathrm{m\ s^{-1}}$ and density $\bar{\rho} = 1.1723\,\mathrm{kg\ m^{-3}}$ distribution. At the boundary $x = L$ a wall is placed, which writes in terms of impedance $Z = \infty$. For the limiting case of a zero baseline flow, viz. $\bar{u} = 0$, an analytical solution for the duct inlet impedance at $x = 0$ can be derived

$$Z_{in} = \frac{1 + e^{2ikL}}{1 - e^{2ikL}}. \tag{F.13}$$

When considering impedances close to infinity illustration of the boundary conditions in terms of admittance $Y_{in} = 1/Z_{in}$ is preferable. Decomposition of the admittance in real and imaginary part, yields

$$\Re(Y) = 0, \text{ and } \quad \Im(Y) = \frac{i \sin(2kL)}{1 + cos(2kL)}. \tag{F.14}$$

Fig. F.2 compares the results of the finite difference code to the analytical solution. In the whole frequency range $f = 0 - 3000$ Hz the agreement is very high.

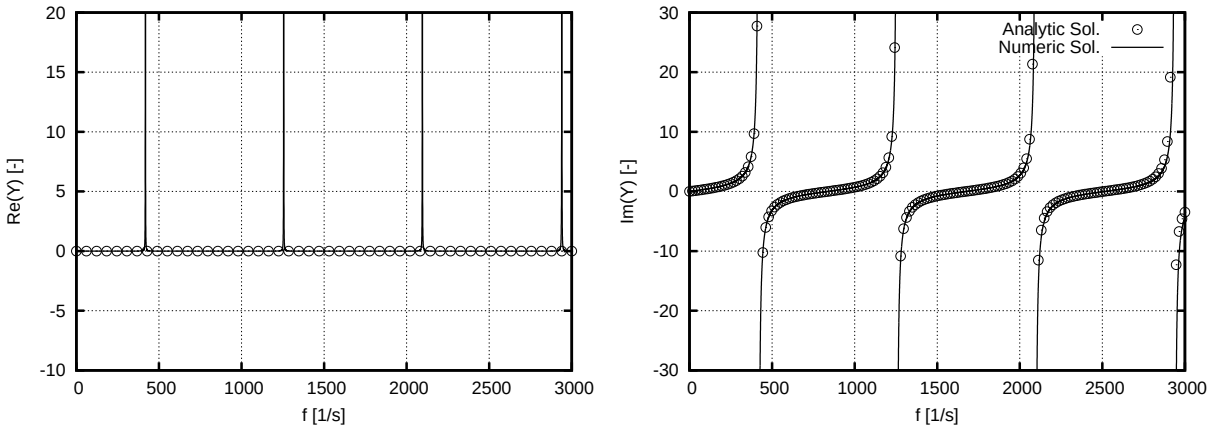

Figure F.2: Real and imaginary part of the acoustic admittance Y_{in} of a duct with constant cross section.

F.4 Subsonic Diffusor Admittance

Next, the subsonic flow through a diffusor is investigated. The flow state upstream of the diffusor is given by $\bar{u}_{in} = 30\,\mathrm{m\,s^{-1}}$, $\bar{T}_{in} = 300\,\mathrm{K}$, $\bar{\rho}_{in} = 1.074\,78\,\mathrm{kg\,m^{-3}}$ and $\bar{p}_{in} = 0.9292\,\mathrm{bar}$. Specific gas constant and ratio of specific heats are $R = 288.19\,\mathrm{J\,kg^{-1}\,K^{-1}}$ and $\kappa = 1.399$, respectively. The same configuration was investigated using a harmonically excited large eddy simulation within the flow solver AVBP as shown in Myrczik (2006). The mean flow state inside the diffusor generated by the LES and the one dimensional code presented herein, are compared in Fig. F.1 against each other. The obtained results are in very high agreement.

The admittance is evaluated at the diffusor exit at $x = 0.2$ which represents the acoustic boundary at the inlet of a combustion chamber. As the

flow is fully subsonic (see also Fig. F.1) an acoustic impedance needs to be prescribed at the upstream boundary. The results are compared to the harmonically results from the LES simulation and are presented in Fig. F.3. In the complete frequency range high agreement between LES and one dimensional LEEs solution is observed. Small discrepancies are shown at a frequency of approximately 2200 Hz.

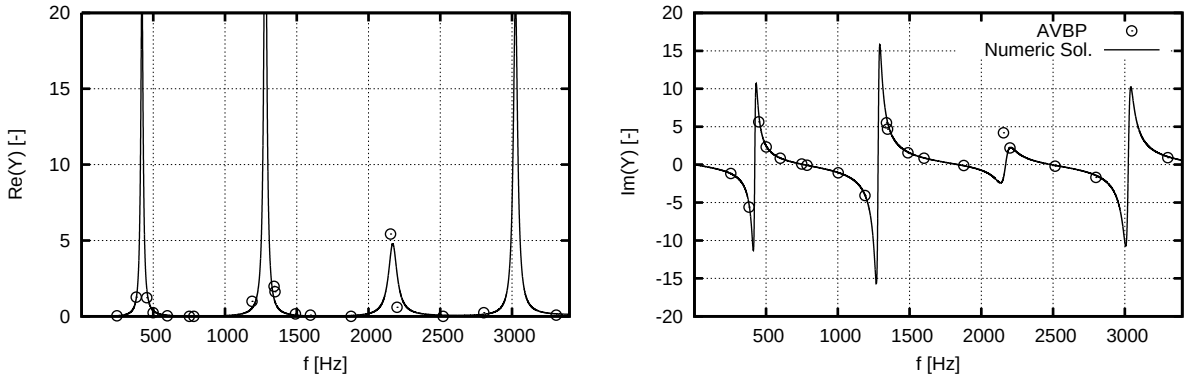

Figure F.3: Real and imaginary part of the acoustic admittance of a subsonic flow through a diffusor. Results of harmonically excited flow simulation within AVBP by Myrczik (2006) and results of the one dimensional LEEs method are compared against frequency.

F.5 Supersonic Nozzle Admittance

In the next test case a choked rocket combustion chamber nozzle is calculated and compared against available measurements of Kathan et al. (2010). The measurements comprise a frequency range $5.8 - 12.3\,\mathrm{kHz}$ at ambient inlet temperatures of $\bar{T}_{in} = 257\,\mathrm{K}$, a density of $\bar{\rho}_{in} = 2.07\,\mathrm{kg\ m^{-3}}$ and pressure $\bar{p}_{in} = 1.654\,\mathrm{bar}$. At the nozzle inlet a Mach number of $Ma_{in} = 0.25$ is reached.

In this case, the nozzle critical section is choked and an analytical solution exists for the impedance of the choked cross section. A high agreement between measurements and numerical routine can be expected. In this frequency range, a peak in the real part of the admittance is observed which corresponds to a change in sign of the imaginary part. Overall, the agreement reached is high as the LEEs solution approximates the measurements with a smooth curve.

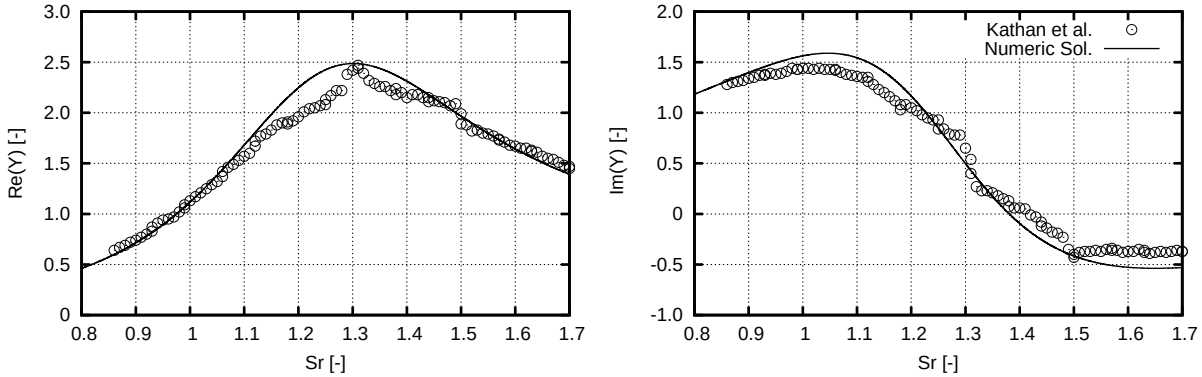

Figure F.4: Real and imaginary part of the acoustic admittance of a choked flow through a rocket combustion chamber outlet nozzle plotted against Strouhal number. Experiments of Kathan et al. (2010) are compared against the one dimensional LEEs solver.

Overall, the above selected validation test cases impressively illustrate that the one dimensional LEEs code is able to approximate inlet and outlet impedances quite well. This includes fully three dimensional flow cases as the one considered in this last section. However, it is noted again that if the flow is unchoked, knowledge of the upstream or downstream impedance of diffusors and nozzles respectively, is essential. Subscribing simplified boundary conditions may lead to the introduction of errors.

List of Figures

List of Tables

Supervised Theses

Associated with this Ph.D. thesis are a number of different "student theses" (Semester- and Diplomarbeiten or Bachelor and Master theses). These theses were prepared at the Lehrstuhl für Thermodynamik in the years 2010 through 2013 under the close supervision of the present author in its full academical and professional breadth and in all context-related concerns. Various issues were investigated contributing to the work presented in this thesis.

Student	**Thesis**
Wolfram Ullrich	*Aeroacoustic characterization of the scattering behavior of a non-reactive highly-swirled combustion chamber flow.* (English), Diplomarbeit, filed in November 2012.
Sebastian Ketterl	*Artificial diffusion schemes for stabilization of convective dominated acoustic equations.* (English), Bachelorarbeit, filed in April 2012.
Moritz Schulze	*Linearized Euler and Navier-Stokes equations for the determination of the acoustic scattering behavior of an area expansion and orifice.* (English), Diplomarbeit, filed in November 2011.
Josef Hasslberger	*Stabilized finite element methods for acoustic problems using the Helmholtz equation.* (German), Semesterarbeit, filed in March 2011.

Student	**Thesis**
Maximilian Steinhuber	*Flame transfer function of gaseous and liquid flames.* (German), Semesterarbeit, filed in November 2012.
Michael Neubert	*LabView supported measurements of kerosene flame transfer functions.* (German), Semesterarbeit, filed in September 2012.
Julian Mihé	*Mach number influence on combustion instabilities of a generic Rijke-tube configuration.* (English), Bachelor Thesis, filed in December 2011.
Matthias Kemmer	*Acoustic behavior of outlet and nozzle guide vanes in annular aero-engine combustors.* (German), Semesterarbeit, filed in January 2011.
Fabian Stoffels	*Combustion chamber design for thermoacoustic measurement applications.* (German), Semesterarbeit, filed in February 2011.
Wolfram Ullrich	*Mach number influence on general and thermoacoustic problems.* (German), Semesterarbeit, filed in November 2010.

References

A. Agarwal, P. J. Morris, and R. Mani. The calculation of sound propagation in nonuniform flows: Suppression of instability waves. *AIAA Journal*, 42 (1):80–88, 2004.

P. R. Alemela. *Measurement and scaling of acoustic transfer matrices of premixed swirl flames*. PhD thesis, Lehrstuhl für Thermodynamik, Technische Universiät München, 2009.

S. Allam and M. Åbom. Investigation of damping and radiation using full plane wave decomposition in ducts. *Journal of Sound and Vibration*, 292 (3-5):519–534, 2006.

S. Allam and M. Åbom. A new type of muffler based on microperforated tubes. *Journal of Vibration and Acoustics*, 133(3):031005–8, 2011.

P. R. Amestoy, I. S. Duff, J. Koster, and J.-Y. L'Excellent. A fully asynchronous multifrontal solver using distributed dynamic scheduling. *SIAM Journal on Matrix Analysis and Applications*, 23(1):15–41, 2001.

W. Arnoldi. The principle of minimized iterations in the solution of the matrix eigenvalue problem. *Quarterly of Applied Mathematics*, 9(1):17–29, 1951.

A. Arnone, M.-S. Liou, and L. A. Povinelli. Integration of navier-stokes equations using dual time stepping and a multigrid. *AIAA Journal*, 33 (6):985–990, 1995.

Y. Aurégan and R. Starobinski. Determination of acoustic energy dissipation/production potentiality from the acoustic transfer functions of a multiport. *Acta Acoustica*, 85(6):788–792, 1999.

O. Axelsson. *Iterative solution methods*. Cambridge University Press, Cambridge, 1996.

S. Bade, M. Wagner, C. Hirsch, and T. Sattelmayer. Design for thermoacoustic stability: Procedure and data base. In *Proceedings of ASME Turbo Expo 2013*, number GT2013-94131, San Antonio, Texas, USA, 2013a.

S. Bade, M. Wagner, C. Hirsch, and T. Sattelmayer. Design for thermoacoustic stability: Modeling of burner and flame dyamics. In *Proceedings of ASME Turbo Expo 2013*, number GT2013-95058, San Antonio, Texas, USA, 2013b.

F. Baillot, D. Durox, and R. Prud'homme. Experimental and theoretical study of a premixed vibrating flame. *Combustion and Flame*, 88(2):149–152, 1992.

C. Bailly and D. Juvé. Numerical solution of acoustic propagation problems using linearized Euler equations. *AIAA Journal*, 38(1):22–29, 2000.

C. Bailly, S. M. Candel, and P. Lafon. Prediction of supersonic jet noise from a statistical acoustic model and a compressible turbulence closure. *Journal of Sound and Vibration*, 194(2):219–242, 1996.

F. Bake, C. Richter, B. Mühlbauer, N. Kings, I. Röhle, F. Thiele, and B. Noll. The entropy wave generator (ewg): A reference case on entropy noise. *Journal of Sound and Vibration*, 326(3-5):574 – 598, 2009.

K. Balasubramanian and R.I. Sujith. Thermoacoustic instability in a Rijke tube: non-normality and nonlinearity. *Physics of Fluids*, 20(4):044103, 2008.

A. B. Bauer. Impedance theory and measurements on porous acoustic liners. *Journal of Aircraft*, 14(8):720–728, 1977.

D. W. Bechert. Sound absorption caused by vorticity shedding, demonstrated with a jet flow. In *Proceedings of the 5th AIAA Aeroacoustic Conference*, page 11, Seattle, March 1979.

D. W. Bechert. Sound absorption caused by vorticity shedding, demonstrated with a jet flow. *Journal of Sound and Vibration*, 70(3):389–405, 1980.

V. Bellucci, P. Flohr, and C.O. Paschereit. Numerical and experimental study of acoustic damping generated by perforated screens. *AIAA Journal*, 42(8):1543–1549, 2004.

L. Benoit. *Prédictions des instabilités thermoacoustiques dans les turbines à gaz - TH/CFD/05/41.* PhD thesis, Université Montpellier II: Spécialité Mathématiques et Modélisation, 2005.

L. Benoit and F. Nicoud. Numerical assessment of thermo-acoustic instabilities in gas turbines. *International Journal for Numerical Methods in Fluids*, 47(8-9):849–855, 2005.

M. Billson, L.-E. Eriksson, and L. Davidson. Acoustic source terms for the linearized Euler equations in conservative form. *AIAA Journal*, 43(4): 752–759, 2005.

H. Bodén and M. Abom. Influence of errors on the two-microphone method for measuring acoustic properties in ducts. *Journal of the Acoustical Society of America*, 79(2):541–549, 1986.

C. Bogey and C. Bailly. Decrease of the effective Reynolds number with eddy-viscosity subgrid-scale modeling. *AIAA Journal*, 43(2):437–439, 2005.

C. Bogey, C. Bailly, and D. Juvé. Computation of flow noise using source terms in linearized Euler's equations. *AIAA Journal*, 40(2):235–243, 2002.

S. Boij and B. Nilsson. Reflection of sound at area expansions in a flow duct. *Journal of Sound and Vibration*, 260(3):477–498, 2003.

S. Boij and B. Nilsson. Scattering and absorption of sound at flow duct expansions. *Journal of Sound and Vibration*, 289(3):577–594, 2006.

E. J. Brambley, M. Darau, and S. W. Rienstra. The critical layer in linear-shear boundary layers over acoustic linings. *Journal of Fluid Mechanics*, 710:545–568, 2012.

A. Brandt. *Multi-level adaptive technique (MLAT) for fast numerical solution to boundary value problems*, volume 1 of *Lecture Notes in Physics*. Springer Verlag, Berlin, 1973.

A. Brandt. *Guide to multigrid development.* Number 960 in Lecture Notes in Mathematics. Springer Verlag, Berlin, Heidelberg, New York, 1981.

A. N. Brooks and T. J. R. Hughes. Streamline upwind/Petrov-Galerkin methods for advection dominated flows with particular emphasis on the incompressible Navier-Stokes equations. *Computer Methods in Applied Mechanics and Engineering*, 32:199–259, 1982.

J. C. Bruggeman. *Flow induced pulsations in pipe systems.* PhD thesis, Eindhoven University of Technology, 1987.

J. C. Bruggeman, A. Hirschberg, M. E. H. van Dongen, A. P. J. Wijnands, and J. Gorter. Self-sustained aero-acoustic pulsations in gas transport systems: Experimental study of the influence of closed side branches. *Journal of Sound and Vibration*, 150(3):371–393, 11 1991.

S. M. Candel. Combustion dynamics and control: Progress and challenges. *Proceedings of the Combustion Institute*, 29(1):1–28, 2002.

B. T. Chu. On the generation of pressure waves at a plane flame front. *4th Symposium (Int.) on Combustion*, pages 603–612, 1953.

B. T. Chu. On the energy transfer to small disturbances in fluid flow (Part I). *Acta Mechanica*, 1(3):215–234, 1965.

B.-T. Chu and L. S. G. Kovasznay. Non-linear interactions in a viscous heat-conducting compressible gas. *Journal of Fluid Mechanics*, 3(5):494–514, 1958.

R. Codina. Comparison of some finite element methods for solving the diffusion-convection-reaction equation. *Computer Methods in Applied Mechanics and Engineering*, 156(1-4):185–210, 1998.

R. Codina. On stabilized finite element methods for linear systems of convection-diffusion-reaction equations. *Computer Methods in Applied Mechanics and Engineering*, 188(1-3):61–82, 2000.

COMSOL Multiphysics. *VERSION 4.1, Users Guide*, 2010.

S. M. Correa. A review of nox formation under gas-turbine combustion conditions. *Combustion Science and Technology*, 87(329–362), 1993.

D. G. Crighton. Basic principles of aerodynamic noise generation. *Progress in Aerospace Sciences*, 16(1):31–96, 1975.

L. Crocco. Aspects of combustion stability in liquid propellant rocket motors. Part I: fundamentals. low frequency instability with monopropellants. *American Rocket Society Journal*, 21(6):163–178, 1951.

L. Crocco. Aspects of combustion stability in liquid propellant rocket motors. Part II: low frequency instability with bipropellants. High frequency instability. *American Rocket Society Journal*, 22(1):7–16, 1952.

L. Crocco. Supercritical gaseous discharge with high frequency oscillations. *L'Aerotecnica*, 33(1):46–53, 1953.

N. Cumpsty and F. E. Marble. The interaction of entropy fluctuations with turbine blade rows; a mechanism of turbojet engine noise. *Proceedings of the Royal Society of London A*, 357:323–344, 1977.

A. Cuquel, D. Durox, and T. Schuller. Experimental determination of flame transfer function using random velocity perturbations. In *Proceeding of ASME Turbo Expo*, number GT2011-45881, Vancouver, Canada, June 2011. ASME.

J. W. Daniel, W. B. Gragg, L. Kaufman, and G. W. Stewart. Reorthogonalization and stable algorithms for updating the gram–schmidt QR factorization. *Mathematics of Computations*, 30(136):772–795, 1976.

J. Dassé, S. Mendez, and F. Nicoud. Large-eddy simulation of the acoustic response of a perforated plate. In *Proceedings of the 14th AIAA/CEAS Aeroacoustic Conference*, number AIAA2008-3007, Vancouver, Canada, May 2008.

P. O. A. L. Davis and K. R. Holland. The measurement and prediction of sound waves of arbitrary amplitude in practical flow ducts. *Journal of Sound and Vibration*, 271(3-5):849–861, 2004.

J. Donea and A. Huerta. *Finite element methods for flow problems*. John Wiley & Sons Ltd, West Sussex, England, 2003.

J. Jr. Douglas and J. Wang. An absolutely stabilized finite element method for the stokes problem. *Mathematics of Computations*, 186:495–508, 1989.

A.P. Dowling. The calculation of thermoacoustic oscillations. *Journal of Sound and Vibration*, 180(4):557–581, 1995.

A.P. Dowling. Nonlinear self-excited oscillations of a ducted flame. *Journal of Fluid Mechanics*, 346(1):271–290, 1997.

A.P. Dowling. A kinematic model of a ducted flame. *Journal of Fluid Mechanics*, 394(1):51–72, 1999.

S. Ducruix, D. Durox, and S. M. Candel. Theoretical and experimental determinations of the transfer function of a laminar premixed flame. *Proceedings of the Combustion Institute*, 28(1):765–773, 2000.

I. S. Duff, A. M. Erisman, and J. K. Reid. *Direct methods for sparse matrices*. Oxford University Press, London, 1986.

J. Eckstein. *On the mechanisms of combustion driven low-frequency oscillations in aero-engines*. PhD thesis, Lehrstuhl für Thermodynamik, Technische Universität München, 2004.

J. Eckstein, E. Freitag, C. Hirsch, and T. Sattelmayer. Experimental study on the role of entropy waves in low-frequency oscillations in a RQL combustor. *Journal of Engineering for Gas Turbines and Power*, 128(2):264–270, 2006.

J. D. Eldredge and A. P. Dowling. The absorption of axial acoustic waves by a perforated liner with bias flow. *Journal of Fluid Mechanics*, 485(1): 307–335, 2003.

J. D. Eldredge, D. J. Bodony, and M. Shoeybi. Numerical investigation of the acoustic behavior of a multi-perforated liner. In *Proceedings of the 13th AIAA/CEAS Aeroacoustic Conference*, number AIAA2007-3683, Rome, May 2007.

S. Evesque and W. Polfike. Low-order acoustic modelling for annular combustors: validation and inclusion of modal coupling. In *Proceedings of ASME Turbo Expo 2002*, number GT-2002-30064, Amsterdam, Netherlands, 2002.

S. Evesque, W. Polfike, and C. Pankiewitz. Spinning and azimuthally standing acoustic modes in annular combustors. In *Proceedings of 9th*

AIAA/CEAS Aeroacoustic Conference, number AIAA 2003-3182, USA, 2003.

R. Ewert and W. Schröder. Acoustic perturbation equations based on flow decomposition via source filtering. *Journal of Computational Physics*, 188 (2):365–398, 2003.

D. Fanaca, R. Alemela, C. Hirsch, and T. Sattelmayer. Comparison of the flow field of a swirl stabilised premixed burner in an annular and single burner combustion chamber. *Journal of Engineering for Gas Turbines and Power*, 132(6):071502, 2010.

R. P. Fedorenko. The speed of convergence of one iterative process. *USSR Computational Mathematics and Mathematical Physics*, 4(3):227–235, 1964.

M. Fleifil, A.M. Annaswamy, Z.A. Ghoneim, and A.F. Ghoniem. Response of a laminar premixed flame to flow oscillations: A kinematic model and thermoacoustic instability results. *Combustion and Flame*, 106(4):487–510, 1996.

R. W. Fletcher. Conjugate gradients methods for indefinite systems. pages 73–89. Springer Verlag, New York, 1975.

S. Föller and W. Polifke. Determination of acoustic transfer matrices via large eddy simulation and system identification. In *Proceedings of 16th AIAA/CEAS Aeroacoustic Conference*, number AIAA 2010-3998, Stockholm, Sweden, June 2010.

S. Föller and W. Polifke. Identification of aero-acoustic scattering matrices from large eddy simulation. application to a sudden area expansion of a duct. *Journal of Sound and Vibration*, 331(13):3096 – 3113, 2012. ISSN 0022-460X.

S. Föller, R. Kaess, and W. Polifke. Determination of acoustic transfer matrices via large eddy simulation and system identification. In *Proceedings of 16th AIAA/CEAS Aeroacoustics Conference*, number AIAA-2010-3998, 2010a.

S. Föller, W. Polifke, and D. Tonon. Aeroacoustic characterization of T-junctions based on large eddy simulation and system identification.

In *Proceedings of 16th AIAA/CEAS Aeroacoustic Conference*, number AIAA-2010-3985, Stockholm, Sweden, 2010b.

L. P. Franca, S. L. Frey, and T. J. R. Hughes. Stabilized finite element methods: I. application to the advective-diffusive model. *Computer Methods in Applied Mechanics and Engineering*, 95:253–276, 1992.

Y. Fukumoto and M. Takayama. Vorticity production at the edge of a slit by sound waves in the presence of a low-mach-number bias flow. *Physics of Fluids*, 3(12):3080–3082, 1991.

C. Fureby and F. F. Grinstein. Large eddy simulation of high-Reynolds-number free and wall-bounded flows. *Journal of Computational Physics*, 181(1):68–97, 2002.

G. Gabard. Discontinuous galerkin methods with plane waves for time-harmonic problems. *Journal for Computational Physics*, 225(2):1961–1984, 2007.

A. Gentemann, C. Hirsch, K. Kunze, F. Kiesewetter, T. Sattelmayer, and W. Polifke. Validation of flame transfer function reconstruction for perfectly premixed swirl flames. In *Proceedings of ASME Turbo Expo 2004*, number GT2004-53776, Vienna, Austria, 2004.

A. George and J. W. Liu. *Computer solution of large sparse positive definite systems*. Prentice-Hall, Englewood Cliffs, 1981.

A. Giauque, L. Selle, T. Poinsot, H. Buechner, P. Kaufmann, and W. Krebs. System identification of a large-scale swirled partially premixed combustor using LES and measurements. *Journal of Turbulence*, 6(21):1–20, 2005.

J. Gikadi, M. Schulze, S. Föller, J. Schwing, and T. Sattelmayer. Linearized Navier-Stokes and Euler equations for the determination of the acoustic scattering behaviour of an area expansion. In *18th AIAA/CEAS Conference*, number AIAA2012-2292, Colorado Springs, CO, June 4-6 2012.

G. H. Golub and C. F. Van Loan. *Matrix computations*. The Johns Hopkins University Press, Baltimore, 1996.

P. M. Gresho and R. L. Sani. *Incompressible flow and the finite element method*. John Wiley & Sons Ltd, Chichester, 1998.

E. Gullaud and F. Nicoud. On the effect of perforated plates on the acoustics of annular combustors. *AIAA Journal*, 50(12):2629–2642, 2012.

I. Gustafsson. A class of first order factorization methods. *BIT*, 18:142–156, 1978.

W. Hackbusch. A fast iterative method for solving helmholtz's equation in a general region. In U. Schumman, editor, *Computers, fast elliptic solvers and applications*, pages 112–124, London, 1978. Advance Publications.

W. Hackbusch. *Multi-grid methods and applications*, volume 4 of *Springer Series in Computational Mathematics*. Springer Verlag, Berlin, Heidelberg, New York, Tokio, 1985.

W. Hackbusch. *Iterative Lösung großer schwachbesetzter Gleichungssysteme*. Teubner, Stuttgart, 2te überarbeitete u. erweiterte edition edition, 1993.

J. Hadamard. Sur les problèmes aux dérivées partielles et leur signification physique. *Princeton University Bulletin*, pages 49–52, 1902.

Y. Hardalupas and M. Orain. Local measurements of the time-dependent heat release rate and equivalence ratio using chemiluminescent emission from a flame. *Combustion and Flame*, 139(3):188–207, 2004.

M. Hauser, C. Hirsch, and T. Sattelmayer. Influence of the confinement on the flame transfer function. In *Proceedings of the 18th International Congress on Sound and Vibration*, Rio de Janeiro, Brazil, July 2011a.

M. Hauser, M. Lorenz, and T. Sattelmayer. Influence of transversal acoustic excitation of the burner approach flow on the flame structure. *Journal of Engineering for Gas Turbines and Power*, 133(4):041501, 2011b.

M. F. Heidmann and P. R. Wieber. Analysis of n-Heptane vaporization in unstable combustor with traveling transverse oscillations. In *NASA TN D3424*, 1966.

M. R. Hestenes and E. Stiefel. Methods of conjugate gradients for solving linear systems. *Journal of Research of the National Bureau of Standards*, 49:409–436, 1952.

C. Hirsch. *Numerical computation of internal and external flows*, volume 2 of *Computational methods for inviscid and viscous flows*. John Wiley & Sons, Baffins Lane, Chister, West Sussex, England, 1990.

C. Hirsch, D. Fanaca, P. R. Reddy, W. Polifke, and T. Sattelmayer. Influence of the swirler design on flame transfer function of premixed flames. In *Proceedings of ASME Turbo Expo 2005*, number GT2005-68195, Nevada, USA, 2005.

G. C. J. Hofmans. *Vortex sound in confined flows*. PhD thesis, Technical University Eindhoven, 1998.

M. S. Howe. Contributions to the theory of aerodynamic sound, with applications to excess jet noise and the theory of a flute. *Journal of Fluid Mechanics*, 71(4):625–673, 1975.

M. S. Howe. On the theory of unsteady high Reynolds number flow through a circular aperture. In *Proceedings of the Royal Society of London. Series A, Mathematical, Physical and Engineering Sciences*, volume 366, pages 205–223, June 1979a.

M. S. Howe. Attenuation of sound in a low Mach number nozzle flow. *Journal of Fluid Mechanics*, 91(2):209–229, 1979b.

M. S. Howe. On the absorption of sound by turbulence and other hydrodynamic flows. *IMA Journal of Applied Mathematics*, 32(1–3):187–209, 1984.

M.S. Howe. The dissipation of sound at an edge. *Journal of Sound and Vibration*, 70(3):407–411, 1980.

M.S. Howe. *Acoustics of fluid-structure interactions*. Cambridge University Press, Cambridge, 1998.

Y. Huang and V. Yang. Dynamics and stability of lean-premixed swirl-stabilized combustion. *Progress in Energy and Combustion Science*, 35 (4):293–364, 2009.

I. J. Hughes and A. P. Dowling. The absorption of sound by perforated linings. *Journal of Fluid Mechanics*, 218(1):299–335, 1990.

T. J. R. Hughes. Recent progress in the development and understanding of SUPG methods with special reference to the compressible Euler and Navier-Stokes equations. *International Journal for Numerical Methods in Fluids*, 7(11):1261–1275, 1987.

T. J. R. Hughes. *The finite element method: Linear static and dynamic finite element analysis*. Lavoisier, 2000.

T. J. R. Hughes and A. N. Brooks. *A multidimensional upwind scheme with no crosswind diffusion*, pages 19–35. Number 34 in Finite Element Methods in Convection Dominated Flows. ASME AMD, 1979.

T. J. R. Hughes, L. P. Franca, and M. Balestra. A new finite element formulation for computational fluid dynamics: V. circumventing the babuska–brezzi condition: A stable Petrov–Galerkin formulation of the stokes problem accommodating equal–order interpolations. *Computer Methods in Applied Mechanics and Engineering*, 59(1):85 – 99, 1986. ISSN 0045-7825.

T. J. R. Hughes, L. P. Franca, and G. M. Hulbert. A new finite element formulation for computational fluid dynamics: 8. The Galerkin/Least-Square method for advective-diffusive equations. *Computer Methods in Applied Mechanics and Engineering*, 73(2):173–189, 1989.

T. J. R. Hughes, G. R. Feijóo, L. Mazzei, and J.-B. Quincy. The variational multiscale method–a paradigm for computational mechanics. *Computer Methods in Applied Mechanics and Engineering*, 166(1-2):3 – 24, 1998.

T. J. R. Hughes, G. Scovazzi, and L. P. Franca. *Multiscale and stabilized methods*. Wiley: Chichester, 2004.

T. J. R. Hughes, G. Scovazzi, and T. E. Tezduyar. Stabilized methods for compressible flows. *Journal of Scientific Computing*, 43(3):343–368, 2010.

T.J.R. Hughes. Multiscale phenomena: Green's functions, the Dirichlet-to-Neumann formulation, subgrid scale models, bubbles and the origins of stabilized methods. *Computer Methods in Applied Mechanics and Engineering*, 127(1-4):387–401, 1995.

T.J.R. Hughes, G. Hauke, K. Jansen, and Z. Johan. *Stabilized finite element methods in fluids: inspirations, origins, status and recent developments*, pages 272–292. Recent developments in finite element methods. CIMNE, Barcelona, 1994.

K. U. Ingard. Influence of fluid motion past a plane boundary on sound reflection, absorption, and transmission. *Journal of the Acoustical Society of America*, 31:1035—1036, 1959.

International Energy Agency. Key world energy statistics 2012. Technical report. URL `http://www.iea.org/publications/freepublications/publication/kwes.pdf`.

P. Jansohn, T. Ruck, C. Steinbach, H. P. Knöpfel, and T. Sattelmayer. Development of the advanced EV (AEV) burner for the ABB GTX100 gas turbine. In *Proceeding of ASME Turbo Asia*, number 97-AA-139, Singapore, 1997.

X. Jing and X. Sun. Experimental investigations of perforated liners with bias flow. *Journal of the Acoustical Society of America*, 106(5):2436–2441, 1999.

V. John and P. Knobloch. On spurious oscillations at layers diminishing (SOLD) methods for convection-diffusion equations: Part I - A review. *Computer Methods in Applied Mechanics and Engineering*, 196: 2197–2215, 2007.

C. Johnson. *Numerical solution of partial differential equations by the finite element method*. Cambridge University Press, 1987.

C. Jörg, J. Gikadi, and T. Sattelmayer. Numerical investigation of the plane-wave reflection coefficient of an exhaust pipe at elevated temperatures using linearized Navier-Stokes equations. In *Proceedings of ASME Turbo Expo 2013*, number GT2013-94843, San Antonio, Texas, USA, June 2013.

R. Kaess, A. Huber, and W. Polifke. A time-domain impedance boundary condition for compressible turbulent flow. In *Proceedings of 14th AIAA/CEAS Aeroacoustic Conference*, number AIAA-2008-2921, Vancouver, Canada, 2008.

F. C. Karal. The analogous acoustical impedance for discontinuities and constrictions of circular cross section. *Journal of the Acoustical Society of America*, 25(2):327–334, 1953.

N. Karimi, M. J. Brear, and W. H. Moase. Acoustic and disturbance energy analysis of a flow with heat communication. *Journal of Fluid Mechanics*, 597(1):67–89, 2008.

M. Karlsson and M. Åbom. Aeroacoustics of T-junctions – an experimental investigation. *Journal of Sound and Vibration*, 329(10):1793–1808, 2010.

R. Kathan, R. Kaess, J. Pieringer, and T. Sattelmayer. Nozzle admittance for higher modes. In *Proceedings of Deutscher Luft- und Raumfahrtkongress*, Hamburg, Germany, 2010.

A. Kaufmann, F. Nicoud, and T. Poinsot. Flow forcing techniques for numerical simulation of combustion instabilities. *Combustion and Flame*, 131(4):371–385, 2002.

J. J. Keller. Thermoacoustic oscillations in combustion chambers of gas turbines. *AIAA Journal*, 33(12):2280–2287, 1995.

J. J. Keller, W. Egli, and J. Hellat. Thermally induced low-frequency oscillations. *Journal of Applied Mathematics and Physics*, 36(12):250–274, 1985.

J. O. Keller and K. Saito. Measurements of the combusting flow in a pulse combustor. *Combustion Science and Technology*, 53(2-3):137–163, 1987.

A. Khavaran, E. A. Krejsa, and C. M. Kim. Computation of super-sonic jet mixing noise for an axisymmetric convergent-divergent nozzle. *Journal of Aircraft*, 31(3):603–609, 1994.

A. Kierkegaard, S. Allam, G. Efraimsson, and M. Åbom. Simulations of whistling and the whistling potentiality of an in-duct orifice with linear aeroacoustics. *Journal of Sound and Vibration*, 331(5):1084 – 1096, 2012a.

A. Kierkegaard, S. Boij, and G. Efraimsson. Simulations of the scattering of sound waves at a sudden area expansion. *Journal of Sound and Vibration*, 331(5):1068 – 1083, 2012b.

K. T. Kim, J. G. Lee, B. D. Quay, and D. A. Santavicca. Impact of the dynamic response of a swirl injector on combustion instability in a model gas turbine combustor. *Combustion and Flame*, 157(9):1718–1730, 2010.

T. Komarek and W. Polifke. Impact of swirl fluctuations on the flame response of a perfectly premixed swirl burner. *Journal of Engineering for Gas Turbines and Power*, 132(6):061503, 2010.

G. Kooijman, A. Hirschberg, and J. Golliard. Acoustical response of orifices under grazing flow: Effect of boundary layer profile and edge geometry. *Journal of Sound and Vibration*, 315(4-5):849–874, 2008.

L. S. G. Kovasznay. Turbulence in supersonic flow. *Journal of the Aeronautical Sciences*, 20(10):657–674, 1953.

C. Külsheimer and H. Büchner. Combustion dynamics of turbulent swirling flames. *Combustion and Flame*, 131(1-2):70–84, 2002.

R. Lacombe, S. Föller, G. Jasor, W. Polifke, Y. Aurégan, and P. Moussou. Identification of aero-acoustic scattering matrices from large eddy simulation application to whistling orifices in duct. *Accepted for publication in: Journal of Sound and Vibration*, 2011.

R. Lacombe, S. Föller, G. Jasor, W. Polfike, Y. Aurégan, and P. Moussou. Identification of aero-acoustic scattering matrices from large eddy simulation: application to whistling orifices in duct. *Journal of Sound and Vibration*, 2013. URL `http://dx.doi.org/10.1016/j.jsv.2013.04.036i`.

N. Lamarque and T. Poinsot. Boundary conditions for acoustic eigenmodes computations in gas turbine combustion chambers. *AIAA Journal*, 46(9): 2282–2292, 2008.

C. Lanczos. An iterative method for the solution of the eigenvalue problem of linear differential and integral operators. *Journal of Research of the National Bureau of Standards*, 45:255–282, 1950.

M. Lauer and T. Sattelmayer. On the adequacy of chemiluminescence as a measure for heat release in turbulent flames with mixture gradients. *Journal of Engineering for Gas Turbines and Power*, 132(6):061502, 2010.

B. E. Launder and D. B. Spalding. *Mathematical models of turbulence*. Academic Press Inc., London, 1972.

G. J. Le Beau, S. E. Ray, S. K. Aliabadi, and T. E. Tezduyar. SUPG infinite element computation of compressible flows with the entropy and conservation variables formulations. *Computer Methods in Applied Mechanics and Engineering*, 104(3):397–422, 1993.

R. Lehoucq, D. Sorensen, and C. Yang. *ARPACK users' guide: Solution of large scale eigenvalue problems with implicitly restarted arnoldi methods.* Society for Industrial and Applied Mathematics, 1998.

S. K. Lele. Computational aeroacoustics - A review. In *AIAA, 35th Aerospace Science Meeting & Exhibit*, number AIAA1997-0018, Reno, NV, January 1997.

K. Levenberg. A method for the solution of certain problems in least-squares. *Quarterly of Applied Mathematics*, 2:164–168, 1944.

H. Levine and J. Schwinger. On the radiation of sound from an unflanged circular pipe. *Physical Review*, 73(4):383–406, 1948.

M Leyko, F. Nicoud, S. Moreau, and T. Poinsot. Numerical and analytical investigation of the indirect noise in a nozzle. In *Proceedings of the Summer Program*, pages 343–354, Center for Turbulence Research, NASA AMES, Stanford University, 2008.

M. Leyko, F. Nicoud, and T. Poinsot. Comparison of direct and indirect combustion noise mechanisms in a model combustor. *AIAA Journal*, 47 (11):2709–2716, 2009.

T. Lieuwen. Modeling premixed combustion-acoustic wave interactions: A review. *Journal of Propulsion and Power*, 19(5):765–781, 2003.

T. Lieuwen and K. McManus. Introduction: Combustion dynamics in lean-premixed prevaporized (LPP) gas turbines. *Journal of Propulsion and Power*, 19(5):721, 2003.

T. Lieuwen and Y. Neumeier. Nonlinear pressure-heat release transfer function measurements in a premixed combustor. *Proceedings of the Combustion Institute*, 29(1):99–105, 2002.

T. Lieuwen and V. Yang. *Combustion instabilities in gas turbine engines: Operational experience, fundamental mechanisms and modeling*, volume 210. Progress in Astronautics and Aeronautics. AIAA, 2005.

T. Lieuwen and B. T. Zinn. The role of equivalence ratio oscillations in driving combustion instabilities in low NOx gas turbines. *Proceedings of the Combustion Institute*, 27(2):1809–1816, 1998.

R. Mani. Low-frequency sound propagation in a quasi-one-dimensional flow. *Journal of Fluid Mechanics*, 104(1):81–92, 1981.

R. R. Mankbadi, R. Hixon, S.-H. Shih, and L. A. Povinelli. Use of linearized Euler equations for supersonic jet noise prediction. *AIAA Journal*, 36(2): 140–147, 1998.

F. E. Marble. Some gasdynamic problems in the flow of condensing vapors. *Astronautica Acta*, 14:585–614, 1969.

F. E. Marble and S. M. Candel. Acoustic attenuation in fans and ducts by vaporization of liquid droplets. *AIAA Journal*, 13(5):634–639, 1975.

F. E. Marble and S. M. Candel. Acoustic disturbance from gas non-uniformities convected through a nozzle. *Journal of Sound and Vibration*, 55(2):225–243, 1977.

F. E. Marble and D. C. Wooten. Sound attenuation in a condensing vapor. *Physics of Fluids*, 13(11):2657–2664, 1970.

S. Marinov, M. Kern, K. Merkle, N. Zarzalis, A. Peschiulli, and F. Turrini. On swirl stabilized flame characteristics near the weak extinction limit. In *Proceedings of ASME Turbo Expo 2010*, volume 2, pages 259–268, Glasgow, UK, 2010.

D. Marquardt. An algorithm for least-squares estimation of nonlinear parameters. *SIAM Journal of Applied Mathematics*, 11:431–441, 1963.

C. Martin, L. Benoit, Y. Sommerer, F. Nicoud, and T. Poinsot. Large eddy simulation and acoustic analysis of a swirled staged turbulent combustor. *AIAA Journal*, 44(4):741–750, 2006.

M. Meissner. Excitation of Helmholtz resonator by grazing air flow. *Journal of Sound and Vibration*, 256(2):382–388, 2002.

A. Meister. Comparison of different Krylov subspace methods embedded in an implicit finite volume scheme for the computation of viscous and inviscid flow fields on unstructured grids. *Journal of Computational Physics*, 140(2):311–345, 1998.

A. Meister. *Numerik linearer Gleichungssysteme*. Friedr. Vieweg und Sohn Verlag, GWV Fachverlag GmbH, Wiesbaden, 3 edition, 2011.

S. Mendez and J. D. Eldredge. Acoustic modeling of perforated plates with bias flow for large eddy simulations. *Journal of Computational Physics*, 228(13):4757–4772, 2009.

H. J. Merk. Analysis of heat-driven oscillations of gas flows. General considerations. *Applied Science Research*, pages 317–336, 1956.

A. Michalke. On spatially growing disturbances in an inviscid shear layer. *Journal of Fluid Mechanics*, 23(3):521–544, 1965.

W. H. Moase, M. J. Brear, and C. Manzie. The forced response of choked nozzles and supersonic diffusors. *Journal of Fluid Mechanics*, 585(1):281–304, 2007.

J. P. Moeck, J.-F. Bourgouin, D. Durox, T. Schuller, and S. M. Candel. Nonlinear interaction between a precessing vortex core and acoustic oscillations in a turbulent swirling flame. *Combustion and Flame*, 159(8): 2650–2668, 2012.

H. C. Mongia, T. J. Held, G. C. Hsiao, and R. P. Pandalai. Challenges and progress in controlling dynamics in gas turbine combustors. *Journal of Propulsion and Power*, 19(5):822–829, 2003.

P. J. Morris and A. Agarwal. Radiation and refraction of sound waves through a 2-d shear layer. In *Proceedings of the 4th CAA Workshop on Benchmark Problems*, number NASA CP2004-212954, pages 23, 24, 2004.

P.M. Morse and K.U. Ingard. *Theoretical acoustics*. Princeton University Press, 1987.

M.L. Munjal and A.G. Doige. The two-microphone method incorporating the effects of mean flow and acoustic damping. *Journal of Sound and Vibration*, 137(1):135–138, 1990a.

M.L. Munjal and A.G. Doige. Theory of a two source-location method for direct experimental evaluation of the four-pole parameters of an aeroacoustic element. *Journal of Sound and Vibration*, 141(2):323–333, 1990b.

R. M. Munt. The interaction of sound with a subsonic jet issuing from a semi-infinite cylindrical pipe. *Journal of Fluid Mechanics*, 83(4):609–640, 1977.

R. M. Munt. Acoustic transmission properties of a jet pipe with subsonic jet flow: I. The cold jet reflection coefficient. *Journal of Sound and Vibration*, 142(3):413–436, 1990.

M. K. Myers. On the acoustic boundary condition in the presence of flow. *Journal of Sound and Vibration*, 71:429–434, 1980.

M. K. Myers. Transport of energy by disturbances in arbitrary steady flows. *Journal of Fluid Mechanics*, 226(1):383–400, 1991.

M. Myrczik. Determination of inlet impedances for acoustic eigenmode computation in combustion chambers. Technical Report WN/CFD/06/58, Toulouse, France, August 2006.

P. A. Nelson, P. E. Halliwell, and P. E. Doak. Fluid dynamics of a flow excited resonance, part I: Experiment. *Journal of Sound and Vibration*, 78(1):15–38, 1981.

P. A. Nelson, P. E. Halliwell, and P. E. Doak. Fluid dynamics of a flow excited resonance, part II: Theory. *Journal of Sound and Vibration*, 91 (3):375–402, 1983.

F. Nicoud and F. Ducros. Subgrid-scale stress modelling based on the square of the velocity gradient tensor. *Journal of Flow, Turbulence and Combustion*, 62:183–200, 1999.

F. Nicoud and T. Poinsot. Thermoacoustic instabilities: Should the Rayleigh criterion be extended to include entropy changes. *Combustion and Flame*, 142(1-2):153–159, 2005.

F. Nicoud and K. Wieczorek. About the zero mach number assumption in the calculation of thermoacoustic instabilities. *International Journal of Spray and Combustion Dynamics*, 1(1):67–111, 2009.

F. Nicoud, L. Benoit, C. Sensiau, and T. Poinsot. Acoustic modes in combustors with complex impedances and multidimensional active flames. *AIAA Journal*, 45(2):426–441, 2007.

N. Noiray, D. Durox, T. Schuller, and S. M. Candel. A unified framework for nonlinear combustion instability analysis based on the flame describing function. *Journal of Fluid Mechanics*, 615(1):139–167, 2008.

K. Oberleithner, S. Schimek, and C. O. Paschereit. On the impact of shear flow instabilities on global heat release rate fluctuations: Linear stability analysis of an isothermal and a reacting swirling jet. In *Proceedings of ASME Turbo Expo 2013*, number GT2012-69774, Copenhagen, Denmark, 2012.

J. R. Olson and G. W. Swift. Similitude in thermoacoustics. *Journal of the Acoustical Society of America*, 95(3):1405–1412, 1994.

P. Palies, D. Durox, T. Schuller, and S. M. Candel. Swirling flame instability analysis bases on the flame describing function methodology. In *Proceedings of ASME Turbo Expo 2010*, number GT2010-22294, Glasgow, UK, 2010.

P. Palies, T. Schuller, D. Durox, and S. Candel. Modeling of premixed swirling flames transfer functions. *Proceedings of the Combustion Institute*, 33(2):2967–2974, 2011.

C. Pankiewitz and T. Sattelmayer. Time domain simulation of combustion instabilities in annular combustors. *Journal of Engineering for Gas Turbines and Power*, 125(3):677–685, 2003.

K. S. Peat. The acoustical impedance at discontinuities of ducts in the presence of a mean flow. *Journal of Sound and Vibration*, 127(1):123–132, 1988.

M. C. A. M. Peters, A. Hirschberg, A. J. Reijnen, and A. P. J. Wijnands. Damping and reflection coefficient measurements for an open pipe at low Mach and low Helmholtz numbers. *Journal of Fluid Mechanics*, 256(1): 499–534, 1993.

M. Plummer. *JAGS Version 3.3.0 User Manual*, 2012.

T. Poinsot and S. K. Lele. Boundary conditions for direct simulations of compressible viscous flows. *Journal of Computational Physics*, 101(1): 104–129, 1992.

T. Poinsot and D. Veynante. *Theoretical and numerical combustion*. Edwards, Philadelphia, 2005.

T. Poinsot, A. C. Trouve, D. P. Veynante, S. M. Candel, and J. Esposito. Vortex-driven acoustically coupled combustion instabilities. *Journal of Fluid Mechanics*, 177:265–292, 1987.

W. Polifke. *Combustion instabilities*. VKI Lecture Series. Von Karman Institute of Fluid Dynamics, March 2003.

W. Polifke, C.O. Paschereit, and K. Döbbeling. Constructive and destructive interference of acoustic and entropy waves in a premixed combustor with a choked exit. *International Journal of Acoustics and Vibration*, 6 (3):135–146, 2001.

C. Prax, F. Golanski, and L. Nadal. Control of the vorticity mode in the linearized euler equations for hybrid aeroacoustic prediction. *Journal of Computational Physics*, 227(12):6044 – 6057, 2008.

R. B. Price, I. R. Hurle, and T. M. Sugden. Optical studies of the generation of noise in turbulent flames. *Symposium on Combustion*, 12(1):1093–1102, 1969.

R. J. Priem. Influence of the combustion process on stability. Technical Report NASA TN D-2957, National Aeronautics and Space Administration, Lewis Research Center, Cleveland, Ohio, 1965.

R. J. Priem and D. C. Guentert. Combustion instability limits determined by a nonlinear theory and a one-dimesnional model. In *NASA TN D-1409*, 1962.

M. Åbom. Measurement of the scattering-matrix of acoustical two-ports. *Mechanical Systems and Signal Processing*, 5(2):89–104, 1991.

M. Åbom and H. Bodén. Modelling of fluid machines as sources of sound in duct and pipe systems. *Acta Acoustica*, 3(6):549–560, 1995.

E. Åkervik. *Global stability and feedback control of boundary layer flows*. PhD thesis, Linné Flow Center, KTH Mechanics, Royal Institute of Technology, Stockholm, Sweden, 2008.

P.P. Rao and P. J. Morris. Use of finite element methods in frequency domain aeroacoustics. *AIAA Journal*, 44(7):1643–1652, 2006.

L. Rayleigh. The explanation of certain acoustic phenomena. *Nature*, 18: 319–321, 1878.

L. Rayleigh. *The theory of sound, volume I & II.* Macmillan and Co., Limited, second edition revised and enlarged edition, 1926.

H. S. Ribner. The generation of sound by turbulent jets. *Advances in Applied Mechanics*, 8(1):103–182, 1964.

C. Richter, H. Lück, L. Panek, and F. Thiele. Methods for suppressing shear layer instabilities for CAA. *Journal of Computational Acoutics*, 19 (2):181–203, 2011.

S. W. Rienstra, M. Darau, and E. J. Brambley. The trailing vorticity field behind a line source in two-dimensional incompressible linear shear flow. *Journal of Fluid Mechanics*, 720:618–636, 2013.

D. Rockwell. Oscillations of impinging shear layers. *AIAA Journal*, 21(5): 656–664, 1983.

D. Rockwell and E. Naudascher. Self-sustained oscillations of impinging free shear layers. *Annual Review of Fluid Mechanics*, 11(1):67–94, 1979.

D. Ronneberger. Theoretische und experimentelle untersuchung der schallausbreitung durch querschnittssprünge und lochplatten in strömungskanälen. Technical report, DFG-Abschlussbericht, Drittes Physikalisches Institut der Universität Göttingen, 1987.

Y. Saad. A flexible inner-outer preconditioned GMRES algorithm. *SIAM Journal on Scientific Computing*, 14(2):461–469, 1993.

Y. Saad. *Iterative methods for sparse linear systems.* Society for Industrial and Applied Mathematics, 2000.

Y. Saad. *Numerical methods for large eigenvalue problems.* Society for Industrial and Applied Mathematics, 2010.

Y. Saad and M. H. Schultz. GMRES: A generalized minimal residual algorithm for solving nonsymmetric linear systems. *SIAM Journal on Scientific and Statistical Computing*, 7(3):856–869, 1986.

T. Sattelmayer. Influence of the combustor aerodynamics on combustion instabilities from equivalence ratio fluctuations. *Journal of Engineering for Gas Turbines and Power*, 125(1):11–19, 2003.

M. Schäfer. *Numerik im Maschinenbau*. Springer Verlag, Berlin, Heidelberg, New York, 1999.

O. Schenk and K. Gärtner. Solving unsymmetric sparse systems of linear equations with PARDISO. *Journal of Future Generation Computer Systems*, 20(3):475–487, 2004.

H. Schlichting, K. Gersten, E. Krause, and H. Oertel. *Grenzschicht-Theorie*. Springer Verlag, Berlin, 10 edition, 2006.

P. J. Schmid and D. S. Henningson. *Stability and transition in shear flows*. Springer Verlag, Berlin, Heidelberg, New York, 2001.

T. Schoenefeld and M. Rudgyard. Steady and unsteady flow simulations using the hybrid flow solver AVBP. *AIAA Journal*, 37(11):1378–1385, 1999.

T. Schuller, D. Durox, and S. M. Candel. A unified model for the prediction of laminar flame transfer functions: Comparisons between conical and V-flames dynamics. *Combustion and Flame*, 134(1-2):21–34, 2003.

L. Selle, G. Lartigue, T. Poinsot, R. Koch, K.-U. Schildmacher, W. Krebs, B. Prade, P. Kaufmann, and D. Veynante. Compressible large eddy simulation of turbulent combustion in complex geometry on unstructured meshes. *Combustion and Flame*, 137(4):489–505, 2004.

L. Selle, L. Benoit, T. Poinsot, F. Nicoud, and W. Krebs. Joint use of compressible large-eddy simulation and Helmholtz solvers for the analysis of rotating modes in an industrial swirled burner. *Combustion and Flame*, 145(1-2):194–205, 2006.

C. Sensiau, F. Nicoud, M. van Gijzen, and J.T. van Leeuwen. A comparison of solvers for quadratic eigenvalue problems from combustion. *International Journal for Numerical Methods in Fluids*, 56(8):1481–1487, 2008.

J.-H. Seo and Y. J. Moon. Perturbed compressible equations for aeroacoustic noise prediction at low mach numbers. *AIAA Journal*, 43(8): 1716–1724, 2005.

M. C. F. Silva. *Numerical study of combustion noise in gas turbines*. PhD thesis, Université Montpellier II, CERFACS, 2011.

G. Sleijpen and H. Van der Vorst. A Jacobi-Davidson iteration method for linear eigenvalue problems. *SIAM Journal on Matrix Analysis and Applications*, 17(2):401–425, 1996.

G. Sleijpen, J. Booten, D. Fokkema, and H. Van der Vorst. Jacobi-Davidson type methods for generalized eigenproblems and polynomial eigenproblems. *BIT Numerical Mathematics*, 36(3):595–633, 1996.

S. A. Slimon, D. W. Davis, and C. A. Wagner. *Far-field aeroacoustic computation of unsteady cavity flow*. Number AIAA1998-0285. American Institute of Aeronautics and Astronautics, 1998.

J.H. Spurk and N. Aksel. *Strömungslehre*. Springer Verlag, Berlin, 2006.

S. R. Stow, A. P. Dowling, and T. P. Hynes. Reflection of circumferential modes in a choked nozzle. *Journal of Fluid Mechanics*, 467(1):215–239, 2002.

N. Syred. A review of oscillation mechanisms and the role of the precessing vortex core (PVC) in swirl combustion systems. *Progress in Energy and Combustion Science*, 32(2):93–161, 2006.

C.-J. Tam, P. D. Orkwis, and P. J. Disimile. Comparison of Baldwin-Lomax turbulence models for two-dimensional open cavity computatins. *AIAA Journal*, 34(3):629–631, 1995.

L. Tay Wo Chong, T. Komarek, R. Kaess, S. Föller, and W. Polifke. Identification of flame transfer functions from LES of a premixed swirl burner. In *Proceedings of ASME Turbo Expo 2010*, number GT2010-22769, Glasgow, Scotland, 2010.

L. Tay Wo Chong, S. Bomberg, A. Ulhaq, T. Komarek, and W. Polifke. Comparative validation study on premixed flame transfer function identification. *Journal of Engineering for Gas Turbines and Power*, 134(2): 021502, 2012.

B. J. Tester, G. Gabard, and Y. Özyörük. Influence of mean flow gradients on fan exhaust noise predictions. In *Proceedings of 14th AIAA/CEAS*

Aeroacoustic Conference, number AIAA 2008-2825, Vancouver, Canada, 2008.

P. Testud, Y. Aurégan, P. Moussou, and A. Hirschberg. The whistling potentiality of an orifice in a confined flow using an energetic criterion. *Journal of Sound and Vibration*, 325(4-5):769–780, 2009.

T. E. Tezduyar, M. Behr, S. K. A. Abadi, and S. E. Ray. A mixed CEBE/CC preconditioning for finite element computations. *Tech. Rep. UMSI 91/160, University of Minnesota, Minnesota Supercomputing Institute, Minneapolis, MN, June*, 1991.

A. Y. Tong and W. A. Sirignano. Multicomponent droplet vaporization in a high temperature gas. *Combustion and Flame*, 66(3):221–235, 1986.

A. Y. Tong and W. A. Sirignano. Vaporization response of fuel droplet in oscillatory field. In *Proceeding of ASME National Heat Transfer Conference*, number 87-HT-58, 1987.

N. Tran, S. Ducruix, and T. Schuller. Damping combustion instabilities with perforates at the premixer inlet of a swirled burner. *Proceedings of the Combustion Institute*, 32(2):2917–2924, 2009.

L. Trefethen and D. Bau. *Numerical linear algebra*. SIAM Philadelphia, 1997.

H.S. Tsien. The transfer function of rocket nozzles. *Journal of the American Rocket Society*, 22(3):139–143, 1952.

U. S. Energy Information Administration. International energy outlook 2010. Technical report, 2010. URL `http://www.eia.doe.gov/oiaf/ieo/highlights.html`.

H. van der Vorst. BI-CGSTAB: A fast and smoothly converging variant of BI-CG for the solution of nonsymmetric linear systems. *SIAM Journal on Scientific and Statistical Computing*, 13(2):631–644, 1992.

H. van der Vorst. *Iterative Krylov methods for large linear systems*. Cambridge Monographs on Applied and Computational Mathematics. Cambridge University Press, 2009.

B. Varoquié, J.-P. Légier, F. Lacas, D. Veynante, and T. Poinsot. Experimental analysis and large eddy simulation to determine the response of non-premixed flames submitted to acoustic forcing. *Proceedings of the Combustion Institute*, 29(2):1965–1970, 2002.

M. Wagner, C. Jörg, and T. Sattelmayer. Comparison of the accuracy of time-domain measurement methods for combustor damping. In *Proceedings of ASME Turbo Expo 2013*, number GT2013-94844, San Antonio, Texas, USA, June 3-7 2013.

W.A. Wall. *Fluid-Struktur-interaktion mit stabilisierten Finiten Elementen*. PhD thesis, Institut für Baustatik, Universität Stuttgart, 1999.

J. C. Wendoloski. Sound absorption by an orifice plate in a flow duct. *Journal of the Acoustical Society of America*, 104(1):122–132, 1998.

P. Wesseling. *An introduction to multigrid methods*. John Wiley and Sons, Chichester, 1992.

J. Wicker, W. Greene, S. Kim, and V. Yang. Triggering of longitudinal combustion instabilities in rocket motors - Nonlinear combustion response. *Journal of Propulsion and Power*, 12(6):1148–1158, 1996.

K. Wieczorek and F. Nicoud. Prediction of thermoacoustic instabilities: numerical study of mach number effects. In *Proceedings of 16th AIAA/CEAS Aeroacoustics Conference*, Stockholm, Sweden, 2010.

K. Wieczorek, C. Sensiau, W. Polifke, and F. Nicoud. Assessing non-normal effects in thermoacoustic systems with non-zero baseline flow. In *Proceedings of n3l Int'l Summer School and Workshop on Non-Normal and Nonlinear Effects in Aero- and Thermoacoustics*, Munich, Germany, May 17-21 2010.

R. Wienands, C. W. Oosterlee, and T. Washio. Fourier analysis of GMRES(m) preconditioned by multigrid. *SIAM Journal on Scientific Computing*, 22(2):582–603, 2000.

V. Yakhot and S. A. Orszag. Renormalization group analysis of turbulence. i. basic theory. *Journal of Scientific Computing*, 1(1), 1986.

V. Yakhot, S. A. Orszag, S. Thangam, T.B. Gatski, and C. G. Speziale. Development of turbulence models for shear flows by a double expansion technique. *Physics of Fluids A*, 4(7):1510–1520, 1992.

V. Yang and F. Culick. On the existence and stability of limit cycles for transverse acoustic oscillations in a cylindrical combustion chamber. 1: standing modes. *Combustion Science and Technology*, 45(1):37–65, 1986.

M. V. Zagarola and A. J. Smits. Mean-flow scaling of turbulent pipe flow. *Journal of Fluid Mechanics*, 373(1):33–79, 1998.

X. Zhang, X. X. Chen, C. L. Morfey, and P. A. Nelson. Computation of spinning modal radiation from an unflanged duct. *AIAA Journal*, 42(9): 1795–1801, 2004.

O. C. Zienkiewicz and R. L. Taylor. *The finite element method, volume 1: the basics*. Butterworth-Heinemann, Oxford, 2000.

B. T. Zinn and T. C. Lieuwen. *Combustion instabilities: basic concepts*. AIAA, 2005.

H. B. Zubair, C. C. W. Leentvaar, and C. W. Oosterlee. Multigrid preconditioners for Bi-CGSTAB for the sparse-grid solution of high-dimensional anisotropic diffusion equation. *Journal of Prime Research in Mathematics*, 3:186–200, 2007.

E. E. Zukoski and J. M. Auerbach. Experiments concerning the response of supersonic nozzles to fluctuating inlet conditions. *Transactions of the ASME, Journal of Engineering for Gas Turbines and Power*, 98(1):60–64, 1976.